DESIGNING COILED-COIL PEPTIDE MATERIALS FOR BIOMEDICAL APPLICATIONS

by

Michael D. Jorgensen

A Dissertation

Submitted to the Faculty of Purdue University

In Partial Fulfillment of the Requirements for the degree of

Doctor of Philosophy

Department of Chemistry

West Lafayette, Indiana

August 2023

THE PURDUE UNIVERSITY GRADUATE SCHOOL
STATEMENT OF COMMITTEE APPROVAL

Dr. Jean Chmielewski, Chair

Department of Chemistry

Dr. Mark Lipton

Department of Chemistry

Dr. Jianguo Mei

Department of Chemistry

Dr. Chengde Mao

Department of Chemistry

Approved by:

Dr. Christine Hrycyna

To my family and friends

ACKNOWLEDGMENTS

First and foremost, I would like to thank my research advisor, Professor Jean Chmielewski. Her dedication to guiding graduate students is admirable, and she has contributed significantly to my success in graduate school. I would also like to thank her for giving me the intellectual freedom to explore my own ideas. She has trained me with the perseverance to tackle difficult research problems and provided me with the tools needed to succeed in my career.

I would also like to thank my committee members Professor Jianguo Mei, Professor Shelley Claridge, and Professor Chengde Mao as well as Professor Mark Lipton for their flexibility in attending my virtual original proposal during the pandemic and for taking the time to attend and provide insight during my seminar and thesis defense. I am also deeply indebted to the research staff at Purdue: Dr. Patricia Bishop (Research Instrumentation Center), Laurie Mueller and Bob Seiler (Electron Imaging Facility), and Bridget Haley and Mike Alley (Cell Culture Facility). Their guidance and eagerness to assist were major contributors to my success in graduate school. I would also like to thank David Kissick and Qingping Xu at Argonne National Laboratory as well as Professor Chittaranjan Das and Rishi Patel for all of their assistance and insight with crystallography data. I also want to thank Professor Ranjie Xu and Yanru Ji for their help and guidance in culturing brain organoids. I also would like to thank the National Science Foundation for supporting this work through grant CHE-2108722.

I would also like to thank both my former and current lab members these past five years. I first want to thank my mentor, Ryan Curtis. His constant guidance and willingness to help are truly the reason I excelled in graduate school. I also want to thank Thomas Dietsche for his help in cell culture and general advice as I navigated through graduate school. Thank you to Corey Johnson for all of his stories and being part of the early morning and late-night crew with me. To Andrew Encinas, for our long research discussions, for always proposing wild ideas with me, co-mentoring the lab together, and for our Canada adventures. I want to thank Monessha Nambiar, Reena Blade, Jenny Rowe, Vallabh Suresh, Moises Morales, Sam Zeiders-Young, and Vinny Menon for welcoming me into the lab when I first joined. Finally, I'd like to thank Anna Pavlishchuk, Zach St. John, Josh Rumple, Ambar Rosario, Nosa Idahagbon, Douglas Chan, Ashutosh Agrahari, Joy Wu, Aly Reichel, Colleen Coady, Ranya Pendyala, and Marianna Chicas for their companionship and advice during graduate school.

I also need to give a huge thank you to all of my friends outside of the lab. Thank you to Kristen Berger, Amir Alwali, and Jen Mishevich for all their comradery and support both in classes and research these past five years. I look forward to seeing where all of our future careers take us. I want to also thank Dung Tran and Yuichiro Watanabe for being the cheerful, friendly faces I would see in the hall each week.

I would also like to thank my friends from UIUC for all their support during graduate school. Thank you to Yijung Chen for, despite being across the world, always being my motivation to try my best and put in my best effort. Thank you to Tae Wook Kim for all of our photography discussions and answering my research questions. To Enos Lee, for checking up on me and always welcoming me back to Chicago. To Will Liu, for constantly being there for me and dropping everything in your busy schedule to help me out. To Jing Lian Ng (and family), for all of my visits back to UIUC, holidays spent together, and always cheering me on in graduate school. Finally, to Adhika Retnanto for keeping my engineering skills sharp and reminding me of my love for teaching.

Finally, I would like to thank my family for all of their love and support throughout my life. Words cannot describe how grateful I am to have them. They have always supported my interests and whatever path I took. Thank you for instilling in me a strong work ethic that helped me persevere through both engineering and graduate school. Their love and kindness have made all of my successes possible. Thank you.

TABLE OF CONTENTS

LIST OF FIGURES

LIST OF TABLES

LIST OF SCHEMES

LIST OF APPENDIX FIGURES

LIST OF APPENDIX TABLES

ABSTRACT

Peptide biomaterials have drawn great attention in recent decades owing to their tunability and biocompatibility. Coiled-coils specifically have become a well-studied scaffold with a clear sequence-to-structure relationship. As such, the Chmielewski lab has extensively studied peptide assemblies based on the GCN4 leucine zipper. First, we present the peptide **TriCross**, where nitrilotriacetic acid (NTA) and di-histidine ligands are installed at the N- and C-terminus, respectively, and a bipyridine ligand installed at a central, solvent exposed position. Through strategic placement of these metal-binding ligands, TriCross assembled into a three-dimensional (3D) mesh in the presence of zinc ions and dissembled following mild ethylenediaminetetraacetic acid (EDTA) treatment. These properties created a 3D network capable of encapsulating cells for extended periods of time (>1 week) and releasing cells upon metal-chelation.

Next, we describe a stabilized nanotube and enhanced crystal assembly through a heterocoiled-coil assembly. Nanotubes composed of the coiled-coil peptide **TriNL** that assembled likely through ionic interactions rapidly degraded in phosphate buffered saline (PBS). To improve stability, a peptide with metal-binding ligands, **p2L**, was introduced through thermal annealing of the two peptides. Low levels of **p2L** (up to 10:1 **TriNL**:**p2L**) retained nanotube morphology while simultaneously introducing NTA and di-histidine ligands. Upon addition of metal, metal-ligand interactions were established within the nanotube and increased stability of the material. Higher levels of **p2L** (2:1 **TriNL**:**p2L**) led to hexagonal crystals similar to **p2L** but now without the use of metal ions. These crystals expanded the scope of protein inclusion by removing the requirement for His-tags on proteins to be incorporated within the material.

Finally, a self-replicating and self-assembling coiled-coil peptide is reported. The coiled-coil **TriNL** was cysteine modified (N20C) to create a peptide capable of native chemical ligation. At low concentrations, the **N20C FL** peptide acted as a template for the cysteine and thioester fragments while high concentrations led to fibrillar structures. The size of the fibrils was controlled through the addition of preassembled seeds into the native chemical ligation system.

CHAPTER 1. RECENT ADVANCES IN COILED-COIL PEPTIDE MATERIALS AND THEIR BIOMEDICAL APPLICATIONS

1.1 Introduction

Engineered biomaterials have been studied extensively for numerous applications, such as drug delivery and tissue regeneration.[1–3] Peptide-based materials specifically have drawn attention for their programmability and biocompatibility.[4–7] The use of natural and unnatural amino acid building blocks allows for facile modification of the peptide sequence and generation of various secondary and supersecondary folds. The coiled-coil motif, for instance, has drawn substantial interest due to its clear sequence-to-structure relationship and ease of tunability.[8,9]

The coiled-coil structure is widely observed in nature, and plays an essential role in many biological processes, including DNA recognition and gene regulation. The coiled-coil motif is composed of two or more alpha-helices that wrap around each other to form a left-handed supercoil (Figure 1.1). Each alpha-helix contains heptad repeats (*abcdefg*), with traditionally hydrophobic *a* and *d* residues influencing the oligomeric state of the coiled-coil from dimers to heptamers.[10–12] The *e* and *g* residues are commonly ionic, with complementary charges between individual helices within the coiled-coil, while the remaining positions (*b*, *c*, and *f*) are solvent exposed and are typically filled with hydrophilic residues.

With these well-established structural parameters, general guidelines to design *de novo* coiled-coils have been developed.[8,9] Meanwhile, others have drawn inspiration from naturally occurring coiled-coils, such as those found in the transcription factors GCN4 and Jun-Fos.[10,13,14] A few recent reviews on the use of these coiled-coil building blocks for higher order assembly have emerged in the past five years. These have been focused on the use of orthogonal coiled-coil sequences within a single chain to create coiled-coil protein origami,[15] the development of multicomponent peptide assemblies with coiled-coils as one example of many other peptide secondary structures,[16] the use of coiled-coils to mediate the assembly of protein structures,[17] a comparison of collagen mimetic and coiled-coil peptides for metal-promoted assembly,[18] and applications of coiled-coil materials in drug delivery.[19] This review focuses on a broader investigation of the range of strategies that have been employed to create higher order assemblies from coiled-coil building blocks, the reversible nature of coiled-coil assemblies, and a selection of their biomedical applications that emphasizes the future potential of this field.

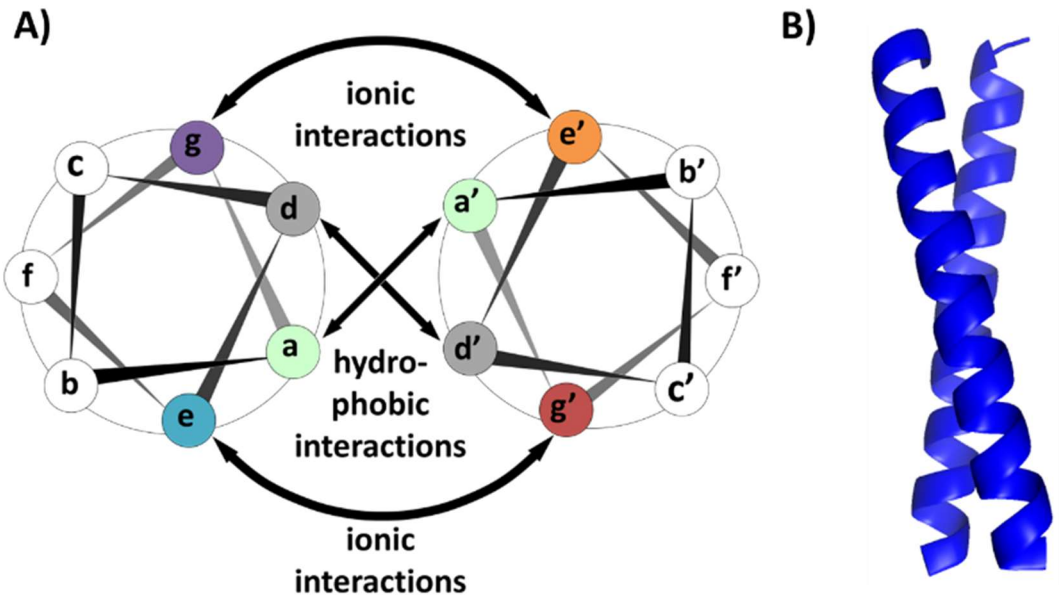

Figure 1.1. (A) Helical wheel diagram of a coiled-coil dimer. (B) 3D model of a dimeric coiled-coil.

1.2 Design Strategies for Assembly

Starting with various oligomeric versions of the coiled-coil motif, a number of strategies have been developed to facilitate higher order assembly of the starting building blocks. These assembly approaches integrate additional interactions within the coiled-coil sequences, including ionic and metal-ligand interactions, and engineering covalent linkages and hetero-oligomeric coiled-coils. Significant effort has been expended to understand and control the morphologies of these coiled-coil-derived materials as described below.

1.2.1 Ionic Interactions

A highly successful method to facilitate higher order assembly of coiled-coil peptides is through ionic interactions. For example, the Woolfson lab has used *de novo* designed dimeric to heptameric coiled-coils as building blocks (**Figure 1.2**A).[20] The peptides included charged residues at the termini to allow assembly in a head-to-tail fashion (**Figure 1.2**A). Specifically, a lysine or glutamate residue was installed at the C-terminus to complement either a glutamate or free amino group at the N-terminus, respectively. This approach to linear assembly led to immediate fiber formation in phosphate buffered saline (PBS, pH 7.4) (100 μM peptide) with

trimeric to heptameric coiled-coil modules. To improve the organization, these assemblies were subsequently thermally annealed to produce different morphologies depending on the oligomeric state of the building block. For instance, the tetrameric peptide (**CC-Tet2-F**) transitioned to thicker fibers (from 60-65 nm to 130-135 nm in width), whereas the pentameric coiled-coil transitioned from fibers to broad, sheet-like structures. This difference in the two morphologies upon annealing may stem from the lack of a complete denaturation for both peptides, suggesting incomplete transitions when annealed. Interestingly, the annealing process of the hexameric coiled-coil, **CC-Hex-T**, produced highly ordered fibers (~70 nm) that allowed for the elucidation of the packing through X-ray crystallography, revealing a square packed arrangement.[20] Additionally, the hydrophobic channel present within the hydrophobic cavity of each pentameric, hexameric, and heptameric coiled-coil (50 μM) was used to sequester the hydrophobic dye 1,6-diphenylhexatriene. The trimeric and tetrameric coiled-coils, however, did not trap the hydrophobic dye presumably because the hydrophobic cores did not contain a cavity.

While Woolfson and coworkers designed de novo coiled-coils as described above, others have used naturally occurring peptide sequences to create ionic-based assemblies. Conticello and coworkers reported a heptameric coiled-coil based on the GCN4 transcription factor (**7HSAP1**).[21] These researchers also used a head-to-tail strategy, but instead, they employed the free C- and N-termini for assembly, with two arginine residues installed at the *f* position to limit lateral association. The peptide (2 mM) formed fibers (479 ± 93 Da/Å, **Figure 1.2**B) in MES buffer (10 mM, pH 6.0) and could trap the dye PRODAN within the hydrophobic cavity of the heptameric coiled-coil. Because of the arginine residues, these fibers were much thinner (3 nm) when compared to those of Woolfson (85 nm). The Montclare lab has studied coiled-coil assemblies derived from the cartilage oligomeric matrix protein (**Q**).[22] This pentameric coiled-coil was designed to include a positively charged histidine-tag at the N-terminus, lysine and arginine residues at the C-terminus, and glutamate and aspartate residues in the middle of the peptide to allow for staggered assembly of the coiled-coil building blocks. This design led to fibril formation at 10 μM **Q** (20-560 nm in diameter) in phosphate buffer (50 mM, pH 4) with a brick-layer-like organization of the coiled-coils (**Figure 1.2**C). The peptide also assembled in the presence of the hydrophobic dye curcumin (5:1 molar ratio of curcumin to peptide). Assembling in the presence of this dye was found to promote packing of the coiled-coils and increase the fibril diameter significantly (16.0 ± 5.6 μm). While some evidence indicated curcumin binding to the hydrophobic

coiled-coil interior, the change in morphology also suggests potential binding between protofibrils. This is in contrast to Woolfson's and Conticello's works where the hydrophobic dyes had no effect on morphology.

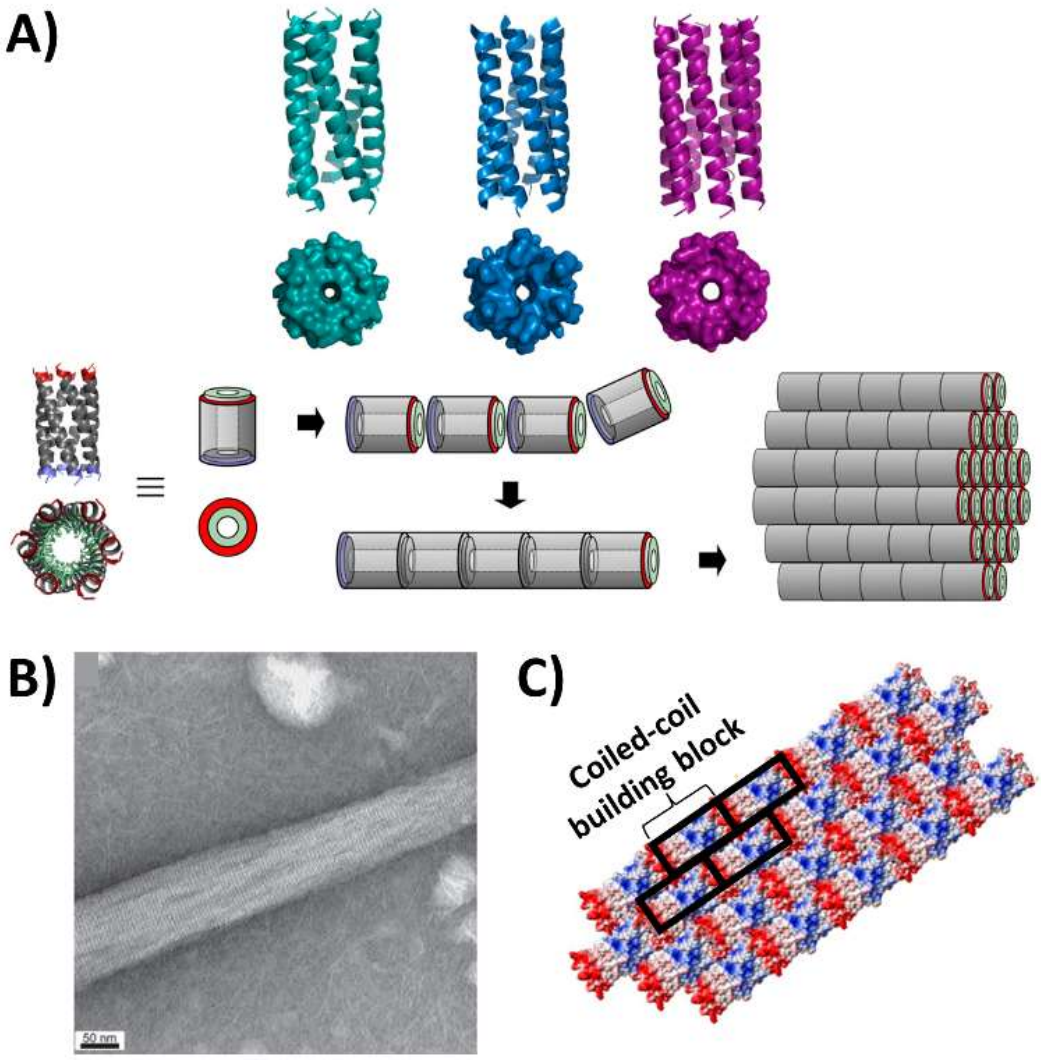

Figure 1.2. (A) X-ray crystal structures of pentameric to heptameric coiled-coils and the proposed mechanism of fiber assembly. (B) Transmission electron microscopy (TEM) micrograph of **7HSAP1** assembled in MES buffer (10 mM, pH 6.0). (C) Schematic representation of peptide **Q** organization upon fiber formation in phosphate buffer (50 mM, pH 4). Reprinted with permission from ref. 15, 16, 17. Copyright 2013, 2014, 2015, American Chemical Society.

Assemblies based on non-covalent interactions can also be reversible using pH. For instance, Conticello and coworkers installed histidine residues at the interior *d* position of the GCN4 trimeric

coiled-coil (**TZ1H**) so that only deprotonated histidine would lead to coiled-coil formation (pH > 5.8).[23] Upon incubation in phosphate buffer (10 mM, pH 8.2), **TZ1H** (1 mg/mL) assembled into bundles of fibers (40–100 nm) over a period of 3 hrs (**Figure 1.3**A). Charged histidine residues, on the other hand, disrupted the coiled-coil structure by destabilizing the hydrophobic pocket, and the absence of this supercoil prevented the higher order assembly via ionic interactions from occurring. The fiber assembly and disassembly, therefore, was controlled through the addition of base or acid, respectively. Alternatively, Dexter and coworkers designed a highly charged *de novo* peptide with histidine, lysine, and glutamate residues at solvent exposed positions of the coiled-coil backbone (**AFD19**).[24] The peptide (1.75 mM), under conditions where the net charge was close to zero (pH 5.9), first formed fibrils due to misalignment of the helices producing overhangs, followed by hydrogel formation on a time scale of seconds to hours depending on the peptide concentration (**Figure 1.3**B). Highly charged versions of **AFD19** led to no assembly and a low viscosity solution. The researchers also demonstrated rapid hydrogel dissolution by adjusting the pH. The Chmielewski lab has also developed a coiled-coil assembly that is responsive to pH.[25] They introduced bipyridine moieties at the solvent exposed *f* position of a trimeric coiled-coil derived from GCN4. One to three bipyridines were installed on the coiled-coil peptide by substituting solvent exposed residues with lysine (D6K, S13K, and N20K) and subsequent bipyridine modification (**TriByp1**, **TriByp2**, and **TriByp3**). Incubation of the peptides (250 μM) in MOPS buffer (10 mM, pH 7.0) promoted radial association of the building blocks via aromatic interactions across the coiled-coils, leading to nano- to micron-scaled rectangular assemblies (**Figure 1.3**C). An increase in the number of bipyridine units led to a decrease in the aspect ratio of the assemblies (16:1 to 0.9:1). When subjected to acidic conditions (pH 3.0), the protonated bipyridine groups caused disruption of the coiled-coil interfaces, rapidly leading to dissolution of the assembly. The material could then reassemble upon addition of base, and this overall process went through numerous cycles without a change in the morphology of the assembly. Despite using different strategies, each lab created a pH-switchable material capable of assembly and disassembly on command.

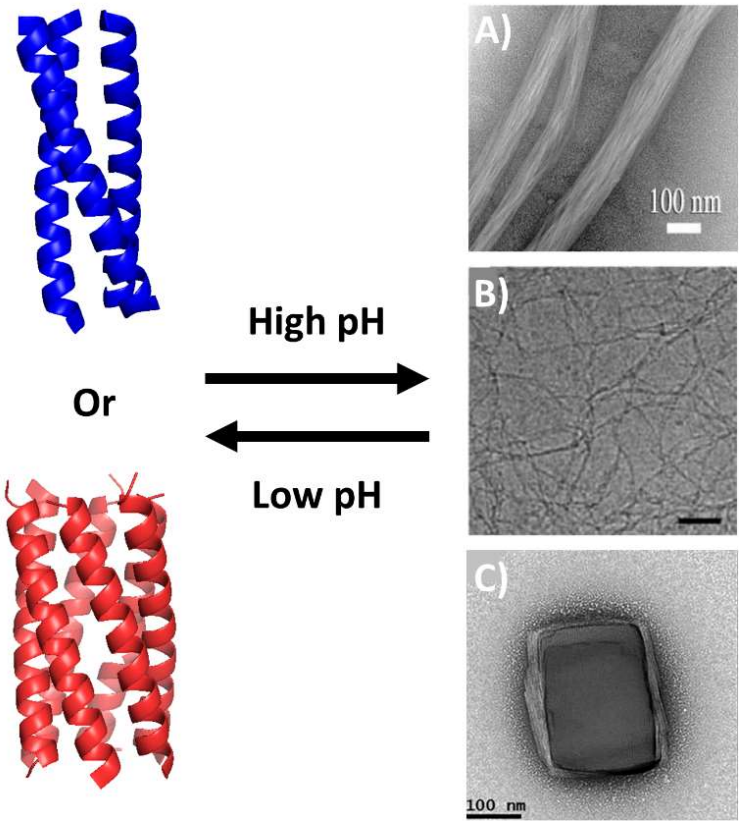

Figure 1.3. TEM images of reversible assemblies via pH. (A) **TZ1H** fibers, (B) **AFD19** fibers, and (C) **TriByp3** assembly. Reprinted with permission from ref. 18, 19, 20. Copyright 2006, 2011, 2018, American Chemical Society and Royal Society of Chemistry.

Changes in pH may also lead to changes in morphology of the assembly. For instance, Montclare and coworkers investigated the hydrogelation properties of peptide **Q** (*vide supra*) as a function of pH.[26] At neutral and basic conditions (pH 7.4 and 10) a fiber-based hydrogel formed with **Q** (2 mM) in 96 and 24 hrs, respectively. Acidic conditions (pH 6.0), on the other hand, led to polydispersed nanoparticles with no gelation after a two-week period (**Figure 1.4**A). This shift in morphology from fibers to nanospheres was due to an increase in electron repulsion of the highly charged coiled-coil. Pochan and coworkers have also found changes in morphology of the assembly of a designed coiled-coil peptide depending on the pH.[27,28] Acidic conditions (10 mM sodium acetate buffer, pH 4.5) led to nanotubes (21.3 ± 2.8 nm in length) with 1 mM peptide, while neutral (10 mM phosphate buffer, pH 7) and basic (10 mM borate buffer, pH 10) conditions led to stacked platelets (50-500 nm in length) and needles (100-250 nm in length), respectively (**Figure 1.4**B).[27] These notable differences arise from the packing of coiled-coils to minimize

electrostatic repulsion. In an acidic environment, the coiled-coils are tilted in the assembly to minimize electron repulsion of the positively charged free N-terminus. Under neutral conditions, the two-dimensional plates form through lysine-aspartate salt bridges whereas basic conditions weaken these salt bridges and lead to a primarily unidirectional assembly.

Overall, the examples provided above demonstrate that ionic-based assemblies are a simple yet powerful strategy to create a diverse range of structures. Loading of additional small molecule cargoes within the structures demonstrates potential for drug loading, and the developed feature of reversibility embedded within some of these materials may be harnessed for drug delivery as well.

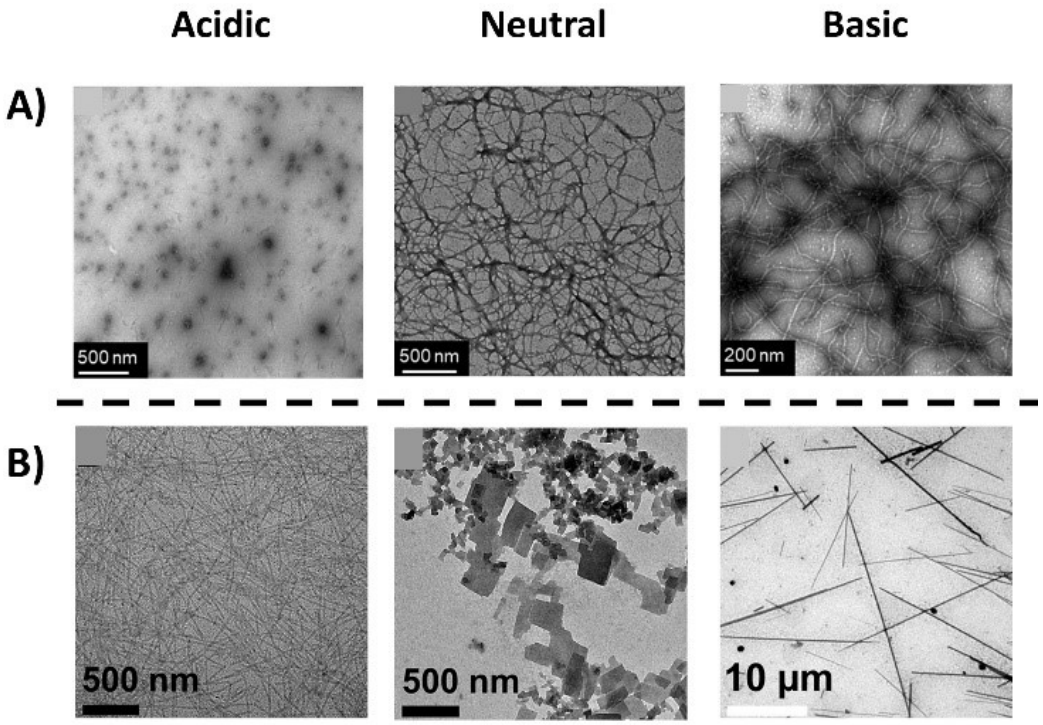

Figure 1.4. pH controlled assemblies. (A) TEM of Montclare's assembled **Q** peptide in acidic, neutral, and basic conditions to produce either nanoparticles or fibers. (B) TEM of Pochan's assembled peptide in acidic, neutral, and basic conditions to produce nanotubes, platelets, and needles, respectively. Reprinted with permission from ref. 21 and 22. Copyright 2018, 2021, American Chemical Society and Royal Society of Chemistry.

1.2.2 Metal-ligand Interactions

The introduction of metal-binding ligands onto the coiled-coil scaffold has been shown to be a powerful technique to facilitate higher order assemblies. Early studies from Ogawa and

coworkers installed a pyridine ligand at a centrally located, solvent exposed *f* position of a dimeric coiled-coil containing an IAALEQK heptad repeat (**AQ-Pal14**).[29,30] Complexation of the dimeric **AQ-Pal14** with platinum at 60 °C for a week was found to induce assembly into both nanometer-scaled globular structures and a smaller population of nanofibrils. In a subsequent study by Ogawa, the pyridyl alanine ligands were substituted with histidine (H21), and this dimeric coiled-coil was treated with cobalt(III) protoporphyrin IX at 60 °C overnight.[31] Evaporating this solution for scanning electron microscopy (SEM) analysis showed that the mixture formed much larger fibrils than the previous study, presumably due to bis-axial ligation between the imidazole ligands of the dimeric coiled-coil and a cobalt complex.[31]

Chmielewski and coworkers have successfully used metal-ligand interactions for assembly using a trimeric coiled-coil building block based on the GCN4 sequence.[32–34] This design is different from the above work of the Ogawa in that the ligands for metal ions are at the termini of the peptide to promote head-to-tail assembly, rather than at a central heptad of the coiled-coil, and a trimeric module was used.[32] The peptide (**p2L**) contained nitrilotriacetic acid (NTA) and di-histidine ligands at the N- and C-termini, respectively. Addition of Zn(II), Cu(II) or Co(II) (0.4 eq) to **p2L** (1 mM) rapidly (30 min) provided well-ordered hexagonal crystals at room temperature, whereas 0.1 eq of zinc produced hexagonal disks. The crystal structure of the zinc-promoted crystals was solved, and a hexagonal open-packed assembly was observed with the ligands directed towards the P3 face of the crystals (**Figure 1.5**A). Alternatively, nanospheres were observed with metal-mediated assembly using Ni(II), a morphology that was observed to some extent at much shorter time periods (5 min) with Zn(II), but which then evolved into crystals.[32] These researchers took advantage of the unsatisfied ligands within and on the P3 face of the growing and preformed crystals, respectively, to introduce His-tagged fluorophores with the crystals in a metal-dependent fashion.

Horne and coworkers have also studied metal-mediated coiled-coil assembly, but in their work, they used *de novo* designed sequences and terpyridine ligands. They investigated three different oligomerization states of the coiled-coil (dimer, trimer and tetramer), each with a different positioning of the ligand(s). For instance, the dimeric coiled-coil (peptide **1**) contained terpyridines in the *f* position of the first heptad, and the *e* position of the last, whereas the trimeric peptide (**2**) had these ligands at the *a* and *c* positions of the first and last heptads. A tetrameric variant (peptide **3**) contained a single ligand at an internal *f* position. Although a number of divalent transition

metals were investigated, only Cu(II) (3-10 mM) was found to promote crystallization of the peptides (~2-4 mM, pH 6-6.5) using the hanging drop vapor diffusion method (time not indicated).[35,36] Crystal structures revealed that the Cu^{2+} ions bind to these ligands in addition to nearby glutamate residues (**Figure 1.5**b) yielding a complex packing arrangement for the peptides **1** and **2**, and a 2D net embedded in the lattice for **3** (**Figure 1.5**C). In an interesting comparison, **TriByp1/2/3** described above (250 μM, pH 7), which contained bipyridine ligands in central heptad repeats based on the trimeric coiled-coil of GCN4, did not require metal ions for assembly. The bipyridine ligands alone mediated aromatic interactions leading to a hexagonal, close-packed assembly of trimeric coiled-coils after 48 hrs.[24]

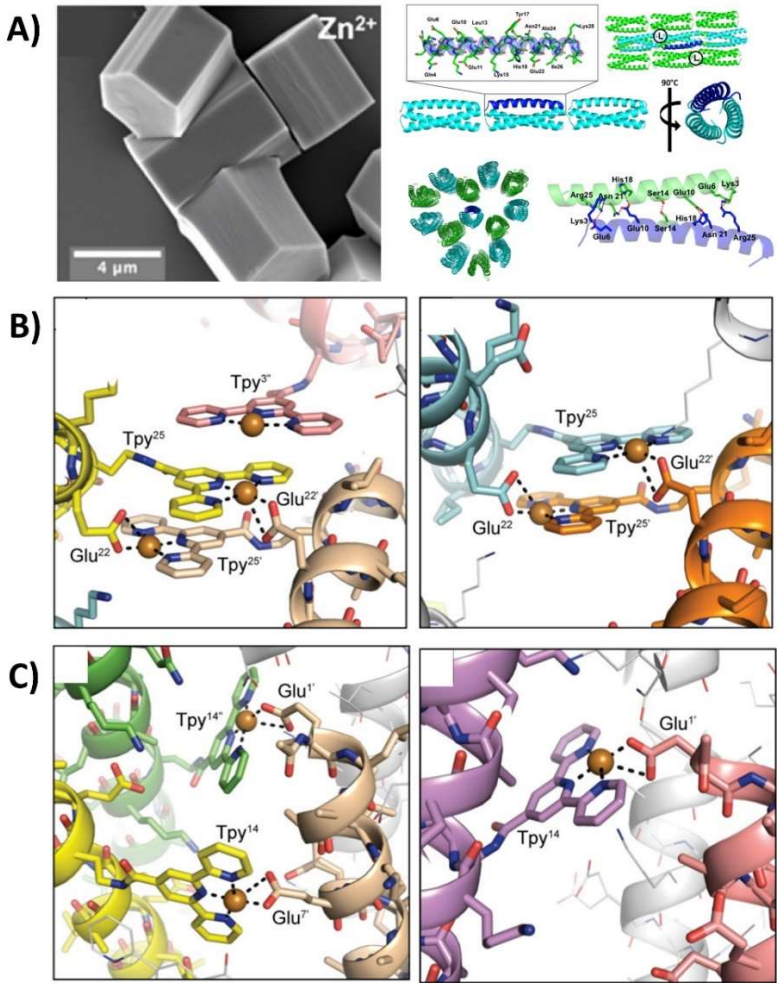

Figure 1.5. (A) Scanning electron micrograph (SEM) of crystals of **p2L** (1 mM) with zinc ions (1 mM) and its corresponding crystal structure. (B) Views of crystal structure of peptide **2** and (C) peptide **3**. Reprinted with permission from ref. 27 and 30. Copyright 2016, 2017, American Chemical Society and Royal Society of Chemistry.

Ogawa and coworkers introduced a single CXXC metal binding motif within oligomeric coiled-coils, with the Cys residues in the interior *a* and *d* positions of the coil.[37,38] Their goal was to form metal complexes inside an individual coiled-coil, however, and not promote higher order assembly of the building block. As described above, Conticello and coworkers, introduced His and Cys ligands also within the hydrophobic core of the coiled-coil.[39,40] In their case, however, three His residues (**TZ1H**) or two Cys residues (**TZ1C2**) were introduced per helix. This allowed individual helices to form staggered coiled-coils in a metal-dependent fashion. Higher order assembly into long aspect ratio fibers and fibrils were observed in the presence of Ag(II) (1 eq) with TZ1H (70 μM) or Cd(II) (2 eq) with TZ1C2 (500 μM) (**Figure 1.6**A).

A strategy to use metal-ligand interactions to make highly crosslinked structures with coiled-coils for tissue engineering has also been investigated by Chmielewski and Jorgensen. In this case the central bipyridine moiety of **TriByp1** was combined with the NTA and His_2 ligands of **p2L** to create the peptide **TriCross**.[33] The use of ligands for metals at both the middle and ends of the coiled-coil indeed created a more complex metal-promoted assembly with Zn(II), Ni(II), Cu(II), Co(II) (1 eq, 1 mM **TriCross**) producing a crosslinked three-dimensional (3D) mesh within minutes (**Figure 1.6**B). The matrix formed from **TriCross** contained micron sized cavities that were suitable for cell encapsulation (*vida infra*). An advantage of metal-mediated assembly is that the association can be abolished with metal-chelating agents. For example, the formations of both the **p2L** (hexagonal crystals, **Figure 1.5**A) and **TriCross** (3D matrix, **Figure 1.6**B)) assemblies were found to be reversible through the addition of low levels of ethylenediaminetetraacetic acid (EDTA).[32,33]

Overall, integrating metal-ligand interactions within coiled-coil peptides is an important advancement in the field, especially as it pertains to the crystalline arrays and 3D matrices generated above. The use of metal ion-promoted assembly is a powerful means to rapidly generate crystals on demand and incorporate cargo in a metal-dependent manner. Additionally, the judicious placement of multiple ligands on the coiled-coil building block allowed for metal-promoted formation of a 3D scaffold that encapsulated cells simultaneously. A notable feature of this strategy for assembly is the inherent reversibility that is available for the dissolution upon treatment with chelators – a feature with interesting potential in tissue engineering.

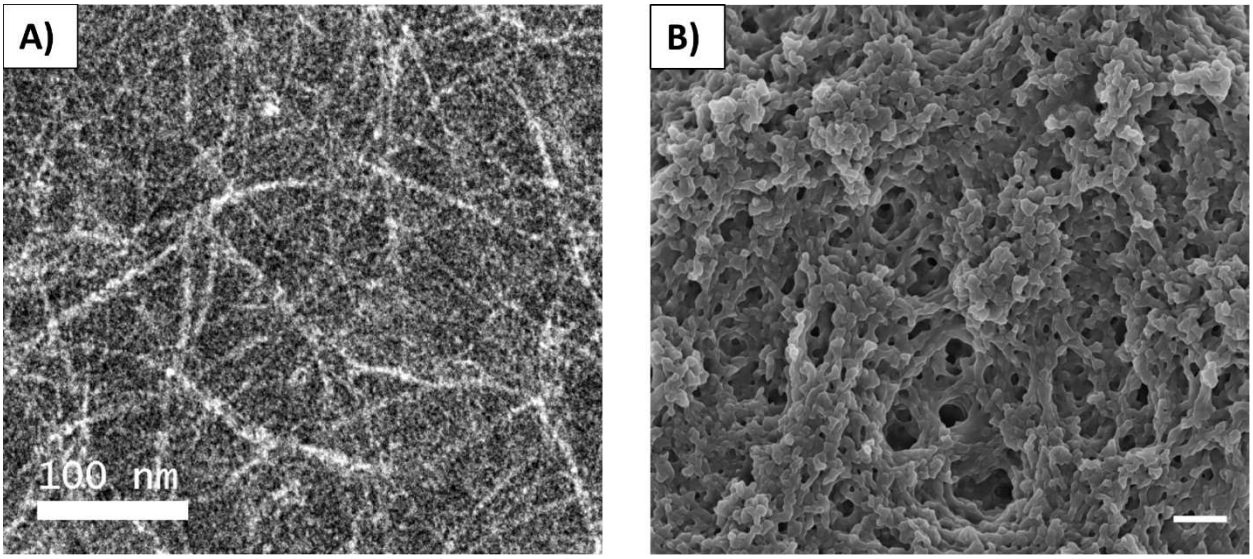

Figure 1.6. (A) TEM image of **TZ1C2** fibrils (500 μM) in TAPS buffer (10 mM, pH 8.5) and NaCl (100 mM) before Cd(II) addition. (B) SEM image of **TriCross** assembly with $ZnCl_2$ (1 mM each) in Dulbecco's Modified Eagle Medium (DMEM) with 10% fetal bovine serum (FBS) after 1 hr. Reprinted with permission from ref. 28 and 35. Copyright 2013, 2021, American Chemical Society and John Wiley and Sons.

1.2.3 Covalent Linkages and Heterocoiled-Coils

An alternate way to generate biomaterials from coiled-coil peptides is to link the building blocks together via covalent bonds. This has been accomplished in one set of examples by using different click chemistries. For instance, Woolfson and coworkers used native chemical ligation between hexameric coiled-coils. **CC-Hex-T**, described above, was optimized to minimize lateral association and maximize linear assembly (**CC-Hex-T + co**).[41] Native chemical ligation was used to link the building blocks using either two cysteine amino acids or two thioester moieties at each terminus of a single coiled-coil. Rather than the previously described ionic driven assembly, the fibers that were generated (30-40 nm after 30 min and 100 nm after 1 week) were due to the covalent bond formed through the ligation chemistry to link the coiled-coils.

Similarly, Pochan and coworkers have used bond formation between coiled-coils using thiol and maleimide moieties. They used two tetrameric coiled-coils, one bearing terminal maleimides (**Peptide 1**) and the other flanked with cysteine residues (**Peptide 2**).[42,43] This design produced nanorods (>30 μm) with an alternating **Peptide 1** and **Peptide 2** pattern. Additionally, the Kirshenbaum lab has used the Huisgen cycloaddition for covalently linking coiled-coils. In this case, the resulting triazole linkage was used to connect a dimeric coiled-coil, based on the

SYNZIP peptide, in a central position with 1-2 different dimeric coiled-coil sequences (**4A** and **4B**).[44] Depending on the location of **4A** and **4B**, a barbell or quadrilateral assembly was observed. These strategies described above provide a facile route to design coiled-coil materials based on chemical reactions.

Yet another covalent technique to induce higher order assembly is to install flexible peptide and polymeric linkers between helices of the coiled-coils. Jerala and coworkers, for example, elegantly designed a tetrahedron assembly using a mixture of homomeric and heteromeric coiled-coils with flexible peptide linkers (**TET12**).[45,46] The tetrahedron material was composed of a single polypeptide chain containing twelve coiled-coil domains each flanked with a flexible tetrapeptide spacer (SGPG) to prevent extended helix formation with a neighboring coiled-coil (**Figure 1.7**A). To confirm the topological fold of the peptide, the N- and C-termini of the polypeptide were grafted with split yellow fluorescent protein fragments that provided a strong fluorescent signal. Tirrell and coworkers have used a triblock design to create an assembly from the protein **EPE**, with **E** representing an elastin-like sequence flanked with cysteines and **P** representing the coiled-coil sequence from cartilage oligomeric matrix protein.[47,48] The **EPE** protein was conjugated to a 4-arm PEG linker to initiate the crosslinked network. To control the strength and rigidity of the hydrogel, the strength of the coiled-coil was altered, either through sequence modification or the addition of denaturants. In a somewhat analogous study from Tirrell and coworkers, triblock peptides were investigated in which two coiled-coil forming peptides were connected with a peptide linker. In this example, a central random coil peptide was connected to a pentameric coiled-coil peptide from the cartilage oligomeric matrix **P** and a tetrameric coiled-coil peptide **A** (**PC10A**). This design generated a crosslinked network that was notably stronger (100-fold increase) when compared to the homodimeric counterparts (**AC10A** and **PC10P**).[49] Similarly, De Vries and coworkers used a self-assembling triblock linked to heterocoiled-coil peptides (**C_2-S^H_{48}-C_2-D^A** and **C_2-S^H_{48}-C_2-D^B**).[50] Without the heterocoiled-coil building blocks, simple fibrils were observed at pH ≥ 6 from **C_2-S^H_{48}-C_2** alone. The installation of the coiled-coils, however, led to a heavily crosslinked morphology of the fibrils (**Figure 1.7**B). The degree of crosslinking was controllable by varying the density of coiled-coil labeled blocks.

Polymeric linkers have also been used to create more extensive structures with coiled-coils. Early work by Ghosh and coworkers used complementary alpha-helices that were conjugated to PAMAM dendrimers through cysteine-maleimide chemistry (**D-EZ_4** and **D-KZ_4**).[51] Upon mixing

the two peptide conjugates in phosphate buffer, the alpha-helices formed coiled-coils and created fibers (> 10 μm in length) after 8 hrs. More recently, Aili and Blank connected alpha helices to four-armed PEG linkers in a design to control the crosslinking properties.[52–54] Aili used dimeric coiled-coils with either isoleucine or valine at the a position (**pEV$_4$**, **pEI$_4$**, **pKV$_4$**, and **pKI$_4$**) to control the strength of the network by taking advantage of the coiled-coil binding affinities (**Figure 1.7**C).[52] The peptides were linked to the PEG polymer via Cys/maleimide chemistry, and hydrogels were formed with the peptide conjugates (250 μM) in phosphate buffer (pH 7) within hours. Hydrogels that were composed of only isoleucine coiled-coils (**pEI$_4$**/**pKI$_4$**) resulted in a stronger gel when compared hydrogels with both valine and isoleucine alpha-helices (**pEI$_4$**/**pKV$_4$**) (G' of 1000 Pa vs 200 Pa). Blank, on the other hand, controlled the strength of the crosslinked network through both covalent coiled-coil formation with a star-PEG polymer and metal-ligand interactions. Specifically, histidine ligands were installed at the solvent exposed *f* position of dimeric coiled-coil forming peptides (**A$_{4H3}$** and **B$_{4H3}$**) to create a second layer of crosslinking.[53,54] The hydrogel formed without added metal ions (0.5 mM peptide conjugate, pH 8.1) exhibited a large linear viscoelastic range, whereas addition of zinc ions (1 eq) increased the degree of crosslinking and transitioned from viscoelastic to elastic-like gels. Similar to metal-mediated assemblies, the addition of metal chelators like EDTA (4 eq) returned the hydrogel to its original state. While Aili explored the binding affinities of covalently linked coiled-coils to control the strength of the hydrogel, Blank used a covalent strategy in conjunction with a metal-mediated strategy to tune hydrogel properties.

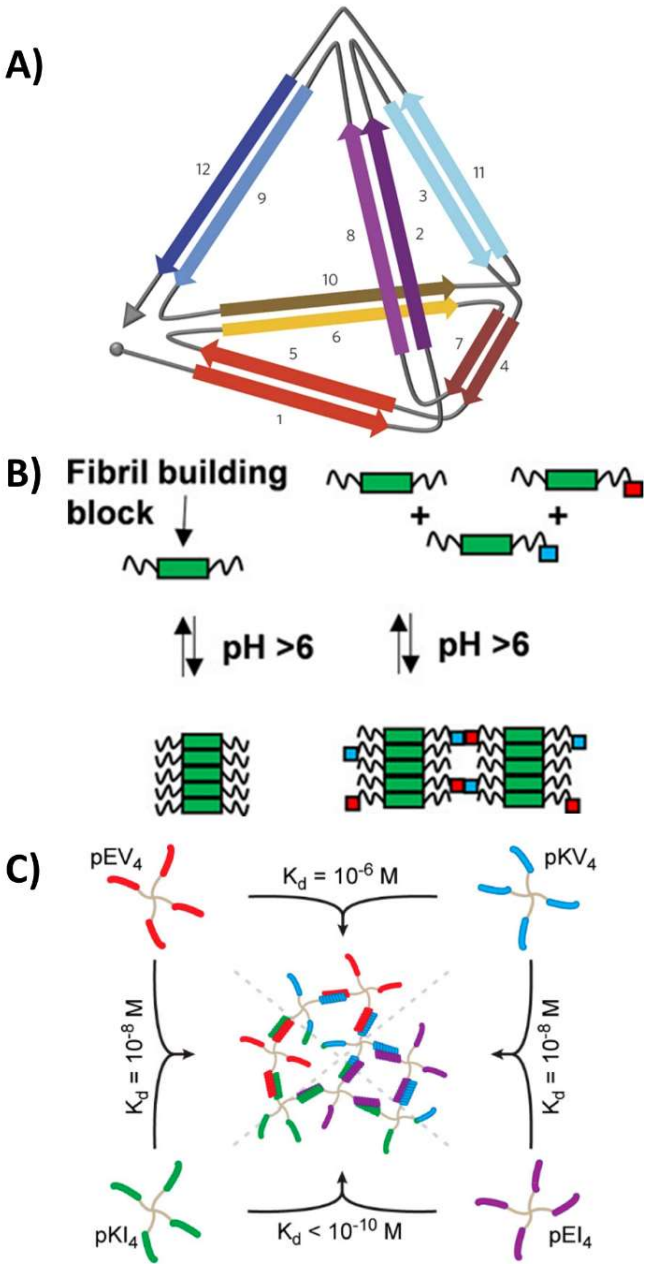

Figure 1.7. (A) Schematic representation of the polypeptide path forming a tetrahedron. (B) Cartoon diagram of fibril forming triblock with and without heterocoiled-coil installation. (C) Relationship between coiled-coils and their corresponding binding affinities. Reprinted with permission from ref. 40, 45, 47. Copyright 2013, 2016, American Chemical Society and Springer Nature.

The covalent strategies outlined above are a powerful means to swiftly link together coiled-coil peptides via various "click" reactions or with peptidic/polymeric linkers. These approaches lead to assemblies with morphologies that are often distinct from those obtained with the coiled-

coil building block alone. The peptide origami approaches are an especially compelling example of the power of using heterocoiled-coils to tune stability and precisely control the resulting assemblies. The chemical approach allows for multiple modifications away from natural amino acids, whereas the ability to express the proteins, as in the case with the origami sequences, may provide a cost-effective way to generate the desired proteins.

1.3 Applications

1.3.1 Cargo Storage and Delivery

Perhaps the most studied application to biomaterials is cargo storage and delivery. While lyophilized powders remain the gold standard for protein storage, the lyophilization process can be harsh for the proteins and lead to degradation.[55,56] Meanwhile drug delivery remains a challenge and continues to be optimized to improve solubility of hydrophobic drugs, increase bioavailability, and minimize off-target effects.[57–59]

Incorporating proteins within coiled-coil assemblies is one possible strategy to stabilize proteins. To this end, Chmielewski and co-workers used their **p2L** coiled-coil crystals described above to include proteins within the crystal. During the metal-mediated assembly, His-tagged protein guests were incorporated in an ordered fashion via metal-ligand interactions inside the crystal host in an hourglass pattern.[32] By incorporating His-tagged enhanced green fluorescent protein (EGFP) and derivatives inside the crystalline matrix, significant stabilization of the folded protein was achieved, even at 100 °C. These data demonstrate the potential of this assembly for room temperature storage of thermally sensitive proteins (**Figure 1.8**A).[34] In an alternate strategy, Clark and coworkers stabilized citrate synthase (CS) by incorporating the enzyme covalently in coiled-coil filaments.[60] These filaments were composed of the coiled-coil peptide building blocks **EE** and **KK** derived from the γPFD protein. While CS aggregates in solution at 43 °C, embedding CS in the filaments through covalent linkages stabilized the enzyme. These two coiled-coil peptide materials, while using different mechanisms of assembly, provide great promise for protein stabilization and may provide a scaffold for enzymes.

Cargo delivery using nanoparticles derived from coiled-coil assemblies has seen notable recent advances. The Xu lab has developed a micelle composed of a coiled-coil peptide with a poly(ethylene glycol) side-conjugate and a terminal hydrophobic tail modification (**1coi-dC18-**

PEG2K, **Figure 1.8**B). In collaboration with the Ferrara and Bankiewicz labs, they investigated the numerous properties of the micelle nanoparticles for anticancer agent delivery.[61–68] For example, doxorubicin-loaded micelles were used to treat prostate and breast cancers in mice.[63] Later generations of these nanoparticles included trimeric and tetrameric coiled-coil species to control the location and cluster size of the drug on the micelle,[67] and cysteine modifications for redox reactive micelles.[68] Similarly, Kobatake and coworkers also reported drug delivery nanoparticles using a coiled-coil motif conjugated to an elastin-like peptide (ELP).[69] In this design, a heterocoiled-coil was used with helix A conjugated to single-chain vascular endothelial growth factor (VEGF) while helix B was conjugated to the ELP. Nanoparticle formation in the presence of paclitaxel created an anticancer delivery vehicle, whereby the external VEGF decoration directed the particles to the VEGF-receptor of cancer cells with paclitaxel ultimately causing cell death.

Different types of nanospheres have also been investigated for cargo delivery. Woolfson and coworkers have designed self-assembling cage-like particles (**SAGEs**) through a combination of heterocoiled-coil design and disulfide linkages (**Figure 1.8**C).[70–72] A homotrimeric coiled-coil (**CC-Tri3**) was linked to either alpha-helix A or B with a disulfide bridge, and subsequent mixing of the two sets led to AB heterocoiled-coil formation. Whereas the nanoparticles developed by Xu and Kobatake had hydrophobic cores, this **SAGE** has a hollow interior. **SAGEs** were modified at their termini with proteins (green fluorescent protein or luciferase) to decorate the interior or exterior of the cages without compromising the integrity of the material.[71] The cages were also modified to optimize cell uptake by introducing charged residues at the surface.[72] Stevens and coworkers, on the other hand, created nanoparticles using a layer-by-layer assembly on a colloidal surface.[73] The layers were generated with heterocoiled-coil components (**JR2EC** and **JR2KC**) linked to a polymer via cysteine-maleimide chemistry. Using this strategy, up to four layers could be assembled, with each layer containing trapped dextran. In this way, controlled release of cargo was accomplished through enzymatic degradation of each layer.

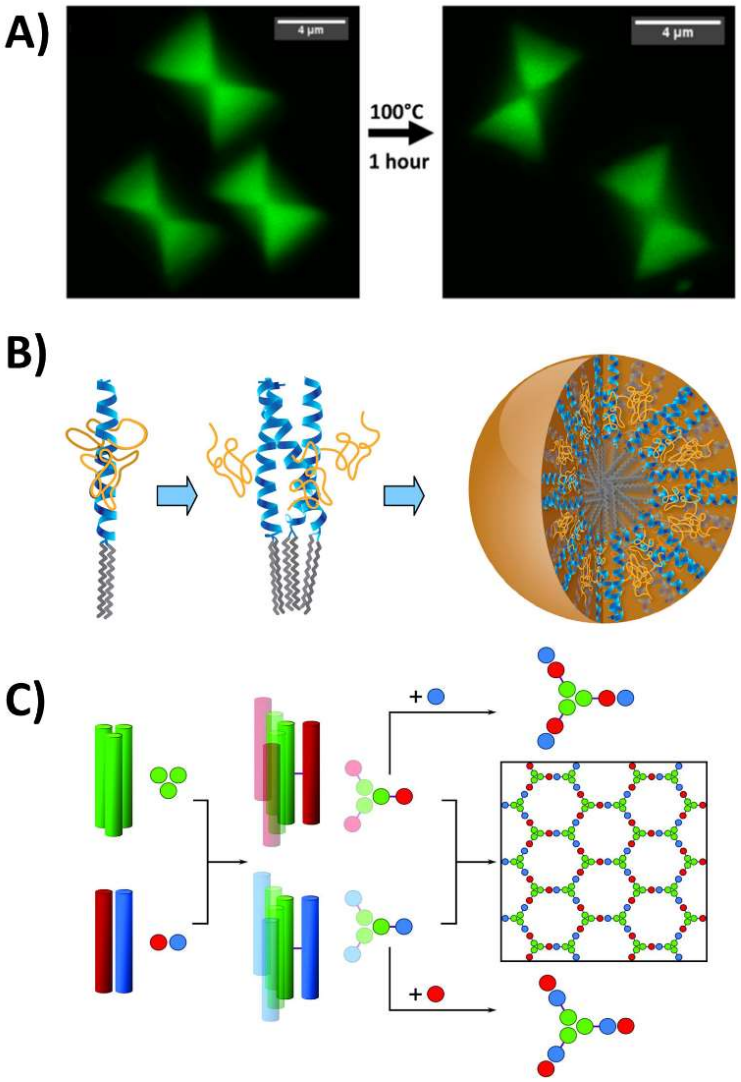

Figure 1.8. (A) Stability of EGFP within **p2L** crystals. Fluorescence confocal images of Chmielewski's **p2L** crystals with enhanced green fluorescent protein guests before and after incubation at 100 °C for 1 hr. (B) Schematic drawing of Xu's micelle, where the shell is composed of the 3-helix bundles and the core is composed of aliphatic chains. (C) Design of Woolfson's peptide cages through disulfide linkages and heterocoiled-coils. Reprinted with permission from ref. 29, 56, 65. Copyright 2012, 2013, 2016, American Chemical Society and American Association for the Advancement of Science.

Coiled-coil assemblies using different morphologies have also been investigated as potential cargo delivery vehicles. Chmielewski and coworkers, for instance, generated nanotubes based on a trimeric GCN4 leucine zipper (**TriNL**) that selectively encapsulated fluorescently labelled anionic dextran.[74] A second generation of these nanotubes was created to stabilize the tubes and thereby expand the scope of this material as a delivery vehicle.[75] By introducing metal-

binding ligands into this nanotube using heterotrimers composed of the coiled-coil peptides **p2L** (*vide supra*) and **TriNL**, the tube stability was increased in a metal-dependent manner as will be discussed in Chapter 3. These tubes were still able to include dextrans within their interior, with inclusion of His-tagged fluorophores at either the ends of the tubes, or throughout, with the addition of metal ions.[70] Montclare and coworkers have created coiled-coil nanofibers (**CCC^{S}**) based on the cartilage oligomeric matrix protein that encapsulate BMS493, a small molecule used for osteoarthritis treatment.[76] BMS493 readily degrades and isomerizes, making delivery of this drug difficult. Trapping the drug in the coiled-coil nanofibers was found to stabilize this therapeutic.

Hydrogels have also been investigated for cargo binding and delivery. For instance, Montclare and coworkers designed a hydrogel from the coiled-coil peptide **Q** for controlled drug release.[77] This hydrogel was successful as a vehicle for sustained release of curcumin. Alternatively, Zhong and coworkers designed a pH-responsive nanogel by conjugating helices of a heterocoiled-coil to hyaluronic acid (**HA-K3** and **HA-E3**).[78] The hyaluronic acid targeted breast cancer cells with overexpressed CD44 receptors, and when saporin, a ribosome inactivating protein, was included as cargo, the nanogel was reported to exhibit potent anticancer activity.

These efforts demonstrate an impressive array of materials with the capacity to bind both small molecules and proteins. Of particular interest is the inclusion of proteins within 3D crystals and filaments. The enhanced thermal stability of the protein guests points to interesting applications in room temperature storage of biopharmaceuticals and enzymes. The ability to bind and release cargo within coiled-coil materials and interact with cells, as demonstrated by the **SAGEs** cages, brings the use of coiled-coil materials as drug delivery vehicles closer to reality.

1.3.2 Three-dimensional Cell Culturing

Creating biocompatible three-dimensional scaffolds has been a major goal in support of tissue engineering. The extracellular matrix is very structurally complex, and 2D cell culturing is severely limited in mimicking *in vivo* settings.[79–81] While natural 3D scaffolds like Matrigel are commonly used, batch to batch variation and an ill-defined composition limit the tunability.[82] Creating highly crosslinked 3D structures from sequence defined coiled-coil peptides has been used to circumvent these issues. Woolfson and coworkers, for instance, have designed coiled-coil sequences that form hydrogels through sticky ends using hydrogen bonding or hydrophobic

interactions (**hSAFs**).[83,84] This, in turn, allowed them to control the strength of the hydrogel through heating. Rat adrenal pheochromocytoma cells and neural stem cells were seeded onto the gels, and gel penetration and subsequent differentiation was observed. In an alternate strategy, Kobatake and coworkers developed a conjugate (**CUBE**) between a tetrameric, antiparallel coiled-coil and elastin-like polypeptide to prepare a hydrogel. By heating (37 °C) **CUBE**, the ELP segments aggregated leading to a crosslinked hydrogel.[85] Upon introducing the cell adhesion sequence RGD and heparin-binding angiogenic growth factors into these hydrogels, HUVEC cells that were encapsulated in the 3D network were found to undergo angiogenesis, a process that is usually only observed within 3D matrices (**Figure 1.9**A). Alternatively, the George lab used a triblock strategy whereby two GCN4 coiled-coil peptides were linked with a random coil peptide containing the RGDS sequence. Strategically placed cysteine residues allowed for hydrogel formation through disulfide bond formation.[86] Added human marrow stem cells adhered to the hydrogel and subsequent neovascularization was observed. Dexter and coworkers modified the **AFD19** sequence described above with an S16K substitution so that a hydrogel could form at physiological pH.[87] This gel exhibited low cell toxicity, and was suitable for the growth of mouse fibroblast cells with a spread morphology.

While hydrogels remain the most prevalent type of three-dimensional networks based on coiled-coil sequences, Chmielewski and Jorgensen have developed a coiled-coil-based assembly (**TriCross**) that achieved the same crosslinked morphology while not exhibiting gelation.[33] Their assembly design, as described above and in Chapter 2, was based on a trimeric GCN4 leucine zipper, and used metal-ligand interactions at both the center and termini of the peptide. The conditions for assembly enabled HeLa cells to be added during the process to fully encapsulate the cells into the 3D matrix (**Figure 1.9**B). The cells showed excellent viability within the scaffold after 6 days, and cells released from the matrix with a mild EDTA treatment demonstrated high viability. The reversibility of this matrix under mild conditions has promise for the isolation of grown tissue.

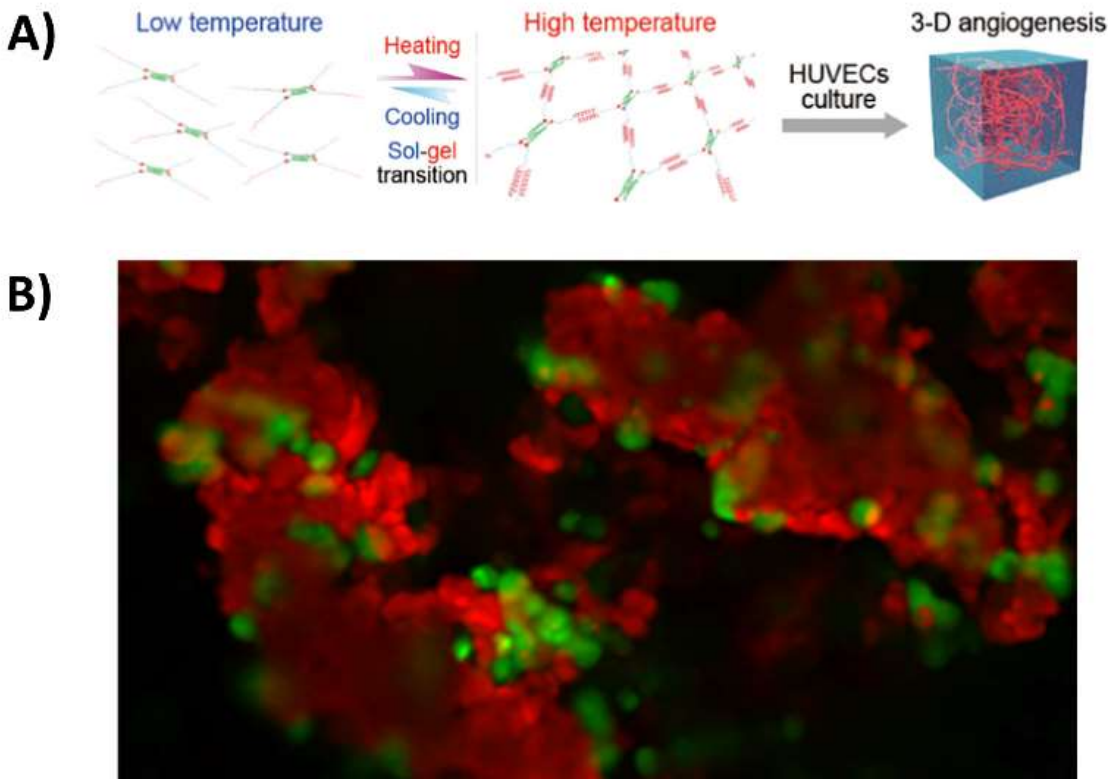

Figure 1.9. (A) Schematic illustration of a temperature-responsive **CUBE** hydrogel and the formation of blood vessels. (B) Confocal microscopy image of live HeLa cells (green) encapsulated within the **TriCross** assembled labeled with Rh-His_6 (red) in DMEM with 10% FBS. Reprinted with permission from ref. 28, 80. Copyright 2020, 2021, American Chemical Society and John Wiley and Sons.

Overall, the examples of coiled-coil crosslinked assemblies provided above demonstrate significant potential as mimics of the extracellular matrix for tissue engineering. The coiled-coil 3D matrices have great potential for implantable materials and for 3D patterning of cell/tissue/material constructs. The ability to reverse the assembly process to release tissue in a chelation-controlled manner, as demonstrated by **TriCross**, could be particularly useful in regenerative medicine applications.

1.3.3 Vaccine Development and Immunology

Vaccines derived from coiled-coil assemblies have recently been developed for multivalent display of epitopes. These potential vaccine candidates show great promise when compared to soluble antigens for their ability to present a high level of antigens and elicit a stronger immune

response.[88] For instance, Burkhard developed a nanoparticle with dodecahedral symmetry that was composed of a trimeric coiled-coil sequence linked to a pentameric coiled-coil sequence via a disulfide (**SAPNs**, **Figure 1.10**).[89,90] The solvent exposed terminus of the peptides within the nanoparticle was functionalized with the coiled-coil of the HIV surface protein gp41 to create an adjuvant-free immunogen.[89,91] A follow up study functionalized the particles with a spike protein epitope for SARS-CoV-1. Animal studies with these nanoparticles revealed potent neutralization activity.[92]

Since then, Burkhard's nanoparticle design has been used for a number of vaccine candidates. Lanar and coworkers, for instance, have installed B and T cell epitopes for malaria within the nanoparticle.[93, 94] Mouse studies showed protection against the malaria parasite *P. berghei* for up to six months with just the B cell epitope, whereas the combined epitopes doubled the length of protection, and also provided protection against transgenic *P. berghei*. Bissati and coworkers have also used these nanoparticles for *toxoplasma gondii* infection,[95–97] whereas Khan and coworkers used this platform to generate vaccine candidates against avian influenza,[98,99] seasonal influenza,[100] and an infectious bronchitis virus.[101] Indeed, this simple coiled-coil platform allows for facile tunability and shows great promise for future vaccine development.

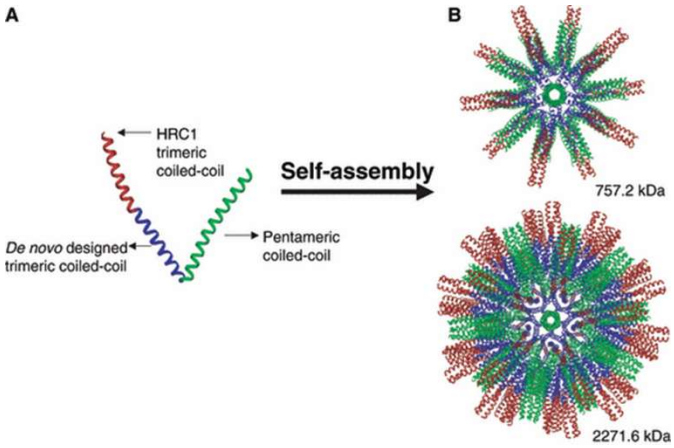

Figure 1.10. (A) 3D monomeric building block of **P6HRC1** composed of a modified pentameric coiled-coil domain from COMP (green) and trimeric de novo designed coiled-coil domain (blue) which is extended by the coiled-coil sequence of SARS HRC1 (red). (B) Computer models of the complete peptide nanoparticle **P6HRC1** with varying degrees of icosahedral symmetry. The calculated diameters of these particles are about 23 and 28 nm and the molecular weight 757 and 2271 kDa, respectively. Reprinted with permission from ref. 87. Copyright 2009, John Wiley and Sons.

Other coiled-coil assemblies have also been used for multivalent display of epitopes for use in potential vaccines. The Robinson lab, for example, designed a virus-like nanoparticle using a coiled-coil peptide with a lipid tail, rather than the two coiled-coils used by Burkhard.[102] The outer shell of the nanoparticle was decorated with an HIV-1 sequence to illicit an immune response. Collier and coworkers used a CD4+ T-cell epitope-containing coiled-coil that assembles into nanofibers and elicits an immune response in mice.[103] This material was subsequently optimized by controlling the length of the nanofibers.[104] Corradin and coworkers used the coiled-coil domains of malaria epitopes and connected them with non-immunogenic linkers.[105] A cellular assay revealed inhibition of parasite growth in the presence of this assembly. Finally, using Woolfson's **SAGEs** described above, Davidson and coworkers decorated the cages with tetanus toxoid, ovalbumin, or hemagglutinin antigens.[106] Both *in vitro* and *in vivo* studies revealed immune responses following exposure to these nanocages.

Coiled-coil nanoparticles are an excellent vehicle for the 3D display of multivalent ligands. This feature is ideal for applications in vaccine development. Additionally, striking animal data is emerging to support the future application of these strategies in humans.

1.4 Conclusions

The coiled-coil motif has been an area of great interest for de novo peptide design. More recently this building block has been successfully employed to generate a wide range of materials with morphologies that include fibrils, fibers, cages, crystals, tetrahera, nanotubes, hydrogels and 3D matrices. Because of the programmability of coiled-coils, assemblies can be formed through a number of methods, including complementary ionic and metal-ligand interactions, and through covalent chemistry. While significant progress has been made in the development of coiled-coil biomaterials, the rules for the various types of assembly are still being elucidated, an area where machine learning approaches may be useful in the future. Whereas we have focused in this review on biomedical applications, a growing number of coiled-coil assemblies are also being used as conductive materials, including photoelectronically active fibrils and conductive nanofilaments using metalloproteins within a coiled-coil assembly.[107–111]

With many of the systems described herein having proven use in protein storage, cargo delivery, cell culture and vaccine development, the future potential of coiled-coil materials to have significant biomedical impact is highly promising. Future applications of coiled-coil materials

could include the combination of multi-layered nanoscale coiled-coil assemblies with cargo loading and cell interactions for the delivery of biological cargoes, such as therapeutic proteins and oligonucleotides. Importantly, such biopharmaceuticals could also be stabilized for room temperature storage and transport through inclusion within coiled-coil crystals and tubes. Additionally, the 3D patterning of cells and the peptide biomaterials, in a reversible manner when needed, would be a powerful means to create complex tissues for drug testing and as implantable materials for *in vivo* use.

1.5 References

(1) Liu, X.; Wang, C.; Liu, Z. Protein-Engineered Biomaterials for Cancer Theranostics. *Adv. Healthc. Mater.* **2018**, *7* (20), 1800913–1800929. https://doi.org/10.1002/adhm.201800913.

(2) Xie, A. W.; Murphy, W. L. Engineered Biomaterials to Mitigate Growth Factor Cost in Cell Biomanufacturing. *Curr. Opin. Biomed. Eng.* **2019**, *10*, 1–10. https://doi.org/10.1016/j.cobme.2018.12.004.

(3) Gaharwar, A. K.; Singh, I.; Khademhosseini, A. Engineered Biomaterials for in Situ Tissue Regeneration. *Nat. Rev. Mater.* **2020**, *5* (9), 686–705. https://doi.org/10.1038/s41578-020-0209-x.

(4) Lau, K. H. A. Peptoids for Biomaterials Science. *Biomater. Sci.* **2014**, *2* (5), 627–633. https://doi.org/10.1039/c3bm60269a.

(5) Durão, J.; Gales, L. Peptide Self-Assembly for Therapeutic Applications. *Curr. Org. Chem.* **2015**, *19*, 1874–1881.

(6) Hendricks, M. P.; Sato, K.; Palmer, L. C.; Stupp, S. I. Supramolecular Assembly of Peptide Amphiphiles. *Acc. Chem. Res.* **2017**, *50* (10), 2440–2448. https://doi.org/10.1021/acs.accounts.7b00297.

(7) Lin, K.; Zhang, D.; Macedo, M. H.; Cui, W.; Sarmento, B.; Shen, G. Advanced Collagen-Based Biomaterials for Regenerative Biomedicine. *Adv. Funct. Mater.* **2019**, *29* (3), 1804943. https://doi.org/10.1002/adfm.201804943.

(8) Yadav, M. K.; Redman, J. E.; Leman, L. J.; Alvarez-Gutiérrez, J. M.; Zhang, Y.; Stout, C. D.; Ghadiri, M. R. Structure-Based Engineering of Internal Cavities in Coiled-Coil Peptides. *Biochemistry* **2005**, *44* (28), 9723–9732. https://doi.org/10.1021/bi050742a.

(9) Dawson, W. M.; Martin, F. J. O.; Rhys, G. G.; Shelley, K. L.; Brady, R. L.; Woolfson, D. N. Coiled Coils 9-to-5: Rational: De Novo Design of α-Helical Barrels with Tunable Oligomeric States. *Chem. Sci.* **2021**, *12* (20), 6923–6928. https://doi.org/10.1039/d1sc00460c.

(10) Harbury, P. B.; Zhang, T.; Kim, P. S.; Alber, T. A Switch between Two-, Three-, and Four-Stranded Coiled Coils. *Science.* **1993**, *262* (5138), 1401–1407.

(11) Zaccai, N. R.; Chi, B.; Thomson, A. R.; Boyle, A. L.; Bartlett, G. J.; Bruning, M.; Linden, N.; Sessions, R. B.; Booth, P. J.; Brady, R. L.; Woolfson, D. N. A de Novo Peptide Hexamer with a Mutable Channel. *Nat. Chem. Biol.* **2011**, *7*, 935–941. https://doi.org/10.1038/nchembio.692.

(12) Liu, J.; Zheng, Q.; Deng, Y.; Cheng, C. S.; Kallenbach, N. R.; Lu, M. A Seven-Helix Coiled Coil. *Proc. Natl. Acad. Sci. U. S. A.* **2006**, *103* (42), 15457–15462. https://doi.org/10.1073/pnas.0604871103.

(13) Mason, J. M.; Schmitz, M. A.; Müller, K. M.; Arndt, K. M. Semirational Design of Jun-Fos Coiled Coils with Increased Affinity: Universal Implications for Leucine Zipper Prediction and Design. *Proc. Natl. Acad. Sci. U. S. A.* **2006**, *103* (24), 8989–8994. https://doi.org/10.1073/pnas.0509880103.

(14) ElGamacy, M.; Hernandez Alvarez, B. Expanding the Versatility of Natural and de Novo Designed Coiled Coils and Helical Bundles. *Curr. Opin. Struct. Biol.* **2021**, *68*, 224–234. https://doi.org/10.1016/j.sbi.2021.03.011.

(15) Lapenta, F.; Aupič, J.; Strmšek, Ž.; Jerala, R. Coiled Coil Protein Origami: From Modular Design Principles towards Biotechnological Applications. *Chem. Soc. Rev.* **2018**, *47* (10), 3530–3542. https://doi.org/10.1039/c7cs00822h.

(16) Raymond, D. M.; Nilsson, B. L. Multicomponent Peptide Assemblies. *Chem. Soc. Rev.* **2018**, *47* (10), 3659–3720. https://doi.org/10.1039/c8cs00115d.

(17) Park, W. M. Coiled-Coils: The Molecular Zippers That Self-Assemble Protein Nanostructures. *Int. J. Mol. Sci.* **2020**, *21* (10). https://doi.org/10.3390/ijms21103584.

(18) Curtis, R. W.; Chmielewski, J. A Comparison of the Collagen Triple Helix and Coiled-Coil Peptide Building Blocks on Metal Ion-Mediated Supramolecular Assembly. *Pept. Sci.* **2021**, *113* (2), e224190. https://doi.org/10.1002/pep2.24190.

(19) Utterström, J.; Naeimipour, S.; Selegård, R.; Aili, D. Coiled Coil-Based Therapeutics and Drug Delivery Systems. *Adv. Drug Deliv. Rev.* **2021**, *170*, 26–43. https://doi.org/10.1016/j.addr.2020.12.012.

(20) Burgess, N. C.; Sharp, T. H.; Thomas, F.; Wood, C. W.; Thomson, A. R.; Zaccai, N. R.; Brady, R. L.; Serpell, L. C.; Woolfson, D. N. Modular Design of Self-Assembling Peptide-Based Nanotubes. *J. Am. Chem. Soc.* **2015**, *137*, 10554–10562. https://doi.org/10.1021/jacs.5b03973.

(21) Xu, C.; Liu, R.; Mehta, A. K.; Guerrero-Ferreira, R. C.; Wright, E. R.; Dunin-Horkawicz, S.; Morris, K.; Serpell, L. C.; Zuo, X.; Wall, J. S.; Conticello, V. P. Rational Design of Helical Nanotubes from Self-Assembly of Coiled-Coil Lock Washers. *J. Am. Chem. Soc.* **2013**, *135* (41), 15565–15578. https://doi.org/10.1021/ja4074529.

(22) Hume, J.; Sun, J.; Jacquet, R.; Renfrew, P. D.; Martin, J. A.; Bonneau, R.; Gilchrist, M. L.; Montclare, J. K. Engineered Coiled-Coil Protein Microfibers. *Biomacromolecules* **2014**, *15* (10), 3503–3510. https://doi.org/10.1021/bm5004948.

(23) Zimenkov, Y.; Dublin, S. N.; Ni, R.; Tu, R. S.; Breedveld, V.; Apkarian, R. P.; Conticello, V. P. Rational Design of a Reversible PH-Responsive Switch for Peptide Self-Assembly. *J. Am. Chem. Soc.* **2006**, *128* (21), 6770–6771. https://doi.org/10.1021/ja0605974.

(24) Fletcher, N. L.; Lockett, C. V.; Dexter, A. F. A PH-Responsive Coiled-Coil Peptide Hydrogel. *Soft Matter* **2011**, *7* (21), 10210–10218. https://doi.org/10.1039/c1sm06261a.

(25) Nambiar, M.; Wang, L. S.; Rotello, V.; Chmielewski, J. Reversible Hierarchical Assembly of Trimeric Coiled-Coil Peptides into Banded Nano- and Microstructures. *J. Am. Chem. Soc.* **2018**, *140* (40), 13028–13033. https://doi.org/10.1021/jacs.8b08163.

(26) Meleties, M.; Katyal, P.; Lin, B.; Britton, D.; Montclare, J. K. Self-Assembly of Stimuli-Responsive Coiled-Coil Fibrous Hydrogels. *Soft Matter* **2021**, *17* (26), 6470–6476. https://doi.org/10.1039/d1sm00780g.

(27) Tian, Y.; Polzer, F. B.; Zhang, H. V.; Kiick, K. L.; Saven, G.; Pochan, D. J. Nanotubes, Plates, and Needles: Pathway-Dependent Self-Assembly of Computationally Designed Peptides. *Biomacromolecules* **2018**, *19*, 4286–4298. https://doi.org/10.1021/acs.biomac.8b01163.

(28) Tian, Y.; Zhang, H. V.; Kiick, K. L.; Saven, J. G.; Pochan, D. J. Fabrication of One- and Two-Dimensional Gold Nanoparticle Arrays on Computationally Designed Self-Assembled Peptide Templates. *Chem. Mater.* **2018**, *30* (23), 8510–8520. https://doi.org/10.1021/acs.chemmater.8b03206.

(29) Tsurkan, M. V; Ogawa, M. Y. Metal-Peptide Nanoassemblies. *Chem. Commun.* **2004**, 2092–2093.

(30) Tsurkan, M. V.; Ogawa, M. Y. Formation of Peptide Nanosphere and Nanofibrils by Metal Coordination. *Biomacromolecules* **2007**, *8* (12), 3908–3913. https://doi.org/10.1021/bm700879t.

(31) Carvalho, I. M. M.; Ogawa, M. Y. Self-Organization of Porphyrin-Peptide Units by Metal-Mediated Peptide Assembly. *J. Braz. Chem. Soc.* **2010**, *21* (7), 1390–1394. https://doi.org/10.1590/S0103-50532010000700027.

(32) Nepal, M.; Sheedlo, M. J.; Das, C.; Chmielewski, J. Accessing Three-Dimensional Crystals with Incorporated Guests through Metal-Directed Coiled-Coil Peptide Assembly. *J. Am. Chem. Soc.* **2016**, *138* (34), 11051–11057. https://doi.org/10.1021/jacs.6b06708.

(33) Jorgensen, M. D.; Chmielewski, J. Reversible Crosslinked Assembly of a Trimeric Coiled-Coil Peptide into a Three-Dimensional Matrix for Cell Encapsulation and Release. *J. Pept. Sci.* **2021**, e3302. https://doi.org/10.1002/psc.3302.

(34) Curtis, R. W.; Scrudders, K. L.; Ulcickas, J. R. W.; Simpson, G. J.; Low-nam, S. T.; Chmielewski, J. Supramolecular Assembly of His-Tagged Fluorescent Protein Guests within Coiled-Coil Peptide Crystal Hosts: Three-Dimensional Ordering and Protein Thermal Stability. *ACS Biomater. Sci. Eng.* **2022**, *8*, 1860–1866. https://doi.org/10.1021/acsbiomaterials.2c00155.

(35) Tavenor, N. A.; Murnin, M. J.; Horne, W. S. Supramolecular Metal-Coordination Polymers, Nets, and Frameworks from Synthetic Coiled-Coil Peptides. *J. Am. Chem. Soc.* **2017**, *139* (6), 2212–2215. https://doi.org/10.1021/jacs.7b00651.

(36) Scheib, K. A.; Tavenor, N. A.; Lawless, M. J.; Saxena, S.; Horne, W. S. Understanding and Controlling the Metal-Directed Assembly of Terpyridine-Functionalized Coiled-Coil Peptides. *Chem. Commun.* **2019**, *55* (54), 7752–7755. https://doi.org/10.1039/c9cc03496j.

(37) Morozov, V. A.; Ogawa, M. Y. Controlled Formation of Emissive Silver Nanoclusters Using Rationally Designed Metal-Binding Proteins. *Inorg. Chem.* **2013**, *52* (16), 9166–9168. https://doi.org/10.1021/ic400760v.

(38) Zaytsev, D. V.; Morozov, V. A.; Fan, J.; Zhu, X.; Mukherjee, M.; Ni, S.; Kennedy, M. A.; Ogawa, M. Y. Metal-Binding Properties and Structural Characterization of a Self-Assembled Coiled Coil: Formation of a Polynuclear Cd-Thiolate Cluster. *J. Inorg. Biochem.* **2013**, *119*, 1–9. https://doi.org/10.1016/j.jinorgbio.2012.10.010.

(39) Dublin, S. N.; Conticello, V. P. Design of a Selective Metal Ion Switch for Self-Assembly of Peptide-Based Fibrils. *J. Am. Chem. Soc.* **2008**, *130* (1), 49–51. https://doi.org/10.1021/ja0775016.

(40) Anzini, P.; Xu, C.; Hughes, S.; Magnotti, E.; Jiang, T.; Hemmingsen, L.; Demeler, B.; Conticello, V. P. Controlling Self-Assembly of a Peptide-Based Material via Metal-Ion Induced Registry Shift. *J. Am. Chem. Soc.* **2013**, *135* (28), 10278–10281. https://doi.org/10.1021/ja404677c.

(41) Thomas, F.; Burgess, N. C.; Thomson, A. R.; Woolfson, D. N. Controlling the Assembly of Coiled-Coil Peptide Nanotubes. *Angew. Chemie - Int. Ed.* **2016**, *55* (3), 987–991. https://doi.org/10.1002/anie.201509304.

(42) Wu, D.; Sinha, N.; Lee, J.; Sutherland, B. P.; Halaszynski, N. I.; Tian, Y.; Caplan, J.; Zhang, H. V.; Saven, J. G.; Kloxin, C. J.; Pochan, D. J. Polymers with Controlled Assembly and Rigidity Made with Click-Functional Peptide Bundles. *Nature* **2019**, *574* (October), 658–662. https://doi.org/10.1038/s41586-019-1683-4.

(43) Kim, K.; Kloxin, C. J.; Saven, G.; Pochan, D. J. Nanofibers Produced by Electrospinning of Ultrarigid Polymer Rods Made from Designed Peptide Bundlemers. *ACS Appl. Mater. Interfaces* **2021**, *13*, 26339–26351. https://doi.org/10.1021/acsami.1c04027.

(44) Jiang, L.; Zuo, X.; Li, J.; Traaseth, N. J.; Kirshenbaum, K. Programmed Supramolecular Assemblies Using Orthogonal Pairs of Heterodimeric Coiled Coil Peptides. *Angew. Chemie Int. Ed.* **2022**, e202201895. https://doi.org/10.1002/anie.202201895.

(45) Gradišar, H.; Božič, S.; Doles, T.; Vengust, D.; Hafner-Bratkovič, I.; Mertelj, A.; Webb, B.; Šali, A.; Klavžar, S.; Jerala, R. Design of a Single-Chain Polypeptide Tetrahedron Assembled from Coiled-Coil Segments. *Nat. Chem. Biol.* **2013**, *9* (6), 362–366. https://doi.org/10.1038/nchembio.1248.

(46) Aupič, J.; Strmšek, Ž.; Lapenta, F.; Pahovnik, D.; Pisanski, T.; Drobnak, I.; Ljubetič, A.; Jerala, R. Designed Folding Pathway of Modular Coiled-Coil-Based Proteins. *Nat. Commun.* **2021**, *12* (1), 1–12. https://doi.org/10.1038/s41467-021-21185-5.

(47) Dooling, L. J.; Buck, M. E.; Zhang, W. Bin; Tirrell, D. A. Programming Molecular Association and Viscoelastic Behavior in Protein Networks. *Adv. Mater.* **2016**, *28* (23), 4651–4657. https://doi.org/10.1002/adma.201506216.

(48) Dooling, L. J.; Tirrell, D. A. Engineering the Dynamic Properties of Protein Networks through Sequence Variation. *ACS Cent. Sci.* **2016**, *2* (11), 812–819. https://doi.org/10.1021/acscentsci.6b00205.

(49) Shen, W.; Zhang, K.; Kornfield, J. A.; Tirrell, D. A. Tuning the Erosion Rate of Artificial Protein Hydrogels through Control of Network Topology. *Nat. Mater.* **2006**, *5* (2), 153–158. https://doi.org/10.1038/nmat1573.

(50) Domeradzka, N. E.; Werten, M. W. T.; De Wolf, F. A.; De Vries, R. Cross-Linking and Bundling of Self-Assembled Protein-Based Polymer Fibrils via Heterodimeric Coiled Coils. *Biomacromolecules* **2016**, *17* (12), 3893–3901. https://doi.org/10.1021/acs.biomac.6b01242.

(51) Zhou, M.; Bentley, D.; Ghosh, I. Helical Supramolecules and Fibers Utilizing Leucine Zipper-Displaying Dendrimers. *J. Am. Chem. Soc.* **2004**, *126*, 734–735.

(52) Dånmark, S.; Aronsson, C.; Aili, D. Tailoring Supramolecular Peptide-Poly(Ethylene Glycol) Hydrogels by Coiled Coil Self-Assembly and Self-Sorting. *Biomacromolecules* **2016**, *17* (6), 2260–2267. https://doi.org/10.1021/acs.biomac.6b00528.

(53) Tunn, I.; De Léon, A. S.; Blank, K. G.; Harrington, M. J. Tuning Coiled Coil Stability with Histidine-Metal Coordination. *Nanoscale* **2018**, *10* (48), 22725–22729. https://doi.org/10.1039/c8nr07259k.

(54) Tunn, I.; Harrington, M. J.; Blank, K. G. Bioinspired Histidine-Zn2+ Coordination for Tuning the Mechanical Properties of Self-Healing Coiled Coil Cross-Linked Hydrogels. *Biomimetics* **2019**, *4* (1), 1–17. https://doi.org/10.3390/biomimetics4010025.

(55) Polizzi, K. M.; Bommarius, A. S.; Broering, J. M.; Chaparro-Riggers, J. F. Stability of Biocatalysts. *Curr. Opin. Chem. Biol.* **2007**, *11* (2), 220–225. https://doi.org/10.1016/j.cbpa.2007.01.685.

(56) Butreddy, A.; Janga, K. Y.; Ajjarapu, S.; Sarabu, S.; Dudhipala, N. Instability of Therapeutic Proteins — An Overview of Stresses, Stabilization Mechanisms and Analytical Techniques Involved in Lyophilized Proteins. *Int. J. Biol. Macromol.* **2021**, *167*, 309–325. https://doi.org/10.1016/j.ijbiomac.2020.11.188.

(57) Juliano, R. Cellular Delivery of Therapeutic Macromolecules Challenges to Macromolecular Drug Delivery. *Biochem. Soc.* **2007**, *35* (August 2006), 29–31.

(58) Boyd, B. J.; Bergström, C. A. S.; Vinarov, Z.; Kuentz, M.; Brouwers, J.; Augustijns, P.; Brandl, M.; Bernkop-Schnürch, A.; Shrestha, N.; Préat, V.; Müllertz, A.; Bauer-Brandl, A.; Jannin, V. Successful Oral Delivery of Poorly Water-Soluble Drugs Both Depends on the Intraluminal Behavior of Drugs and of Appropriate Advanced Drug Delivery Systems. *Eur. J. Pharm. Sci.* **2019**, *137* (June), 104967. https://doi.org/10.1016/j.ejps.2019.104967.

(59) Ahmad, M. Z.; Rizwanullah, M.; Ahmad, J.; Alasmary, M. Y.; Akhter, M. H.; Abdel-Wahab, B. A.; Warsi, M. H.; Haque, A. Progress in Nanomedicine-Based Drug Delivery in Designing of Chitosan Nanoparticles for Cancer Therapy. *Int. J. Polym. Mater. Polym. Biomater.* **2022**, *71* (8), 602–623. https://doi.org/10.1080/00914037.2020.1869737.

(60) Glover, D. J.; Lim, S.; Xu, D.; Sloan, N. B.; Zhang, Y.; Clark, D. S. Assembly of Multicomponent Protein Filaments Using Engineered Subunit Interfaces. *ACS Synth. Biol.* **2018**, *7* (10), 2447–2456. https://doi.org/10.1021/acssynbio.8b00241.

(61) Dong, H.; Dube, N.; Shu, J. Y.; Seo, J. W.; Mahakian, L. M.; Ferrara, K. W.; Xu, T. Long-Circulating 15 Nm Micelles Based on Amphiphilic 3-Helix Peptide-Peg Conjugates. *ACS Nano* **2012**, *6* (6), 5320–5329. https://doi.org/10.1021/nn301142r.

(62) Shu, J. Y.; Lund, R.; Xu, T. Solution Structural Characterization of Coiled-Coil Peptide-Polymer Side-Conjugates. *Biomacromolecules* **2012**, *13* (6), 1945–1955. https://doi.org/10.1021/bm300561y.

(63) Dube, N.; Shu, J. Y.; Dong, H.; Seo, J. W.; Ingham, E.; Kheirolomoom, A.; Chen, P. Y.; Forsayeth, J.; Bankiewicz, K.; Ferrara, K. W.; Xu, T. Evaluation of Doxorubicin-Loaded 3-Helix Micelles as Nanocarriers. *Biomacromolecules* **2013**, *14* (10), 3697–3705. https://doi.org/10.1021/bm4010518.

(64) Dube, N.; Seo, J. W.; Dong, H.; Shu, J. Y.; Lund, R.; Mahakian, L. M.; Ferrara, K. W.; Xu, T. Effect of Alkyl Length of Peptide-Polymer Amphiphile on Cargo Encapsulation Stability and Pharmacokinetics of 3-Helix Micelles. *Biomacromolecules* **2014**, *15* (8), 2963–2970. https://doi.org/10.1021/bm5005788.

(65) Seo, J. W.; Ang, J. C.; Mahakian, L. M.; Tam, S.; Fite, B.; Ingham, E. S.; Beyer, J.; Forsayeth, J.; Bankiewicz, K. S.; Xu, T.; Ferrara, K. W. Self-Assembled 20-Nm 64Cu-Micelles Enhance Accumulation in Rat Glioblastoma. *J. Control. Release* **2015**, *220*, 51–60. https://doi.org/10.1016/j.jconrel.2015.09.057.

(66) Ang, J.; Ma, D.; Lund, R.; Keten, S.; Xu, T. Internal Structure of 15 Nm 3-Helix Micelle Revealed by Small-Angle Neutron Scattering and Coarse-Grained MD Simulation. *Biomacromolecules* **2016**, *17* (10), 3262–3267. https://doi.org/10.1021/acs.biomac.6b00986.

(67) Ang, J.; Ma, D.; Jung, B. T.; Keten, S.; Xu, T. Sub-20 Nm Stable Micelles Based on a Mixture of Coiled-Coils: A Platform for Controlled Ligand Presentation. *Biomacromolecules* **2017**, *18* (11), 3572–3580. https://doi.org/10.1021/acs.biomac.7b00917.

(68) Xue, Y.; Jung, B. T.; Xu, T. Redox Degradable 3-Helix Micelles with Tunable Sensitivity. *Pept. Sci.* **2020**, *112* (1), e24117. https://doi.org/10.1002/pep2.24117.

(69) Assal, Y.; Mizuguchi, Y.; Mie, M.; Kobatake, E. Growth Factor Tethering to Protein Nanoparticles via Coiled-Coil Formation for Targeted Drug Delivery. *Bioconjug. Chem.* **2015**, *26* (8), 1672–1677. https://doi.org/10.1021/acs.bioconjchem.5b00266.

(70) Fletcher, J. M.; Harniman, R. L.; Barnes, F. R. H.; Boyle, A. L.; Collins, A.; Mantell, J.; Sharp, T. H.; Antognozzi, M.; Booth, P. J.; Linden, N.; Miles, M. J.; Sessions, R. B.; Verkade, P.; Woolfson, D. N. Self-Assembling Cages from Coiled-Coil Peptide Modules. *Science (80-.).* **2013**, *340* (6132), 595–599. https://doi.org/10.1126/science.1233936.

(71) Ross, J. F.; Bridges, A.; Fletcher, J. M.; Shoemark, D.; Alibhai, D.; Bray, H. E. V.; Beesley, J. L.; Dawson, W. M.; Hodgson, L. R.; Mantell, J.; Verkade, P.; Edge, C. M.; Sessions, R. B.; Tew, D.; Woolfson, D. N. Decorating Self-Assembled Peptide Cages with Proteins. *ACS Nano* **2017**, *11* (8), 7901–7914. https://doi.org/10.1021/acsnano.7b02368.

(72) Beesley, J. L.; Baum, H. E.; Hodgson, L. R.; Verkade, P.; Banting, G. S.; Woolfson, D. N. Modifying Self-Assembled Peptide Cages to Control Internalization into Mammalian Cells. *Nano Lett.* **2018**, *18* (9), 5933–5937. https://doi.org/10.1021/acs.nanolett.8b02633.

(73) Gormley, A. J.; Chandrawati, R.; Christofferson, A. J.; Loynachan, C.; Jumeaux, C.; Artzy-Schnirman, A.; Aili, D.; Yarovsky, I.; Stevens, M. M. Layer-by-Layer Self-Assembly of Polymer Films and Capsules through Coiled-Coil Peptides. *Chem. Mater.* **2015**, *27* (16), 5820–5824. https://doi.org/10.1021/acs.chemmater.5b02514.

(74) Nambiar, M.; Nepal, M.; Chmielewski, J. Self-Assembling Coiled-Coil Peptide Nanotubes with Biomolecular Cargo Encapsulation. *ACS Biomater. Sci. Eng.* **2019**, *5* (10), 5082–5087. https://doi.org/10.1021/acsbiomaterials.9b01304.

(75) Jorgensen, M. D.; Chmielewski, J. Co-Assembled Coiled-Coil Peptide Nanotubes with Enhanced Stability and Metal-Dependent Cargo Loading. *ACS Omega* **2022**, *7*, 20945–20951. https://doi.org/10.1021/acsomega.2c01669.

(76) Yin, L.; Agustinus, A. S.; Yuvienco, C.; Minashima, T.; Schnabel, N. L.; Kirsch, T.; Montclare, J. K. Engineered Coiled-Coil Protein for Delivery of Inverse Agonist for Osteoarthritis. *Biomacromolecules* **2018**, *19* (5), 1614–1624. https://doi.org/10.1021/acs.biomac.8b00158.

(77) Hill, L. K.; Meleties, M.; Katyal, P.; Xie, X.; Delgado-Fukushima, E.; Jihad, T.; Liu, C. F.; O'Neill, S.; Tu, R. S.; Renfrew, P. D.; Bonneau, R.; Wadghiri, Y. Z.; Montclare, J. K. Thermoresponsive Protein-Engineered Coiled-Coil Hydrogel for Sustained Small Molecule Release. *Biomacromolecules* **2019**, *20* (9), 3340–3351. https://doi.org/10.1021/acs.biomac.9b00107.

(78) Ding, L.; Jiang, Y.; Zhang, J.; Klok, H. A.; Zhong, Z. PH-Sensitive Coiled-Coil Peptide-Cross-Linked Hyaluronic Acid Nanogels: Synthesis and Targeted Intracellular Protein Delivery to CD44 Positive Cancer Cells. *Biomacromolecules* **2018**, *19* (2), 555–562. https://doi.org/10.1021/acs.biomac.7b01664.

(79) Frantz, C.; Stewart, K. M.; Weaver, V. M. The Extracellular Matrix at a Glance. *J. Cell Sci.* **2010**, *123* (24), 4195–4200. https://doi.org/10.1242/jcs.023820.

(80) Langhans, S. A. Three-Dimensional in Vitro Cell Culture Models in Drug Discovery and Drug Repositioning. *Front. Pharmacol.* **2018**, *9* (JAN), 1–14. https://doi.org/10.3389/fphar.2018.00006.

(81) Nii, T.; Makino, K.; Tabata, Y. Three-Dimensional Culture System of Cancer Cells Combined with Biomaterials for Drug Screening. *Cancers (Basel).* **2020**, *12* (10), 2754. https://doi.org/10.3390/cancers12102754.

(82) Aisenbrey, E. A.; Murphy, W. L. Synthetic Alternatives to Matrigel. *Nat. Rev. Mater.* **2020**, *5* (7), 539–551. https://doi.org/10.1038/s41578-020-0199-8.

(83) Banwell, E. F.; Abelardo, E. S.; Adams, D. J.; Birchall, M. A.; Corrigan, A.; Donald, A. M.; Kirkland, M.; Serpell, L. C.; Butler, M. F.; Woolfson, D. N. Rational Design and Application of Responsive α-Helical Peptide Hydrogels. *Nat. Mater.* **2009**, *8* (7), 596–600. https://doi.org/10.1038/nmat2479.

(84) Mehrban, N.; Zhu, B.; Tamagnini, F.; Young, F. I.; Wasmuth, A.; Hudson, K. L.; Thomson, A. R.; Birchall, M. A.; Randall, A. D.; Song, B.; Woolfson, D. N. Functionalized α-Helical Peptide Hydrogels for Neural Tissue Engineering. *ACS Biomater. Sci. Eng.* **2015**, *1* (6), 431–439. https://doi.org/10.1021/acsbiomaterials.5b00051.

(85) Mizuguchi, Y.; Mashimo, Y.; Mie, M.; Kobatake, E. Temperature-Responsive Multifunctional Protein Hydrogels with Elastin-like Polypeptides for 3-D Angiogenesis. *Biomacromolecules* **2020**, *21* (3), 1126–1135. https://doi.org/10.1021/acs.biomac.9b01496.

(86) Huang, C. C.; Ravindran, S.; Yin, Z.; George, A. 3-D Self-Assembling Leucine Zipper Hydrogel with Tunable Properties for Tissue Engineering. *Biomaterials* **2014**, *35* (20), 5316–5326. https://doi.org/10.1016/j.biomaterials.2014.03.035.

(87) Dexter, A. F.; Fletcher, N. L.; Creasey, R. G.; Filardo, F.; Boehm, M. W.; Jack, K. S. Fabrication and Characterization of Hydrogels Formed from Designer Coiled-Coil Fibril-Forming Peptides. *RSC Adv.* **2017**, *7* (44), 27260–27271. https://doi.org/10.1039/c7ra02811c.

(88) Snapper, C. M. Distinct Immunologic Properties of Soluble versus Particulate Antigens. *Front. Immunol.* **2018**, *9* (MAR), 598. https://doi.org/10.3389/fimmu.2018.00598.

(89) Raman, S.; Machaidze, G.; Lustig, A.; Aebi, U.; Burkhard, P. Structure-Based Design of Peptides That Self-Assemble into Regular Polyhedral Nanoparticles. *Nanomedicine Nanotechnology, Biol. Med.* **2006**, *2* (2), 95–102. https://doi.org/10.1016/j.nano.2006.04.007.

(90) Doll, T. A. P. F.; Dey, R.; Burkhard, P. Design and Optimization of Peptide Nanoparticles. *J. Nanobiotechnology* **2015**, *13* (1), 1–12. https://doi.org/10.1186/s12951-015-0119-z.

(91) Wahome, N.; Pfeiffer, T.; Ambiel, I.; Yang, Y.; Keppler, O. T.; Bosch, V.; Burkhard, P. Conformation-Specific Display of 4E10 and 2F5 Epitopes on Self-Assembling Protein Nanoparticles as a Potential HIV Vaccine. *Chem. Biol. Drug Des.* **2012**, *80* (3), 349–357. https://doi.org/10.1111/j.1747-0285.2012.01423.x.

(92) Pimentel, T. A. P. F.; Yan, Z.; Jeffers, S. A.; Holmes, K. V.; Hodges, R. S.; Burkhard, P. Peptide Nanoparticles as Novel Immunogens: Design and Analysis of a Prototypic Severe Acute Respiratory Syndrome Vaccine. *Chem. Biol. Drug Des.* **2009**, *73* (1), 53–61. https://doi.org/10.1111/j.1747-0285.2008.00746.x.

(93) Kaba, S. A.; Brando, C.; Guo, Q.; Mittelholzer, C.; Raman, S.; Tropel, D.; Aebi, U.; Burkhard, P.; Lanar, D. E. A Nonadjuvanted Polypeptide Nanoparticle Vaccine Confers Long-Lasting Protection against Rodent Malaria. *J. Immunol.* **2009**, *183* (11), 7268–7277. https://doi.org/10.4049/jimmunol.0901957.

(94) Kaba, S. A.; McCoy, M. E.; Doll, T. A. P. F.; Brando, C.; Guo, Q.; Dasgupta, D.; Yang, Y.; Mittelholzer, C.; Spaccapelo, R.; Crisanti, A.; Burkhard, P.; Lanar, D. E. Protective Antibody and CD8+ T-Cell Responses to the Plasmodium Falciparum Circumsporozoite Protein Induced by a Nanoparticle Vaccine. *PLoS One* **2012**, *7* (10), e48304. https://doi.org/10.1371/journal.pone.0048304.

(95) El Bissati, K.; Zhou, Y.; Dasgupta, D.; Cobb, D.; Dubey, J. P.; Burkhard, P.; Lanar, D. E.; McLeod, R. Effectiveness of a Novel Immunogenic Nanoparticle Platform for Toxoplasma Peptide Vaccine in HLA Transgenic Mice. *Vaccine* **2014**, *32* (26), 3243–3248. https://doi.org/10.1016/j.vaccine.2014.03.092.

(96) El Bissati, K.; Zhou, Y.; Paulillo, S. M.; Raman, S. K.; Karch, C. P.; Roberts, C. W.; Lanar, D. E.; Reed, S.; Fox, C.; Carter, D.; Alexander, J.; Sette, A.; Sidney, J.; Lorenzi, H.; Begeman, I. J.; Burkhard, P.; McLeod, R. Protein Nanovaccine Confers Robust Immunity against Toxoplasma. *npj Vaccines* **2017**, *2* (1), 1–11. https://doi.org/10.1038/s41541-017-0024-6.

(97) El Bissati, K.; Zhou, Y.; Paulillo, S. M.; Raman, S. K.; Karch, C. P.; Reed, S.; Estes, A.; Estes, A.; Lykins, J.; Burkhard, P.; McLeod, R. Engineering and Characterization of a Novel Self Assembling Protein for Toxoplasma Peptide Vaccine in HLA-A*11:01, HLA-A*02:01 and HLA-B*07:02 Transgenic Mice. *Sci. Rep.* **2020**, *10* (1), 1–13. https://doi.org/10.1038/s41598-020-73210-0.

(98) Babapoor, S.; Neef, T.; Mittelholzer, C.; Girshick, T.; Garmendia, A.; Shang, H.; Khan, M. I.; Burkhard, P. A Novel Vaccine Using Nanoparticle Platform to Present Immunogenic M2e against Avian Influenza Infection. *Influenza Res. Treat.* **2011**, *2011*, 1–12. https://doi.org/10.1155/2011/126794.

(99) Li, J.; Helal, Z.; Ladman, B.; Karch, C.; Gelb Jr, J.; Burkhard, P.; Khan, M. I. Nanoparticle Vaccine for Avian Influenza Virus: A Challenge Study against Highly Pathogenic H5N2 Subtype. *J. Virol. Antivir. Res.* **2018**, *7* (1), 1–5. https://doi.org/10.4172/2324-8955.1000179.

(100) Karch, C. P.; Li, J.; Kulangara, C.; Paulillo, S. M.; Raman, S. K.; Emadi, S.; Tan, A.; Helal, Z. H.; Fan, Q.; Khan, M. I.; Burkhard, P. Vaccination with Self-Adjuvanted Protein Nanoparticles Provides Protection against Lethal Influenza Challenge. *Nanomedicine Nanotechnology, Biol. Med.* **2017**, *13* (1), 241–251. https://doi.org/10.1016/j.nano.2016.08.030.

(101) Li, J.; Helal, Z. H.; Karch, C. P.; Mishra, N.; Girshick, T.; Garmendia, A.; Burkhard, P.; Khan, M. I. A Self-Adjuvanted Nanoparticle Based Vaccine against Infectious Bronchitis Virus. *PLoS One* **2018**, *13* (9), 1–17. https://doi.org/10.1371/journal.pone.0203771.

(102) Boato, F.; Thomas, R. M.; Ghasparian, A.; Freund-Renard, A.; Moehle, K.; Robinson, J. A. Synthetic Virus-like Particles from Self-Assembling Coiled-Coil Lipopeptides and Their Use in Antigen Display to the Immune System. *Angewandte Chemie - International Edition*. 2007, pp 9015–9018. https://doi.org/10.1002/anie.200702805.

(103) Wu, Y.; Norberg, P. K.; Reap, E. A.; Congdon, K. L.; Fries, C. N.; Kelly, S. H.; Sampson, J. H.; Conticello, V. P.; Collier, J. H. A Supramolecular Vaccine Platform Based on α-Helical Peptide Nanofibers. *ACS Biomater. Sci. Eng.* **2017**, *3* (12), 3128–3132. https://doi.org/10.1021/acsbiomaterials.7b00561.

(104) Fries, C. N.; Wu, Y.; Kelly, S. H.; Wolf, M.; Votaw, N. L.; Zauscher, S.; Collier, J. H. Controlled Lengthwise Assembly of Helical Peptide Nanofibers to Modulate CD8+ T-Cell Responses. *Advanced Materials*. 2020, p 2003310. https://doi.org/10.1002/adma.202003310.

(105) Olugbile, S.; Villard, V.; Bertholet, S.; Jafarshad, A.; Kulangara, C.; Roussilhon, C.; Frank, G.; Agak, G. W.; Felger, I.; Nebie, I.; Konate, K.; Kajava, A. V.; Schuck, P.; Druilhe, P.; Spertini, F.; Corradin, G. Malaria Vaccine Candidate: Design of a Multivalent Subunit α-Helical Coiled Coil Poly-Epitope. *Vaccine* **2011**, *29* (40), 7090–7099. https://doi.org/10.1016/j.vaccine.2011.06.122.

(106) Morris, C.; Glennie, S. J.; Lam, H. S.; Baum, H. E.; Kandage, D.; Williams, N. A.; Morgan, D. J.; Woolfson, D. N.; Davidson, A. D. A Modular Vaccine Platform Combining Self-Assembled Peptide Cages and Immunogenic Peptides. *Adv. Funct. Mater.* **2019**, *29* (8), 1807357. https://doi.org/10.1002/adfm.201807357.

(107) Wagner, D. E.; Phillips, C. L.; Ali, W. M.; Nybakken, G. E.; Crawford, E. D.; Schwab, A. D.; Smith, W. F.; Fairman, R. Toward the Development of Peptide Nanofilaments and Nanoropes as Smart Materials. *Proc. Natl. Acad. Sci. U. S. A.* **2005**, *102* (36), 12656–12661. https://doi.org/10.1073/pnas.0505871102.

(108) Kokona, B.; Kim, A. M.; Roden, R. C.; Daniels, J. P.; Pepe-mooney, B. J.; Kovaric, B. C.; Paula, J. C. De; Johnson, K. A.; Fairman, R. Self Assembly of Coiled-Coil Peptide-Porphyrin Complexes. *Biomacromolecules* **2009**, *10*, 1454–1459.

(109) Pepe-Mooney, B. J.; Kokona, B.; Fairman, R. Characterization of Mesoscale Coiled-Coil Peptide-Porphyrin Complexes. *Biomacromolecules* **2011**, *12* (12), 4196–4203. https://doi.org/10.1021/bm201354m.

(110) Taggart, J. C.; Welch, E. Z.; Mulqueen, M. F.; Dioguardi, V. B.; Cauer, A. G.; Kokona, B.; Fairman, R. Testing the Role of Charge and Structure on the Stability of Peptide-Porphyrin Complexes. *Biomacromolecules* **2014**, *15* (12), 4544–4550. https://doi.org/10.1021/bm5013426.

(111) Chen, Y. X.; Ing, N. L.; Wang, F.; Xu, D.; Sloan, N. B.; Lam, N. T.; Winter, D. L.; Egelman, E. H.; Hochbaum, A. I.; Clark, D. S.; Glover, D. J. Structural Determination of a Filamentous Chaperone to Fabricate Electronically Conductive Metalloprotein Nanowires. *ACS Nano* **2020**, *14* (6), 6559–6569. https://doi.org/10.1021/acsnano.9b09405.

CHAPTER 2. REVERSIBLE CROSSLINKED ASSEMBLY OF A TRIMERIC COILED-COIL PEPTIDE INTO A THREE-DIMENSIONAL MATRIX FOR CELL ENCAPSULATION AND GROWTH

2.1 Introduction

The extracellular matrix (ECM) is composed primarily of proteoglycans and fibrous proteins that provide complex microenvironments for cell and tissue growth.[1] As such, mimicking the ECM has been a goal for tissue engineering in recent decades. While two-dimensional cell culturing has been the standard method for experimentation, these methods are significantly limited in their ability to mimic *in vivo* settings. By creating three-dimensional (3D) cell culture, however, scaffolds can act as mimetics that are closer to *in vivo* environments.

To this end, natural materials have been extensively explored for tissue engineering. Materials like Matrigel and collagen gels have been used to culture various cell types,[2–4] as well as act as scaffolds for tumor modeling.[5,6] While these materials mimic many components in the ECM, batch to batch differences remains a common problem due to their variable and ill-defined composition.[1,7]

Alternatively, self-assembling peptides have emerged as promising biomaterials for cell culture and tissue growth.[8–11] A range of peptide motifs have been investigated, including coiled-coils,[12–15] collagen mimetic peptides,[16–22] and amphiphilic peptides.[23–38] Coiled-coils have previously been reported that undergo reversible assembly via temperature, pH, and introduction of phosphate buffered saline (PBS).[13–15] Herein, we describe the higher order assembly of a designed trimeric coiled-coil (**TriCross**) based on the leucine zipper region of the transcription factor GCN4 using metal-mediated crosslinking. Through this approach, a 3D matrix was obtained that provided a scaffold for cell encapsulation and growth, with the ability of releasing the cells under mild conditions.

2.2 Results and Discussion

2.2.1 Peptide Design and Synthesis

The peptide design was based on the well-studied GCN4 leucine-zipper motif with modifications for a crosslinked growth. The coiled-coil domain of this transcription factor has been

studied for self-assembly, as well as for encapsulating small molecules for drug delivery.[39–41] We envisioned installing ligands for metal ions at both the N- and C-termini and the center portion of a trimeric variant of the GCN4 coiled-coil sequence. With this in mind, di-histidine and nitrilotriacetic acid (NTA) ligands were installed at the C- and N-termini, respectively (**Figure 2.1**), to facilitate metal ion-promoted linear growth. A bipyridine moiety was also installed within the peptide at a central location on the *f*-face of the coiled-coil to promote radial growth through metal-ligand interactions. The bipyridine ligand installation was completed by replacing Ser14 with a 4-methyltrityl (Mtt) protected Lys14. In this way, the three ligands on each peptide strand of the trimer would be organized within the coiled-coil trimer to promote crosslinked assembly in the presence of metal ions. This unique peptide was dubbed **TriCross** to represent the Trimeric oligomeric state and its Crosslinked growth (**Figure 2.1**).

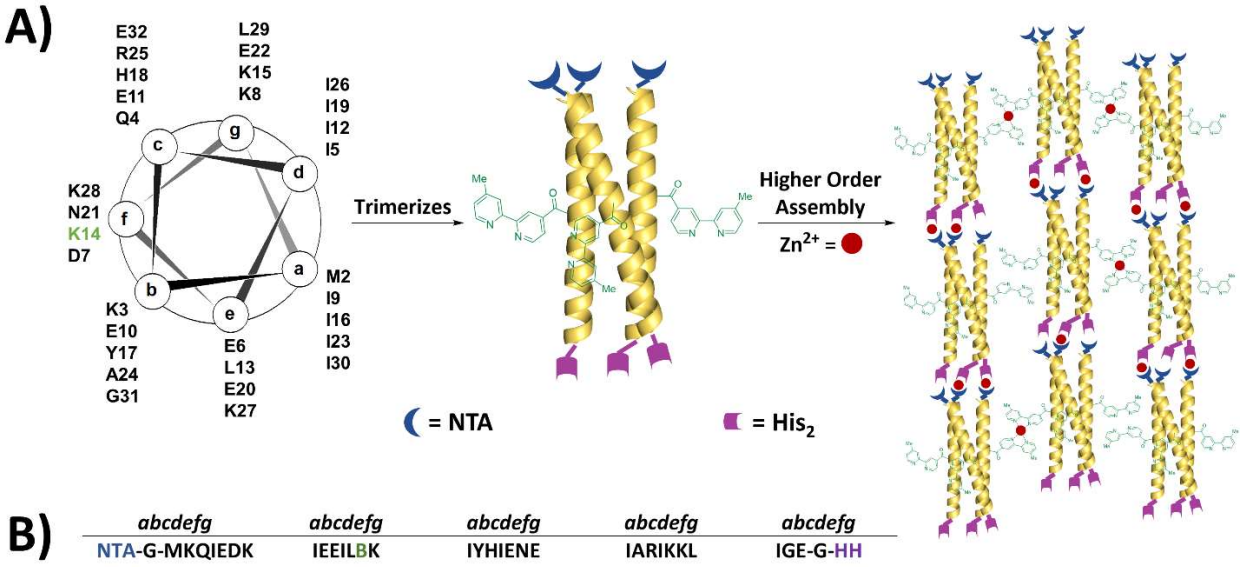

Figure 2.1. TriCross peptide design. (A) Helical wheel representation of **TriCross** with K14 (green) as the site of the bipyridine modification with residues at the *a* and *d* positions dictating a trimeric oligomeric state. Upon addition of metal ions, **TriCross** assembles into a higher order crosslinked structure. (B) GCN4 sequence with modifications for linear (NTA and His_2) and radial (B – bipyridine) growth.

Standard solid-phase peptide synthesis was conducted for the preparation of **TriCross** using ChemMatrix resin containing a Rink amide linker. The NTA and bipyridine ligands were synthesized using protocols described previously, and the NTA moiety was installed at the N-

terminus.[42,43] Selective removal of the Mtt protecting group using 1,1,1,3,3,3-hexafluoroisopropanol (HFIP), followed by treatment with 4'-methyl-2,2'-bipyridine-4-carboxylic acid installed the bipyridine moiety within the peptide. The peptide was cleaved from resin using a trifluoroacetic acid (TFA) cocktail, purified to homogeneity via reverse phase high-performance liquid chromatography (RP-HPLC), and characterized by matrix-assisted laser desorption ionization time-of-flight (MALDI-ToF) mass spectrometry.

2.2.2 Assembly of TriCross

The triple functionalization of the trimeric variant of the GCN4 coiled-coil could potentially lead to a disruption of the helical conformation of the peptide. The structure of **TriCross** was investigated using circular dichroism (CD) spectroscopy (**Figure 2.2**). The spectrum revealed an alpha helical conformation with ~60% helicity, indicated by the local minima at 208 nm and 222 nm and a local maximum at 194 nm. Though the bipyridine, NTA, and di-histidine moieties did decrease the helicity somewhat when compared to the native trimeric peptide (90% helicity),[44] **TriCross** retained an alpha helical conformation. Furthermore, the coiled-coil nature of **TriCross** was confirmed through comparison of the magnitude of the ellipticities at 208 nm and 222 nm. A value of $\theta_{222}/\theta_{208} \geq 1$ has been shown for coiled-coil peptides, and the value for TriCross (1.4) confirms the coiled-coil nature of this sequence.[45]

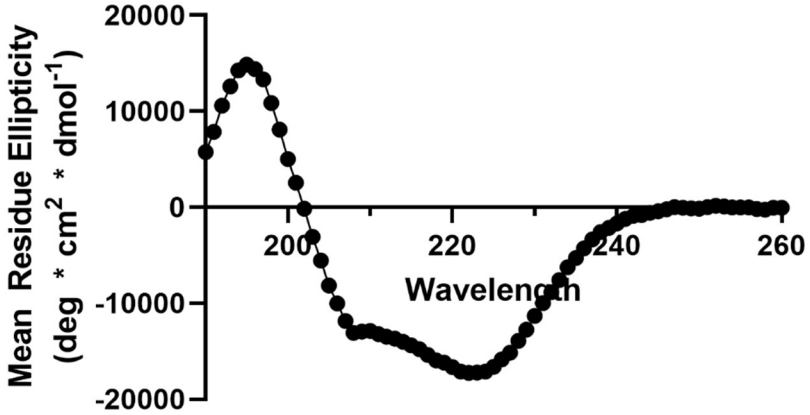

Figure 2.2. CD spectrum of the coiled-coil peptide, **TriCross** (50 μM), measured in citrate buffer (20 mM, pH 3.0).

With the vision of using **TriCross** as a scaffold for 3D cell culturing, the metal-mediated peptide assembly was attempted in Dulbecco's Modified Eagle Medium (DMEM) with 10% fetal bovine serum (FBS) using a 1 mM concentration of **TriCross** and $ZnCl_2$. An immediate (~1 min) precipitate was observed upon addition of the metal, and the morphology of the peptide assembly was studied using SEM following a 1-hour incubation at 37 °C. These assembly conditions (1:1 peptide:metal ratio) led to a 3D matrix structure (Figure 2.3A). Additional peptide to metal ratios of 1:0.4 and 1:0.1 were analyzed, and as the concentration of the metal ion was decreased there was a corresponding decrease in the amount of assembly observed (**Figure 2.3**B-C). A 1:2 ratio led to a similar morphology as that obtained for the 1:1 ratio (**Figure 2.3**D). Therefore, to limit potential excess of metal ions, a 1:1 ratio of **TriCross** to Zn^{2+} was pursued for cell studies. Different metal ions were tested, including Ni^{2+}, Cu^{2+}, and Co^{2+}, and these led to similar morphologies as the Zn^{2+} experiments (**Figure 2.3**E-G).

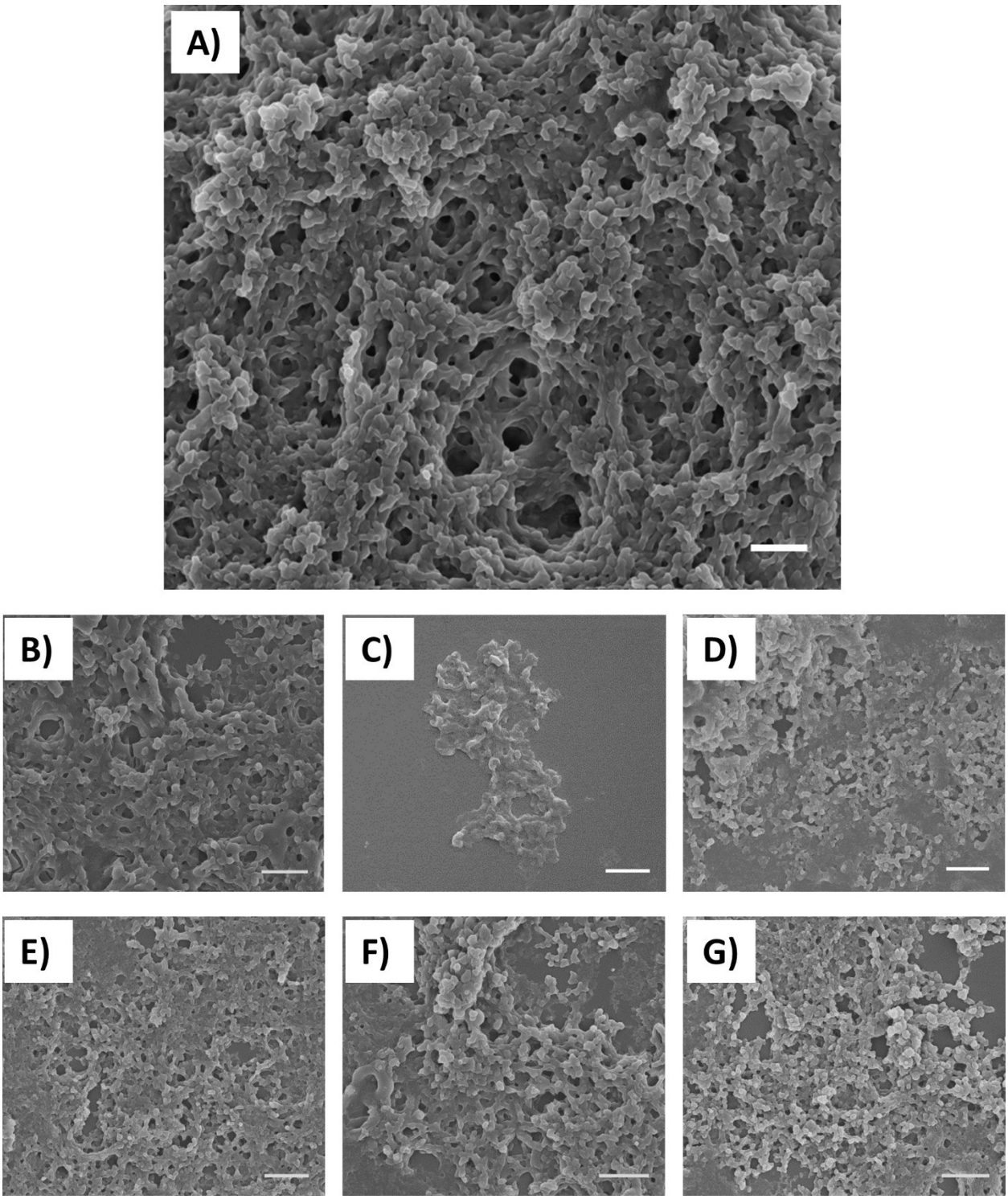

Figure 2.3. (A) SEM image of **TriCross** assembly with $ZnCl_2$ (1 mM each) in DMEM with 10% FBS after 1 hr (scale bar: 1 μm). (B-D) **TriCross** assemblies at varying **TriCross** to Zn^{2+} ratios. (B) 1:2, (C) 1:0.4, (D) 1:0.1 (scale bar: 2 μm). (E-G) **TriCross** assemblies upon addition of other divalent metals. (E) Ni^{2+}, (F) Cu^{2+}, (G) Co^{2+} (scale bar: 2 μm).

Previous hierarchical assembly of coiled-coils revealed a banding pattern representative of the length of a coiled-coil.[46] With this in mind, we investigated the **TriCross** assemblies formed in 3-(N-morpholino)propanesulfonic acid (MOPS) buffer (20 mM, pH 7.4) by transmission electron microscopy (TEM). Evidence of pronounced banding was observed with assemblies in MOPS buffer (**Figure 2.4**). The separation of the bands in this pattern (4.5 ± 0.7 nm, n=15) correlates to the length of the **TriCross** coiled-coil (4.8 nm), indicating organized structural features within the assembly.

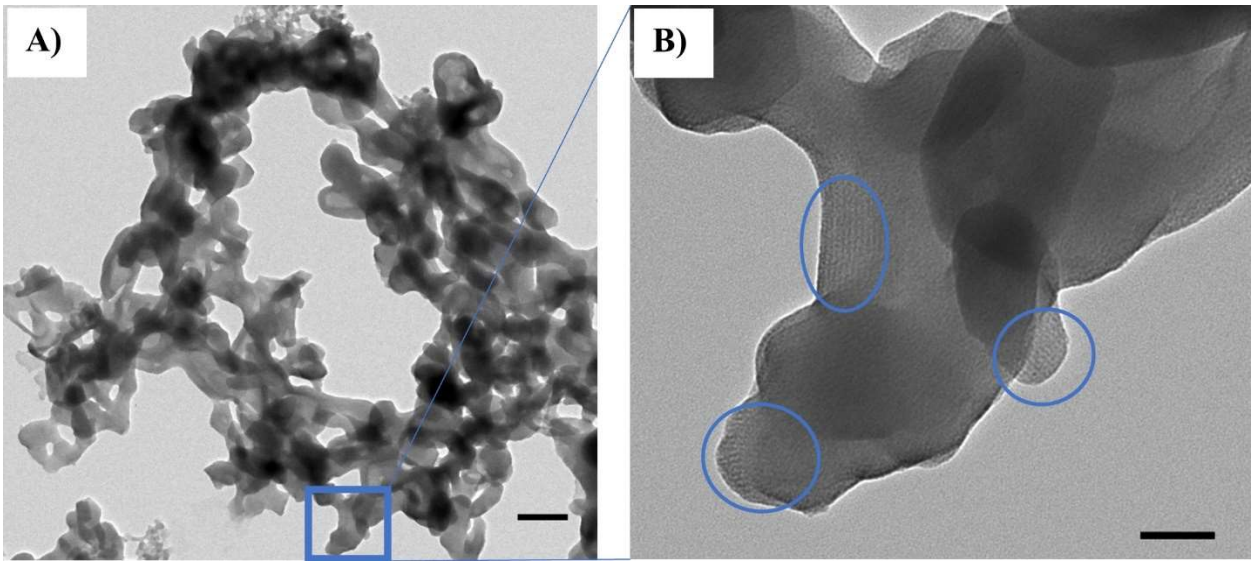

Figure 2.4. TEM images of **TriCross** assembly with $ZnCl_2$ (1 mM each) in 20 mM MOPS buffer (pH 7.4) after 1 hr. (A) A wider view (scale bar: 250 nm) and (B) a closer view with some areas of banding indicated with blue circles (scale bar: 50 nm).

With a robust **TriCross** assembly, cells might be encapsulated and grown over an extended period of time. Therefore, it is essential that the assembly was stable to prolonged treatment with media. To this end, **TriCross** was incubated with DMEM with 10% FBS at 37 °C for seven days. SEM micrographs showed minimal changes in the morphology of the matrix (**Figure 2.5**), indicating that this material could be used for 3D cell culturing. Interestingly, the **TriCross** matrix could be disassembled under mild conditions with ethylenediaminetetraacetic acid (EDTA) (**Figure 2.6**), thereby providing a potential means to release cells from the 3D matrix on demand.

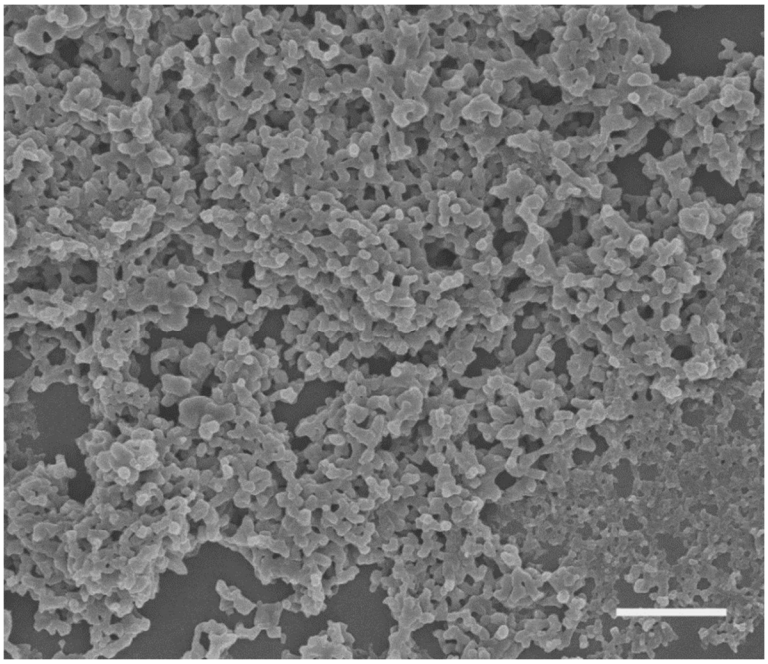

Figure 2.5. SEM micrograph of **TriCross** after a 7-day incubation in DMEM media with FBS at 37 °C (scale bar: 3 μM).

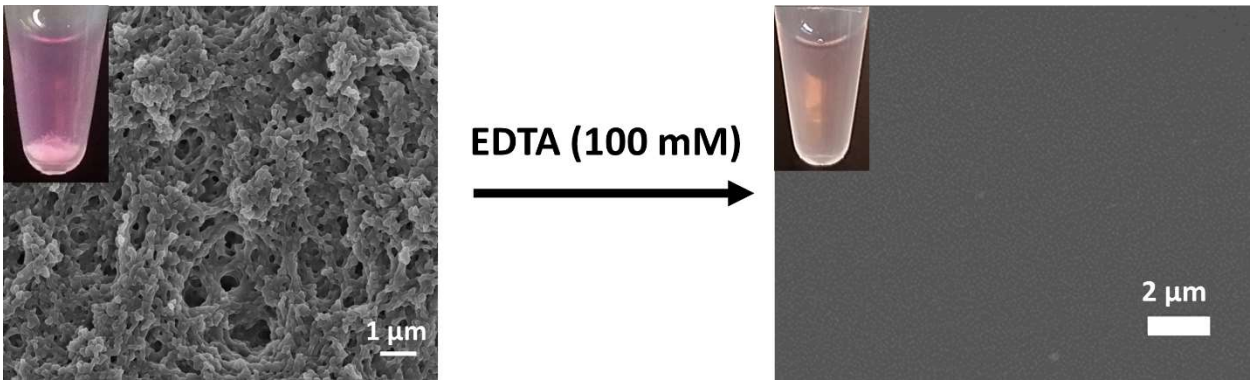

Figure 2.6. SEM images of **TriCross** assembly and disassembly in DMEM (pink) with 10% FBS through addition of EDTA (100 mM).

2.2.3 HeLa Cell Encapsulation

With the ability to assemble and disassemble **TriCross** under mild conditions suitable for cells, we sought to encapsulate cells within the 3D matrix. HeLa cells were first suspended in DMEM with 10% FBS, followed by addition of **TriCross** and $ZnCl_2$ (1 mM each) to the cells in media to create the 3D scaffold around the cells. In order to visualize the matrix, we added Rh-His_6 (20 μM) during the assembly, thereby incorporating the fluorophore through His_6-metal ion interactions and staining the matrix red. Live cells were stained post-assembly with calcein AM

(2.5 μM) (**Figure 2.7**). Through visualization of varying planes of focus with confocal microscopy, it was confirmed that the HeLa cells were indeed encapsulated within the 3D matrix.

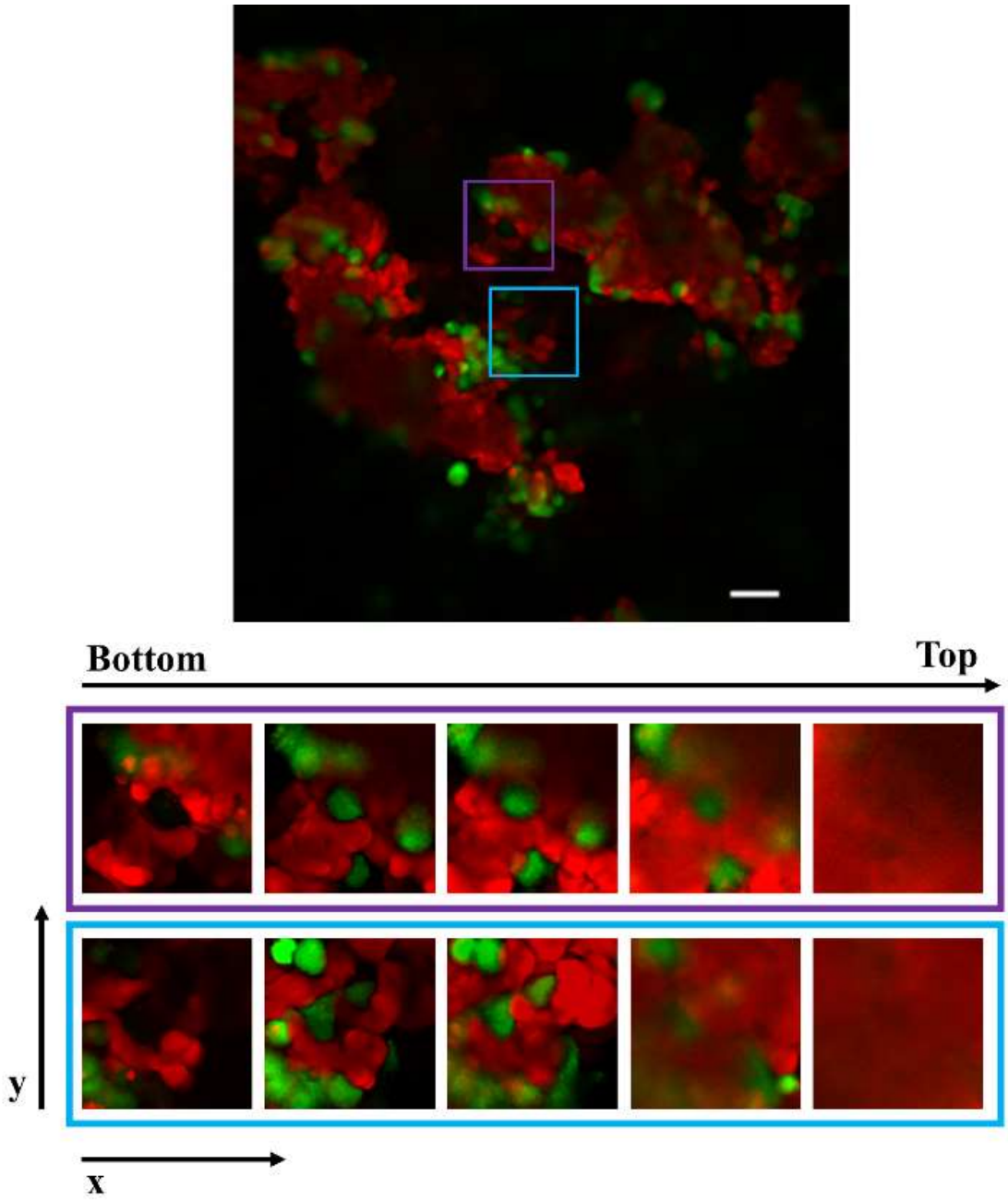

Figure 2.7. Confocal microscopy image of live HeLa cells (green) encapsulated within the **TriCross** assembly labeled with Rh-His_6 (red) in DMEM with 10% FBS (scale bar: 50 μm).

Following the initial encapsulation, cell viability in this 3D cell culture environment was studied over extended time periods. HeLa cells were suspended in DMEM with 10% FBS and encapsulated upon addition of **TriCross** and $ZnCl_2$ (1 mM each) as described above. While encapsulated, live and dead cells were stained after a 3-day period using calcein AM and PI, respectively (2.5 μM each), and visualized by confocal microscopy. The cells encapsulated within the 3D matrix displayed significant viability (**Figure 2.8**), as was also observed after a 6-day period (**Figure 2.9**).

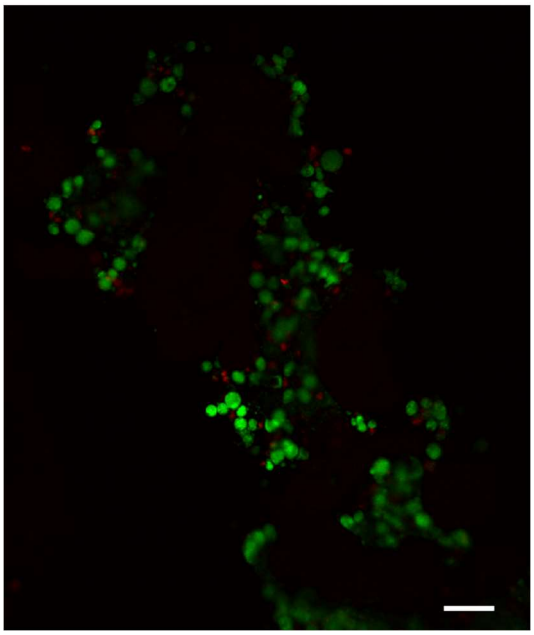

Figure 2.8. Confocal microscopy image of HeLa cells encapsulated within the **TriCross** assembly in DMEM with 10% FBS (live – green and dead - red) after a 3-day encapsulation period (scale bar: 50 μm).

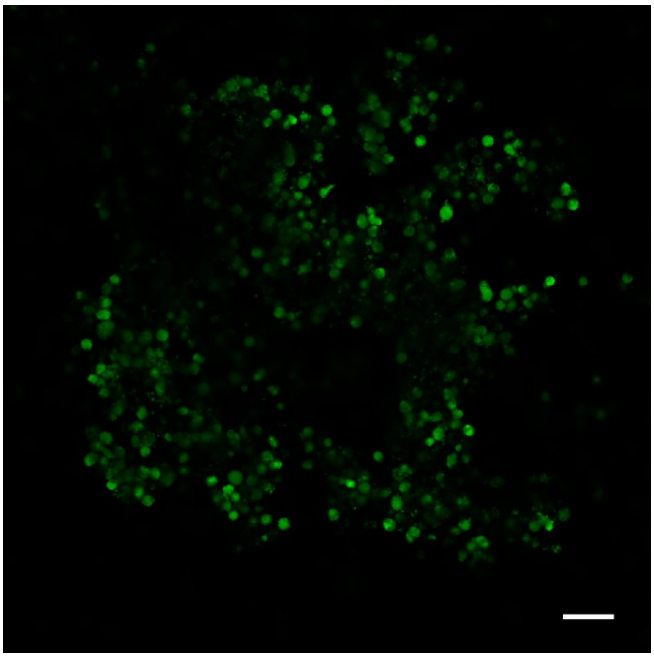

Figure 2.9. Confocal microscopy image of encapsulated live HeLa cells (green) after a six-day incubation (scale bar: 50 μm).

2.2.4 Release of Encapsulated Cells

Finally, the viability of the encapsulated cells was quantified following disassembly of the 3D scaffold with EDTA. After a 3-day encapsulation period, the matrix was collected and subjected EDTA (100 mM, 50 μL) for 15 minutes at 37 °C. The added EDTA chelates Zn^{2+}, effectively reversing metal-ligand interactions between coiled-coils and disassembles the matrix. Upon breakdown of the material, the cells were collected, washed with DMEM and stained with 0.4% trypan blue for 1 minute. Live/dead cell populations were counted and viability was compared to untreated cells and cells subjected to taxol (10 μM) (**Figure 2.10**). Excellent cell viability was observed with cells encapsulated within the **TriCross** material for 3 days (~92%). These data demonstrate that the assembly and disassembly of **TriCross** occurs under conditions that are mild to cells, and the scaffold is suitable for 3D cell culture.

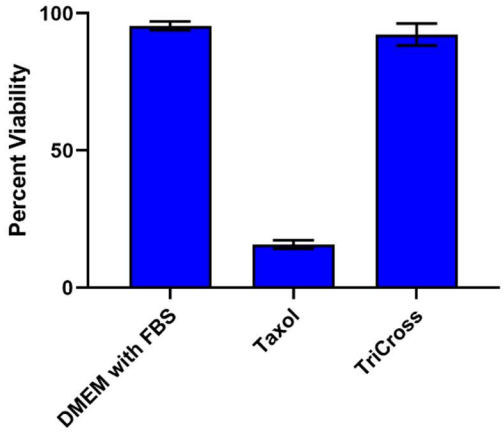

Figure 2.10. Viability of HeLa cells upon disassembly of the **TriCross** matrix with EDTA as compared to untreated cells (DMEM and 10% FBS) and cells treated with taxol (10 μM).

2.3 Future Directions (HBN)

With these promising results, the next step was to use this peptide as well as its collagen triple helix equivalent, **HBN**[17,21], to effectively mimic the ECM for more complex systems. Specifically, we strived to encapsulate human-induced pluripotent stem cells (hiPSC) neural progenitor cells (NPCs) in the hopes of creating brain organoids and controlling cell differentiation. While these stem cells aggregate through traditional cell culture means, previous reports have shown that these cells exhibit different behavior when encapsulated within a hydrogel.[47] With this in mind, the effects of peptide-based materials on these cells were investigated.

HBN was first used to encapsulate hiPSCs with and without **HBRGDS**, an **HBN** derivative with the cell adhesion sequence RGDS.[17] HiPSCs were suspended in phosphate buffer (200 mM, pH 7.2), followed by addition of **HBN** (1 mM) or **HBN**:**HBRGDS** (1 mM, 4:1 ratio) and $NiCl_2$ (1 mM) to the cells to create a 3D scaffold around the cells. After the peptide assembled (~2 min), the solution was diluted with NPC media (2 mL). While cells look healthy after a three-week encapsulation period, only small organoids were seen in both samples (~3-5 cell clumps, **Figure 2.11** and **Figure 2.12**).

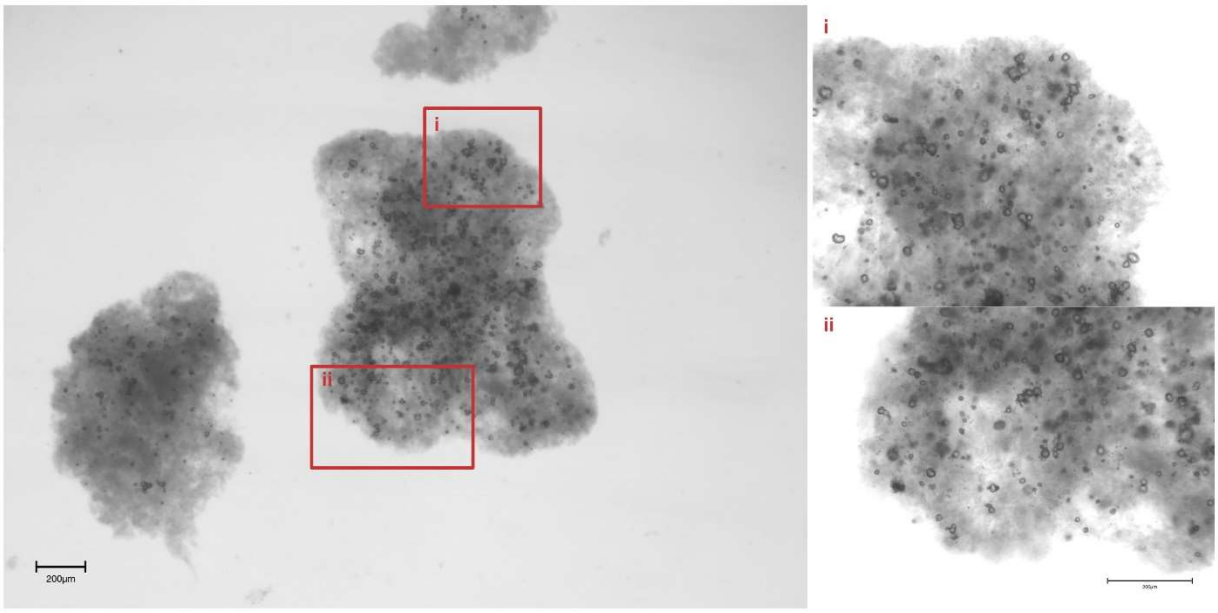

Figure 2.11. Light microscope images of hiPSCs encapsulated in **HBN** after three weeks.

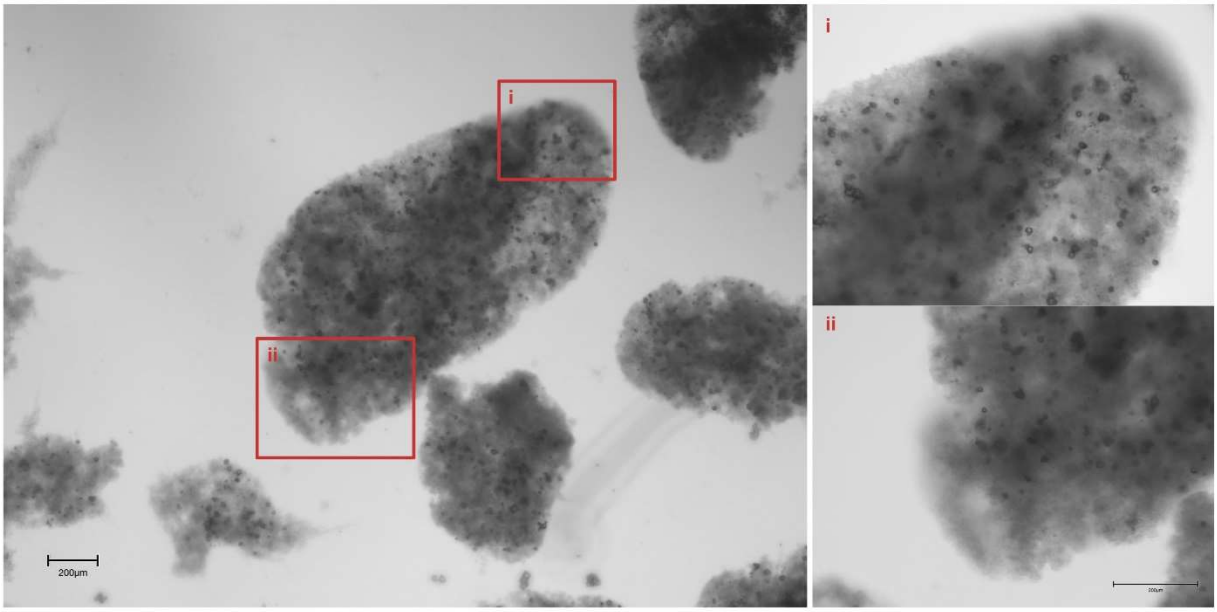

Figure 2.12. Light microscope images of hiPSCs encapsulated in **HBN**:**HBRGDS** (4:1 ratio) after three weeks.

Further studies are needed to investigate the formation of organoids within the peptide matrices. More cells may need to be used during the encapsulation process to produce spheroids.

Using another peptide-based material, **TriCross** and **TriCross** derivatives with cell adhesion sequences covalently bonded, may also provide more mobility for the cells. Finally, using His-tagged cell adhesion sequences rather than displayed through covalent bonds may increase cell mobility to form spheroids.

2.4 Conclusions

To summarize, the trimeric variant of the GCN4 coiled-coil was modified to facilitate a cross-linked, higher order assembly through installation of metal binding ligands at the termini and center of the peptide. This approach led to assembly of a robust 3D matrix in media with serum, that remained stable for extended periods of time. Utilizing the reversibility of the assembly through addition and removal of metal, HeLa cells were encapsulated and subsequently released from the **TriCross** 3D scaffold with minimal cytotoxicity. Overall, the design of the **TriCross** peptide led to an ECM mimic with controllable functions *in vitro*.

2.5 Materials and Methods

2.5.1 Materials

All amino acids and reagents for peptide synthesis were purchased from Chem-Impex Inc and ChemPep. All solvents were purchased from Fisher Scientific. Triisopropylsilane (TIPS), and propidium iodide (PI) were purchased from Sigma-Aldrich. Diisopropylethylamine (DIEA), and all metal salts were purchased from Alfa Aesar. Trifluoroacetic acid (TFA) was purchased from Acros Organics. NovaPEG Rink Amide resin LL was purchased from Novabiochem. The mixed isomer 5/6-carboxy-tetramethyl-rhodamine succinimidyl ester was purchased from ThermoFisher Scientific. Dulbecco's Modified Eagle Medium (DMEM) was purchased from Corning Inc. and fetal bovine serum (FBS) was purchased from R&D Systems. Calcein AM was purchased from BioLegend.

2.5.2 General Peptide Synthesis and Purification

TriCross was synthesized using standard Fmoc peptide chemistry on ChemMatrix RinkAmide resin (300 mg). Specifically, Fmoc-His (4 eq) was coupled to NovaPEG Rink Amide

resin LL with hexafluorophosphate azabenzotriazole tetramethyl uranium (HATU, 4 eq) and DIEA (8 eq) in dimethylformamide (DMF, 10 mL) for 2.5 hrs. The resin was washed with DMF (3 x 10 mL), dichloromethane (DCM, 3 x 10 mL), methanol (MeOH, 3 x 10 mL), DCM (3 x 10 mL), and DMF (3 x 10 mL). The newly added histidine was deprotected in 25% piperidine in DMF (V/V, 10 mL) for 30 min. The resin was washed as above, and the next amino acid was coupled. This process was repeated for the remainder of the peptide. After deprotection of the final glycine with piperidine/DMF, tert-butyl protected nitrilotriacetic acid[42] (NTA, 6 eq) was coupled with HATU (6 eq) and DIEA (8 eq) at room temperature for 6 hrs and washed. Selective on-resin deprotection of the 4-methyltrityl (Mtt) group on lysine was conducted with 30% 1,1,1,3,3,3-hexafluoroisopropanol (HFIP) in DCM (2 x 10 mL) and the resin was washed as above. Treatment with 4'-methyl-2,2'-bipyridine-4-carboxylic acid[43] (6 eq), HATU (6 eq) and DIEA (8 eq) for 6 hours followed by the same washing steps afforded the final peptide.

The resin was dried under reduced pressure and cleaved using a 95% TFA, 2.5% TIPS, 2.5% H_2O (10 mL) cocktail for 2.5 hours. The resin was washed once with the cleavage cocktail and twice with DCM. The washes were combined and the solvent was removed under reduced pressure. The peptide was precipitated using cold diethyl ether (30 mL). The precipitate was centrifuged at 2000 g for 10 minutes and the supernatant was decanted. The solid was dried under reduced pressure and dissolved in water to create a 10 mg/mL solution. The peptide was purified to homogeneity on a Waters reverse phase high performance liquid chromatography (RP-HPLC) instrument using a Luna C18 semi-prep column with an eluent consisting of solvent A (CH_3CN/0.1% TFA) and solvent B (H_2O/0.1% TFA), a 60 min gradient consisting of 20 to 80 % A, and a flow rate of 10 mL/min. The peptide was characterized using matrix-assisted laser desorption ionization time-of-flight mass spectrometry (mass calculated: 4595 g/mol, mass observed: 4593 g/mol).

2.5.3 Circular Dichroism

A solution of peptide (50 μM) was prepared in citrate buffer (20 mM, pH 3.0) in 200 μL total volume. The CD spectrum was taken using a JASCO J-810 CD spectropolarimeter (Jasco Inc.) at room temperature, averaging 3 scans between 190-260 nm. The data pitch was 0.1 nm with a 1 nm bandwidth and the scan rate was 100 nm/min with a 1 second response time.

2.5.4 TriCross Assembly

TriCross was assembled using a 1 mM peptide and metal concentration ($ZnCl_2$, $NiCl_2$, $CuCl_2$, and $CoCl_2$) in either MOPS buffer (20 mM, pH = 7.4) or DMEM with 10% FBS in 50 μL total volume. The mixture was incubated at 37 °C for 1 hr. The assembly was centrifuged at 10 g for 3 minutes and the supernatant removed and replaced with water (50 μL). This process was repeated twice. The pelleted assembly were resuspended and stored in 50 μL water.

2.5.5 Scanning Electron Microscopy

Aliquots of the assemblies described in Section 2.5.4 (3 μL) were placed on a glass side attached to a metal stub with copper tape. The sample was allowed to air dry and coated with platinum for 60 seconds. The sample was imaged using an FEI NOVA NANO SEM field emission scanning electron microscope (SEM) using an Everhart-Thornley for magnifications < 10,000 or high-resolution through the lens detector for magnifications ≥ 10,000. Samples were imaged at an accelerating voltage of 5 kV and a working distance of 3-5 mm with a 30 μm aperture.

2.5.6 Transmission Electron Microscopy

Aliquots of the assemblies described in Section 2.5.4 (3 μL) were placed onto a glow discharged 400-mesh copper grid coated in formvar with a carbon film (Electron Microscopy Sciences) and allowed to absorb for 1 min. The droplet was wicked away and stained using 2% uranyl acetate (Electron Microscopy Sciences). The assembly was visualized using a FEI Tecnai T20 transmission electron microscope operated at 100 kV, with a spot size of 3, 200 μm condenser aperture, and 70 μm objective aperture. Images were captured using a Gatan US1000 2Kx2K CCD camera (Scientific Instruments and Application).

2.5.7 Cell Encapsulation

HeLa cells were cultured in DMEM supplemented with 10% FBS and 1% penicillin/streptomycin at 37 °C and 5% CO_2. A suspension of HeLa cells (50,000 per well) in DMEM with 10% FBS was prepared in an 8-well Lab-Tek chambered slide. **TriCross** (1 mM), $ZnCl_2$ (1 mM), and rhodamine-labelled His_6 (Rh-His_6)[40] (20 μM, when applicable) were added to the HeLa cells (100 μL total volume) and the mixture was allowed to assemble at 37 °C and 5%

CO_2 for 2 minutes to allow for encapsulation of the cells within the matrix. Each well was then diluted with 400 μL of DMEM with 10% FBS and incubated for 1, 3, or 6 days at 37 °C and 5% CO_2. Cells were then stained with calcein AM (2.5 μM) and PI (2.5 μM, when applicable) for 15 min with subsequent washing using DMEM with 10% FBS (400 μL). The samples were imaged using a Nikon A1R multiphoton inverted confocal microscope under a 20x oil objective. Rh-His_6 and PI were excited using a 561 nm laser while calcein AM was excited using a 488 nm laser.

2.5.8 Cell Release

After encapsulation of HeLa cells within the matrix using the protocol above, the contents of the wells were transferred to Eppendorf tubes and a solution of ethylenediaminetetraacetic acid (EDTA, 100 mM, 50 μL) was added to the mixture to breakdown the matrix. The mixture was incubated at 37 °C for 15 minutes. The cells were centrifuged at 1200 revolutions per minute for 7 minutes and washed with DMEM with 10% FBS followed staining with 0.4% trypan blue at room temperature for 1 minute. The cells were then counted using a Neubauer Hemacytometer with DMEM and 10% FBS alone used as a negative control and a treatment with taxol (10 μM) for 3 days in DMEM with 10% FBS as the positive control.

2.5.9 Neural Stem Cell Encapsulation

Human-induced pluripotent stem cells (hiPSC) were cultured in NPC media (DMEM/F-12 media supplemented with neurobasal medium (1x), N2 supplement (1x), B27 supplement (1x), basic fibroblast growth factor (bFGF, 20 ng/mL), penicillin/streptomycin (1x), and Y-compound (10 mM)). A suspension of hiPSCs (700,000 per well) in phosphate buffer (200 mM, pH 7.2, 200 μL) were prepared in low-adherent 6-well plates. The cells were diluted with water (600 μL) and HBN (10 mM, 100 μL) or HBN:HBRGDS (10 mM, 4:1, 100 μL). A $NiCl_2$ solution (10 mM, 100 μL) was added to each well, and the peptide assembled for 2 min. The wells were gently diluted with NPC media (2.5 mL). The media was gently exchanged every two days for three weeks. While these cells are traditionally incubated on a shaker, encapsulated cells were not agitated.

2.6 References

(1) Frantz, C.; Stewart, K. M.; Weaver, V. M. The Extracellular Matrix at a Glance. *J. Cell Sci.* **2010**, *123* (24), 4195–4200. https://doi.org/10.1242/jcs.023820.

(2) Lee, S. W.; Lee, H. J.; Hwang, H. S.; Ko, K.; Han, D. W.; Ko, K. Optimization of Matrigel-Based Culture for Expansion of Neural Stem Cells. *Animal Cells Syst. (Seoul).* **2015**, *19* (3), 175–180. https://doi.org/10.1080/19768354.2015.1035750.

(3) Laflamme, M. A.; Chen, K. Y.; Naumova, A. V.; Muskheli, V.; Fugate, J. A.; Dupras, S. K.; Reinecke, H.; Xu, C.; Hassanipour, M.; Police, S.; O'Sullivan, C.; Collins, L.; Chen, Y.; Minami, E.; Gill, E. A.; Ueno, S.; Yuan, C.; Gold, J.; Murry, C. E. Cardiomyocytes Derived from Human Embryonic Stem Cells in Pro-Survival Factors Enhance Function of Infarcted Rat Hearts. *Nat. Biotechnol.* **2007**, *25* (9), 1015–1024. https://doi.org/10.1038/nbt1327.

(4) Ghanaati, S.; Schlee, M.; Webber, M. J.; Willershausen, I.; Barbeck, M.; Balic, E.; Görlach, C.; Stupp, S. I.; Sader, R. A.; Kirkpatrick, C. J. Evaluation of the Tissue Reaction to a New Bilayered Collagen Matrix in Vivo and Its Translation to the Clinic. *Biomed. Mater.* **2011**, *6* (1), 015010. https://doi.org/10.1088/1748-6041/6/1/015010.

(5) Liu, Z.; Vunjak-Novakovic, G. Modeling Tumor Microenvironments Using Custom-Designed Biomaterial Scaffolds. *Curr. Opin. Chem. Eng.* **2016**, *11*, 94–105. https://doi.org/10.1016/j.coche.2016.01.012.

(6) Lv, D.; Hu, Z.; Lu, L.; Lu, H.; Xu, X. Three-Dimensional Cell Culture: A Powerful Tool in Tumor Research and Drug Discovery. *Oncol. Lett.* **2017**, *14* (6), 6999–7010. https://doi.org/10.3892/ol.2017.7134.

(7) Aisenbrey, E. A.; Murphy, W. L. Synthetic Alternatives to Matrigel. *Nat. Rev. Mater.* **2020**, *5* (7), 539–551. https://doi.org/10.1038/s41578-020-0199-8.

(8) Wu, Y.; Collier, J. H. α-Helical Coiled-Coil Peptide Materials for Biomedical Applications. *WIREs Nanomed Nanobiotechnol* **2017**, *9* (April), 1–17. https://doi.org/10.1002/wnan.1424.

(9) Acar, H.; Srivastava, S.; Chung, E. J.; Schnorenberg, M. R.; Barrett, J. C.; LaBelle, J. L.; Tirrell, M. Self-Assembling Peptide-Based Building Blocks in Medical Applications. *Adv. Drug Deliv. Rev.* **2017**, *110–111*, 65–79. https://doi.org/10.1016/j.addr.2016.08.006.

(10) Yang, Z.; Xu, H.; Zhao, X. Designer Self-Assembling Peptide Hydrogels to Engineer 3D Cell Microenvironments for Cell Constructs Formation and Precise Oncology Remodeling in Ovarian Cancer. *Adv. Sci.* **2020**, *7* (9), 1903718. https://doi.org/10.1002/advs.201903718.

(11) Strauss, K.; Chmielewski, J. Advances in the Design and Higher-Order Assembly of Collagen Mimetic Peptides for Regenerative Medicine. *Curr. Opin. Biotechnol.* **2017**, *46*, 34–41. https://doi.org/10.1016/j.copbio.2016.10.013.

(12) Banwell, E. F.; Abelardo, E. S.; Adams, D. J.; Birchall, M. A.; Corrigan, A.; Donald, A. M.; Kirkland, M.; Serpell, L. C.; Butler, M. F.; Woolfson, D. N. Rational Design and Application of Responsive α-Helical Peptide Hydrogels. *Nat. Mater.* **2009**, *8* (7), 596–600. https://doi.org/10.1038/nmat2479.

(13) Yao, M. H.; Yang, J.; Du, M. S.; Song, J. T.; Yu, Y.; Chen, W.; Zhao, Y. Di; Liu, B. Polypeptide-Engineered Physical Hydrogels Designed from the Coiled-Coil Region of Cartilage Oligomeric Matrix Protein for Three-Dimensional Cell Culture. *J. Mater. Chem. B* **2014**, *2* (20), 3123–3132. https://doi.org/10.1039/c4tb00107a.

(14) Dexter, A. F.; Fletcher, N. L.; Creasey, R. G.; Filardo, F.; Boehm, M. W.; Jack, K. S. Fabrication and Characterization of Hydrogels Formed from Designer Coiled-Coil Fibril-Forming Peptides. *RSC Adv.* **2017**, *7* (44), 27260–27271. https://doi.org/10.1039/c7ra02811c.

(15) Mizuguchi, Y.; Mashimo, Y.; Mie, M.; Kobatake, E. Temperature-Responsive Multifunctional Protein Hydrogels with Elastin-like Polypeptides for 3-D Angiogenesis. *Biomacromolecules* **2020**, *21* (3), 1126–1135. https://doi.org/10.1021/acs.biomac.9b01496.

(16) Sun, X.; He, M.; Wang, L.; Luo, L.; Wang, J.; Xiao, J. Luminescent Biofunctional Collagen Mimetic Nanofibers. *ACS Omega* **2019**, *4* (15), 16270–16279. https://doi.org/10.1021/acsomega.9b00740.

(17) Hernandez-Gordillo, V.; Chmielewski, J. Mimicking the Extracellular Matrix with Functionalized, Metal-Assembled Collagen Peptide Scaffolds. *Biomaterials* **2014**, *35* (26), 7363–7373. https://doi.org/10.1016/j.biomaterials.2014.05.019.

(18) Jin, H. E.; Jang, J.; Chung, J.; Lee, H. J.; Wang, E.; Lee, S. W.; Chung, W. J. Biomimetic Self-Templated Hierarchical Structures of Collagen-Like Peptide Amphiphiles. *Nano Lett.* **2015**, *15* (10), 7138–7145. https://doi.org/10.1021/acs.nanolett.5b03313.

(19) Strauss, K.; Chmielewski, J. Metal-Promoted Assembly of Two Collagen Mimetic Peptides into a Biofunctional "Spiraled Horn" Scaffold. *Materials (Basel).* **2016**, *9* (10), 838. https://doi.org/10.3390/ma9100838.

(20) Rubert Pérez, C. M.; Panitch, A.; Chmielewski, J. A Collagen Peptide-Based Physical Hydrogel for Cell Encapsulation. *Macromol. Biosci.* **2011**, *11* (10), 1426–1431. https://doi.org/10.1002/mabi.201100230.

(21) Pires, M. M.; Przybyla, D. E.; Chmielewski, J. A Metal-Collagen Peptide Framework for Three-Dimensional Cell Culture. *Angew. Chemie* **2009**, *121* (42), 7953–7957. https://doi.org/10.1002/ange.200902375.

(22) Luo, J.; Tong, Y. W. Self-Assembly of Collagen-Mimetic Peptide Amphiphiles into Biofunctional Nanofiber. *ACS Nano* **2011**, *5* (10), 7739–7747. https://doi.org/10.1021/nn202822f.

(23) Onak, G.; Gökmen, O.; Yaralı, Z. B.; Karaman, O. Enhanced Osteogenesis of Human Mesenchymal Stem Cells by Self-Assembled Peptide Hydrogel Functionalized with Glutamic Acid Templated Peptides. *J. Tissue Eng. Regen. Med.* **2020**, *14* (9), 1236–1249. https://doi.org/10.1002/term.3095.

(24) Yamada, Y.; Patel, N. L.; Kalen, J. D.; Schneider, J. P. Design of a Peptide-Based Electronegative Hydrogel for the Direct Encapsulation, 3D Culturing, in Vivo Syringe-Based Delivery, and Long-Term Tissue Engraftment of Cells. *ACS Appl. Mater. Interfaces* **2019**, *11* (38), 34688–34697. https://doi.org/10.1021/acsami.9b12152.

(25) Semino, C. E.; Kasahara, J.; Hayashi, Y.; Zhang, S. Entrapment of Migrating Hippocampal Neural Cells in Three-Dimensional Peptide Nanofiber Scaffold. *Tissue Eng.* **2004**, *10* (3–4), 643–655. https://doi.org/10.1089/107632704323061997.

(26) Gungormus, M.; Branco, M.; Fong, H.; Schneider, J. P.; Tamerler, C.; Sarikaya, M. Self Assembled Bi-Functional Peptide Hydrogels with Biomineralization-Directing Peptides. *Biomaterials* **2010**, *31* (28), 7266–7274. https://doi.org/10.1016/j.biomaterials.2010.06.010.

(27) Haines-Butterick, L.; Rajagopal, K.; Branco, M.; Salick, D.; Rughani, R.; Pilarz, M.; Lamm, M. S.; Pochan, D. J.; Schneider, J. P. Controlling Hydrogelation Kinetics by Peptide Design for Three-Dimensional Encapsulation and Injectable Delivery of Cells. *Proc. Natl. Acad. Sci. U. S. A.* **2007**, *104* (19), 7791–7796. https://doi.org/10.1073/pnas.0701980104.

(28) Zhang, S. Extensive Neurite Outgrowth and Active Synapse Formation on Self-Assembling Peptide Matrix Scaffolds. *Second Smith Nephew Int. Symp. - Tissue Eng. 2000 Adv. Tissue Eng. Biomater. Cell Signal.* **2000**, *97* (12), 12. https://doi.org/10.1073/pnas.97.12.6728.

(29) Gelain, F.; Bottai, D.; Vescovi, A.; Zhang, S. Designer Self-Assembling Peptide Nanofiber Scaffolds for Adult Mouse Neural Stem Cell 3-Dimensional Cultures. *PLoS One* **2006**, *1* (1), e119. https://doi.org/10.1371/journal.pone.0000119.

(30) Beniash, E.; Hartgerink, J. D.; Storrie, H.; Stendahl, J. C.; Stupp, S. I. Self-Assembling Peptide Amphiphile Nanofiber Matrices for Cell Entrapment. *Acta Biomater.* **2005**, *1* (4), 387–397. https://doi.org/10.1016/j.actbio.2005.04.002.

(31) Koutsopoulos, S.; Zhang, S. Long-Term Three-Dimensional Neural Tissue Cultures in Functionalized Self-Assembling Peptide Hydrogels, Matrigel and Collagen I. *Acta Biomater.* **2013**, *9* (2), 5162–5169. https://doi.org/10.1016/j.actbio.2012.09.010.

(32) Hogrebe, N. J.; Gooch, K. J. Direct Influence of Culture Dimensionality on Human Mesenchymal Stem Cell Differentiation at Various Matrix Stiffnesses Using a Fibrous Self-Assembling Peptide Hydrogel. *J. Biomed. Mater. Res. - Part A* **2016**, *104* (9), 2356–2368. https://doi.org/10.1002/jbm.a.35755.

(33) Zhao, Y.; Zhang, S.; Chan, D. W.; He, M. Prediction Signaling Transduction Pathways of Cancer-Related Apoptosis Protein Par-4. *Zhongshan Daxue Xuebao/Acta Sci. Natralium Univ. Sunyatseni* **2010**, *49* (6), 83–88.

(34) Wee, Y.; Moore, A. N.; Jia, S.; Zhou, J.; Colombo, J. S.; D'Souza, R. N. A Single-Step Self-Assembly Approach for the Fabrication of Aligned and Multilayered Three-Dimensional Tissue Constructs Using Multidomain Peptide Hydrogel. *SLAS Technol.* **2019**, *24* (1), 55–65. https://doi.org/10.1177/2472630318777759.

(35) Black, K. A.; Lin, B. F.; Wonder, E. A.; Desai, S. S.; Chung, E. J.; Ulery, B. D.; Katari, R. S.; Tirrell, M. V. Biocompatibility and Characterization of a Peptide Amphiphile Hydrogel for Applications in Peripheral Nerve Regeneration. *Tissue Eng. - Part A* **2015**, *21* (7–8), 1333–1342. https://doi.org/10.1089/ten.tea.2014.0297.

(36) Ji, W.; Álvarez, Z.; Edelbrock, A. N.; Sato, K.; Stupp, S. I. Bioactive Nanofibers Induce Neural Transdifferentiation of Human Bone Marrow Mesenchymal Stem Cells. *ACS Appl. Mater. Interfaces* **2018**, *10* (48), 41046–41055. https://doi.org/10.1021/acsami.8b13653.

(37) Greene, J. J.; McClendon, M. T.; Stephanopoulos, N.; Álvarez, Z.; Stupp, S. I.; Richter, C. P. Electrophysiological Assessment of a Peptide Amphiphile Nanofiber Nerve Graft for Facial Nerve Repair. *J. Tissue Eng. Regen. Med.* **2018**, *12* (6), 1389–1401. https://doi.org/10.1002/term.2669.

(38) Stevenson, M. D.; Piristine, H.; Hogrebe, N. J.; Nocera, T. M.; Boehm, M. W.; Reen, R. K.; Koelling, K. W.; Agarwal, G.; Sarang-Sieminski, A. L.; Gooch, K. J. A Self-Assembling Peptide Matrix Used to Control Stiffness and Binding Site Density Supports the Formation of Microvascular Networks in Three Dimensions. *Acta Biomater.* **2013**, *9* (8), 7651–7661. https://doi.org/10.1016/j.actbio.2013.04.002.

(39) Nambiar, M.; Nepal, M.; Chmielewski, J. Self-Assembling Coiled-Coil Peptide Nanotubes with Biomolecular Cargo Encapsulation. *ACS Biomater. Sci. Eng.* **2019**, *5* (10), 5082–5087. https://doi.org/10.1021/acsbiomaterials.9b01304.

(40) Nepal, M.; Sheedlo, M. J.; Das, C.; Chmielewski, J. Accessing Three-Dimensional Crystals with Incorporated Guests through Metal-Directed Coiled-Coil Peptide Assembly. *J. Am. Chem. Soc.* **2016**, *138* (34), 11051–11057. https://doi.org/10.1021/jacs.6b06708.

(41) More, H. T.; Zhang, K. S.; Srivastava, N.; Frezzo, J. A.; Montclare, J. K. Influence of Fluorination on Protein-Engineered Coiled-Coil Fibers. *Biomacromolecules* **2015**, *16* (4), 1210–1217. https://doi.org/10.1021/bm5019062.

(42) Huang, Z.; Park, J. I.; Watson, D. S.; Hwang, P.; Szoka, F. C. Facile Synthesis of Multivalent Nitrilotriacetic Acid (NTA) and NTA Conjugates for Analytical and Drug Delivery Applications. *Bioconjug. Chem.* **2006**, *17* (6), 1592–1600. https://doi.org/10.1021/bc0602228.

(43) Banerjee, T.; Rawalekar, S.; Das, A.; Ghosh, H. N. Interfacial Electron Transfer Dynamics of Two Newly Synthesized Catecholate Bound RuII Polypyridyl-Based Sensitizers on TiO2 Nanoparticle Surface - A Femtosecond Pump Probe Spectroscopic Study. *Eur. J. Inorg. Chem.* **2011**, No. 27, 4187–4197. https://doi.org/10.1002/ejic.201100411.

(44) O'Shea, E. K.; Rutkowski, R.; Kim, P. S. Evidence That the Leucine Zipper Is a Coiled Coil. *Science* **1989**, *243* (4890), 538–542. https://doi.org/10.1126/science.2911757.

(45) Lau, S. Y. M.; Taneja, A. K.; Hodges, R. S. Synthesis of a Model Protein of Defined Secondary and Quaternary Structure. Effect of Chain Length on the Stabilization and Formation of Two-Stranded α-Helical Coiled-Coils. *J. Biol. Chem.* **1984**, *259* (21), 13253–13261. https://doi.org/10.1016/s0021-9258(18)90686-1.

(46) Nambiar, M.; Wang, L. S.; Rotello, V.; Chmielewski, J. Reversible Hierarchical Assembly of Trimeric Coiled-Coil Peptides into Banded Nano- and Microstructures. *J. Am. Chem. Soc.* **2018**, *140* (40), 13028–13033. https://doi.org/10.1021/jacs.8b08163.

(47) Wu, S.; Xu, R.; Duan, B.; Jiang, P. Three-Dimensional Hyaluronic Acid Hydrogel-Based Models for in Vitro Human IPSC-Derived NPC Culture and Differentiation. *J. Mater. Chem. B* **2017**, *5* (21), 3870–3878. https://doi.org/10.1039/c7tb00721c.

CHAPTER 3. CO-ASSEMBLED COILED-COIL PEPTIDE NANOTUBES WITH ENHANCED STABILITY AND METAL-DEPENDENT CARGO LOADING

3.1 Introduction

Nanotube biomaterials have drawn significant attention for their applications ranging from piezoelectric devices to cargo delivery.[1] While less common than simpler nanofibrils, these three-dimensional materials contain an inner cavity and outer shell to allow for multifunctionality. Peptide-based nanotubes specifically are an attractive choice owing to their tunability and biocompatibility.[2–4] As such, peptide nanotubes have been derived from a diverse collection of structures including dipeptides,[5–9] cyclic peptides,[10–25] peptoids,[26–29] triple helices,[30,31] β-sheets,[32–35] and coiled-coils.[36–42]

The assembly and morphology of peptide nanotubes provides the opportunity for a range of interesting biological applications. For example, early studies with cyclic peptide nanotubes focused on interactions with the cell membrane to mimic membrane bound proteins and form ion channels.[10,11,19–21,23] Since then, nanotubes have been developed with antibacterial properties, including dipeptide nanotubes clearing biofilms[7] and cyclic peptide nanotubes lysing bacterial membranes.[12,25] β-sheet nanotubes have been used for directed delivery of an anticancer agent to metastatic melanoma,[34] whereas coiled-coil nanotubes, composed of the peptide **TriNL**, for instance, have been loaded with biopolymer cargo.[42]

Coiled-coil nanotubes of **TriNL** have potential for molecular storage and drug delivery, but instability in phosphate buffered saline (PBS) limited biological applications. Herein we demonstrate the co-assembly of **TriNL** with a variant containing metal-binding ligands that produces nanotubes with enhanced PBS stability in a metal-dependent manner, while also promoting His-tagged cargo binding.

3.2 Results and Discussion

3.2.1 Co-Assembled Peptide Nanotube Design

The design of the stabilized nanotubes is based on the leucine-zipper motif of the transcription factor GCN4. A dimeric coiled-coil in its native form, the GCN4 sequence has been

modified to form trimeric coiled-coils.[43] This trimeric sequence was the basis of the **TriNL** peptide (Figure 3.1A) that assembles into nanotubes while encapsulating biopolymer cargo.[42] However, upon exposure to PBS these coiled-coil peptide tubes were found to rapidly deteriorate. To promote stability, therefore, we hypothesized that the introduction of a coiled-coil peptide with metal-binding ligands as a part of the nanotubes might strengthen the interactions between coiled-coils in a metal-dependent fashion, and, potentially decrease the rate of tube degradation (Figure 3.1B). To this end, we looked to the coiled-coil peptide **p2L** with di-histidine and nitrilotriacetic acid (NTA) ligands at the C- and N-termini, respectively (Figure 3.1A).[44] The **p2L** peptide alone has been shown to form hexagonal crystals with zinc ions,[44] but here we wished to investigate what levels of **p2L** could be added to **TriNL** while retaining the tube morphology, and whether stabilized nanotubes would result (Figure 3.1B).

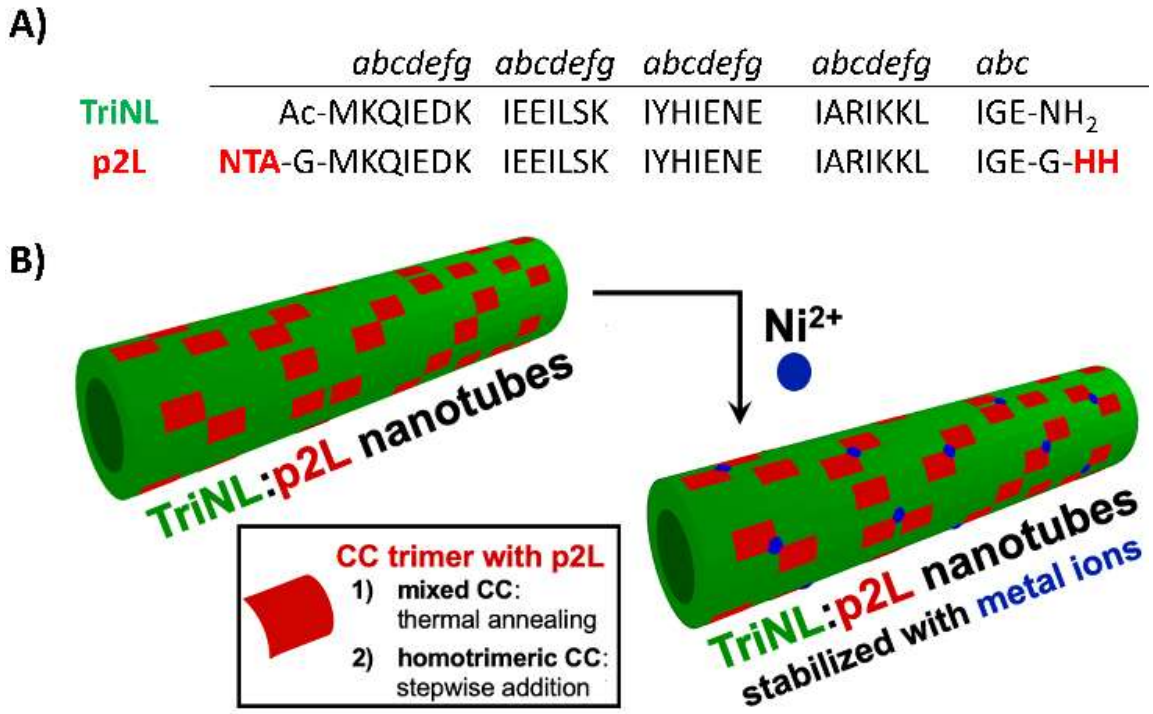

Figure 3.1. Peptide nanotube co-assemblies. (A) Peptide sequences of the coiled-coil (CC) peptides **TriNL** and **p2L**. (B) Schematic of co-assembly startegies for incoroprating **p2L** into **TriNL** nanotubes for potential stabilization with metal ions: forming mixed peptide CCs through thermal annealing, and using stepwise addition to bring in CC trimers of **p2L**.

In the design of nanotubes comprised of two peptides, heterotrimeric coiled-coil mixtures composed of both **TriNL** and **p2L** or individual homotrimers of **TriNL** and **p2L** could be used as building blocks (Figure 3.1B). Herein, both coiled-coil assemblies were explored, either through prior thermal annealing or sequential addition of the two peptides, to allow for spatial control of **p2L** within the nanotubes. These co-assemblies, in turn, may allow us to tune nanotube stability and bring in His-tagged cargo in a metal-dependent fashion.

3.2.2 Peptide Synthesis

Peptides were synthesized using standard Fmoc-based solid-phase peptide synthesis on the ChemMatrix Rink Amide resin with hexafluorophosphate azabenzotriazole tetramethyl uronium (HATU) as a coupling reagent. The protected NTA amino acid was synthesized as previously described.[45] The peptides were cleaved from the resin using a trifluoroacetic acid (TFA) cocktail, purified to homogeneity via reverse-phase high performance liquid chromatography (HPLC) and characterized via matrix-assisted laser desorption ionization time-of-flight (MALDI-ToF) mass spectrometry.

3.2.3 Intermixed Coiled-coil Formation: Thermal Annealing

Previous studies have shown that thermal annealing of two different dimeric coiled-coils can give rise to mixed coiled-coils at statistical levels with their homodimeric counterparts.[46] Motivated by this work, and that of others studying mixed coiled-coils,[47–66] we first pursued a strategy to co-assemble **p2L** and **TriNL** within nanotubes by intermixing the peptides at the supersecondary structure level using thermal annealing. In this way we could create a mixture of coiled-coils with some containing both **TriNL** and **p2L**.

Circular dichroism (CD) was initially used to study coiled-coil folding by monitoring the two negative absorption bands at 222 and 208 nm. CD spectra were taken at 4 and 90 °C using a 2:1 ratio of **TriNL** and **p2L** (500 μM total peptide concentration, Figure 3.2). Elevated temperature (90 °C) led to a decrease in helical content from 90% to 58%, and subsequent cooling to 4 °C promoted refolding to 97% α-helicity. It is worth noting, that in the low temperature spectra, the magnitude of the absorption at 222 nm is higher than that at 208 nm ($\theta_{222}/\theta_{208}$ ~1.5), which has

been shown to be indicative of the presence of a coiled-coil.[67] At 90 °C, however, this ratio decreased to ~1.1, demonstrating lower levels of the coiled-coil fold.

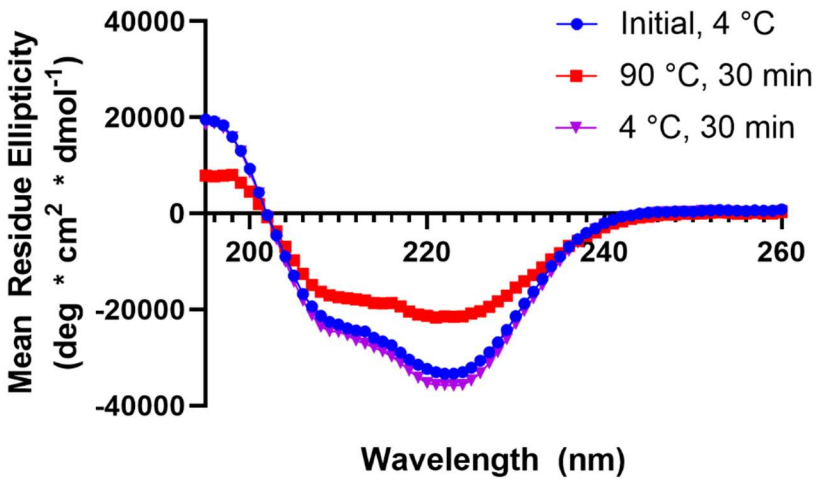

Figure 3.2. Circular dichroism spectra monitoring the unfolding and refolding of a 2:1 **TriNL**:**p2L** solution (500 μM total peptide concentration) in citrate buffer (20 mM, pH 3.0).

With CD supporting the refolding of the coiled-coils through thermal annealing, the formation of heterotrimeric coiled-coils was verified using the fluorometric assay of Xiao and coworkers.[68] This assay relies on fluorescence self-quenching of fluorophores at the termini of peptides trimeric assemblies. With this in mind, fluorescein was installed at the N-terminus of **TriNL** (**TriNL-Fl**). If unlabeled **p2L** is introduced into the labeled coiled-coil through thermal annealing, an increase in fluorescence due to less fluorescein self-quenching should result. The coiled-coil refolding process was monitored by measuring the fluorescence of **TriNL-Fl** (8.5 μM) with varying amounts of **p2L** before and after thermal annealing (Figure 3.3A). All solutions exhibited similar initial fluorescence readings prior to annealing. Following annealing, however, an increase in fluorescence was observed relative to the amount of **p2L** in solution, with up to a 1.9-fold increase at a ratio of 2:1 **TriNL-Fl**:**p2L** (**Figure 3.3**A). Additionally, the fluorescence of **TriNL-Fl** did not increase when annealed in the absence of **p2L**, further demonstrating that any observed increase in fluorescence was due to intermixed coiled-coil formation rather than the annealing process. Further evidence to support the formation of heterocoiled-coils is through a metal-mediated assembly approach. An unannealed 10:1 ratio of **TriNL**:**p2L** subjected to MES

buffer (50 mM, pH 6.0) and $NiCl_2$ (1 mM) resulted in both nanotubes and amorphous material resulting from the two peptides **TriNL** and **p2L** (**Figure 3.3**B). In contrasted, an annealed **TriNL**:**p2L** solution resulted in only the formation of nanotubes, suggesting minimal **p2L** homotrimers in solution (**Figure 3.3**C).

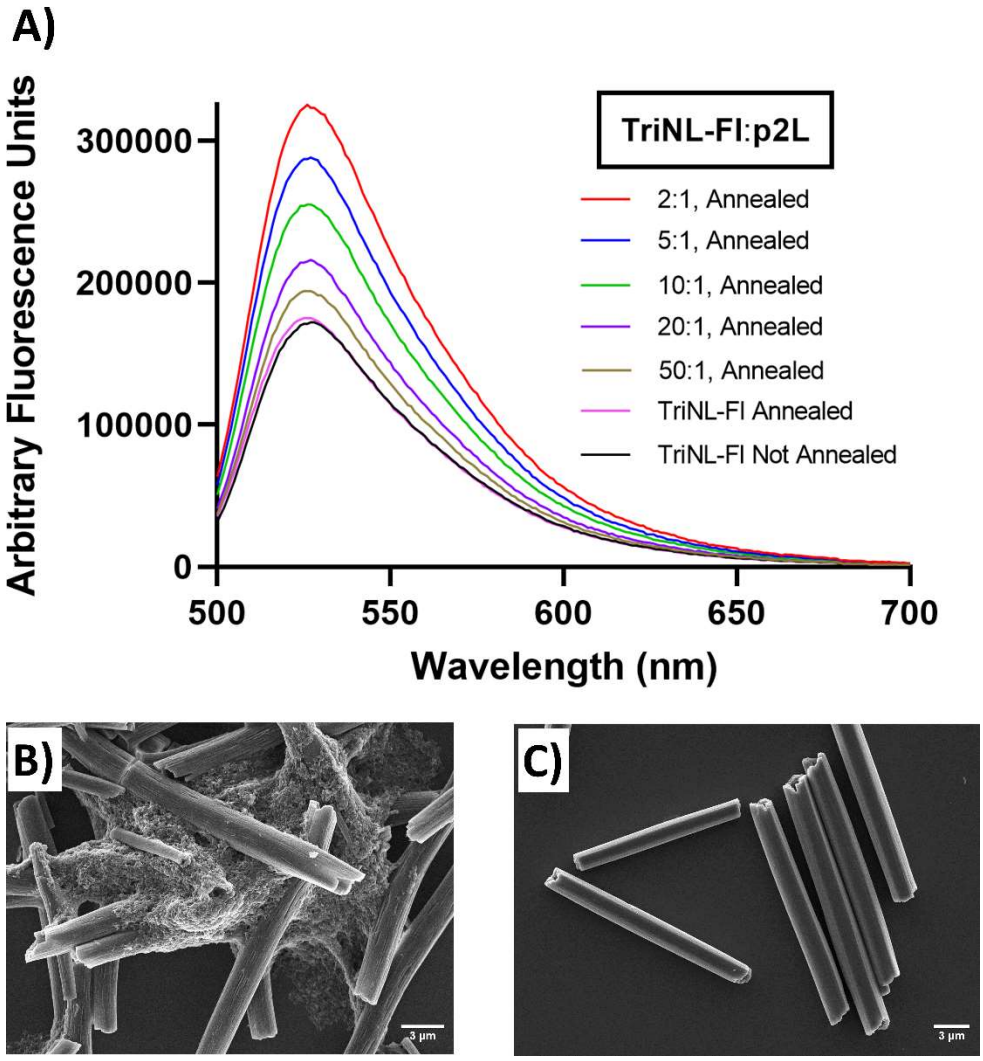

Figure 3.3. (A) Fluorescence spectra of **TriNL-Fl** (8.5 µM) before and after annealing in the presence of increasing levels of **p2L**. (B) An unannealed and (C) annealed 10:1 **TriNL**:**p2L** sample (500 µM total peptide concentration) subjected to MES buffer (50 mM, pH 6.0) and $NiCl_2$ (1 mM) for 30 min.

3.2.4 Nanotube Formation: Thermally Annealed Samples

With intermixed coiled-coils available through thermal annealing, nanotube formation was investigated. All assembly experiments were conducted with a total peptide concentration of 500 μM in MES buffer (50 mM, pH 6.0) at room temperature for 30 min, with a range of **TriNL**:**p2L** ratios (2:1 to 50:1). Upon assembly, the precipitate was collected via centrifugation and washed. Peptide levels within the assemblies were determined by first dissolving the material with aqueous HCl, followed by quantitation using reverse phase UPLC (Figure 3.4 and Table 3.1). The experimentally determined ratios of **TriNL** and **p2L** in the assemblies were quite similar to starting ratios of the two peptides in solution, indicating that both of the peptides entered the materials and at levels close to the added amounts.

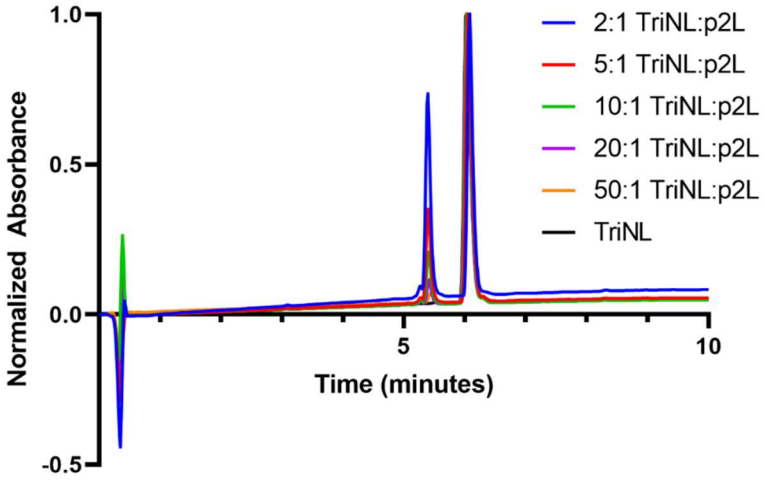

Figure 3.4. UPLC traces of annealed **TriNL**:**p2L** (500 μM total peptide concentration) assemblies at various peptide ratios using a 20-70% acetonitrile/water (0.1% TFA) gradient.

Table 3.1. Quantified ratios of **TriNL**:**p2L** assemblies via thermal annealing.

Theoretical TriNL:p2L Ratio	Measured TriNL:p2L Ratio
50:1	50:1.4
20:1	20:1.2
10:1	10:1.2
5:1	5:1.2
2:1	2:1.3

Scanning electron microscopy (SEM) was used to determine if the **TriNL** nanotube morphology (Figure 3.5A) was maintained with the added **p2L**. Indeed, upon increasing the amount of **p2L** up to a ratio of 10:1 **TriNL**:**p2L** (Figure 3.5B-D), we observed definitive nanotubes, with lengths in the 10-15 micron range and inner diameters in the range of 400 to 800 nm (n=10). From these experiments and the UPLC data, we can confirm that up to 9% incorporation of **p2L** (10:1) still allows the nanotubes to form. Interestingly, assemblies that form with 17% to 33% of **p2L** (5:1 and 2:1) have a hexagonal rod morphology (Figure 3.5E-F), with an inner channel in the case of the 5:1 ratio. Although no metals are used in these experiments, this observed morphology is reminiscent of the assemblies formed with **p2L** and metal ions, albeit the current assemblies have an increased aspect ratio (~3.5-times increase in the length/diameter).[44] Increasing the **p2L** content to 50% led to a similar morphology but had more difficulty assembling (**Figure 3.6**). Subjecting 100% **p2L** to buffer led to no assembly (**Figure 3.7**).

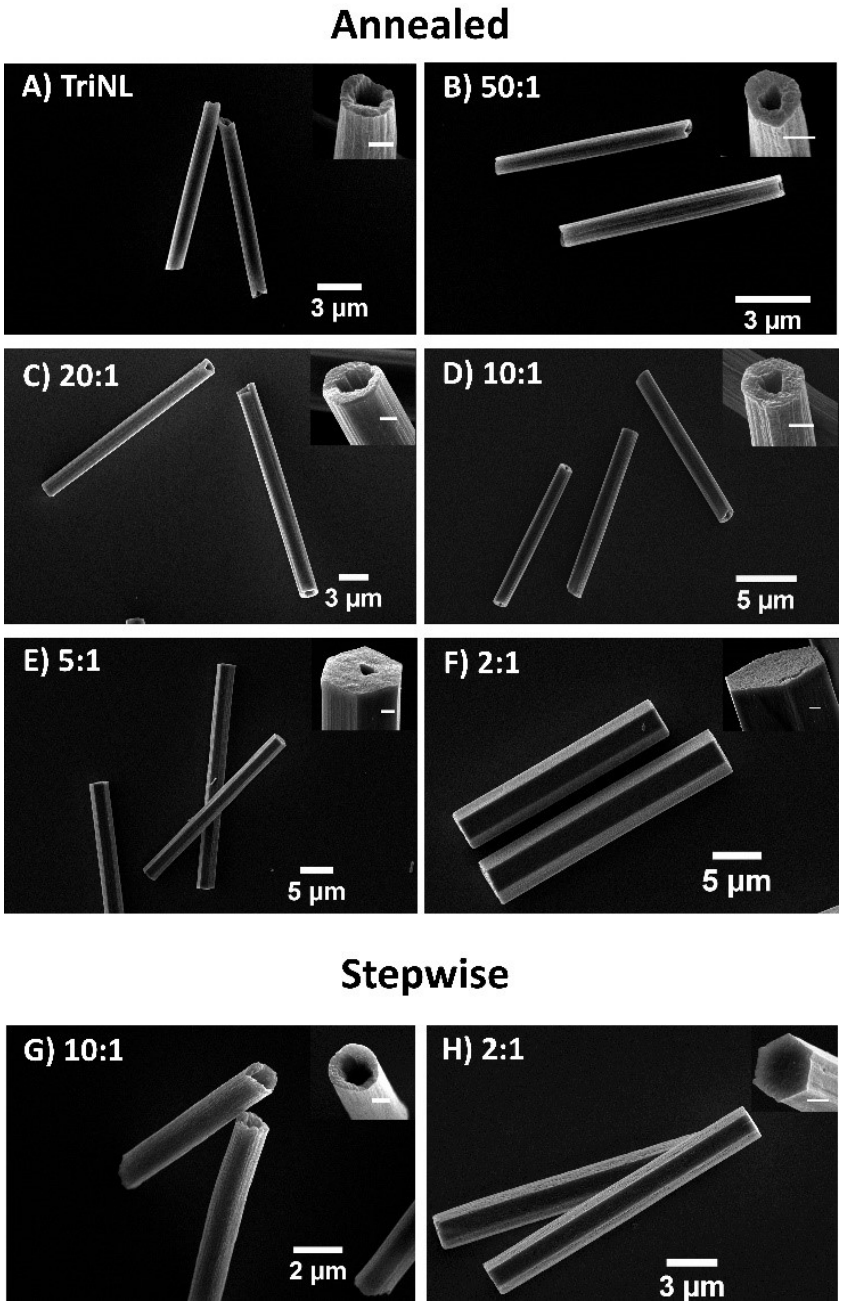

Figure 3.5. SEM visualization of assemblies at different ratios of **TriNL**:**p2L**. (A-F) annealed samples, (G-H) stepwise addition of peptide. Insets show the interior morphology of the assemblies (inset scale bar: 500 nm).

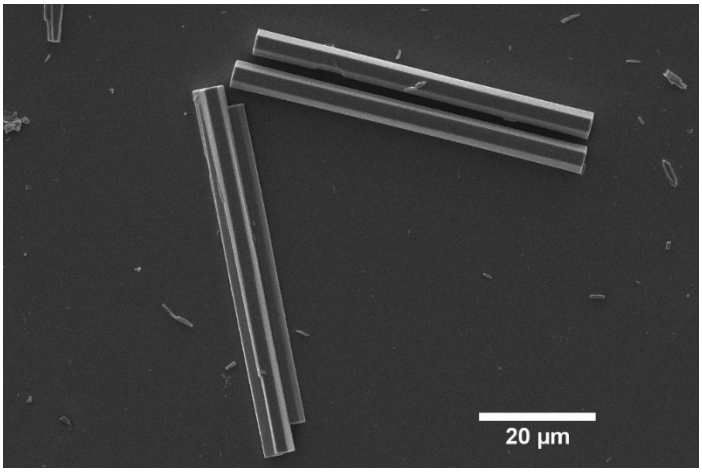

Figure 3.6. SEM image of 1:1 **TriNL**:**p2L** (500 µM) after 30 min in MES buffer (50 mM, pH 6.0).

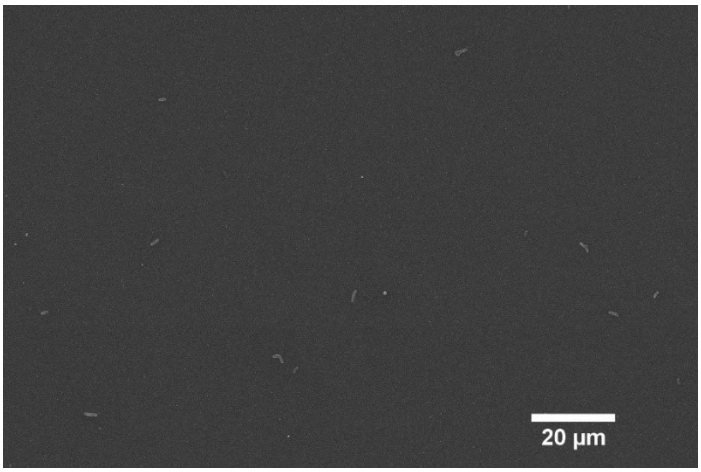

Figure 3.7. SEM image of annealed **p2L** assembly (500 µM) after 30 min in MES buffer (50 mM, pH 6.0)

3.2.5 Nanotube Stability Studies: Thermally Annealed Samples

Nanotubes formed only with **TriNL** exhibit limited stability in the presence of PBS buffer with degradation of the tubes at the termini and dissolution into shard-like tube fragments (Figure 3.8A).[42] The introduction of the ligand-containing **p2L** peptide, through thermal annealing, allows for the potential of using metal-ligand interactions to increase the stability of the tubes. With this in mind, the degradation of the nanotube co-assemblies in PBS was investigated at different **TriNL**:**p2L** ratios with added Ni(II), a metal ion that has been used extensively for His-tags with NTA. Preformed nanotubes were first incubated in $NiCl_2$ (1 mM, 1 hr) and subsequently

resuspended in PBS (10 mM phosphate, 137 mM NaCl, pH 7.4) for 24 hrs. The resulting materials were imaged using SEM (Figure 3.8). With low levels of **p2L** (2-5%), there was distinct erosion at the ends into the center of the nanotubes upon exposure to PBS (Figure 3.8B-C). Increasing the **p2L** content to 9%, however, resulted in intact nanotubes (Figure 3.8D). In the absence of Ni(II), the co-assembled nanotubes were found to degrade more substantially than with **TriNL** alone, with only small pieces of nanotubes remaining tubes due to the charge ligands at each terminus (**Figure 3.9**). Overall, these data support the idea that the observed nanotube stabilization is derived from metal-ligand interactions from **p2L** within the nanotubes.

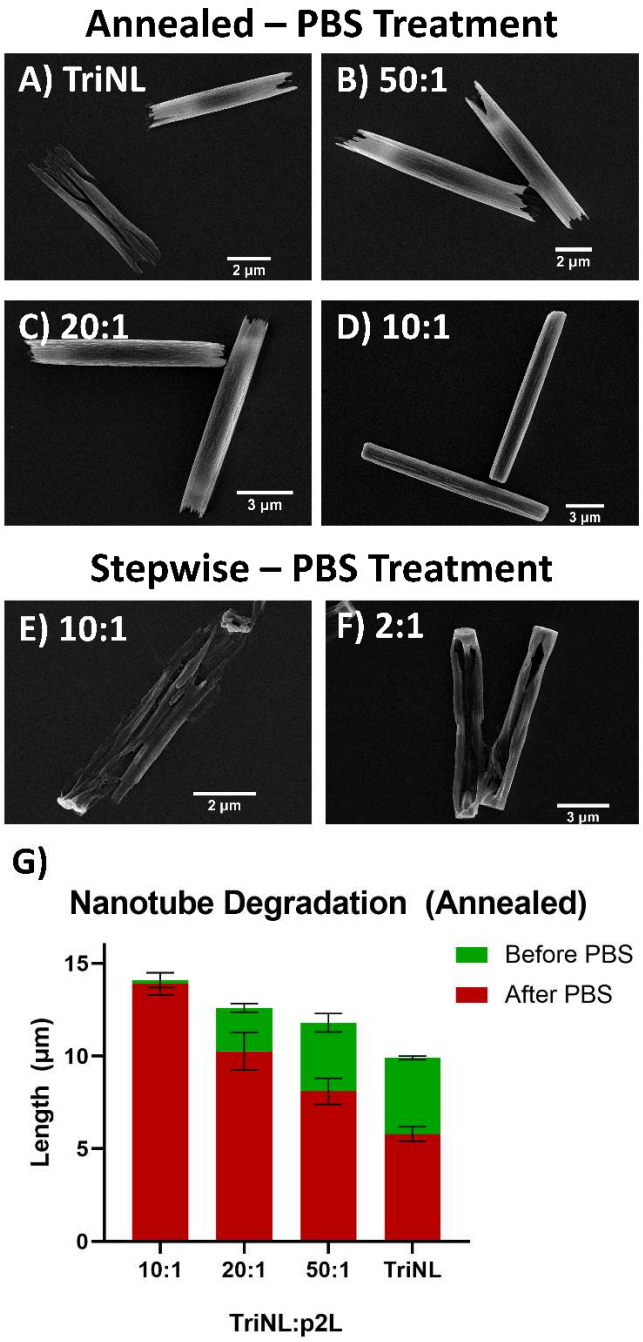

Figure 3.8. Stability of nanotubes formed with **TriNL** or **TriNL**:**p2L** ratios after a 24 hr incubation with PBS. (A) **TriNL** alone; (B-D) pre-annealed **TriNL**:**p2L** at a (B) 50:1 ratio, (C) 20:1 ratio, and (D) 10:1 ratio; and (E, F) stepwise addition of **TriNL**:**p2L** at a (E) 10:1 ratio and (F) 2:1 ratio. (G) Quantified values of the length of nanotubes before and after PBS incubation in annealed samples (n = 20).

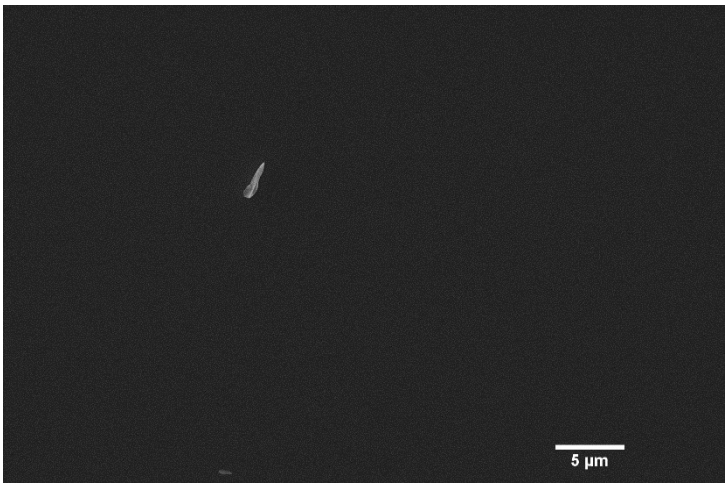

Figure 3.9. SEM image of 10:1 **TriNL**:**p2L** assembly after a 24 hr PBS incubation without the addition of $NiCl_2$.

3.2.6 Nanotube Cargo Loading: Thermally Annealed Samples

The presence of ligands for metal ions within the mixed coiled-coil nanotubes presents the opportunity of using these interactions to facilitate the binding of cargo functionalized with metal-binding ligands. Previously, the **TriNL** nanotubes were shown to encapsulate fluorescently-labeled anionic dextrans within their interior.[42] Similarly, the co-assembled nanotubes resulting from thermally annealed peptide mixtures also encapsulated anionic, fluorescein-labeled dextrans (Figure 3.10A). However, after treating both of these tubes with $NiCl_2$ (1 mM, 1 hr), followed by treatment with His-tagged rhodamine (Rh-His_6, 20 µM, 48 hrs) only the nanotubes co-assembled with **p2L** were found to have rhodamine fluorescence throughout the tubes (Figure 3.10B versus Figure 3.11A). Also, without the addition of Ni(II), no Rh-His_6 association with the mixed coiled-coil tubes was observed (Figure 3.11B). These data demonstrate the importance of metal-loaded ligands within the nanotubes for His-tagged fluorophore binding, and suggest that **p2L** is distributed throughout the assembly.

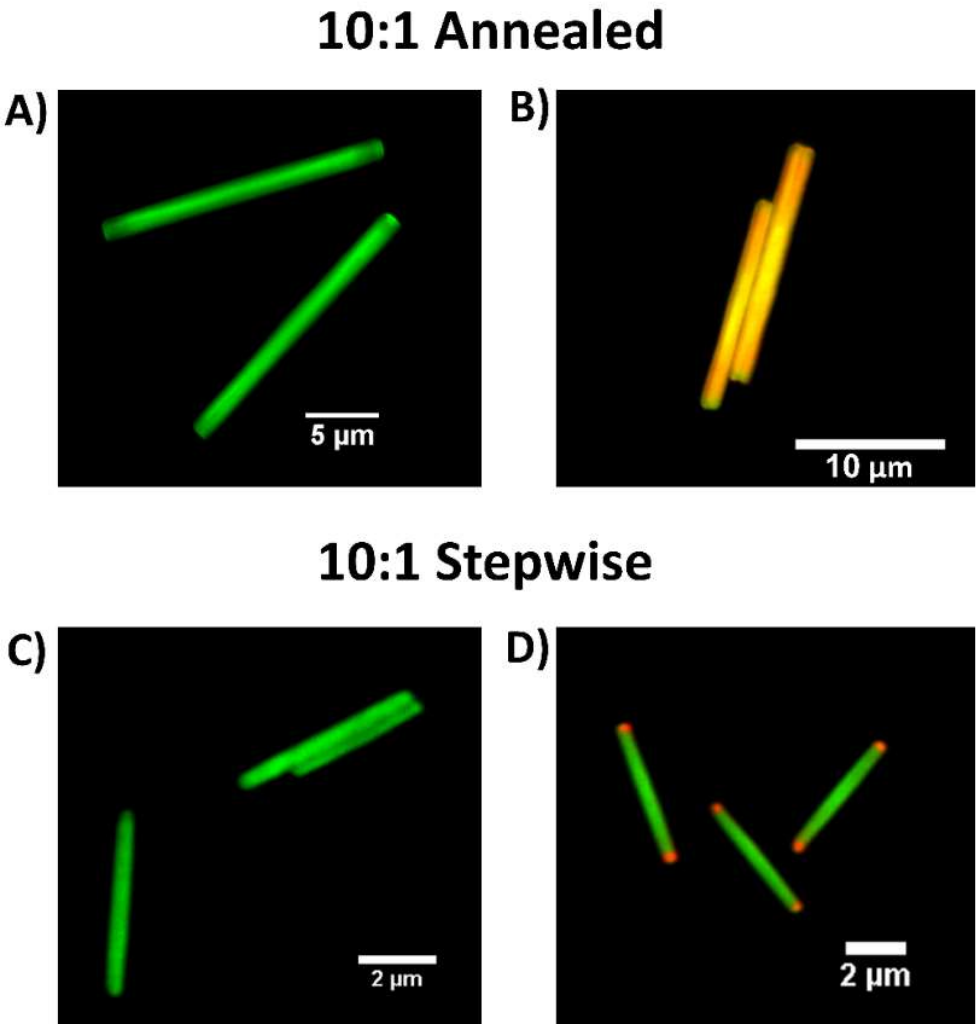

Figure 3.10. Confocal microscopy of co-assembled **TriNL**:**p2L** nanotubes. (A, B) Annealed nanotubes with encapsulated fluorescein-labeled dextran (1 mg/mL, 40 kDa) (A) alone and (B) with pretreated $NiCl_2$ (1 mM) followed by Rh-His_6 (20 µM). (C, D) Nanotubes from stepwise addition with encapsulated fluorescein-labeled dextran (1 mg/mL, 40 kDa) (C) alone and (D) with pretreated $NiCl_2$ (1 mM) followed by Rh-His_6 (20 µM). (B) and (D) Overlay of both red and green channels.

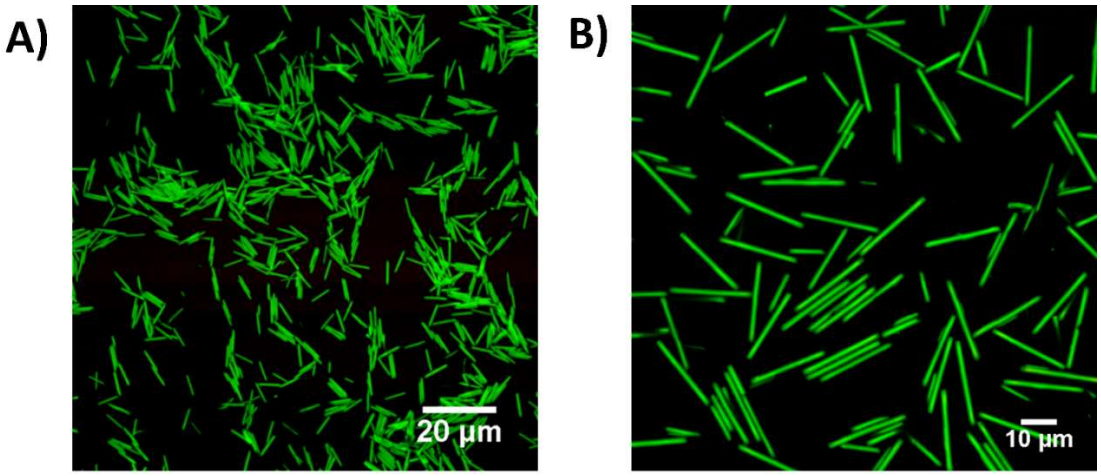

Figure 3.11. (A) Confocal image of pure **TriNL** annealed nanotubes with encapsulated anionic dextran and incubated with $NiCl_2$ (1 mM) followed by Rh-His_6 (20 µM, 48 hrs). (B) Confocal image of 10:1 **TriNL**:**p2L** annealed nanotubes incubated with Rh-His_6 (20 µM, 48 hrs) without $NiCl_2$.

3.2.7 Nanotube Formation and Stability: Stepwise Addition

Motivated by the results of nanotube cargo loading and stability after including **p2L** into the **TriNL** tubes using thermal annealing, we sought an additional way to control the location of the ligand-containing **p2L** peptide within the nanotubes. To this end, we investigated the addition of individual coiled-coils of **TriNL** and **p2L** in a stepwise fashion at 10:1 and 2:1 ratios. Attempts to simultaneously add the two peptides led to results that were difficult to replicate. Therefore, we chose to add the **p2L** coiled-coils to **TriNL** trimers after a two-minute incubation of the latter peptide in MES buffer (50 mM, pH 6.0). The combined peptides (500 µM total) where then incubated at room temperature for 30 minutes, and the precipitates were collected and washed. SEM analysis of the assemblies demonstrated morphologies that were similar to those obtained with the thermally annealed, co-assembled nanotubes. The 10:1 **TriNL**:**p2L** ratio provided nanotubes (Figure 3.5G), whereas the 2:1 ratio led to hexagonal rods with an aspect ratio of ~9 (length/diameter) (Figure 3.5H). UPLC analysis was used to determine the levels of **p2L** in the tubes/rods after acid treatment to dissolve the assemblies. As opposed to the thermally annealed samples, the assemblies formed from stepwise addition contained substantially lower levels of the ligand-containing **p2L** (10:0.3 and 2:0.5 **TriNL**:**p2L** ratios, respectively) (Table 3.2).

Table 3.2. Quantified ratios of **TriNL**:**p2L** assemblies via sequential addition.

Theoretical TriNL:p2L Ratio	Measured TriNL:p2L Ratio, Before PBS	Measured TriNL:p2L Ratio, After PBS
10:1	10:0.3	10:0.8
2:1	2:0.5	2:3.4

Although the nanotubes obtained from the two different assembly techniques at a 10:1 ratio of peptides looked similar at the micron scale, the two sets of tubes behaved quite differently when treated first with $NiCl_2$ and then with PBS. The nanotube morphology was retained in the thermally annealed co-assemblies in PBS after metal ion treatment (Figure 3.8D), whereas the sequential assemblies showed notable disintegration of the tube interior with PBS, with the ends of the tubes remained somewhat intact (Figure 3.8E). This latter PBS degradation pattern was also observed after Ni(II) treatment of the nanorods derived from sequential assembly of the 2:1 ratio of peptides (Figure 3.8F). Regions of the interior of the hexagonal rods were eaten away leaving hollow shells with defined ends. These data may indicate that the ends of these nanotubes/rods are rich in **p2L** coiled-coils and addition of metal ions could stabilize these regions. To determine if these terminal ends contain more **p2L** than the entire structure, the 10:1 and 2:1 stepwise assemblies and their corresponding PBS-degraded materials (Figure 3.8E-F) were dissolved with aqueous HCl, and their peptide contents were quantified via UPLC (Table 3.2). We observed an increase in the **p2L** levels after PBS treatment of 2.7- and 6.8-fold, respectively, compared to the intact nanotubes/rods. These data indicate that the percentage of **p2L** is higher at the ends than in the center of the material. It is likely that substantial nanotube/rod formation occurs with **TriNL** in the 2 minutes prior to **p2L** addition, thereby leading to an abundance of **p2L** near the ends of the assemblies.

3.2.8 Nanotube Cargo Loading: Sequential Coiled-coil Addition

As an additional means to verify the location of the metal-binding **p2L**, we also investigated where His-tagged rhodamine binds to the co-assembled nanotubes formed from sequential addition. Preformed nanotubes (10:1) with encapsulated dextran (Figure 3.10C) were subjected to Ni(II) incubation followed by Rh-His_6. Even after extended periods of time (48 hrs), rhodamine fluorescence was only observed at the termini of the nanotubes (Figure 3.10D). In contrast to the annealed assemblies where the **p2L** peptide is likely distributed throughout the

tubes, all of the above observations provide support for the **p2L** coiled-coils being substantially localized near the end of the nanotubes when added sequentially (Figure 3.12).

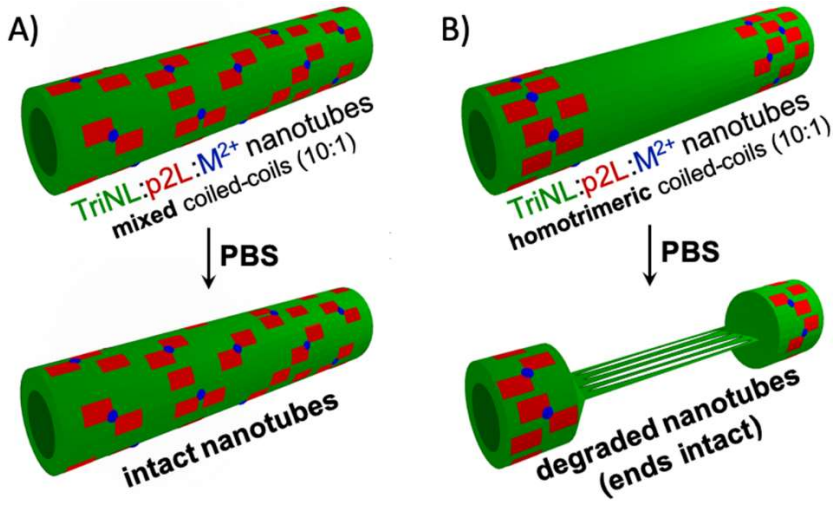

Figure 3.12. Schematic of PBS stability results for the two strategies of **p2L** incorporation into **TriNL** nanotubes. (A) Annealed samples led to **p2L** distribution throughout the tubes via intermixed coiled-coils resulting in metal ion stabilization throughout the length of the nanotubes. (B) Stepwise addition of individual coiled-coils led to the concentration of **p2L** near the ends of the nanotubes, followed by treatment with metal ions, resulting in PBS degradation of the center of the tubes.

3.2.9 Nanotube Stabilization Through PEG Crosslinkers

Despite the increase in stability through incorporating metal-binding ligands, stability in cell culture media remained a challenge. As such, we sought out an alternative method for nanotube stabilization, specifically through polyethylene glycol (PEG) crosslinkers. The lysine residues of the coiled-coil could potentially act as warheads to a PEG linker flanked with N-hydroxysuccinimide (NHS) esters and thus create intercoiled-coil linkers either linearly or radially (Figure 3.13A). The lysine residues of interest were K2, K26, and K27 (Figure 3.13B). Residues K13 and K14 were oriented for salt bridges and away from other lysine residues. With distances between lysine residues roughly ~17 Å (Figure 3.13C and Table 3.3), bis-PEG5-NHS ester was selected as the optimal tether (~21 Å in length).

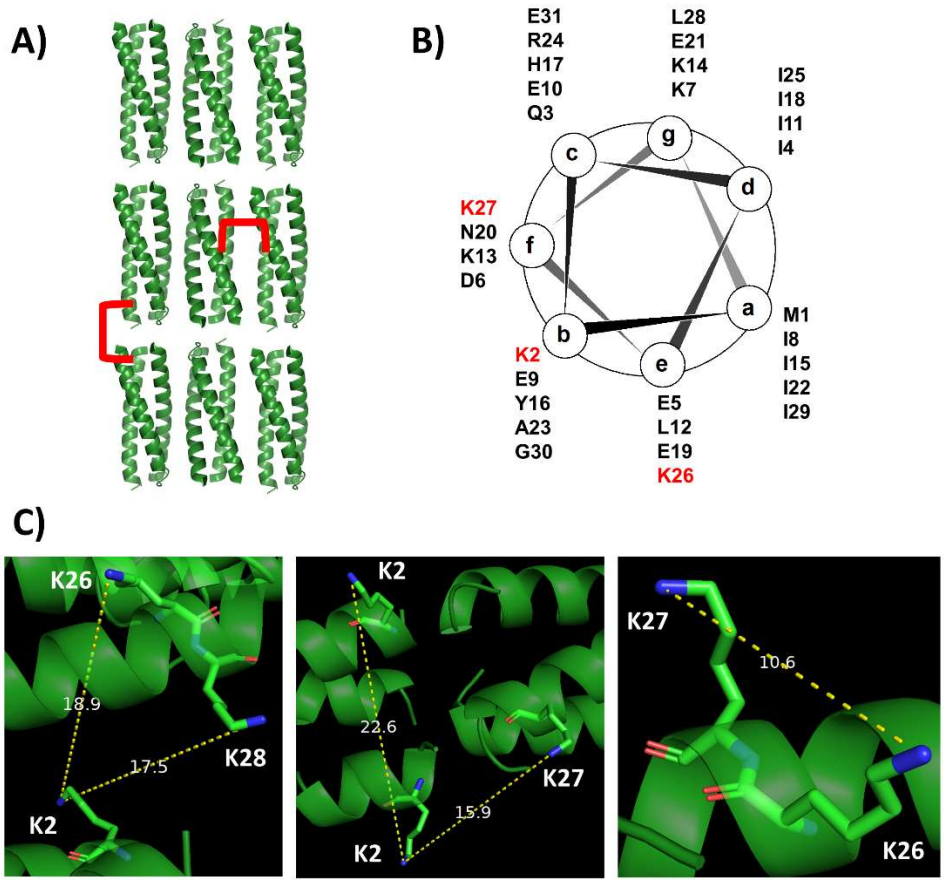

Figure 3.13. (A) Strategy for nanotube stabilization using PEG crosslinkers. (B) Helical wheel of **TriNL** with key lysine residues labeled in red. (C) Measured distances between lysine residues of interest.

Table 3.3. Measured distances between lysine residues of interest.

Interaction	Distance
K3 and K27 (radial)[a]	18.9 Å
K3 and K28 (radial)[a]	17.5 Å
K3 and K28 (linear)[a]	15.9 Å
K27 and K28 (same α-helix)[b]	10.6 Å
K3 and K3 (same coiled-coil)[b]	22.6 Å

a = desired, *b* = Undesired

Preformed **TriNL** nanotubes (1 mM) were subjected to the NHS-PEG linker (2 mM or 10 mM, 50 μL) for 1 hr at ambient temperature. After washing, the material was incubated in 1x PBS (50 μL) for 24 hrs at room temperature. The material was collected, washed, and visualized via SEM (Figure 3.14). Nanotube stability increased upon crosslinking with a more dramatic effect

observed from the higher concentrated PEG solution. The nanotubes with two equivalents of the PEG linker retained their nanotube shape but appeared somewhat collapsed or hollowed (Figure 3.14B). This is perhaps due to the crosslinker only reaching the surface of the nanotube before hydrolysis and, in turn, not stabilize the interior walls. Nanotubes treated with more crosslinker (10 eq) appeared thicker and more intact (Figure 3.14C). Preliminary mass spectrometry revealed the presence of dimeric **TriNL,** but further analysis and optimization is required.

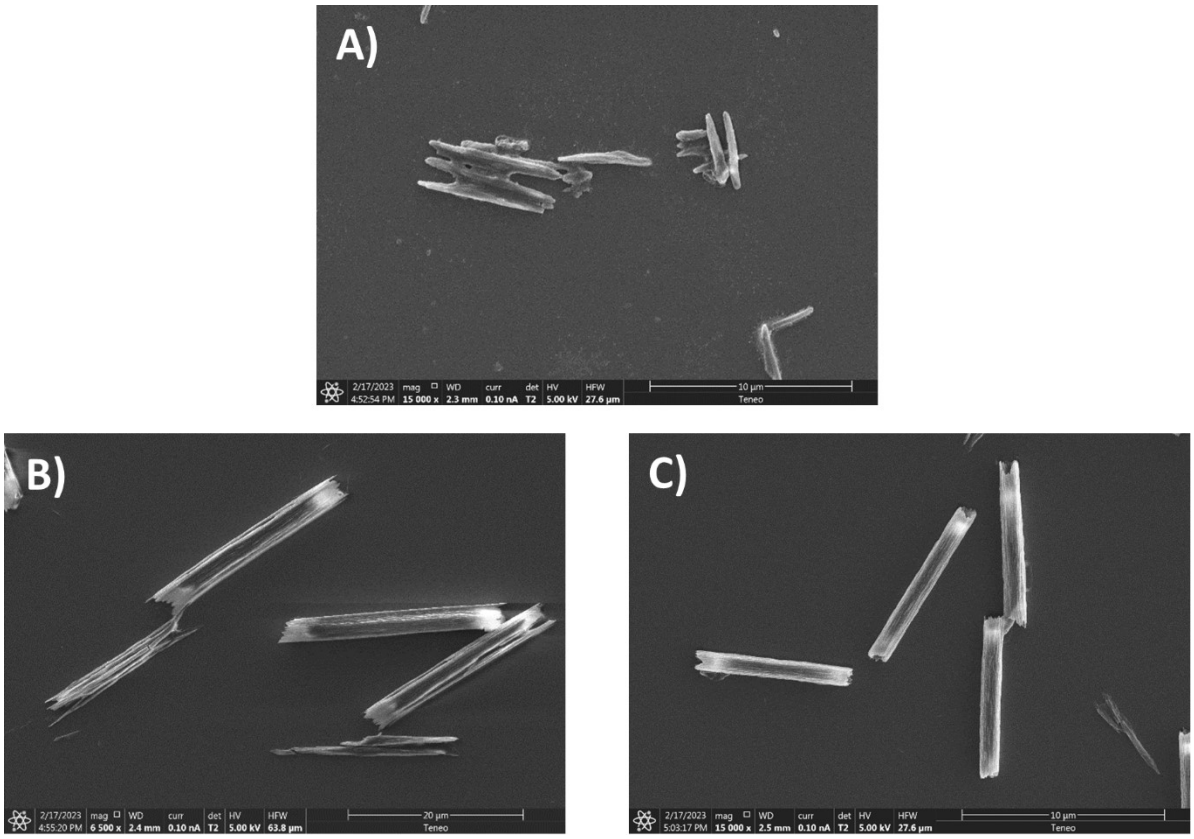

Figure 3.14. TriNL nanotube stability in PBS (24 hrs) after treatment with (A) 0 eq, (B) 2 eq, and (C) 10 eq of bis-PEG5-NHS crosslinker for 1 hr.

3.3 Conclusion

Peptide-based nanotubes hold great promise for molecular storage and drug delivery. Coiled-coil nanotubes derived from the peptide **TriNL** have been shown to encapsulate biopolymers, but instability to PBS has limited their bio-applications.[42] Herein, we have demonstrated a means of incorporating the coiled-coil forming peptide **p2L**, that contains ligands for metal ions at both termini, into nanotube assemblies with **TriNL**. It was possible to tune the position of **p2L** in the

assemblies, either distributed throughout the tubes or localized near the ends, depending on whether intermixed or individual coiled-coils of **p2L** and **TriNL** were used. Indeed, this spatial control of the position of **p2L** has led to both stabilized nanotubes or tubes with stabilized ends, upon addition of metal ions (Figure 3.12). Metal-charged ligands derived from **p2L** were also harnessed to bring His-tagged fluorophores to the full length or the termini of the nanotubes, providing an additional readout for the placement of the **p2L** peptide in the assemblies. Future experiments will focus on the range of cargoes that may be place on and within the structure of these coiled-coil nanotubes as well as further stabilizing the nanotubes with both metal-binding ligands and crosslinkers.

3.4 Materials and Methods

3.4.1 Materials

All amino acids and reagents for peptide synthesis were purchased from ChemPep or Chem-Impex. All solvents, fluorescein-labelled anionic dextran (MW 40,000) the mixed isomer 5/6-carboxy-tetramethyl-fluorescein succinimidyl ester and 5/6-carboxy-tetramethyl-rhodamine succinimidyl ester were purchased from Fisher Scientific. N-Succinimidyl 7-(diethylamino)coumarin-3-carboxylate was purchased from TCI Chemicals. Diisopropylethylamine (DIEA) and $NiCl_2$ were purchased from Alfa Aesar. Triisopropylsilane (TIPS) was purchased from Sigma-Aldrich. NovaPEG Rink Amide resin LL was purchased from Novabiochem.

3.4.2 General Peptide Synthesis and Purification

Peptides were synthesized using standard Fmoc-based chemistry on ChemMatrix Rink Amide low loading resin (300 mg). Specifically, the first amino acid (4 eq) was coupled on resin with hexafluorophosphate azabenzotriazole tetramethyl uronium (HATU, 4 eq) and DIEA (8 eq) in dimethylformamide (DMF, 10 mL) for 2.5 hrs. The resin was washed with DMF (3 x 10 mL), dichloromethane (DCM, 3 x 10 mL) methanol (MeOH, 3 x 10 mL), DCM (3 x 10 mL), and DMF (3 x 10 mL). The newly added amino acid was subsequently deprotected in 25% piperidine in DMF (v/v) for 30 min. After washing like above, the next amino acid was coupled. Nitrilotriacetic acid (6 eq) was coupled with HATU (6 eq) and DIEA (12 eq) in DMF (10 mL) for 6 hours and

installed at the N-terminus through an amide linkage following a glycine spacer. The resin was dried and the peptides were cleaved from resin using a 95% trifluoroacetic acid (TFA), 2.5% TIPS, 2.5% H_2O cocktail in a 10 mL total volume. The cocktail solution was concentrated under reduced pressure, and the peptide was precipitated using cold diethyl ether (30 mL). The solid was centrifuged at 2000 g, decanted, and was dissolved in a 10 mg/mL solution with H_2O. The peptides were purified to homogeneity via reverse-phase high performance liquid chromatography (HPLC) instrument using a Luna C18 semi-prep column with an eluent consisting of solvent A (CH_3CN/0.1% TFA) and solvent B (H_2O/0.1% TFA), a 60-min gradient consisting of 20% to 70% A, and a flow rate of 12 mL/min. The peptides were characterized via matrix-assisted laser desorption ionization time-of-flight mass spectrometry (MALDI-ToF).

3.4.3 Circular Dichroism

A **TriNL-Fl** solution (50 μM) was prepared in citrate buffer (10 mM, pH 3.0) in a 200 μL total volume. The circular dichroism (CD) spectrum was taken using a JASCO J-810 CD spectropolarimeter at 4 °C and at 90 °C and averaging three scans between 190 nm and 260 nm. The data pitch was 0.1 nm with a 1-nm bandwidth and a scan rate of 100 nm/min with a 1 s response time.

3.4.4 Fluorometry

A 15 μL aliquot of a 550 μM **TriNL-Fl** solution with varying **p2L** concentrations was annealed (90 °C for 30 min, 4 °C for >18 hrs). The samples were diluted with 985 μL of PBS and transferred to a Starna Cell 1 cm quartz cuvette. Fluorescence measurements were conducted using Edinburgh Instruments Fluorometer with an excitation wavelength of 490±2.5 nm and an emission bandwidth 0.5 nm.

3.4.5 Annealed Assemblies

Peptide solutions were prepared in 15 μL aliquots and annealed using a Techne 3PRIMEBASE Thermal Cycler (90 °C for 30 min, 4 °C for > 18 hrs). These aliquots were added to 35 μL of 2-(N-morpholino)ethanesulfonic acid buffer (MES, pH 6.0) to create a final buffer concentration of 50 mM and total peptide concentration of 500 μM. Following a 30 min incubation

at room temperature, the assemblies were centrifuged at 10,000 g for 3 minutes where the supernatant was removed and replaced with water. This process was repeated two more times. The pelleted assemblies were resuspended and stored in 50 μL water.

3.4.6 Step-wise Assemblies

Assemblies were conducted with a total peptide concentration of 500 μM in a final MES buffer concentration of 50 mM (pH 6.0) in 50 μL total volume. Specifically, **TriNL** and **p2L** were separately added to MES buffer in the same buffer ratio as peptide ratio. After a two-minute incubation at room temperature, **p2L** was added to **TriNL** and allowed to assemble for an additional 30 min. The samples were centrifuged at 10,000 g for 3 minutes. The supernatant was removed, replaced with water, and the process was repeated twice. The pelleted assemblies were resuspended and stored in 50 μL water.

3.4.7 Scanning Electron Microscopy

Aliquots of the assemblies described Sections 3.4.5 and 3.4.6 (3 μL) were placed on a glass coverslip attached to a metal stub via copper tape. The samples were either air dried or lyophilized and platinum coated for 60 seconds using a Cressington sputter coater. Samples were imaged using an FEI Teneo Volumescope field emission scanning electron microscope using Everhart-Thornley detector (ETD) for magnifications < 10,000 or the high-resolution through the lens detector (TLD) for magnifications ≥ 10,000. Samples were imaged at an accelerating voltage of 5 kV and a working distance of 2-4 mm with a 30-μm aperture.

3.4.8 Degradation Studies: Metal-binding Ligands

Peptides were assembled using the protocol above. Following washing, the samples were incubated in 1 mM $NiCl_2$ (50 μL) for 1 hr at room temperature. The material was centrifuged at 10,000 g for 3 min, the supernatant was removed, and the samples were resuspended in 50 μL 1x PBS for 24 hrs at room temperature. The samples were centrifuged at 10,000 g for 3 minutes. The supernatant was removed, replaced with water, and the process was repeated twice. The pelleted assemblies were resuspended and stored in 50 μL water.

3.4.9 Cargo Binding

Peptides were assembled using the protocol above in the presence of 1 mg/mL fluorescein-labelled anionic dextran (MW 40,000). Following washing, the samples were incubated in 1 mM $NiCl_2$ (50 μL) for 1 hr at room temperature. The material was centrifuged at 10,000 g for 3 min and the supernatant was removed followed by resuspension in 50 mM MES buffer (pH 6.0) and 20 μM Rh-His_6 (50 μL total volume). After a 48 hr incubation, the samples were washed as above and (when applicable), incubated in 20 μM Cou-His_6 for 48 hrs (50 μL total volume). After washing as above, the samples were imaged on a Nikon A1R multiphoton inverted confocal microscope under a 100X oil objective using 405 nm, 488 nm, and 561 nm excitation lasers.

3.4.10 Degradation Studies: PEG Linkers

Peptides were assembled using the protocol in Section 3.4.5. The samples were subsequently incubated in either 2 mM or 10 mM bis-PEG5-NHS (50 μL) for 1 hr at room temperature. The material was centrifuged at 10,000 g for 3 min, the supernatant was removed, and the samples were resuspended in 1x PBS (50 μL) for 24 hrs at room temperature. The samples were centrifuged at 10,000 g for 3 minutes. The supernatant was removed, replaced with water, and the process was repeated twice. The pelleted assemblies were resuspended and stored in 50 μL water.

3.5 References

(1) Shimizu, T.; Ding, W.; Kameta, N. Soft-Matter Nanotubes: A Platform for Diverse Functions and Applications. *Chem. Rev.* **2020**, *120* (4), 2347–2407. https://doi.org/10.1021/acs.chemrev.9b00509.

(2) Hamley, I. W. Peptide Nanotubes. *Angew. Chemie - Int. Ed.* **2014**, *53* (27), 6866–6881. https://doi.org/10.1002/anie.201310006.

(3) Rodríguez-Vázquez, N.; Amorín, M.; Granja, J. R. Recent Advances in Controlling the Internal and External Properties of Self-Assembling Cyclic Peptide Nanotubes and Dimers. *Org. Biomol. Chem.* **2017**, *15* (21), 4490–4505. https://doi.org/10.1039/c7ob00351j.

(4) Song, Q.; Cheng, Z.; Kariuki, M.; Hall, S. C. L.; Hill, S. K.; Rho, J. Y.; Perrier, S. Molecular Self-Assembly and Supramolecular Chemistry of Cyclic Peptides. *Chem. Rev.* **2021**. https://doi.org/10.1021/acs.chemrev.0c01291.

(5) Yemini, M.; Reches, M.; Gazit, E.; Rishpon, J. Peptide Nanotube-Modified Electrodes for Enzyme - Biosensor Applications. *Anal. Chem.* **2005**, *77* (16), 5155–5159.

(6) Emtiazi, G.; Zohrabi, T.; Lee, L. Y.; Habibi, N.; Zarrabi, A. Covalent Diphenylalanine Peptide Nanotube Conjugated to Folic Acid/Magnetic Nanoparticles for Anti-Cancer Drug Delivery. *J. Drug Deliv. Sci. Technol.* **2017**, *41*, 90–98. https://doi.org/10.1016/j.jddst.2017.06.005.

(7) Porter, S. L.; Coulter, S. M.; Pentlavalli, S.; Thompson, T. P.; Laverty, G. Self-Assembling Diphenylalanine Peptide Nanotubes Selectively Eradicate Bacterial Biofilm Infection. *Acta Biomater.* **2018**, *77*, 96–105. https://doi.org/10.1016/j.actbio.2018.07.033.

(8) Saha, P. C.; Bera, T.; Chatterjee, T.; Samanta, J.; Sengupta, A.; Bhattacharyya, M.; Guha, S. Supramolecular Dipeptide-Based Near-Infrared Fluorescent Nanotubes for Cellular Mitochondria Targeted Imaging and Early Apoptosis. *Bioconjug. Chem.* **2021**, *32* (4), 833–841. https://doi.org/10.1021/acs.bioconjchem.1c00106.

(9) Yaman, Y. T.; Bolat, G.; Abaci, S.; Saygin, T. B. Peptide Nanotube Functionalized Molecularly Imprinted Polydopamine Based Single-Use Sensor for Impedimetric Detection of Malathion. *Anal. Bioanal. Chem.* **2021**, No. 0123456789. https://doi.org/10.1007/s00216-021-03737-2.

(10) Ghadiri, M. R.; Granja, J. R.; Buehler, L. K. Artificial Transmembrane Ion Channels from Self-Assembling Peptide Nanotubes. *Nature* **1994**, *369* (6478), 301–304. https://doi.org/10.1038/369301a0.

(11) Granja, J. R.; Ghadiri, M. R. Channel-Mediated Transport of Glucose across Lipid Bilayers. *J. Am. Chem. Soc.* **1994**, *116*, 10785–10786. https://doi.org/10.1021/ja00102a054.

(12) González-Freire, E.; Novelli, F.; Pérez-Estévez, A.; Seoane, R.; Amorín, M.; Granja, J. R. Double Orthogonal Click Reactions for the Development of Antimicrobial Peptide Nanotubes. *Chem. - A Eur. J.* **2021**, *27* (9), 3029–3038. https://doi.org/10.1002/chem.202004127.

(13) Novelli, F.; Vilela, M.; Pazó, A.; Amorín, M.; Granja, J. R. Molecular Plumbing to Bend Self-Assembling Peptide Nanotubes. *Angew. Chemie - Int. Ed.* **2021**, *60* (34), 18838–18844. https://doi.org/10.1002/anie.202107034.

(14) Lee, Y. H.; Chang, S. F.; Liaw, J. Anti-Apoptotic Gene Delivery with Cyclo-(D-Trp-Tyr) Peptide Nanotube via Eye Drop Following Corneal Epithelial Debridement. *Pharmaceutics* **2015**, *7* (3), 122–136. https://doi.org/10.3390/pharmaceutics7030122.

(15) Ellacott, S. H.; Sanchez-Cano, C.; Mansfield, E. D. H.; Rho, J. Y.; Song, J. I.; Peltier, R.; Perrier, S. Comparative Study of the Cellular Uptake and Intracellular Behavior of a Library of Cyclic Peptide-Polymer Nanotubes with Different Self-Assembling Properties. *Biomacromolecules* **2021**, *22* (2), 710–722. https://doi.org/10.1021/acs.biomac.0c01512.

(16) Silk, M. R.; Price, J. R.; Mohanty, B.; Leiros, H. K. S.; Lund, B. A.; Thompson, P. E.; Chalmers, D. K. Side-Chain Interactions in d/l Peptide Nanotubes: Studies by Crystallography, NMR Spectroscopy and Molecular Dynamics. *Chem. - A Eur. J.* **2021**, 14489–14500. https://doi.org/10.1002/chem.202102106.

(17) Roy, S.; Zheng, L.; Silberbush, O.; Engel, M.; Atsmon-Raz, Y.; Miller, Y.; Migliore, A.; Beratan, D. N.; Ashkenasy, N. Mechanism of Side Chain-Controlled Proton Conductivity in Bioinspired Peptidic Nanostructures. *J. Phys. Chem. B* **2021**. https://doi.org/10.1021/acs.jpcb.1c08857.

(18) Hartgerink, J. D.; Granja, J. R.; Milligan, R. A.; Ghadiri, M. R. Self-Assembling Peptide Nanotubes. *J. Am. Chem. Soc.* **1996**, *118*, 43–50. https://doi.org/10.1016/S1748-0132(08)70041-0.

(19) Motesharei, K.; Ghadiri, M. R. Diffusion-Limited Size-Selective Ion Sensing Based on SAM-Supported Peptide Nanotubes. *J. Am. Chem. Soc.* **1997**, *119*, 11306–11312. https://doi.org/10.1021/ja9727171.

(20) Kim, H. S.; Hartgerink, J. D.; Ghadiri, M. R. Oriented Self-Assembly of Cyclic Peptide Nanotubes in Lipid Membranes. *J. Am. Chem. Soc.* **1998**, *120*, 4417–4424. https://doi.org/10.1021/ja9735315.

(21) Karle, I. L.; Perozzo, M. A.; Mishra, V. K.; Balaram, P. Crystal Structure of the Channel-Forming Polypeptide Antiamoebin in a Membrane-Mimetic Environment. *Proc. Natl. Acad. Sci. USA* **1998**, *95* (10), 5501–5504. https://doi.org/10.1073/pnas.95.10.5501.

(22) Ranganathan, D.; Lakshmi, C.; Karle, I. L. Hydrogen-Bonded Self-Assembled Peptide Nanotubes from Cystine-Based Macrocyclic Bisureas. *J. Am. Chem. Soc.* **1999**, *121* (26), 6103–6106. https://doi.org/10.1021/ja9903025.

(23) Karle, I. L.; Ranganathan, D.; Kumar, M. G.; Nagaraj, R. Design, Synthesis, Conformational and Membrane Ion Transport Studies of Proline-Adamantane Hybrid Cyclic Depsipeptides. *Biopolymers* **2008**, *89* (5), 471–478. https://doi.org/10.1002/bip.20903.

(24) Rodríguez-Vázquez, N.; García-Fandiño, R.; Aldegunde, M. J.; Brea, J.; Loza, M. I.; Amorín, M.; Granja, J. R. Cis-Platinum Complex Encapsulated in Self-Assembling Cyclic Peptide Dimers. *Org. Lett.* **2017**, *19* (10), 2560–2563. https://doi.org/10.1021/acs.orglett.7b00871.

(25) Claro, B.; González-Freire, E.; Calvelo, M.; Bessa, L. J.; Goormaghtigh, E.; Amorín, M.; Granja, J. R.; Garcia-Fandiño, R.; Bastos, M. Membrane Targeting Antimicrobial Cyclic Peptide Nanotubes – an Experimental and Computational Study. *Colloids Surfaces B Biointerfaces* **2020**, *196* (April). https://doi.org/10.1016/j.colsurfb.2020.111349.

(26) Vollrath, S. B. L.; Hu, C.; Bräse, S.; Kirshenbaum, K. Peptoid Nanotubes: An Oligomer Macrocycle That Reversibly Sequesters Water via Single-Crystal-to-Single-Crystal Transformations. *Chem. Commun.* **2013**, *49* (23), 2317–2319. https://doi.org/10.1039/c3cc37163h.

(27) Sun, J.; Jiang, X.; Lund, R.; Downing, K. H.; Balsara, N. P.; Zuckermann, R. N. Self-Assembly of Crystalline Nanotubes from Monodisperse Amphiphilic Diblock Copolypeptoid Tiles. *Proc. Natl. Acad. Sci. U. S. A.* **2016**, *113* (15), 3954–3959. https://doi.org/10.1073/pnas.1517169113.

(28) Jin, H.; Ding, Y. H.; Wang, M.; Song, Y.; Liao, Z.; Newcomb, C. J.; Wu, X.; Tang, X. Q.; Li, Z.; Lin, Y.; Yan, F.; Jian, T.; Mu, P.; Chen, C. L. Designable and Dynamic Single-Walled Stiff Nanotubes Assembled from Sequence-Defined Peptoids. *Nat. Commun.* **2018**, *9* (1), 1–11. https://doi.org/10.1038/s41467-017-02059-1.

(29) Luo, Y.; Song, Y.; Wang, M.; Jian, T.; Ding, S.; Mu, P.; Liao, Z.; Shi, Q.; Cai, X.; Jin, H.; Du, D.; Dong, W. J.; Chen, C. L.; Lin, Y. Bioinspired Peptoid Nanotubes for Targeted Tumor Cell Imaging and Chemo-Photodynamic Therapy. *Small* **2019**, *15* (43), 1–8. https://doi.org/10.1002/smll.201902485.

(30) Merg, A. D.; Touponse, G.; Genderen, E. Van; Blum, T. B.; Zuo, X.; Bazrafshan, A.; Siaw, H. M. H.; McCanna, A.; Brian Dyer, R.; Salaita, K.; Abrahams, J. P.; Conticello, V. P. Shape-Shifting Peptide Nanomaterials: Surface Asymmetry Enables PH-Dependent Formation and Interconversion of Collagen Tubes and Sheets. *J. Am. Chem. Soc.* **2020**, *142* (47), 19956–19968. https://doi.org/10.1021/jacs.0c08174.

(31) Jin, Y.; Cai, L.; Yang, Q.; Luo, Z.; Liang, L.; Liang, Y.; Wu, B.; Ding, L.; Zhang, D.; Xu, X.; Zhang, L.; Zhou, F. Anti-Leukemia Activities of Selenium Nanoparticles Embedded in Nanotube Consisted of Triple-Helix β -D-Glucan. *Carbohydr. Polym.* **2020**, *240*, 116329. https://doi.org/10.1016/j.carbpol.2020.116329.

(32) Han, C.; Sun, X.; Liu, L.; Jiang, H.; Shen, Y.; Xu, X.; Li, J.; Zhang, G.; Huang, J.; Lin, Z.; Xiong, N.; Wang, T. Exosomes and Their Therapeutic Potentials of Stem Cells. *Stem Cells Int.* **2016**, *2016*, 1–11. https://doi.org/10.1155/2016/7653489.

(33) Hamley, I. W.; Burholt, S.; Hutchinson, J.; Castelletto, V.; Da Silva, E. R.; Alves, W.; Gutfreund, P.; Porcar, L.; Dattani, R.; Hermida-Merino, D.; Newby, G.; Reza, M.; Ruokolainen, J.; Stasiak, J. Shear Alignment of Bola-Amphiphilic Arginine-Coated Peptide Nanotubes. *Biomacromolecules* **2017**, *18* (1), 141–149. https://doi.org/10.1021/acs.biomac.6b01425.

(34) Lei, L.; Xu, Z.; Hu, X.; Lai, Y.; Xu, J.; Hou, B.; Wang, Y.; Yu, H.; Tian, Y.; Zhang, W. Bioinspired Multivalent Peptide Nanotubes for Sialic Acid Targeting and Imaging-Guided Treatment of Metastatic Melanoma. *Small* **2019**, *15* (22), 1–11. https://doi.org/10.1002/smll.201900157.

(35) Reja, A.; Afrose, S. P.; Das, D. Aldolase Cascade Facilitated by Self-Assembled Nanotubes from Short Peptide Amphiphiles. *Angew. Chemie - Int. Ed.* **2020**, *59* (11), 4329–4334. https://doi.org/10.1002/anie.201914633.

(36) Xu, C.; Liu, R.; Mehta, A. K.; Guerrero-Ferreira, R. C.; Wright, E. R.; Dunin-Horkawicz, S.; Morris, K.; Serpell, L. C.; Zuo, X.; Wall, J. S.; Conticello, V. P. Rational Design of Helical Nanotubes from Self-Assembly of Coiled-Coil Lock Washers. *J. Am. Chem. Soc.* **2013**, *135* (41), 15565–15578. https://doi.org/10.1021/ja4074529.

(37) Wang, F.; Gnewou, O.; Modlin, C.; Beltran, L. C.; Xu, C.; Su, Z.; Juneja, P.; Grigoryan, G.; Egelman, E. H.; Conticello, V. P. Structural Analysis of Cross α-Helical Nanotubes Provides Insight into the Designability of Filamentous Peptide Nanomaterials. *Nat. Commun.* **2021**, *12* (1), 1–14. https://doi.org/10.1038/s41467-020-20689-w.

(38) Thomson, A. R.; Wood, C. W.; Burton, A. J.; Bartlett, G. J.; Sessions, R. B.; Brady, R. L.; Woolfson, D. N. Computational Design of Water-Soluble α-Helical Barrels. *Science* **2014**, *346* (6208), 485–489. https://doi.org/10.1126/science.1257452.

(39) Burgess, N. C.; Sharp, T. H.; Thomas, F.; Wood, C. W.; Thomson, A. R.; Zaccai, N. R.; Brady, R. L.; Serpell, L. C.; Woolfson, D. N. Modular Design of Self-Assembling Peptide-Based Nanotubes. *J. Am. Chem. Soc.* **2015**, *137*, 10554–10562. https://doi.org/10.1021/jacs.5b03973.

(40) Thomas, F.; Burgess, N. C.; Thomson, A. R.; Woolfson, D. N. Controlling the Assembly of Coiled-Coil Peptide Nanotubes. *Angew. Chemie - Int. Ed.* **2016**, *55* (3), 987–991. https://doi.org/10.1002/anie.201509304.

(41) Thanasupawat, T.; Bergen, H.; Hombach-Klonisch, S.; Krcek, J.; Ghavami, S.; Del Bigio, M. R.; Krawitz, S.; Stelmack, G.; Halayko, A.; McDougall, M.; Meier, M.; Stetefeld, J.; Klonisch, T. Platinum (IV) Coiled Coil Nanotubes Selectively Kill Human Glioblastoma Cells. *Nanomedicine Nanotechnology, Biol. Med.* **2015**, *11* (4), 913–925. https://doi.org/10.1016/j.nano.2015.01.014.

(42) Nambiar, M.; Nepal, M.; Chmielewski, J. Self-Assembling Coiled-Coil Peptide Nanotubes with Biomolecular Cargo Encapsulation. *ACS Biomater. Sci. Eng.* **2019**, *5* (10), 5082–5087. https://doi.org/10.1021/acsbiomaterials.9b01304.

(43) Harbury, P. B.; Zhang, T.; Kim, P. S.; Alber, T. A Switch between Two-, Three-, and Four-Stranded Coiled Coils in GCN4 Leucine Zipper Mutants. *Science* **1993**, *262* (5138), 1401–1407. https://doi.org/10.1126/science.8248779.

(44) Nepal, M.; Sheedlo, M. J.; Das, C.; Chmielewski, J. Accessing Three-Dimensional Crystals with Incorporated Guests through Metal-Directed Coiled-Coil Peptide Assembly. *J. Am. Chem. Soc.* **2016**, *138* (34), 11051–11057. https://doi.org/10.1021/jacs.6b06708.

(45) Huang, Z.; Park, J. I.; Watson, D. S.; Hwang, P.; Szoka, F. C. Facile Synthesis of Multivalent Nitrilotriacetic Acid (NTA) and NTA Conjugates for Analytical and Drug Delivery Applications. *Bioconjug. Chem.* **2006**, *17* (6), 1592–1600. https://doi.org/10.1021/bc0602228.

(46) Holtzer, M. E.; Breiner, T.; Holtzer, A. Hetero-α-Helical, Two-Chain, Coiled Coils: Aβ Hybrid Tropomysin. *Biopolymers* **1984**, *23*, 1811–1833. https://doi.org/10.1002/bip.360231003.

(47) Gauba, V.; Hartgerink, J. D. Self-Assembled Heterotrimeric Collagen Triple Helices Directed through Electrostatic Interactions. *J. Am. Chem. Soc.* **2007**, *129* (9), 2683–2690. https://doi.org/10.1021/ja0683640.

(48) Acevedo-Jake, A. M.; Clements, K. A.; Hartgerink, J. D. Synthetic, Register-Specific, AAB Heterotrimers to Investigate Single Point Glycine Mutations in Osteogenesis Imperfecta. *Biomacromolecules* **2016**, *17* (3), 914–921. https://doi.org/10.1021/acs.biomac.5b01562.

(49) O'Shea, E. K.; Lumb, K. J.; Kim, P. S. Peptide "Velcro": Design of a Heterodimeric Coiled Coil. *Curr. Biol.* **1993**, *3* (10), 658–667. https://doi.org/10.1016/0960-9822(93)90063-T.

(50) Zhang, K.; Diehl, M. R.; Tirrell, D. A. Artificial Polypeptide Scaffold for Protein Immobilization. *J. Am. Chem. Soc.* **2005**, *127* (29), 10136–10137. https://doi.org/10.1021/ja051457h.

(51) Mason, J. M.; Schmitz, M. A.; Müller, K. M.; Arndt, K. M. Semirational Design of Jun-Fos Coiled Coils with Increased Affinity: Universal Implications for Leucine Zipper Prediction and Design. *Proc. Natl. Acad. Sci. U. S. A.* **2006**, *103* (24), 8989–8994. https://doi.org/10.1073/pnas.0509880103.

(52) Thompson, K. E.; Bashor, C. J.; Lim, W. A.; Keating, A. E. Synzip Protein Interaction Toolbox: In Vitro and in Vivo Specifications of Heterospecific Coiled-Coil Interaction Domains. *ACS Synth. Biol.* **2012**, *1* (4), 118–129. https://doi.org/10.1021/sb200015u.

(53) Domeradzka, N. E.; Werten, M. W. T.; De Wolf, F. A.; De Vries, R. Cross-Linking and Bundling of Self-Assembled Protein-Based Polymer Fibrils via Heterodimeric Coiled Coils. *Biomacromolecules* **2016**, *17* (12), 3893–3901. https://doi.org/10.1021/acs.biomac.6b01242.

(54) Oude Blenke, E. E.; Van Den Dikkenberg, J.; Van Kolck, B.; Kros, A.; Mastrobattista, E. Coiled Coil Interactions for the Targeting of Liposomes for Nucleic Acid Delivery. *Nanoscale* **2016**, *8* (16), 8955–8965. https://doi.org/10.1039/c6nr00711b.

(55) Zheng, T.; Bulacu, M.; Daudey, G.; Versluis, F.; Voskuhl, J.; Martelli, G.; Raap, J.; Sevink, G. J. A.; Kros, A.; Boyle, A. L. A Non-Zipper-like Tetrameric Coiled Coil Promotes Membrane Fusion. *RSC Adv.* **2016**, *6* (10), 7990–7998. https://doi.org/10.1039/c5ra26175a.

(56) Chiang, C. H.; Fu, Y. H.; Horng, J. C. Formation of AAB-Type Collagen Heterotrimers from Designed Cationic and Aromatic Collagen-Mimetic Peptides: Evaluation of the C-Terminal Cation-π Interactions. *Biomacromolecules* **2017**, *18* (3), 985–993. https://doi.org/10.1021/acs.biomac.6b01838.

(57) Groth, M. C.; Rink, W. M.; Meyer, N. F.; Thomas, F. Kinetic Studies on Strand Displacement in: De Novo Designed Parallel Heterodimeric Coiled Coils. *Chem. Sci.* **2018**, *9* (18), 4308–4316. https://doi.org/10.1039/c7sc05342h.

(58) Tunn, I.; Harrington, M. J.; Blank, K. G. Bioinspired Histidine-Zn2+ Coordination for Tuning the Mechanical Properties of Self-Healing Coiled Coil Cross-Linked Hydrogels. *Biomimetics* **2019**, *4* (1), 1–17. https://doi.org/10.3390/biomimetics4010025.

(59) Li, I. C.; Hulgan, S. A. H.; Walker, D. R.; Farndale, R. W.; Hartgerink, J. D.; Jalan, A. A. Covalent Capture of a Heterotrimeric Collagen Helix. *Org. Lett.* **2019**, *21* (14), 5480–5484. https://doi.org/10.1021/acs.orglett.9b01771.

(60) Walker, D. R.; Hulgan, S. A. H.; Peterson, C. M.; Li, I. C.; Gonzalez, K. J.; Hartgerink, J. D. Predicting the Stability of Homotrimeric and Heterotrimeric Collagen Helices. *Nat. Chem.* **2021**, *13* (3), 260–269. https://doi.org/10.1038/s41557-020-00626-6.

(61) Bromley, E. H. C.; Sessions, R. B.; Thomson, A. R.; Woolfson, D. N. Designed α-Helical Tectons for Constructing Multicomponent Synthetic Biological Systems. *J. Am. Chem. Soc.* **2009**, *131* (3), 928–930. https://doi.org/10.1021/ja804231a.

(62) Fletcher, J. M.; Harniman, R. L.; Barnes, F. R. H.; Boyle, A. L.; Collins, A.; Mantell, J.; Sharp, T. H.; Antognozzi, M.; Booth, P. J.; Linden, N.; Miles, M. J.; Sessions, R. B.; Verkade, P.; Woolfson, D. N. Self-Assembling Cages from Coiled-Coil Peptide Modules. *Science* **2013**, *340* (6132), 595–599. https://doi.org/10.1126/science.1233936.

(63) Thomas, F.; Boyle, A. L.; Burton, A. J.; Woolfson, D. N. A Set of de Novo Designed Parallel Heterodimeric Coiled Coils with Quantified Dissociation Constants in the Micromolar to Sub-Nanomolar Regime. *J. Am. Chem. Soc.* **2013**, *135* (13), 5161–5166. https://doi.org/10.1021/ja312310g.

(64) Nautiyal, S.; Woolfson, D. N.; King, D. S.; Alber, T. A Designed Heterotrimeric Coiled Coil. *Biochemistry* **1995**, *34* (37), 11645–11651. https://doi.org/10.1021/bi00037a001.

(65) Chains, P.; Chao, H.; Houston, M. E.; Grothe, S.; Kay, C. M.; Connor-mccourt, M. O.; Irvin, R. T.; Hodges, R. S. Kinetic Study on the Formation of a de Novo Designed Heterodimeric Coiled-Coil: Use of Surface Plasmon Resonance To Monitor the Association and Dissociation of Polypeptide Chains. *Biochemistry* **1996**, *35*, 12175–12185. https://doi.org/10.1021/bi9530604.

(66) Litowski, J. R.; Hodges, R. S. Designing Heterodimeric Two-Stranded α-Helical Coiled-Coils. Effects of Hydrophobicity and α-Helical Propensity on Protein Folding, Stability, and Specificity. *J. Biol. Chem.* **2002**, *277* (40), 37272–37279. https://doi.org/10.1074/jbc.M204257200.

(67) Lau, S. Y. M.; Taneja, A. K.; Hodges, R. S. Synthesis of a Model Protein of Defined Secondary and Quaternary Structure. Effect of Chain Length on the Stabilization and Formation of Two-Stranded α-Helical Coiled-Coils. *J. Biol. Chem.* **1984**, *259* (21), 13253–13261. https://doi.org/10.1016/s0021-9258(18)90686-1.

(68) Sun, X.; Fan, J.; Li, X.; Zhang, S.; Liu, X.; Xiao, J. Colorimetric and Fluorometric Monitoring of the Helix Composition of Collagen-like Peptides at the NM Level. *Chem. Commun.* **2016**, *52* (15), 3107–3110. https://doi.org/10.1039/c5cc09565d.

CHAPTER 4. PROTEIN INCORPORATION WITHIN COILED-COIL PEPTIDE CRYSTALS FOR IMPROVED THERMAL STABILITY

4.1 Introduction

Proteins continue to play a significant role in biology and remain a key topic of interest. With their complex tertiary and quaternary structures, proteins have been utilized for a variety of applications, such as biocatalysis, biopharmaceuticals, and stimuli-responsive or biodegradable materials.[1–6] Elucidating the structure of a protein also plays a crucial role in understanding the protein's function and structure-activity relationships.[7–10]

This structural complexity, however, makes proteins prone to thermal instability and aggregation, where minor changes in folding can significantly reduce a protein's activity.[11,12] As such, a number of researchers have worked on protein inclusion into biomaterials. Two-dimensional arrays of proteins can prevent aggregation and have been utilized for high-throughput screening and electronics.[13–15] Proteins have also been incorporated into three-dimensional crystals to improve thermal stability and act as solid-state catalysts.[16–27]

Previously, the Chmielewski lab developed a crystalline assembly composed of a coiled-coil peptide **p2L** based on the GCN4 transcription factor.[28,29] These crystals incorporated enhanced green fluorescent protein (EGFP) at high levels in an ordered fashion with a significant increase in thermal stability. The **p2L** crystals required the protein to be His-tagged in order to participate in this metal-mediated assembly, and required metal chelators to release the cargo once encapsulated. Herein, we report a peptide-based system that can undergo higher-order assembly to form crystals without metals, combined with an investigation of protein inclusion within the material.

4.2 Results and Discussion

4.2.1 Co-assembled Peptide Crystals and Structure

In the previous chapter, a strategy to stabilize peptide nanotubes using a **TriNL**:**p2L** coassembly was described (see Chapter 3). We discovered that high **p2L** levels in the co-assembly (2:1 **TriNL**:**p2L**) resulted in hexagonal crystals similar to **p2L**, but now without the need for metal

ions to promote the assembly.[30] Since metal ions are not a part of the assembly process, it may be possible to remove the requirement for cargo to be His-tagged to be incorporated within the crystals, and thereby expand the scope of protein incorporation. Furthermore, degradation of these crystals in phosphate buffered saline (PBS), as described in Chapter 3, would allow for a facile mechanism of protein release. Since heterocoiled-coils formed more reliable and uniform materials,[30] crystal assemblies with **TriNL** and **p2L** homotrimers were not investigated.

The crystals were obtained as described in Chapter 3. Namely, a 2:1 **TriNL**:**p2L** solution was first thermally annealed to produce a mixture of heterocoiled-coils.[30,31] Heating the coiled-coils to 90 °C unfolded the peptides and the rapid cooling of the solution to 4 °C caused the peptides to refold and form coiled-coils composed of both **TriNL** and **p2L** α-helices (**Figure 4.1**). Once in hand, the peptides (1 mM total peptide concentration) were incubated in 2-(N-morpholino)ethansulfonic acid (MES) buffer (100 mM, pH 6.0) for 1 hr at room temperature. SEM visualization of the resulting material revealed a strikingly similar morphology to pure **p2L** hexagonal crystals, but with crystals that were larger in size (~25 μm in length compared to ~4 μm) (**Figure 4.2**).[28]

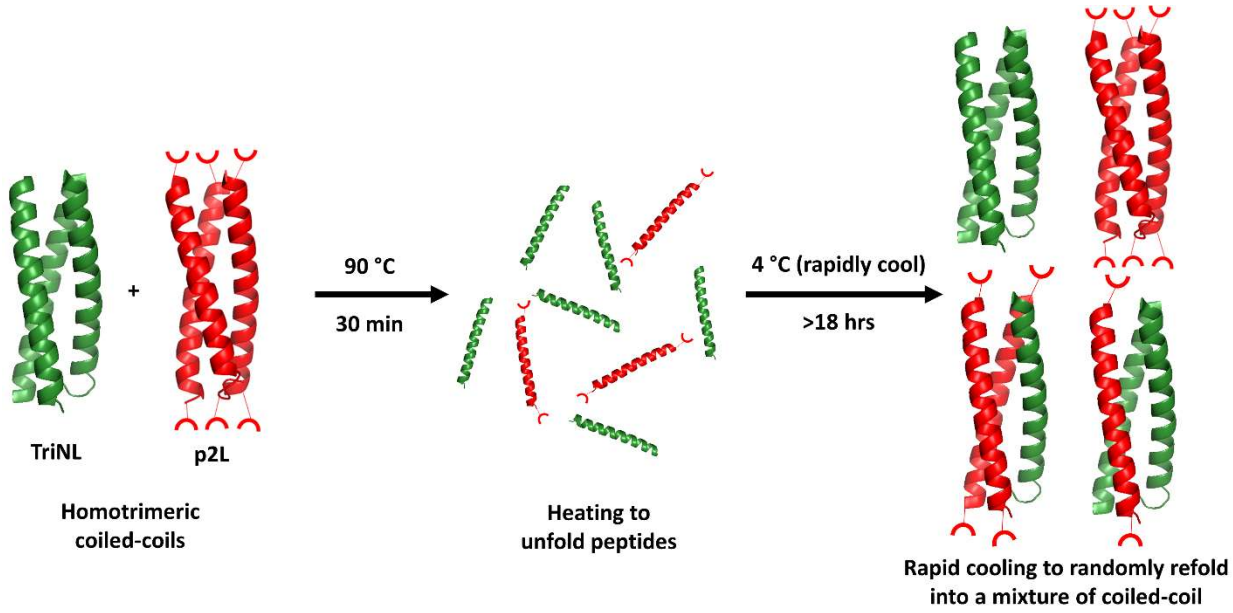

Figure 4.1. The formation of a mixture of heterocoiled-coils through thermal annealing.

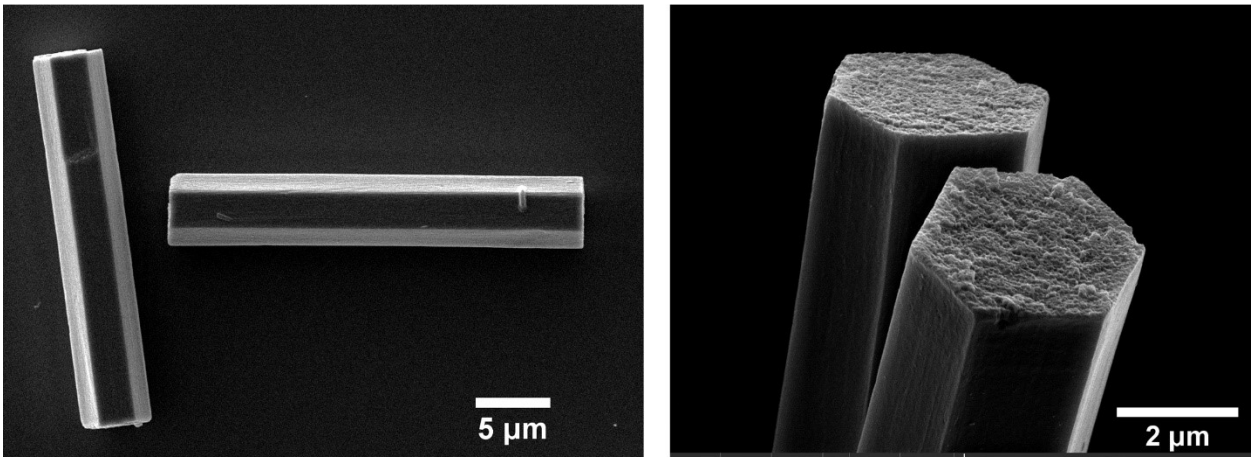

Figure 4.2. SEM visualization of 2:1 **TriNL**:**p2L** crystals (1 mM) assembled in MES buffer (100 mM, pH 6.0).

The packing of the peptide crystals was first analyzed using small- and wide-angle X-ray scattering (SWAXS) (**Figure 4.3**A). q values of 1.46, 3.54, and 6.38 nm^{-1} were obtained and correspond to d-spacings of 4.3, 1.76, and 0.98 nm, respectively. The d-spacing of 4.3 nm is the repeating unit in the z-direction and corresponds to the length of the coiled-coil (**Figure 4.3**B). The d-spacings of 1.76 nm and 0.98 nm correspond to distances between coiled-coil planes at the P3 face (**Figure 4.3**C). To obtain the lattice parameter (a), the height of the rhombus was first determined. Using the two d-spacings at the P3 face, the height was calculated to be 2.74 nm (1.76/2 nm + 0.98 nm + 1.76/2 nm). Furthermore, the acute angle of the lattice parameter is 60° because the rhombus intersects one-sixth of hexagonal packing (360°/6 = 60°) With these two values, the lattice parameter (a) was calculated to be 3.2 nm (2.74 nm/sin(60°)). Large lattice parameters (~3-4 nm) indicate an open-faced hexagonal packing of a crystal while a smaller lattice parameter (~2 nm) indicate closed hexagonal packing.[32–34] This suggest that the 2:1 **TriNL**:**p2L** crystals have open-faced hexagonal packing such as that observed for **p2L**/Zn(II) crystals.[28] The q value of 12.64 nm^{-1} corresponds to a d-spacing of 0.50 nm and may be a result of intertrimer hydrogen bonding and electrostatic interactions.[33,34]

For a more detailed look at the structure, 2:1 **TriNL**:**p2L** crystals were analyzed via X-ray crystallography using the Advanced Photon Source at Argonne National Laboratory by Dr. David Kissick and Dr. Qingping Xu. The peptide crystal structure was solved with a 1.5 Å resolution in the P321 space group. The arrangement of coiled-coils was strikingly similar to the **p2L**/Zn system and corroborates the SWAXS data above. The diffraction data was refined only once, and this is

likely why the KIEE residues within the coiled-coil (positions 8-11) are not part of the α-helix folding in the crystal structure. Along the length of the crystal, coiled-coils were lined in a head-to-tail fashion, and the P3 face exhibited an open-faced hexagonal packing. The coiled-coils were also arranged in an antiparallel fashion (denoted with green and cyan) where neighboring coiled-coils were oriented in opposite directions (**Figure 4.3**B-D). The flexibility of the ligands prevented structural data for NTA and histidine to be obtained, and therefore **TriNL** and **p2L** could not be distinguished from one another in the structure.

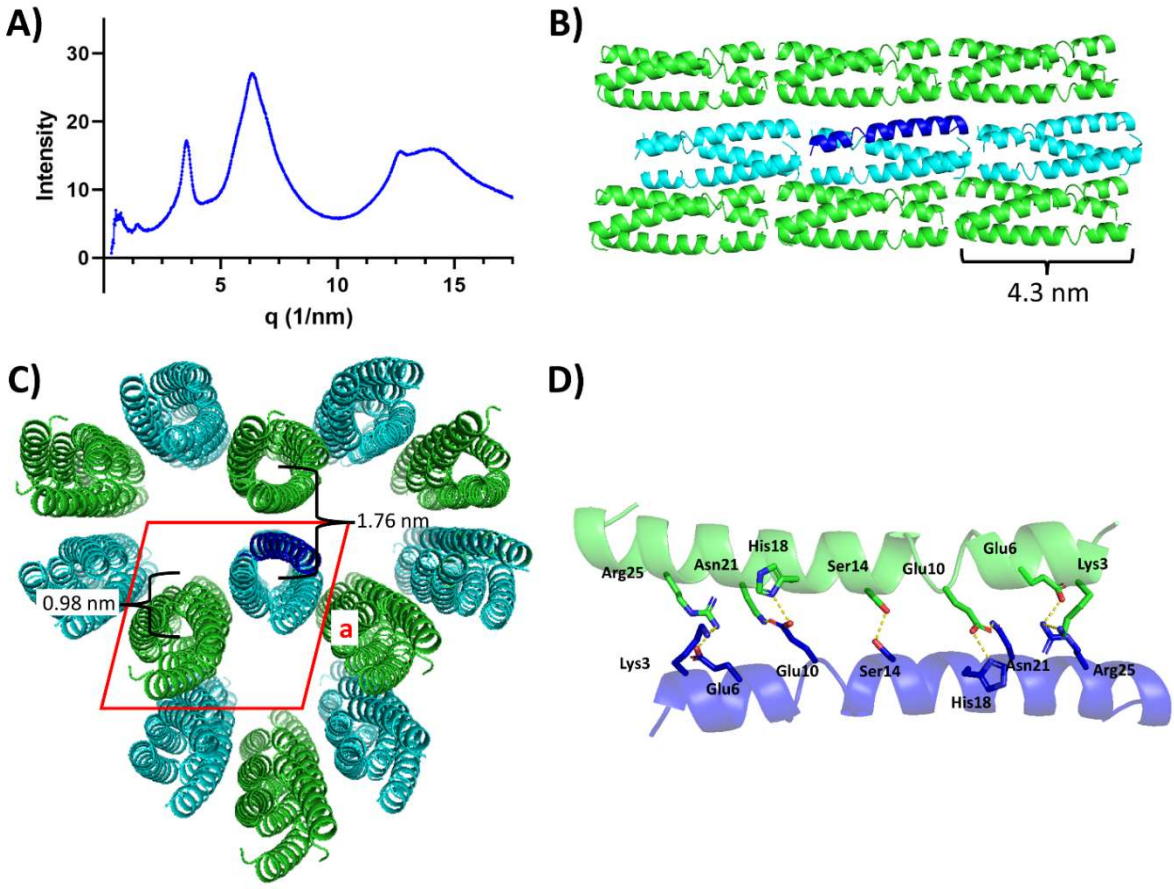

Figure 4.3. (A) SWAXS of 2:1 **TriNL**:**p2L** crystals. (B) Head-to-tail assembly of coiled-coils and (C) P3 face of the crystal with open-faced hexagonal packing. (D) Interactions at the interface of neighboring coiled-coils within the hexagonal crystal.

4.2.2 Protein Inclusion

With the **TriNL**/**p2L** crystal structure nearly identical to **p2L**/Zn crystals, we investigated the scope of protein inclusion to compare the two systems. When crystals of **p2L** and Zn(II) were formed in the presence of His-tagged EGFP, high levels of protein incorporation (1:30 protein:trimer) were observed within the hourglass pattern.[29] However, it was found that **p2L**/Zn(II) crystals had a limited scope for inclusion of His-tagged proteins of varying charge and size.[35] Crystals composed of the heterotrimeric coiled-coils assemble through a different mechanism. Namely, these crystals are likely formed through ionic interactions between coiled-coils, rather than being mediated by metal-ligand interactions, as observed for **p2L** homotrimers. However, the crystals composed of heterotrimers still retain the metal-binding ligands NTA and di-histidine. Consequently, the P3 face of the crystal displays negatively charged NTA and positively charged histidine. With this charged P3 face, we envisioned a wider scope of protein inclusion through ionic interactions rather than through metal/His-tagged binding.

The effects of protein surface charge were probed using His-tagged GFP derivatives developed by David Liu and coworkers.[36–38] Wild type EGFP has a theoretical surface charge of -11. Liu developed GFPs with surface charges of -30, +9, and +36 through modifications of solvent-exposed residues to either positively or negatively charged amino acids (**Figure 4.4**). These proteins were expressed using standard protein expression methods. Specifically, the GFP plasmids were added to BL21(DE3) *E. coli* cells on ice, and the cells were heat shocked to semipermeabilize the membrane of the bacteria and transform the plasmid. The *E. coli* were cultured on an LB/Ampicillin agar plate, and a single colony was selected and cultured. Protein expression was induced with either arabinose (10 mM for EGFP) or isopropyl β-D-1-thiogalactopyranoside (IPTG, 0.6 mM for His-Neg30GFP, His-Pos9GFP, His-Pos36GFP). The bacteria were subsequently lysed and the desired proteins were purified using a Ni-NTA resin.

The effects of protein size and shape in protein inclusion were also investigated using commercially available proteins. Specifically, hemoglobin (64.5 kDa) and bovine serum albumin (BSA, 66 kDa) were selected as larger proteins, as compared to EGFP, and lysozyme (14.3 kDa) was chosen as a smaller protein (**Figure 4.4**). Unlike EGFP, these proteins are not inherently fluorescent. As such, each protein was fluorescently labeled utilizing exposed lysine residues on the protein and N-hydroxysuccinimide (NHS) esters of fluorophores. Hemoglobin and BSA were labeled with NHS-fluorescein (2 eq) for 1 hr at room temperature. Lysozyme precipitated out of

solution when labeled with fluorescein and was instead labeled with the NHS ester of coumarin (2 eq). Each protein was concentrated and washed with 1x PBS three times to remove excess fluorophore. Because the proteins were labeled using lysine residues, the surface charges of these proteins are likely modified somewhat from that shown in **Figure 4.4**.

The final two proteins of interest were commercially available SAvPhire monomeric streptavidin and horseradish peroxidase (HRP) (**Figure 4.4**). Streptavidin has a strong binding affinity to the small molecule biotin. As such, it would be of interest to transport small biomolecules conjugated to biotin into the crystals utilizing the streptavidin-biotin binding affinity. The enzyme HRP oxidizes substrates such as 3,3',5,5'-tetramethylbenzidine (TMB) in the presence of hydrogen peroxide and leads to a color change of the solution. This would provide an excellent avenue for future enzyme activity experiments while within the crystal.

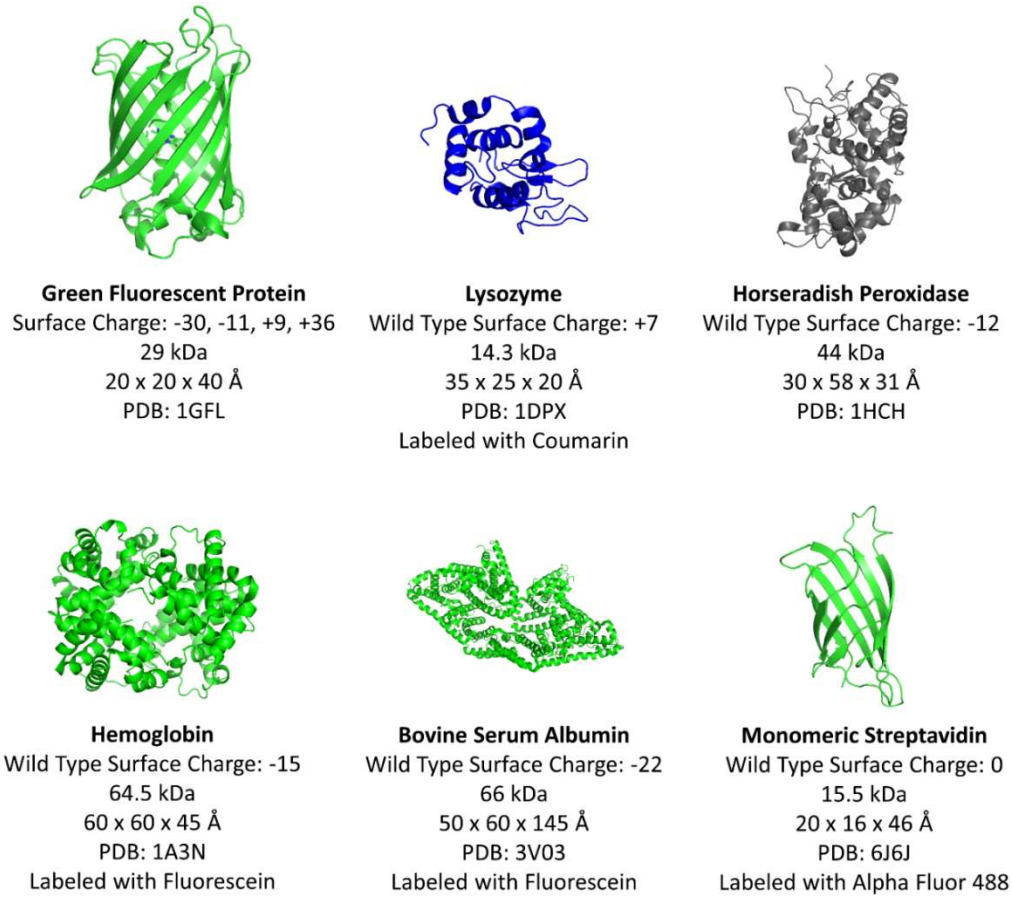

Figure 4.4. Proteins tested to determine scope of protein inclusion in **TriNL**:**p2L** crystals.

With proteins in hand, protein guest inclusion into peptide crystals was evaluated. Specifically, to a heterocoiled-coil solution in water (2:1 **TriNL**:**p2L,** final 1 mM) was added MES buffer (final 100 mM, pH 6.0) and EGFP or EGFP mutants (final 7 μM) with surface charges ranging from -30 to +36. After 1 hr at room temperature, the crystals were collected, washed and visualized by scanning electron microscopy (SEM) and confocal microscopy (**Figure 4.5**). Hexagonal crystals were still formed with all protein conditions (Figure 4.5A,C,E,G). Interestingly, all GFP mutants were found within the crystals (**Figure 4.5**B,D,F,H). This is a stark contrast to pure **p2L**/Zn(II) crystals where only wild type EGFP (-11 charge) was incorporated. Observation of the protein incorporation with the 2:1 **TriNL**:**p2L** crystals showed a bowtie-like pattern of fluorescence within the crystals. This pattern is a result of the protein guests favoring the P3 face over other faces of the crystal. As the crystal grows, the P3 face grows symmetrically outward in two directions. This face of the crystal is where the NTA and di-histidine ligands are located. As a result, the proteins may create ionic interactions with these ligands. The highly charged proteins (His-Neg30GFP and His-Pos36GFP) also led to some fluorescence in areas outside of the bowtie region of the crystal (**Figure 4.5**D,H). This may be the result of the protein interacting with charged sidechains along the solvent exposed regions of the coiled-coil such as glutamate (or aspartate) and lysine residues in the *b*, *c*, or *f* positions of the heptad repeat (**Figure 4.6**).

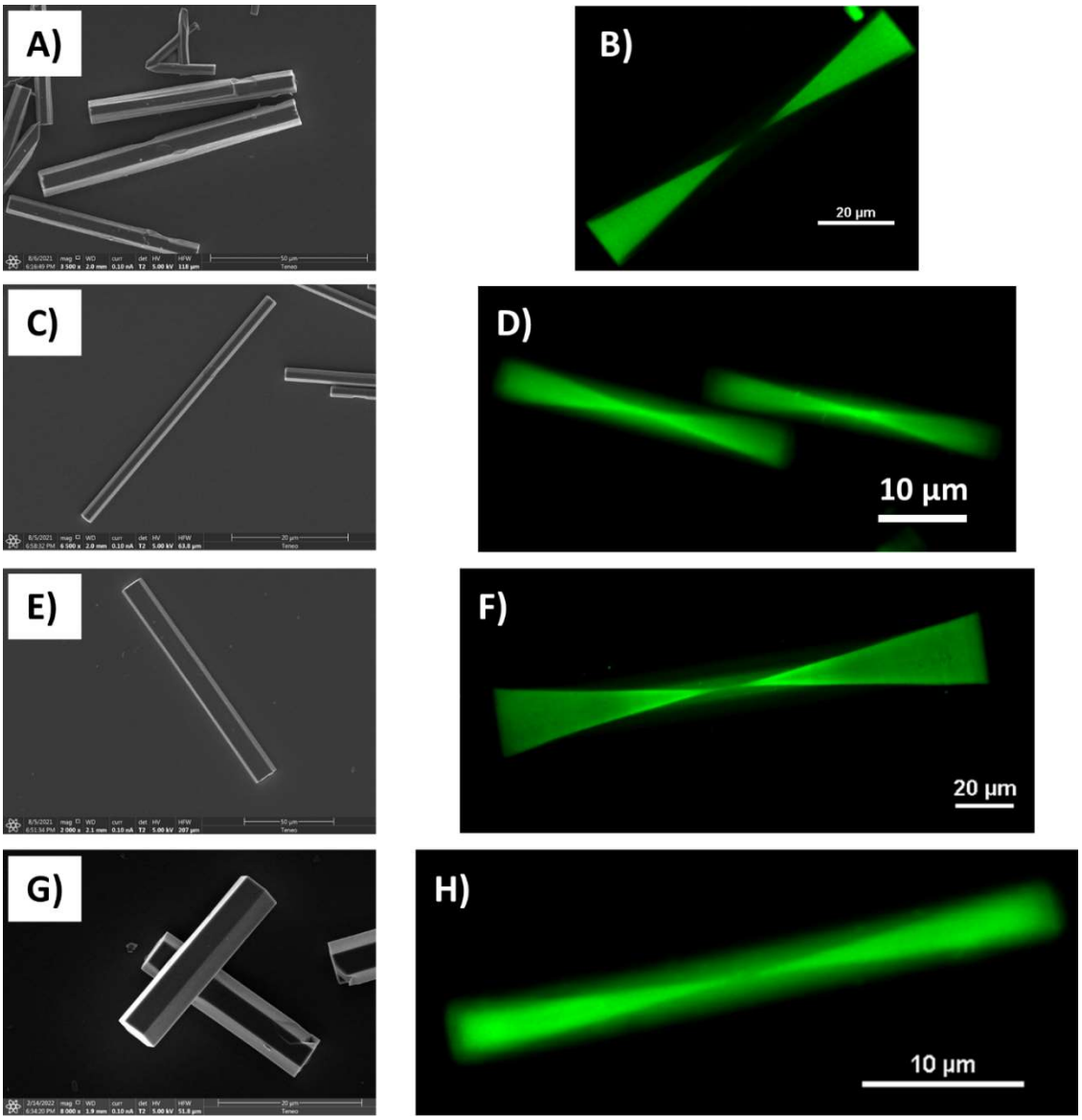

Figure 4.5. Protein inclusion of GFP mutants (7 µM) in 2:1 **TriNL**:**p2L** crystals (1 mM). (A) SEM and (B) confocal visualization with His-EGFP (-11) inclusion, (C) SEM and (D) confocal visualization with His-Neg30GFP inclusion, (E) SEM and (F) confocal visualization with His-Pos9GFP inclusion, and (G) SEM and (H) confocal visualization with His-Pos36GFP inclusion.

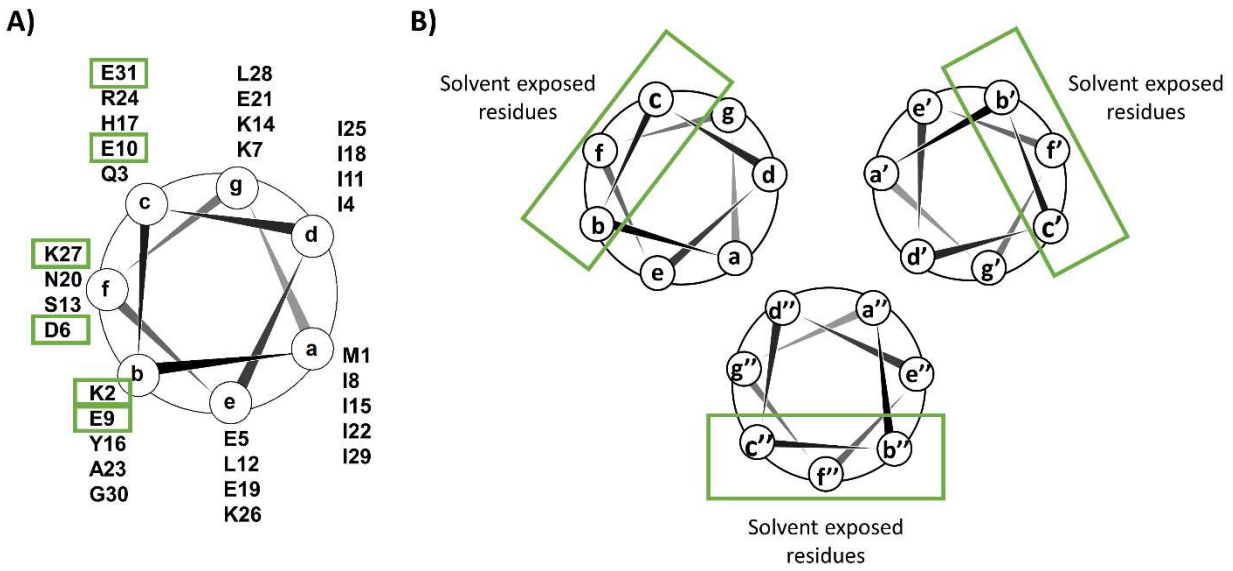

Figure 4.6. (A) Helical wheel of **TriNL**/**p2L** with charged residues at solvent exposed positions labeled in green. (B) Trimeric coiled-coil schematic with solvent exposed positions labeled in green.

Commercially available lysozyme, hemoglobin, and BSA were also used to investigate the effects of protein size on protein guest inclusion. Hemoglobin and BSA are significantly larger than GFP both in size and mass while lysozyme is smaller in both aspects (**Figure 4.4**). Using the same conditions as described above, the **TriNL**:**p2L** heterotrimers were crystallized in the presence of each protein (7 μM). The crystals were collected and visualized using both SEM and confocal microscopy (**Figure 4.7**). Similar to the GFP derivatives, hexagonal crystals were produced with protein incorporated within the crystal in a bowtie-like pattern (**Figure 4.7**). Additional fluorescence was also observed outside of this bowtie region for hemoglobin and BSA. Similar to the GFPs, the excess charge of hemoglobin (wild type: -15) and BSA (wild type: -22), further increased by the conjugation of surface exposed lysine residues, may have caused binding between the protein and the coiled-coil backbone in other areas of the crystal. The surface charge of lysozyme is closer to being neutral (wild type: +7) and primarily resided within the bowtie similar to EGFP (-11 charge) and Pos9GFP.

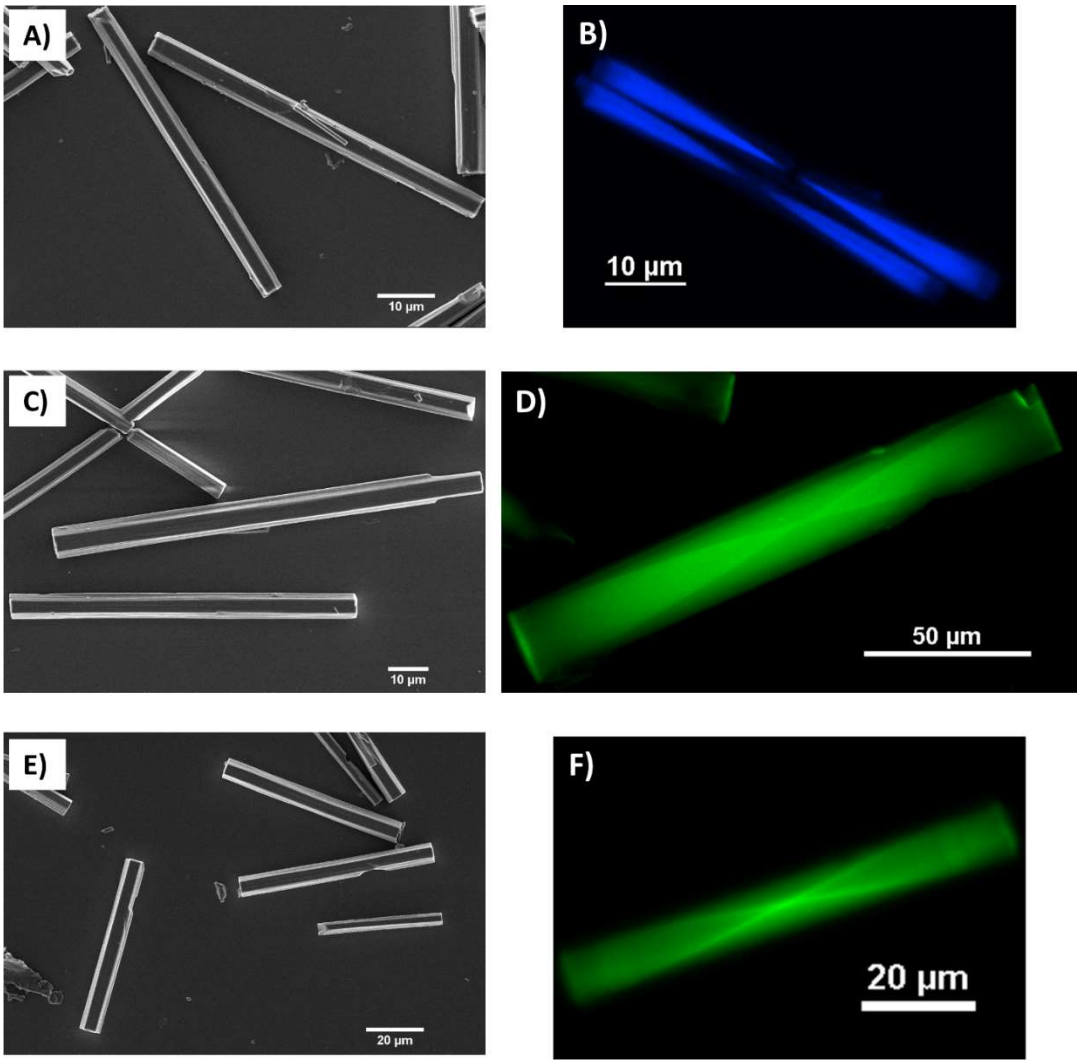

Figure 4.7. Protein inclusion using varying sized proteins (7 µM) in 2:1 **TriNL**:**p2L** crystals (1 mM). (A) SEM and (B) confocal visualization with Cou-lysozyme inclusion, (C) SEM and (D) confocal visualization with Fl-hemoglobin inclusion, and (E) SEM and (F) confocal visualization with Fl-BSA inclusion.

4.2.3 Protein Quantification

With confocal microscopy confirming a wide range of protein incorporation, the protein:peptide ratio of the crystals was quantified for various proteins. To a heterocoiled-coil solution in water (2:1 **TriNL**:**p2L,** final 1 mM) was added MES buffer (final 100 mM, pH 6.0) and EGFP (final 7 µM). After 1 hr at room temperature, the crystals were collected and washed. After the final centrifugation, the supernatant was removed, and the crystals were resuspended in 1x PBS (100 µL) for 5 min to dissolve the crystals. EGFP (nmol) was quantified by measuring the

fluorescence (415 nm excitation and 535 nm emission) against a fluorescence standard curve (**Figure 4.8**D). The peptides (nmol) were quantified via absorbance (214 nm) against a UPLC standard curve (**Figure 4.8**A-B and **Figure 4.9**A). EGFP and **p2L**, however, were unable to be separated via UPLC. As such, the peak area of EGFP on UPLC (214 nm) was calculated using the already quantified EGFP and an EGFP absorbance standard curve (214 nm) (**Figure 4.8**C). This value was subtracted from the integrated **p2L** peak to properly quantify **p2L** (nmol) within the assembly.

Because the EGFP inclusion was favored at the P3 face, the volume fraction of the bowtie within the crystal was considered. The volume of the entire crystal, a hexagonal prism, is

$$V_{Crystal} = \frac{3\sqrt{3}W^2L}{2} \quad (1)$$

where W is the width of the crystal and L is the length. The bowtie pattern within the crystal is composed of two hexagonal pyramids. Consequently, the volume of the bowtie within the crystal is

$$V_{Bowtie} = 2(\frac{\sqrt{3}W^2L}{4}) \quad (2)$$

where W is the width of the crystal and L is the length. The quotient of these two indicates that the volume of the bowtie corresponds to about a third of the entire crystal volume. With this, a 1:270 protein:peptide ratio was observed within the crystal and a 1:90 ratio inside the bowtie area. Taking into consideration the trimeric nature of the peptide, a 1:30 protein:trimer ratio was observed within the bowtie area (**Table 4.1**). This is a striking level of protein incorporation without disruption of the crystal formation and is similar to homotrimeric **p2L** crystals.

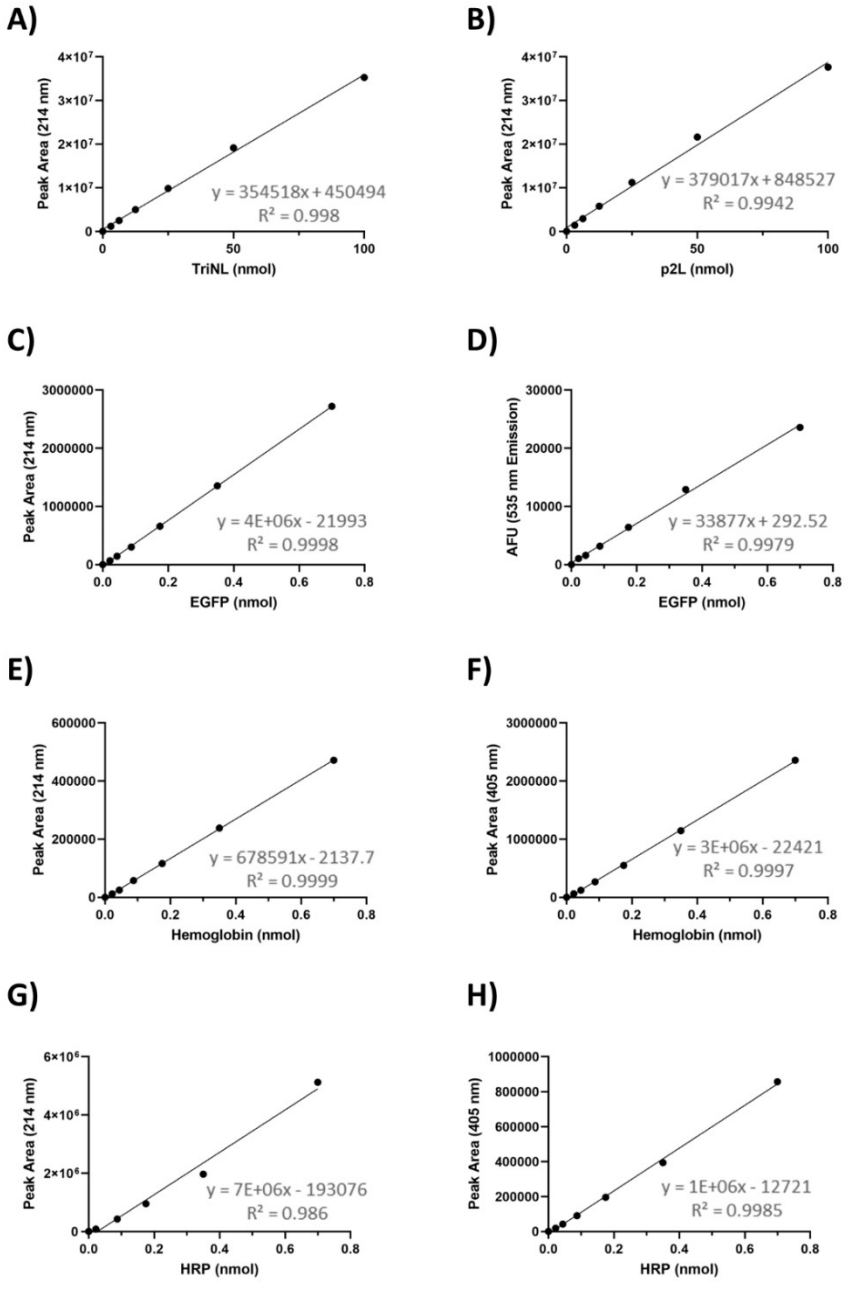

Figure 4.8. Standard curves of peptides and proteins. (A) **TriNL** (absorbance, 214 nm), (B) **p2L** (absorbance, 214 nm), (C) EGFP (absorbance, 214 nm), (D) EGFP (fluorescence, 535 nm emission), (E) hemoglobin (absorbance, 214 nm), (F) hemoglobin (absorbance, 405 nm), (G) HRP (absorbance, 214 m), (H) HRP (absorbance, 405 nm).

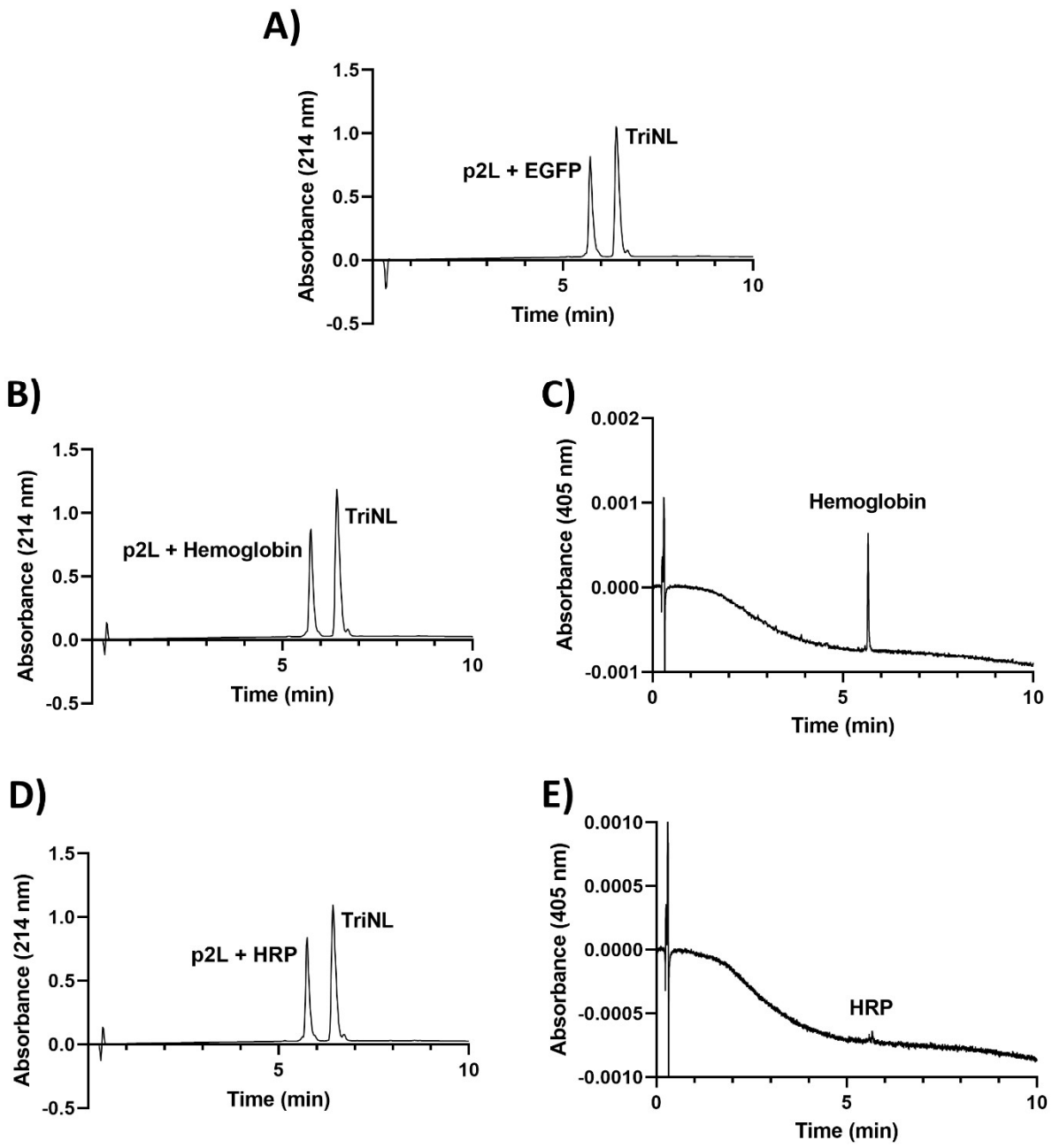

Figure 4.9. UPLC traces of 2:1 **TriNL**:**p2L** crystals (1 mM) with EGFP, hemoglobin, or HRP (7 μM). (A) EGFP crystals, (B) hemoglobin crystals (214 nm), (C) hemoglobin crystals (405 nm), (D) HRP crystals (214 nm), (E) HRP crystals (405 nm).

Table 4.1. Peptide and protein quantification from EGFP crystals (7 μM).

EGFP fluorescence (Ex: 415 nm, Em: 535 nm)	4100
EGFP in assembly (nmol)	**0.11**
EGFP UPLC area (214 nm)	4.3×10^5
p2L + EGFP UPLC area (214 nm)	4.9×10^6
p2L UPLC area (214 nm)	4.5×10^6
p2L in assembly (nmol)	9.7
TriNL UPLC area (214 nm)	8.2×10^6
TriNL in assembly(nmol)	21.7
Total peptide in assembly (nmol)	**31.4**
EGFP:peptide	1:280
EGFP:peptide in bowtie	1:90
EGFP:trimer in bowtie	**1:30**

Hemoglobin and HRP incorporation were also quantified to further investigate protein inclusion within the crystals. Unlabeled hemoglobin was used for this study to prevent the effect of a fluorophore on protein inclusion. Because both proteins are not fluorescent, the absorbance at 405 nm was measured against standard curves corresponding to the hemes in the proteins (**Figure 4.8**F,H). To a heterocoiled-coil solution in water (2:1 **TriNL**:**p2L,** final 1 mM) was added MES buffer (final 100 mM, pH 6.0) and hemoglobin or HRP (final 7 μM). After 1 hr at room temperature, the crystals were collected and washed. The samples was first visualized via SEM to confirm crystal formation (**Figure 4.10**). Hemoglobin and HRP do not disrupt the assembly, and hexagonal crystals were observed. Similar to above, samples with either hemoglobin or HRP were resuspended in 1x PBS (100 μL) to dissolve the material and quantified via absorbance. Although both hemoglobin and HRP were still incorporated inside of the crystals, a much smaller amount of protein was observed (**Figure 4.9**B-E, **Table 4.2**, and **Table 4.3**). Hemoglobin crystals had a 1:1400 protein to trimer ratio, and HRP had a 1:900 protein to trimer ratio within the crystal. Because these nonfluorescent proteins may not have a bowtie pattern, a protein to trimer ratio within the bowtie was not calculated. The incorporation of both hemoglobin and HRP was significantly less when compared to the 1:90 EGFP:trimer ratio within the crystal. This may be a result of the size difference between proteins. Protein guest inclusion requires the ability for the peptide to overgrow the guest and continue the crystallization process. With a larger protein such as hemoglobin and HRP, the process to overgrow the protein is more difficult. Because all three

proteins have similar charges (EGFP: -11, hemoglobin: -15, and HRP: -12), it is unlikely that the surface charge played a role in this decrease.

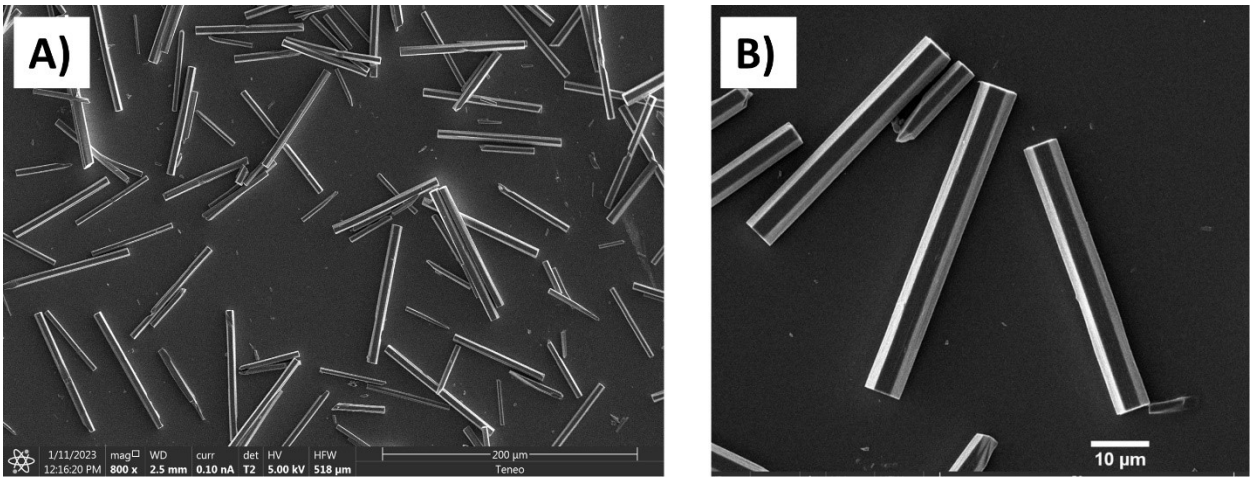

Figure 4.10. SEM image of 2:1 **TriNL**:**p2L** crystals (1 mM) with (A) hemoglobin (7 µM) and (B) HRP incorporated (7 µM).

Table 4.2. Peptide and protein quantification from hemoglobin crystals (7 µM).

Hemoglobin UPLC area (405 nm)	3080
Hemoglobin in assembly (nmol)	**0.0085**
Hemoglobin UPLC area (214 nm)	~0
p2L UPLC area (214 nm)	4.9
p2L in assembly (nmol)	10.6
TriNL UPLC area (214 nm)	9.3
TriNL in assembly (nmol)	24.9
Total peptide in assembly (nmol)	**35.5**
Hemoglobin:peptide	1:4200
Hemoglobin:trimer	**1:1400**

Table 4.3. Peptide and protein quantification from HRP crystals (7 μM).

HRP UPLC area (405 nm)	125
HRP in assembly (nmol)	**0.013**
HRP UPLC area (214 nm)	~0
p2L UPLC area	4.9×10^6
p2L in assembly (nmol)	10.7
TriNL UPLC area (214 nm)	8.6×10^6
TriNL in assembly (nmol)	23
Total peptide in assembly (nmol)	**33.7**
HRP:peptide	1:2700
HRP:trimer	**1:900**

In an effort to increase protein content within the crystal, higher concentrations of protein were tested. When the 2:1 **TriNL**:**p2L** peptide solution (1 mM) was added to MES buffer (100 mM, pH 6.0) and EGFP (14 μM), crystals still formed (**Figure 4.11**A). Furthermore, a bowtie pattern of fluorescence was observed in these crystals (**Figure 4.11**B). When a 2:1 **TriNL**:**p2L** peptide solution (1 mM) was added to MES buffer (100 mM, pH 6.0) with a higher EGFP concentration (20 μM), the crystal formation was disrupted, where broken crystals and shards were visualized (**Figure 4.11**C). This may be a result of the coiled-coils unable to overgrow the high concentration of protein as the material crystallized. As such, peptide solutions (1 mM) with hemoglobin and HRP were crystallized at a 14 μM protein concentration, rather than 20 μM, in MES buffer (100 mM, pH 6.0). Hexagonal crystals were also observed for these assemblies (**Figure 4.11**D-E).

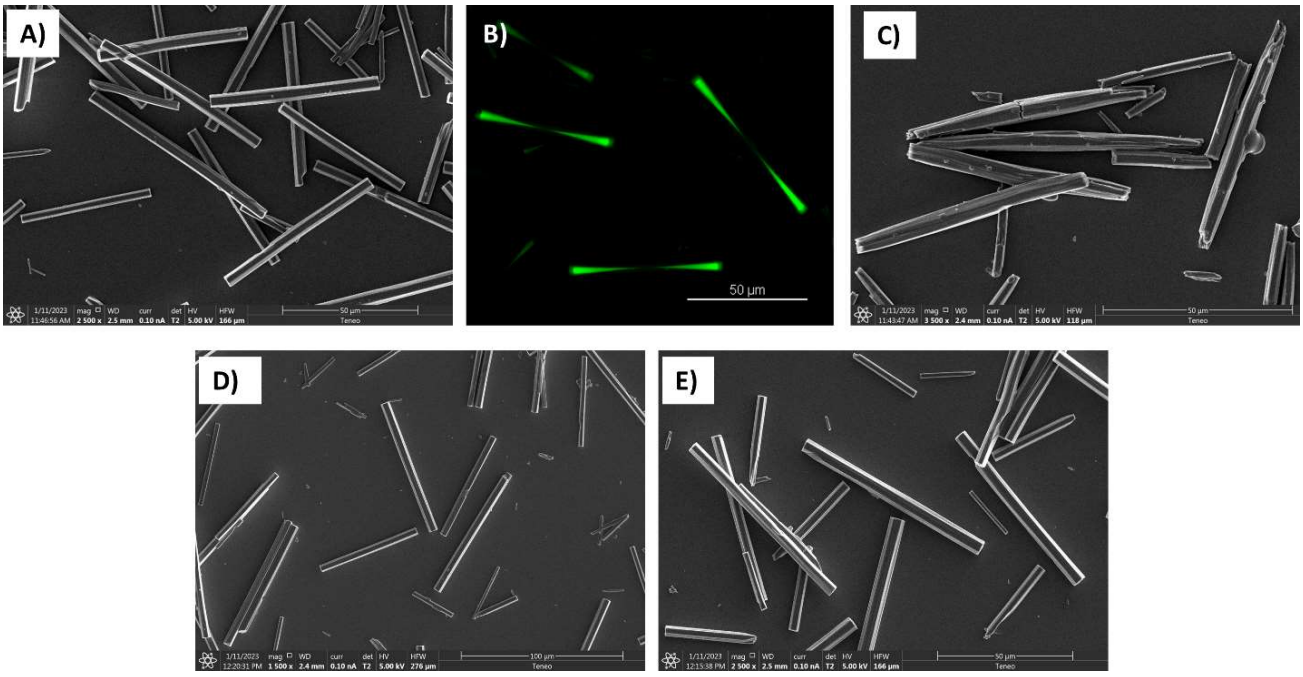

Figure 4.11. (A) SEM and (B) confocal visualization of 2:1 **TriNL**:**p2L** (1 mM) crystals with EGFP incorporation (14 µM). (C) SEM visualization of 2:1 **TriNL**:**p2L** (1 mM) assembly with EGFP incorporation (20 µM). (D) SEM visualization of 2:1 TriNL:p2L (1 mM) with HRP (14 µM) and (E) hemoglobin (14 µM).

With crystals successfully formed at a 14 µM protein concentration, these materials were subsequently investigated for protein incorporation. Similar to other crystals, the assemblies were dissolved in 1x PBS (100 µL) for five minutes. Protein content was measured via fluorescence (EGFP, 415 nm excitation and 535 nm emission) or absorbance (hemoglobin and HRP, 405 nm) (**Figure 4.12**C,E) and **TriNL** and **p2L** were quantified via absorbance (214 nm) (**Figure 4.12**A,B,D). Among all crystal samples, protein content was increased. The EGFP:trimer ratio within the bowtie increased from 1:30 to 1:16 (**Table 4.4**). The hemoglobin and HRP ratios within the crystal also increased from 1:1400 to 1:900 (**Table 4.5**) and from 1:900 to 1:600 (**Table 4.6**), respectively. A 1:16 EGFP:trimer ratio without disruption of the crystallization process is impressive. While an increase in hemoglobin and HRP inclusion was observed, future studies will include further optimization for the proteins' inclusion.

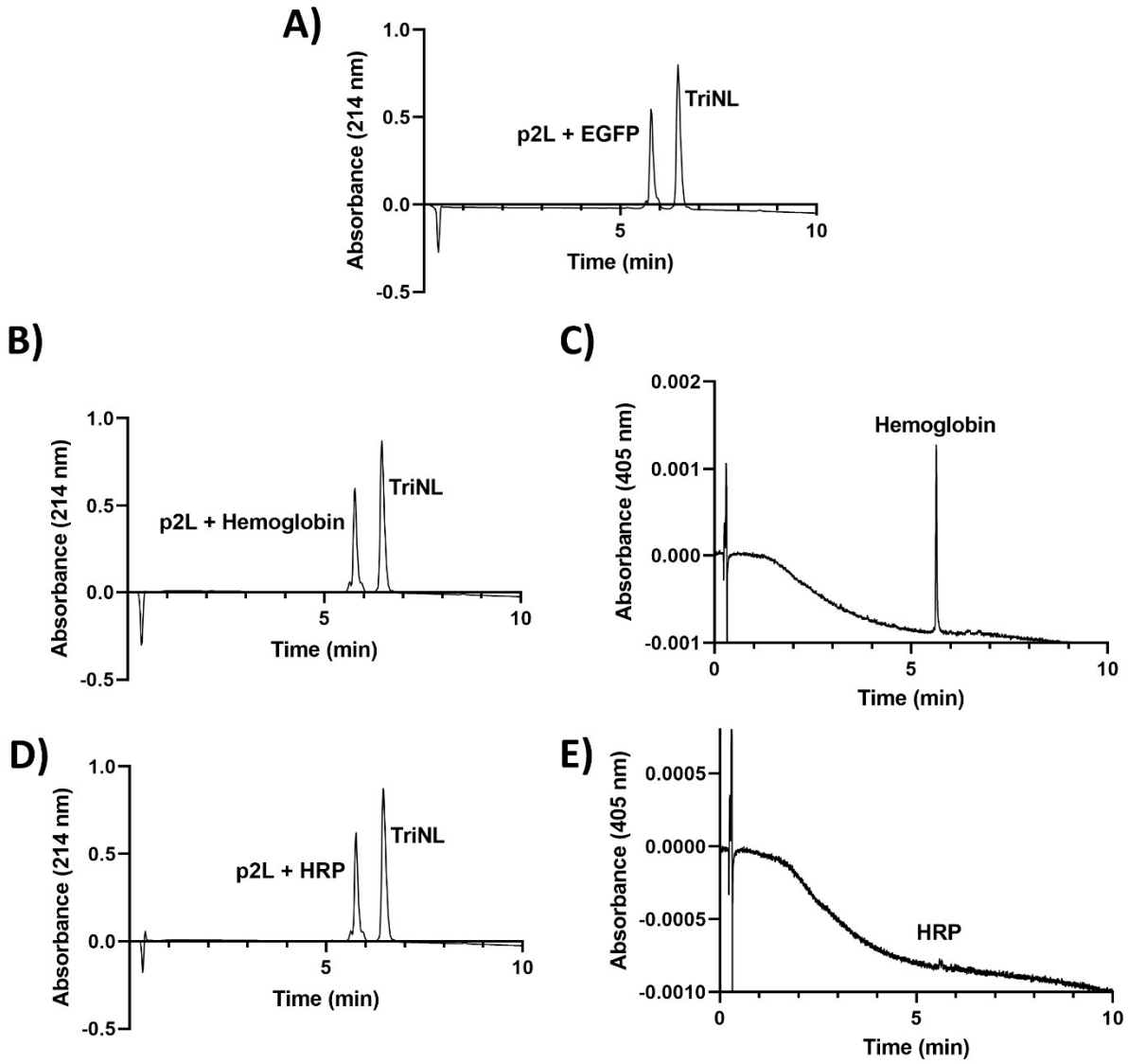

Figure 4.12. UPLC traces of 2:1 **TriNL**:**p2L** crystals (1 mM) with EGFP, hemoglobin, or HRP (14 μM). (A) EGFP crystals (214 nm), (B) hemoglobin crystals (214 nm), (C) hemoglobin crystals (405 nm), (D) HRP crystals (214 nm), (E) HRP crystals (405 nm).

Table 4.4. Peptide and protein quantification from EGFP crystals (14 μM).

EGFP fluorescence (Ex: 415 nm, Em: 535 nm)	5200
EGFP in assembly (nmol)	0.14
EGFP UPLC area (214 nm)	7.3×10^5
p2L + EGFP UPLC area (214 nm)	3.4×10^6
p2L UPLC area (214 nm)	2.7×10^6
p2L in assembly (nmol)	4.9
TriNL UPLC area (214 nm)	5.9×10^6
TriNL in assembly (nmol)	15.2
Total peptide in assembly (nmol)	**20.1**
EGFP:peptide	1:140
EGFP:peptide in bowtie	1:47
EGFP:trimer in bowtie	**1:16**

Table 4.5. Peptide and protein quantification from hemoglobin crystals (14 μM).

Hemoglobin UPLC area (405 nm)	4739
Hemoglobin in assembly (nmol)	**0.009**
Hemoglobin UPLC area (214 nm)	0
p2L UPLC area (214 nm)	3.6×10^6
p2L in assembly (nmol)	7.2
TriNL UPLC area (214 nm)	6.6×10^6
TriNL in assembly (nmol)	17.3
Total peptide in assembly (nmol)	**24.5**
Protein:peptide	1:2700
Protein:trimer	**1:900**

Table 4.6. Peptide and protein quantification from HRP crystals (14 μM).

HRP UPLC area (405 nm)	214
HRP in assembly (nmol)	**0.014**
HRP UPLC area (214 nm)	~0
p2L UPLC area	3.7×10^6
p2L in assembly (nmol)	7.5
TriNL UPLC area (214 nm)	6.8×10^6
TriNL in assembly (nmol)	17.8
Total peptide in assembly (nmol)	**25.3**
Protein:peptide	1:1800
Protein:trimer	**1:600**

4.2.4 Protein Stability

With the 2:1 **TriNL**:**p2L** crystal system expanding the scope of protein incorporation, it was important to confirm that proteins incorporated within these crystals exhibited thermal stability, as we had previously found with the pure **p2L** crystals.[29] EGFP was chosen for stability experiments since the protein loses its fluorescence when denatured.[39] With this in mind, a peptide solution (1 mM) was added to MES buffer (100 mM, pH 6.0) and EGFP (7 μM) in a 50 μL total volume. After the crystals were collected and washed, the material was imaged via confocal microscopy. The crystals were subsequently heated to 100 °C for 1 hr and imaged again via using the same laser intensity. While EGFP in solution would exhibit a complete loss of fluorescence at these conditions,[29] the crystals remained significantly fluorescent after heating (Figure 4.13). Because the crystal remained fluorescent, the protein inside the crystal was still properly folded even after being stored in harsh conditions. This may be a result of the protein tightly packed within the crystal, where neighboring coiled-coils stabilize the protein and prevent unfolding. These data qualitatively show an increase in stability of the protein while inside the peptide crystals.

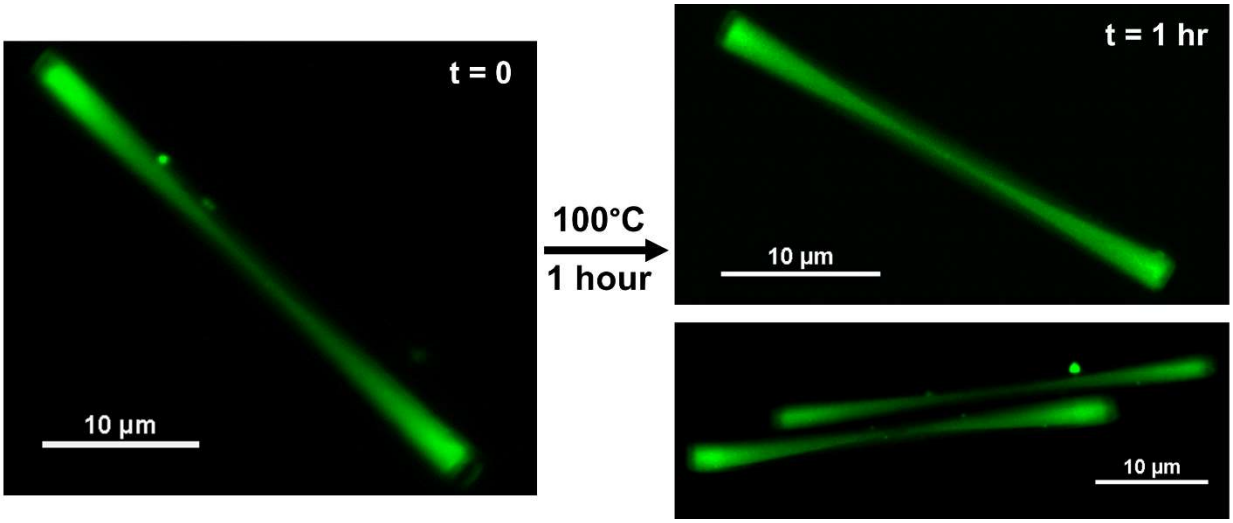

Figure 4.13. Confocal microscopy of 2:1 **TriNL**:**p2L** crystals with EGFP before and after incubation at 100 °C for 1 hr.

4.2.5 Biotin-streptavidin Binding

With the knowledge that proteins could be incorporated within the crystal lattice of **TriNL**:**p2L**, and did not denature at high temperatures, we wished to determine if the biological activity of proteins within the three-dimensional matrix could be maintained. With this motivation, commercially available monomeric streptavidin, labeled with Alpha Fluor 488, and its binding to biotin, labeled with rhodamine, were used to probe this idea. This pair of biomolecules exhibits one of the strongest binding affinities in nature, and is commonly used as a model system.[40,41] Using similar methods to above, a solution of 2:1 **TriNL**:**p2L** heterocoiled-coils (1 mM) was combined with MES buffer (100 mM, pH 6.0) and monomeric streptavidin (7 μM). We observed that the protein was incorporated within the crystals (Figure 4.14A). Interestingly, we observed fluorescence throughout the crystals rather than a bowtie pattern. This may be a result of the net neutral surface charge on the protein. Without an overall positive or negative surface charge, the protein may not favor the charged P3 face of the crystal over other faces.

Biotin was subsequently used to investigate the biological activity of monomeric streptavidin within the crystal. To visualize the small molecule, biotin was first fluorescently labeled using NHS-rhodamine (1.2 eq) and DIEA (2.4 eq) in DMSO for 12 hrs (**Scheme 4.1**). The reaction was purified via high-performance liquid chromatography (HPLC) and characterized via matrix assisted laser desorption ionization time-of-flight (MALDI-ToF). Once in hand, the **TriNL**/**p2L** crystals with monomeric streptavidin guests were subsequently incubated with the biotin conjugate (biotin-Rh, 20 μM) in water (50 μL) for 48 hrs. The crystals were incubated with biotin-Rh for an extended period of time to ensure proper diffusion of the molecule within the solid crystal. Visualization via confocal microscopy revealed colocalization (yellow) of both the protein and biotin (Figure 4.14B). The ends of the crystals appeared to contain more biotin-Rh when compared to the center. This may be a result of biotin-Rh diffusing into the crystal through the P3 face. The open-faced hexagonal packing of the P3 face is likely retained when protein guests are inside the crystal (*vide infra*). As such, the cavity of the hexagonal packing may be the point of entry for biotin rather than through the sides of the crystal. In this way, a concentration gradient of biotin-Rh would result with higher concentrations at the ends of the crystal. Importantly, when the crystals were incubated with biotin-Rh in the absence of monomeric streptavidin, no fluorescence was observed (Figure 4.14C). This confirms that biotin incorporation is indeed from

a streptavidin-biotin interaction rather than other interactions with the coiled-coil. This biotin-streptavidin binding indicates that the protein remains active while it is a guest inside the crystal.

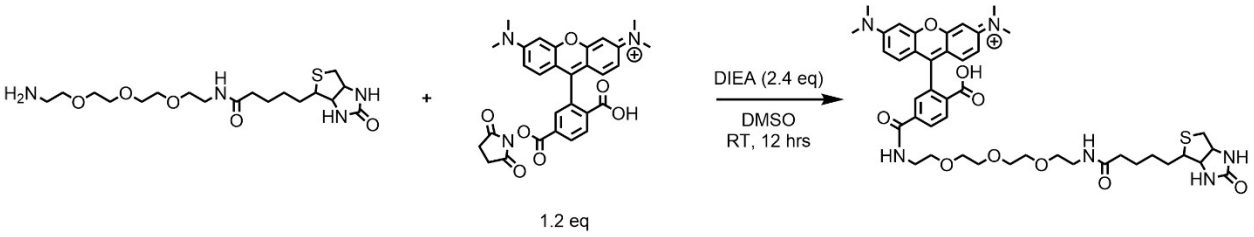

Scheme 4.1. Reaction to form Biotin-Rh.

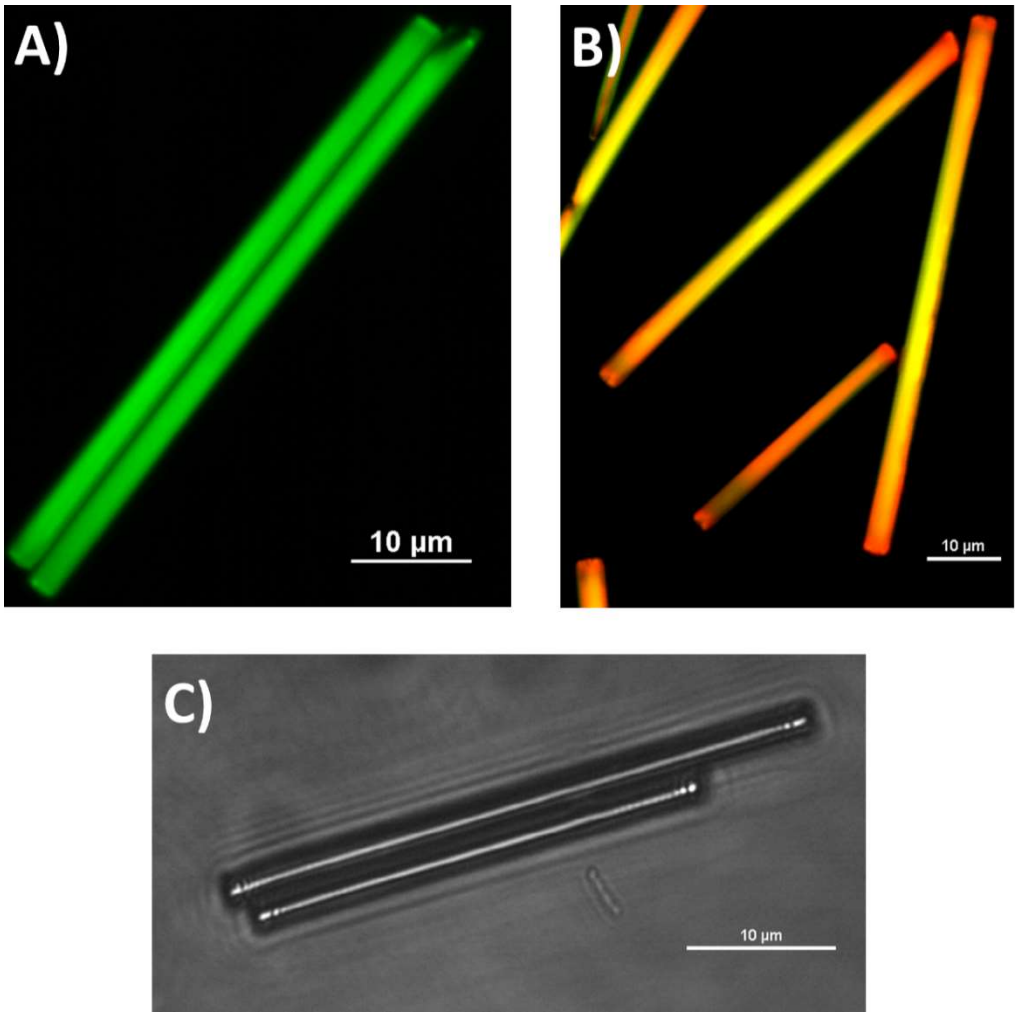

Figure 4.14. (A) Confocal microscopy of 2:1 **TriNL**:**p2L** crystals (1 mM) with monomeric streptavidin incorporation (7 µM). (B) Peptide crystals with streptavidin after biotin-Rh (20 µM) incubation. (C) Peptide crystals incubated with biotin-Rh in the absence of monomeric streptavidin.

4.2.6 Analysis of Crystals with Protein Guests by X-ray Scattering

The packing of the **TriNL**/**p2L** crystals with a protein guest was subsequently investigated. While the **TriNL**/**p2L** crystals form in an open-faced hexagonal pattern (**Figure 4.3**), it is possible a protein guest may disrupt the packing. With this in mind, the SWAXS of crystals with and without EGFP was investigated. The SWAXS diffraction pattern of **TriNL**:**p2L** crystals with EGFP incorporated led to a nearly identical diffraction pattern when compared to crystals without protein (**Figure 4.15**). The similar spectrum of the crystal with protein guests suggests that the open-faced hexagonal packing was maintained, and the protein did not disrupt the organization of the crystal.

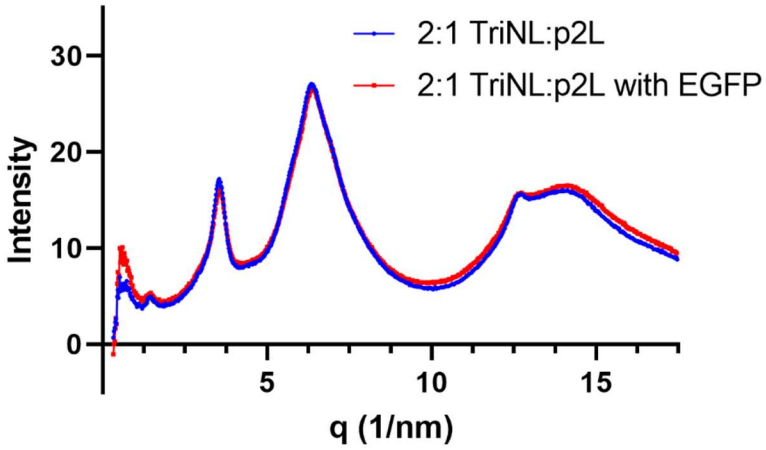

Figure 4.15. SWAXS of 2:1 **TriNL**:**p2L** crystals with and without EGFP.

4.3 Conclusion

In summary, using heterocoiled-coils formed from a 2:1 ratio of **TriNL** and **p2L** provided a promising alternative crystal system to the zinc-mediated **p2L** crystals. The crystal structure of the peptide assembly revealed an open-faced hexagonal packing similar to pure **p2L** crystals. These heterocoiled-coils formed crystals likely through an ionic-based assembly, allowing for proteins to be incorporated without a His-tag and with a wide range of protein surface charges (-30 to +36). These crystals incorporated both small (14.3 kDa) and large proteins (66 kDa). EGFP inside the crystal also displayed significant thermal stability. Furthermore, monomeric streptavidin retained activity while encapsulated and bound biotin within the crystal. Future studies include protein

structure elucidation using this crystal system and quantifying enzyme activity within the crystals. These heterocoiled-coils provide a facile and rapid approach for co-crystallization of peptide and protein with applications for biologic storage and protein structure elucidation.

4.4 Materials and Methods

4.4.1 Materials

All amino acids and reagents for peptide synthesis were purchased from ChemPep or Chem-Impex. All solvents, the mixed isomer 5/6-carboxy-tetramethyl-fluorescein succinimidyl ester (Fl-NHS), lysozyme, BL21 (DE3) competent cells (*E. coli*), and Ni-NTA resin were purchased from Fisher Scientific. N-Succinimidyl 7-(diethylamino)coumarin-3-carboxylate (Cou-NHS) was purchased from TCI Chemicals. DIEA was purchased from Alfa Aesar. Triisopropylsilane (TIPS), SIGMAFAST Protease Inhibitor Cocktail tablets, hemoglobin, and bovine serum albumin (BSA) were purchased from Sigma-Aldrich. SAvPhire Monomeric Streptavidin Alpha Fluor 488 was purchased from Millipore Sigma. NovaPEG Rink Amide resin LL was purchased from Novabiochem. Isopropyl β-D-1-thiogalactopyranoside (IPTG) and arabinose were purchased from GoldBio. Biotin-PEG3-amine was purchased from BroadPharm.

4.4.2 Protein Expression

The plasmid for EGFP [EGFP-pBAD, Addgene plasmid #54762; http://n2t.net/addgene:54762; RRID:Addgene_54762] was obtained as a gift from Michael Davidson. The plasmids for Neg30GFP [pET-6xHis-(-30)GFP, Addgene plasmid #62936; http://n2t.net/addgene:62936; RRID:Addgene_62936], Pos9GFP [pET-6xHis-(pos9)GFP, Addgene plasmid #89247; http://n2t.net/addgene:89247; RRID:Addgene_89247), and Pos36GFP [pET-6xHis-(pos36)GFP, Addgene plasmid #62937; http://n2t.net/addgene:62937; RRID:Addgene_62937) were obtained as a gift from David Liu.[42]

All protein expression was conducted using sterile technique. Plasmid (10 ng) was first added to BL21 (DE3) competent *E. coli* cells and incubated at 0 °C for 30 min. The cells were heat shocked at 42 °C for 40 seconds and placed back on ice for 5 min. Each aliquot of bacteria was resuspended in 250 μL of super optimal catabolite (SOC) media and incubated at 37 °C for 1 hr. An aliquot of the cells (20 μL) was spread evenly on a pre-warmed LB/Ampicillin agar plate. The

plate was incubated at 37 °C overnight. A single colony was taken with a pipette tip and added to 5 mL of LB media with ampicillin (100 μg/mL). The bacteria were incubated at 37 °C and shaken at 220 rpm overnight (16 hrs). The media was transferred to 500 mL of LB media with ampicillin (100 μg/mL). The cells were incubated at 37 °C and shaken at 220 rpm until an OD_{600} of 0.6 (~4 hrs). The bacteria were subsequently induced with either arabinose (His-EGFP, 10 mM) or IPTG (His-Pos9GFP, His-Pos36GFP, His-Neg30GFP, 0.6 mM) and shaken at 175 rpm at room temperature overnight. The culture was pelleted at 5000 rpm for 10 min and the supernatant was discarded. The cells were stored at -80 °C.

To sterile water (74.9 mL), Tris-HCl (1 M, pH 7.4, 5 mL, final concentration: 50 mM), NaCl (1 M, 20 mL, final concentration: 200 mM), $MgCl_2$ (1 M, 100 μL, final concentration: 1 mM), and a SIGMAFAST Protease Inhibitor Cocktail tablet were added to create a 100 mL solution of lysis buffer. A wash buffer was prepared using lysis buffer (19.84 mL) and imidazole (5 M, 160 μL, final concentration: 40 mM). A KCl wash buffer was prepared using lysis buffer (19.84 mL), imidazole (5 M, 160 μL, final concentration: 40 mM), and KCl (735.5 mg, 9.8 mmol, final concentration: 500 mM). An elution buffer was prepared using lysis buffer (14.1 mL) and imidazole (5 M, 900 μL, final concentration: 300 mM). The cells were resuspended in lysis buffer (20 mL) and incubated on ice for 15 min. The bacteria were frozen in a dry ice and isopropanol bath (20 min). The solution was thawed at room temperature (20 min). This freeze-thaw cycle was repeated once more. The cells were subsequently sonicated (50 bursts, 0.5 sec each) on ice. The solution was centrifuged at 8500 RPM for 20 min. The supernatant was added to Ni-NTA resin (4 mL) and mixed by gently rocking at 4 °C for 20 min. The resin was centrifuged at 1200 RPM for 2 min and the supernatant was discarded. Wash buffer (10 mL) was added to the resin and the solution was mixed by gently rocking at 4 °C for 10 min. The resin was centrifuged at 1200 RPM for 2 min and the supernatant was discarded. This process was repeated with the remaining wash buffer (10 mL) and KCl wash buffer (10 mL). After the supernatant was removed, the remaining KCl wash buffer (10 mL) was added to the resin and the resin was transferred to a column. After the solution drained, the elution buffer (15 mL) was added. The flow through was collected and the protein was concentrated using a 10 kDa MWCO at 4500 RPM for 15 min. Proteins were characterized via SDS-PAGE gels.

4.4.3 Protein Fluorescent Labeling

Lysozyme (5 mg, 0.35 μmol) was dissolved in bicarbonate buffer (50 mM, pH 8.5, 1 mL). Cou-NHS (10 mg, 0.03 mmol) was dissolved in anhydrous dimethylsulfoxide (DMSO, 1 mL) to make a 30 mM solution. An aliquot of the Cou-NHS solution (2 eq, 0.7 μmol, 24 μL) was added to the protein solution and was incubated at room temperature for 1 hr covered in foil. The solution was transferred to a 10 kDa MWCO and centrifuged at 15,000 g for 15 min. The flow through was discarded and the protein was diluted with 1x PBS (1 mL). This process was repeated two more times and the protein was stored in 1x PBS (1 mL) at 4 °C.

Hemoglobin (5 mg, 0.08 μmol) was dissolved in bicarbonate buffer (1 mL, 50 mM, pH 8.5). Fl-NHS (9.4 mg, 0.02 mmol) was dissolved in anhydrous DMSO (1 mL) to make a 20 mM solution. An aliquot of the Fl-NHS solution (2 eq, 0.16 μmol, 8 μL) was added to the protein solution and was incubated at room temperature for 1 hr covered in foil. The solution was transferred to a 10 kDa MWCO and centrifuged at 15,000 g for 15 min. The flow through was discarded and the protein was diluted with 1x PBS (1 mL). This process was repeated two more times and the protein was stored in 1x PBS (1 mL) at 4 °C.

BSA (5 mg, 0.07 μmol) was dissolved in bicarbonate buffer (1 mL, 50 mM, pH 8.5). Fl-NHS (9.4 mg, 0.02 mmol) was dissolved in anhydrous DMSO (1 mL) to make a 20 mM solution. An aliquot of the Fl-NHS solution (2 eq, 0.14 μmol, 7 μL) was added to the protein solution and was incubated at room temperature for 1 hr covered in foil. The solution was transferred to a 10 kDa MWCO and centrifuged at 15,000 g for 15 min. The flow through was discarded and the protein was washed with 1x PBS (1 mL) to remove excess Fl-NHS. The flow through was discarded and the protein was diluted with 1x PBS (1 mL). This process was repeated two more times and the protein was stored in 1x PBS (1 mL) at 4 °C.

4.4.4 Crystal Formation and Protein Inclusion

TriNL (10 mM, 3.4 μL) and **p2L** (10 mM, 1.7 μL) were added to water (9.9 μL) and annealed using a Techne 3PRIMEBASE Thermal Cycler (90 °C for 30 min, 4 °C for > 18 hrs). Annealed peptide solutions were added to 2-(N-morpholino)ethanesulfonic acid buffer (200 mM MES, pH 6.0, 25 μL), protein when applicable (0 μL, 0.5 μL, 1.0 μL, or 1.4 μL) and water (8.6-10 μL) to create a 50 μL solution with a final buffer concentration of 100 mM, peptide concentration

of 1 mM, and protein concentration of 0 μM, 7 μM, 14 μM, or 20 μM, respectively. Following a 1 hr incubation at room temperature, the assemblies were centrifuged at 10,000 g for 3 min. The supernatant was removed and replaced with water (50 μL). This process was repeated two more times. The pelleted crystals were resuspended and stored in 50 μL water.

4.4.5 Scanning Electron Microscopy

Aliquots of the assemblies described in Section 4.4.4 (3 μL) were placed on a glass coverslip attached to a metal stub via copper tape. The samples were either air dried for 1 hr or lyophilized for 1 hr and platinum coated for 60 seconds using a Cressington sputter coater. Samples were imaged using an FEI Teneo Volumescope field emission scanning electron microscope using Everhart-Thornley detector (ETD) for magnifications < 10,000 or the high-resolution through the lens detector (TLD) for magnifications ≥ 10,000. Samples were imaged at an accelerating voltage of 5 kV and a working distance of 2-4 mm with a 30-μm aperture.

4.4.6 X-ray Diffraction

SWAXS data was collected using an Anton-Paar SAXSpoint 2.0 system with a Cu X-ray source. The samples were prepared by dropping aliquots of an assembly described in Section 4.4.4 (1 μL) onto cellophane tape and allowing the sample to air dry for 1 hr. This process was repeated 50 times until the entire assembly was dropped on the tape. Diffraction patterns were acquired by averaging 6 x 5-minute scans using a 2D EIGER R series hybrid photon counting detector and a high-resolutions WAXS module. Measurements were obtained at a distance of 113 nm between the sample and detector.

Diffraction data for the crystals were collected using the Advanced Photon Source at Argonne National Laboratory at a 1.5 Å resolution at a wavelength of 1.0332 Å. The high resolution data set underwent a round of molecular replacement in MolRep (in the CCP4 suite), using the previously solved **p2L** crystal structure (PDB 5kkv).[28] The solution was subsequently fit into the observed density in COOT and refined once using Phenix Refine.[43,44]

4.4.7 Confocal Microscopy

Aliquots of the assemblies described in Section 4.4.4 (3 μL) were placed in an 18-well confocal chamber and allowed to air dry for 1 hr. The samples were imaged using a 60X objective on a Nikon A1R MP confocal microscope. Fluorescence was measured with excitation wavelengths of 405 nm (blue), 488 nm (green), and 561 nm (red).

4.4.8 Protein Quantification

A sample of EGFP crystals described in Section 4.4.4 was centrifuged at 10,000 g for 3 min. The supernatant was removed, and the material was resuspended in 1x PBS (100 μL) for 5 min to dissolve the assembly. EGFP incorporation (nmol) was quantified by measuring the fluorescence of the solution and comparing it to a standard curve of EGFP fluorescence (415 nm excitation and 535 nm emission). Using the quantified EGFP (nmol), the peak area of EGFP on UPLC at 214 nm was calculated using an EGFP absorbance standard curve (214 nm). The extent of peptide assembly was quantified by integrating the peak areas of UPLC traces at 214 nm (10 μL injections) and subtracting the EGFP peak area. The difference was compared to a standard curve of the peptides' absorbance (214 nm). Fluorescent measurements were taken in a black 96-well plate using a Tecan infinite 200Pro plate reader. UPLC conditions: C18 column, 20-70% gradient of acetonitrile with H_2O with 0.1% TFA over 10 minutes.

A sample of either hemoglobin or HRP crystals described in Section 4.4.4 were centrifuged at 10,000 g for 3 min. The supernatant was removed, and the material was resuspended in 1x PBS (100 μL) for 5 min to dissolve the assembly. Protein incorporation were quantified by integrating the peak areas of UPLC traces at 405 nm with 10 μL injections and compared to a standard curve of hemoglobin or HRP absorbance (405 nm). The extent of peptide assembly was quantified by integrating the peak areas of UPLC traces at 214 nm with 10 μL injections and compared to a standard curve of the peptides' absorbance (214 nm). UPLC conditions: C18 column, 20-70% gradient of acetonitrile with H_2O with 0.1% TFA over 10 minutes.

4.4.9 Protein Stability Study

A sample of **TriNL**/**p2L** crystals with EGFP guests described in Section 4.4.4 was spotted on an 18-well confocal chamber and air dried for 1 hr. The crystals were imaged using confocal microscopy with a 488 nm excitation laser. The 18-well confocal chamber was subsequently transferred to a 100 °C oven and heated for 1 hr. The confocal chamber was removed from the oven and the same crystal sample was imaged with same laser excitation and intensity.

4.4.10 Biotin Labeling

Biotin-PEG3-amine (31.5 mg, 0.08 mmol) and NHS-rhodamine (1.2 eq, 48 mg, 0.1 mmol) were added to DIEA (2.4 eq, 31.4 μL, 0.19 mmol) and anhydrous DMSO (7 mL) and stirred at room temperature for 12 hrs. The reaction was purified to homogeneity via HPLC and characterized via MALDI-ToF. HPLC conditions: C18 column, 15-40% gradient of acetonitrile with H_2O with 0.1% TFA over 60 minutes.

4.4.11 Streptavidin-Biotin Binding Experiments

A sample of **TriNL**:**p2L** crystals with monomeric-streptavidin guests described in Section 4.4.4 was centrifuged at 10,000 g for 3 min. The supernatant was removed and the material was resuspended in a Biotin-Rh solution (20 μM, 50 μL) for 48 hrs at room temperature. The crystals were centrifuged at 10,000 g for 3 min. The supernatant was removed and replaced with 50 μL of water. This process was repeated two more times and after the final wash, the crystals were resuspended in 50 μL of water. An aliquot of the crystals (3 μL) was spotted on an 18-well confocal chamber and air dried for 1 hr. The samples were imaged using a 60X objective on a Nikon A1R MP confocal microscope. Fluorescence was measured with excitation wavelengths of 488 nm (green) and 561 nm (red).

4.5 References

(1) Sheldon, R. A.; Pereira, P. C. Biocatalysis Engineering: The Big Picture. *Chem. Soc. Rev.* **2017**, *46* (10), 2678–2691. https://doi.org/10.1039/c6cs00854b.

(2) Bell, E. L.; Finnigan, W.; France, S. P.; Green, A. P.; Hayes, M. A.; Hepworth, L. J.; Lovelock, S. L.; Niikura, H.; Osuna, S.; Romero, E.; Ryan, K. S.; Turner, N. J.; Flitsch, S. L. Biocatalysis. *Nat. Rev. Methods Prim.* **2021**, *1* (1), 1–21. https://doi.org/10.1038/s43586-021-00044-z.

(3) Peng, X.; Wang, J.; Peng, W.; Wu, F. X.; Pan, Y. Protein-Protein Interactions: Detection, Reliability Assessment and Applications. *Brief. Bioinform.* **2017**, *18* (5), 798–819. https://doi.org/10.1093/bib/bbw066.

(4) Scheibel, T. Protein Fibers as Performance Proteins: New Technologies and Applications. *Curr. Opin. Biotechnol.* **2005**, *16* (4), 427–433. https://doi.org/10.1016/j.copbio.2005.05.005.

(5) Gupta, P.; Nayak, K. K. Characteristics of Protein-Based Biopolymer and Its Application. *Polym. Eng. Sci.* **2015**, *55* (3), 485–498. https://doi.org/10.1002/pen.23928.

(6) Tang, Y.; Xue, L.; Yu, Q.; Chen, D.; Cheng, Z.; Wang, W.; Shao, J.; Dong, X. Smart Aza-BODIPY Photosensitizer for Tumor Microenvironment-Enhanced Cancer Phototherapy. *ACS Appl. Bio Mater.* **2019**, *2* (12), 5888–5897. https://doi.org/10.1021/acsabm.9b00836.

(7) Whisstock, J. C.; Lesk, A. M. Prediction of Protein Function from Protein Sequence and Structure. *Q. Rev. Biophys.* **2003**, *36* (3), 307–340. https://doi.org/10.1017/S0033583503003901.

(8) Dill, K. A.; Maccallum, J. L. The Protein-Folding Problem, 50 Years On. *Science.* **2012**, *338* (NOVEMBER), 1042–1047. https://doi.org/10.1126/science.1219021.

(9) Gerstberger, S.; Hafner, M.; Tuschl, T. A Census of Human RNA-Binding Proteins. *Nat. Rev. Genet.* **2014**, *15* (12), 829–845. https://doi.org/10.1038/nrg3813.

(10) Li, F. Structure, Function, and Evolution of Coronavirus Spike Proteins. *Annu. Rev. Virol.* **2016**, *3*, 237–261. https://doi.org/10.1146/annurev-virology-110615-042301.

(11) Dobson, C. M. Protein Folding and Misfolding. *Nature* **2003**, *426* (December), 1–4. https://doi.org/10.1038/nature02261.

(12) Fields, G. B.; Alonso, O. V; Stigter, D.; Ken, A. Theory for the Aggregation of Proteins and Copolymers. *J. Phys. Chem.* **1992**, *96*, 3974–3981. https://doi.org/https://doi.org/10.1021/j100189a013.

(13) Thompson, D. H.; Zhou, M.; Grey, J.; Kim, H. K. Design, Synthesis, and Performance of NTA-Modified Lipids as Templates for Histidine-Tagged Protein Crystallization. *Chem. Lett.* **2007**, *36* (8), 956–975. https://doi.org/10.1246/cl.2007.956.

(14) Wasserberg, D.; Cabanas-Danés, J.; Prangsma, J.; O'Mahony, S.; Cazade, P. A.; Tromp, E.; Blum, C.; Thompson, D.; Huskens, J.; Subramaniam, V.; Jonkheijm, P. Controlling Protein Surface Orientation by Strategic Placement of Oligo-Histidine Tags. *ACS Nano* **2017**, *11* (9), 9068–9083. https://doi.org/10.1021/acsnano.7b03717.

(15) Zhou, G.; Ren, Z.; Wang, L.; Sun, B.; Duan, S.; Song, Q. Artificial and Wearable Albumen Protein Memristor Arrays with Integrated Memory Logic Gate Functionality. *Mater. Horizons* **2019**, *6* (9), 1877–1882. https://doi.org/10.1039/c9mh00468h.

(16) Chmielewski, J.; Lewis, J. J.; Lovell, S.; Zutshi, R.; Savickas, P.; Mitchell, C. A.; Subramony, J. A.; Kahr, B. Single-Crystal Matrix Isolation of Biopolymers. *J. Am. Chem. Soc.* **1997**, *119* (43), 10565–10566. https://doi.org/10.1021/ja971370z.

(17) Kurimoto, M.; Subramony, P.; Gurney, R. W.; Lovell, S.; Chmielewski, J.; Kahr, B. Kinetic Stabilization of Biopolymers in Single-Crystal Hosts: Green Fluorescent Protein in α-Lactose Monohydrate. *J. Am. Chem. Soc.* **1999**, *121* (29), 6952–6953. https://doi.org/10.1021/ja991069d.

(18) Li, Z.; Liu, L.; Zheng, M.; Zhao, J.; Seeman, N. C.; Mao, C. Making Engineered 3D DNA Crystals Robust. *J. Am. Chem. Soc.* **2019**, *141* (40), 15850–15855. https://doi.org/10.1021/jacs.9b06613.

(19) Mao, D.; Li, Q.; Li, Q.; Wang, P.; Mao, C. A Conformational Study of the 10-23 DNAzyme via Programmed DNA Self-Assembly. *Chem. Commun.* **2022**, *58* (42), 6188–6191. https://doi.org/10.1039/d2cc01144a.

(20) Wang, H. C.; Kurimoto, M.; Kahr, B.; Chmielewski, J. α-Lactose Monohydrate Single Crystals as Hosts for Matrix Isolation of Guest Biopolymers. *Bioorganic Med. Chem.* **2001**, *9* (9), 2279–2283. https://doi.org/10.1016/s0968-0896(01)00129-8.

(21) Geng, C.; Paukstelis, P. J. DNA Crystals as Vehicles for Biocatalysis. *J. Am. Chem. Soc.* **2014**, *136* (22), 7817–7820. https://doi.org/10.1021/ja502356m.

(22) Abe, S.; Ijiri, H.; Negishi, H.; Yamanaka, H.; Sasaki, K.; Hirata, K.; Mori, H.; Ueno, T. Design of Enzyme-Encapsulated Protein Containers by in Vivo Crystal Engineering. *Advanced Materials*. 2015, pp 7951–7956. https://doi.org/10.1002/adma.201503827.

(23) Shtukenberg, A. G.; Tripathi, K.; Ketchum, R.; Jeon, J. J.; Sanda, A.; Kahr, B. Incorporation of Macromolecules into α-Lactose Monohydrate Crystals. *Cryst. Growth Des.* **2016**, *16* (8), 4589–4598. https://doi.org/10.1021/acs.cgd.6b00686.

(24) Huber, T. R.; Hartje, L. F.; McPherson, E. C.; Kowalski, A. E.; Snow, C. D. Programmed Assembly of Host–Guest Protein Crystals. *Small* **2017**, *13* (7), 1–6. https://doi.org/10.1002/smll.201602703.

(25) Kowalski, A. E.; Johnson, L. B.; Dierl, H. K.; Park, S.; Huber, T. R.; Snow, C. D. Porous Protein Crystals as Scaffolds for Enzyme Immobilization. *Biomater. Sci.* **2019**, *7*, 1898–1904. https://doi.org/10.1039/c8bm01378k.

(26) Ernst, P.; Plückthun, A.; Mittl, P. R. E. Structural Analysis of Biological Targets by Host:Guest Crystal Lattice Engineering. *Sci. Rep.* **2019**, *9* (1), 1–11. https://doi.org/10.1038/s41598-019-51017-y.

(27) Hashimoto, T.; Ye, Y.; Ui, M.; Ogawa, T.; Matsui, T.; Tanaka, Y. Protein Encapsulation in the Hollow Space of Hemocyanin Crystals Containing a Covalently Conjugated Ligand. *Biochem. Biophys. Res. Commun.* **2019**, *514* (1), 31–36. https://doi.org/10.1016/j.bbrc.2019.04.062.

(28) Nepal, M.; Sheedlo, M. J.; Das, C.; Chmielewski, J. Accessing Three-Dimensional Crystals with Incorporated Guests through Metal-Directed Coiled-Coil Peptide Assembly. *J. Am. Chem. Soc.* **2016**, *138* (34), 11051–11057. https://doi.org/10.1021/jacs.6b06708.

(29) Curtis, R. W.; Scrudders, K. L.; Ulcickas, J. R. W.; Simpson, G. J.; Low-nam, S. T.; Chmielewski, J. Supramolecular Assembly of His-Tagged Fluorescent Protein Guests within Coiled-Coil Peptide Crystal Hosts: Three-Dimensional Ordering and Protein Thermal Stability. *ACS Biomater. Sci. Eng.* **2022**, *8*, 1860–1866. https://doi.org/10.1021/acsbiomaterials.2c00155.

(30) Jorgensen, M. D.; Chmielewski, J. Co-Assembled Coiled-Coil Peptide Nanotubes with Enhanced Stability and Metal-Dependent Cargo Loading. *ACS Omega* **2022**, *7*, 20945–20951. https://doi.org/10.1021/acsomega.2c01669.

(31) Holtzer, M. E.; Breiner, T.; Holtzer, A. Hetero-α-Helical, Two-Chain, Coiled Coils: Aβ Hybrid Tropomysin. *Biopolymers* **1984**, *23*, 1811–1833. https://doi.org/10.1002/bip.360231003.

(32) Lanci, C. J.; MacDermaid, C. M.; Kang, S. G.; Acharya, R.; North, B.; Yang, X.; Qiu, X. J.; DeGrado, W. F.; Saven, J. G. Computational Design of a Protein Crystal. *Proc. Natl. Acad. Sci. U. S. A.* **2012**, *109* (19), 7304–7309. https://doi.org/10.1073/pnas.1112595109.

(33) Nambiar, M.; Wang, L. S.; Rotello, V.; Chmielewski, J. Reversible Hierarchical Assembly of Trimeric Coiled-Coil Peptides into Banded Nano- and Microstructures. *J. Am. Chem. Soc.* **2018**, *140* (40), 13028–13033. https://doi.org/10.1021/jacs.8b08163.

(34) Nambiar, M.; Nepal, M.; Chmielewski, J. Self-Assembling Coiled-Coil Peptide Nanotubes with Biomolecular Cargo Encapsulation. *ACS Biomater. Sci. Eng.* **2019**, *5* (10), 5082–5087. https://doi.org/10.1021/acsbiomaterials.9b01304.

(35) Curtis, R. Hierarchical Assembly of Coiled-Coil Peptides: Protein Inclusion and Self-Replication, 2022.

(36) Lawrence, M. S.; Phillips, K. J.; Liu, D. R. Supercharging Proteins Can Impart Unusual Resilience. *J. Am. Chem. Soc.* **2007**, *129* (33), 10110–10112. https://doi.org/10.1021/ja071641y.

(37) Simon, A. J.; Zhou, Y.; Ramasubramani, V.; Glaser, J.; Pothukuchy, A.; Gollihar, J.; Gerberich, J. C.; Leggere, J. C.; Morrow, B. R.; Jung, C.; Glotzer, S. C.; Taylor, D. W.; Ellington, A. D. Supercharging Enables Organized Assembly of Synthetic Biomolecules. *Nat. Chem.* **2019**, *11* (3), 204–212. https://doi.org/10.1038/s41557-018-0196-3.

(38) Dautel, D. R.; Champion, J. A. Protein Vesicles Self-Assembled from Functional Globular Proteins with Different Charge and Size. *Biomacromolecules* **2021**, *22* (1), 116–125. https://doi.org/10.1021/acs.biomac.0c00671.

(39) Chalfie, M. Green Fluorescent Protein. *Photochem. Photobiol.* **1995**, *62* (4), 651–656. https://doi.org/10.1111/j.1751-1097.1995.tb08712.x.

(40) Dundas, C. M.; Demonte, D.; Park, S. Streptavidin-Biotin Technology: Improvements and Innovations in Chemical and Biological Applications. *Appl. Microbiol. Biotechnol.* **2013**, *97* (21), 9343–9353. https://doi.org/10.1007/s00253-013-5232-z.

(41) Lowe, B. M.; Sun, K.; Zeimpekis, I.; Skylaris, C. K.; Green, N. G. Field-Effect Sensors-from PH Sensing to Biosensing: Sensitivity Enhancement Using Streptavidin-Biotin as a Model System. *Analyst* **2017**, *142* (22), 4173–4200. https://doi.org/10.1039/c7an00455a.

(42) Zuris, J. A.; Thompson, D. B.; Shu, Y.; Guilinger, J. P.; Bessen, J. L.; Hu, J. H.; Maeder, M. L.; Joung, J. K.; Chen, Z. Y.; Liu, D. R. Cationic Lipid-Mediated Delivery of Proteins Enables Efficient Protein-Based Genome Editing in Vitro and in Vivo. *Nat. Biotechnol.* **2015**, *33* (1), 73–80. https://doi.org/10.1038/nbt.3081.

(43) Murshudov, G. N.; Vagin, A. A.; Dodson, E. J. Refinement of Macromolecular Structures by the Maximum-Likelihood Method. *Acta Crystallogr. Sect. D Biol. Crystallogr.* **1997**, *53* (3), 240–255. https://doi.org/10.1107/S0907444996012255.

(44) Emsley, P.; Lohkamp, B.; Scott, W. G.; Cowtan, K. Features and Development of Coot. *Acta Crystallogr. Sect. D Biol. Crystallogr.* **2010**, *66* (4), 486–501. https://doi.org/10.1107/S0907444910007493.

CHAPTER 5. DEVELOPMENT OF A SELF-REPLICATING COILED-COIL PEPTIDE MATERIAL

5.1 Introduction

Understanding the molecular origins of life has been a long-standing area of research interest, with chemistry being at the forefront in this field.[1] Two major requirements for the existence of pre-biotic systems are the ability to self-assemble and self-replicate.[2] Systems of self-replicating biopolymers were first pioneered by von Kiedrowski using nucleotides.[3] The Ghadiri and Chmielewski groups subsequently discovered that coiled-coil peptides could form the basis for self-replicating systems.[4,5,14,6–13] In these systems, a single α-helix of a coiled-coil acts as a template for the ligation of two complementary peptide fragments. The two peptide fragments ligate when in close proximity and form a new α-helical peptide template.

More recently, self-replicating peptides have been designed to undergo higher order assembly. For instance, Otto and co-workers developed a short β-sheet forming peptide with an N-terminal 2,4-dithiobenzene group. Upon oxidation, disulfide formation promoted the emergence of a small combinatorial library of macrocycles. Upon mechanical agitation, the 6-mer and 7-mer macrocycles began to assemble into fibers.[15] This fiber formation subsequently promotes the further formation of the 6-mer or 7-mer macrocycle from this library preferentially over any smaller macrocycles.[15–17] This self-replication process which was promoted by self-assembly of di-sulfide macrocycles has also been studied with peptide sequences containing appended nucleobases,[18] unnatural amino acids,[19] or moieties which promote foldamer formation (**Figure 5.1**).[20,21] Additionally, longer β-sheet and fibril-forming peptide sequences have been used as templates to bring electrophilic and nucleophilic peptide fragments into close proximity via hydrophobic interactions.[22–24] The peptides subsequently undergo native chemical ligation to form the full-length template peptide, forming the basis of a self-replicating system.

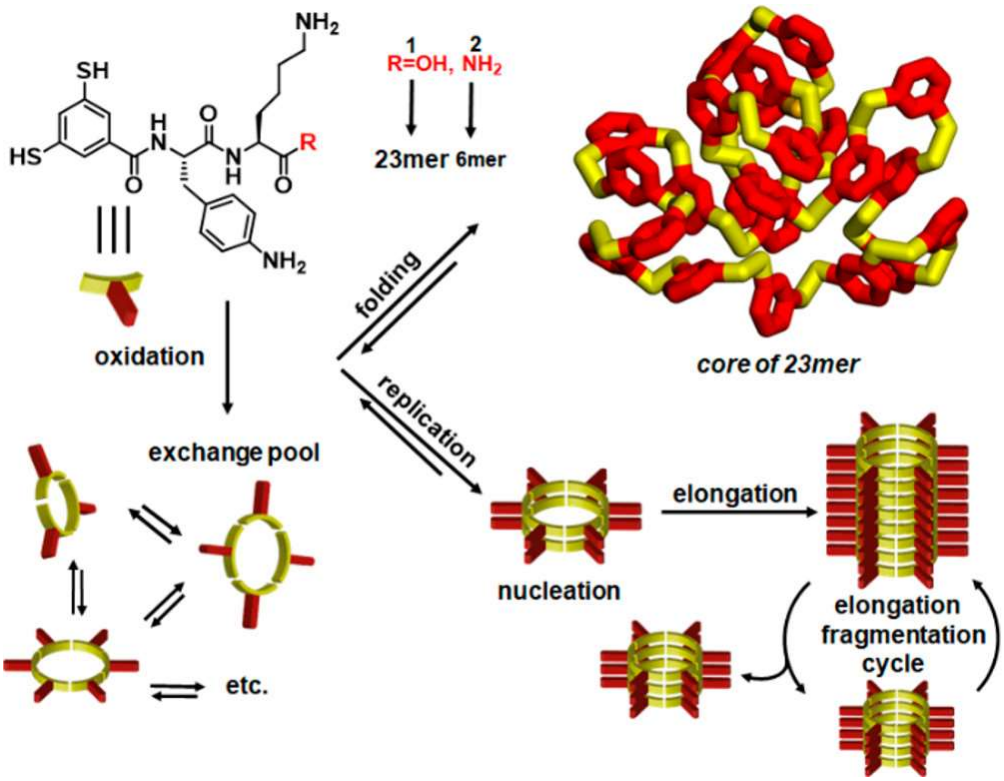

Figure 5.1. Schematic of a self-replicating peptide developed by Otto and coworkers. Oxidation of the peptide results in disulfides to produce macrocycles that subsequently undergo higher order assembly. Reprinted with permission from ref. 21. Copyright 2021, American Chemical Society.

We sought to develop a system of coiled-coil peptides with the ability to both template and self-assemble, and further study how these two phenomena interact. We hypothesized that such a system would promote templating of the fragments at low concentrations and self-assembly at higher concentrations (Figure 5.2).

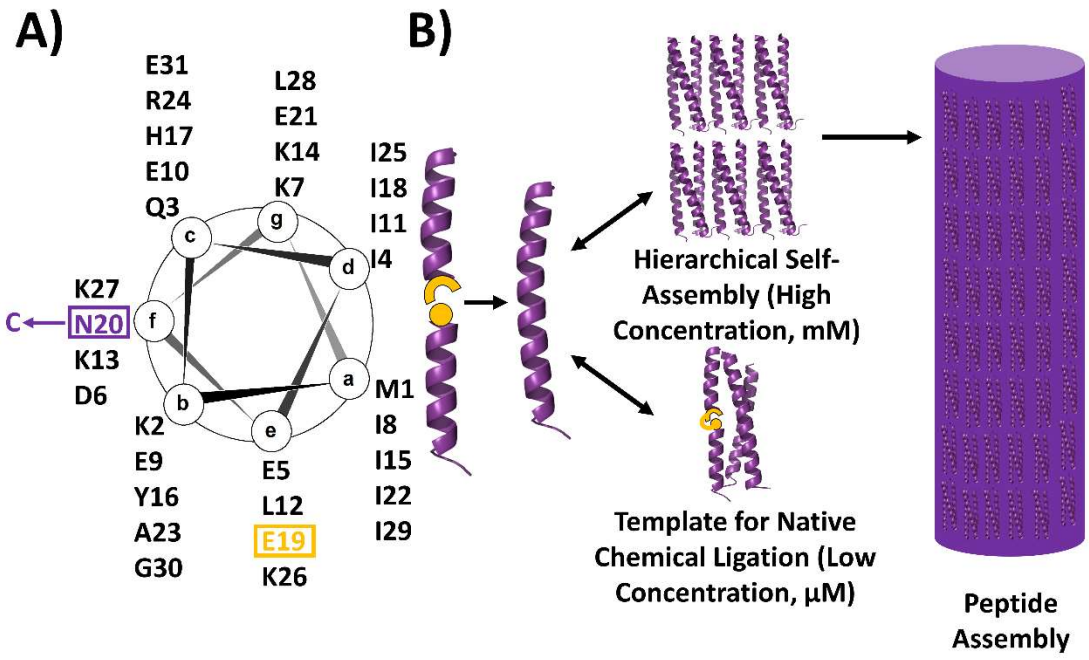

C)

	abcdefg	*abcdefg*	*abcdefg*	*abcdefg*	*abc*
TriNL	Ac-MKQIEDK	IEEILSK	IYHIENE	IARIKKL	IGE-NH_2
N20C FL	Ac-MKQIEDK	IEEILSK	IYHIECE	IARIKKL	IGE-NH_2
N20C F1			H_2N-CE	IARIKKL	IGE-NH_2
N20C F2	Ac-MKQIEDK	IEEILSK	IYHIE-SR		

Figure 5.2. Self-assembling peptide using a native chemical ligation system. (A) Helical wheel representation of **TriNL** and its N20C mutation modified for native chemical ligation. (B) Self-replicating design of the **N20C FL** peptide. Low concentrations of **N20C FL** may template the fragments for the native chemical ligation reaction. Higher concentrations may lead to a peptide assembly. (C) Sequences of the coiled-coil peptides and fragments.

5.2 Results and Discussion

5.2.1 Peptide Design

The leucine zipper of the GCN4 transcription factor was used as a model for the self-replicating material.[25,26] The trimeric variant **TriNL** has displayed the ability to rapidly self-assemble into nanotubes.[27,28] We hoped to utilize this ability to develop a system of self-replicating peptide materials whereby two peptide fragments undergo native chemical ligation and the full

length product subsequently self-assembles.[29] The relationship between the self-assembling process and self-replicating process was explored.

To facilitate the study, a mutant of **TriNL** containing a centrally located cysteine residue was required. An asparagine-to-cysteine mutation at position 20 (N20C) was designed to introduce a solvent exposed cysteine to the full-length sequence. Using standard native chemical ligation techniques, a nucleophilic peptide fragment with an N-terminal cysteine residue (**N20C F1**), and an electrophilic peptide fragment with a C-terminal thioester (**N20C F2**) were designed. The result of this native chemical ligation reaction would be a full-length peptide (**N20C FL**) with a newly formed covalent amide bond at the cysteine residue.

5.2.2 Peptide Synthesis

TriNL, **N20C FL**, and **N20C F1** were synthesized using standard solid-phase Fmoc-based chemistry on ChemMatrix Rink Amide resin with hexafluorophosphate azabenzotriazole tetramethyl uronium (HATU) as a coupling agent and diisopropylethylamine (DIEA). The N-terminus of **TriNL** and **N20C FL** were acetylated and all three peptides were cleaved from resin using a trifluoroacetic acid (TFA) cocktail. The peptides were purified to homogeneity via reverse-phase high-performance liquid chromatography (RP-HPLC), and characterized via matrix-assisted laser desorption ionization time-of-flight (MALDI-ToF) mass spectrometry.

The thioester fragment, **N20C F2**, was synthesized using a side-chain linker strategy with C-terminal allyl-protected Fmoc-Glu(Wang resin)-Oallyl resin (**Scheme 5.1**).[30,31] After standard solid-phase peptide synthesis, the C-terminus was deprotected using tetrakis(triphenylphosphine)palladium(0) (0.5 eq) with phenyl silane (40 eq). Benzyl mercaptan (S-Bzl, 24 eq) was subsequently coupled on resin with N,N'-diisopropylcarbodiimide (DIC, 30 eq), hydroxybenzotriazole (HOBt, 30 eq) and DIEA (36 eq) for 12 hrs. The peptide was cleaved from resin using a TFA cocktail, purified to homogeneity using RP-HPLC, and characterized via MALDI-ToF mass spectrometry.

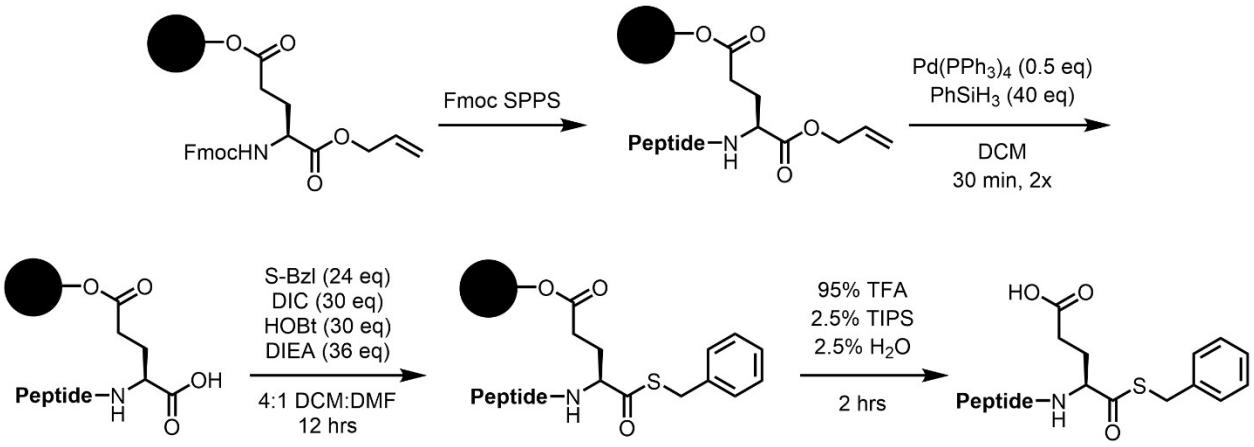

Scheme 5.1. Synthesis of benzyl thioester fragment through a side-chain linker strategy.

While the thioester fragment was produced in good yield, the peptide exhibited solubility concerns above 2 mM. Consequently, the hydrophilic thiol, 2-mercaptoethane sulfonate sodium (Mesna), was used to improve solubility of the peptide.[32–34] However, the weak nucleophilicity of Mesna prevented thioesterification on resin with the conditions in **Scheme 5.1**. Instead, a thiol exchange was conducted in solution with a large excess of Mesna (**Scheme 5.2**). The benzyl thioester (1.5 mM) was dissolved in phosphate buffer (200 mM, pH 6.5) with denaturant guanidine hydrochloride (Guan. HCl, 6 M), reducing agent tris(2-carboxyethyl)phosphine) (TCEP, 50 mM), and Mesna (200 mM). After 12 hrs, the peptide was purified to homogeneity via RP-HPLC and was soluble in a solution of at least 10 mM.

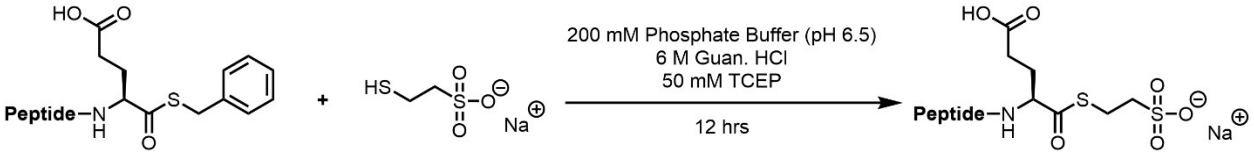

Scheme 5.2. Thioester exchange of the benzyl thioester fragment to **N20C F2**.

5.2.3 Properties of Cysteine-modified N20C FL

The N20C mutation could potentially disrupt the coiled-coil peptide folding and consequently disrupt the self-assembling properties of the peptide. To first confirm that the cysteine mutation did not alter the supersecondary structure, circular dichroism (CD) of **N20C FL** was compared to that of native **TriNL** (Figure 5.3). Both peptides (50 μM each) exhibited α-helical

character with minima at 208 nm and 222 nm and a maximum at 195 nm in phosphate buffer (20 mM, pH 7.4). The strong α-helical behavior of **TriNL** was revealed by the 222 nm signal in the spectrum, where the peptide exhibited 86% α-helicity. While the magnitude of the 222 nm signal decreased somewhat in **N20C FL**, strong α-helical behavior was still observed with a 77% α-helicity. **N20C FL** also remained a coiled-coil, as the signal at 222 nm remained larger in magnitude than the 208 nm signal.[35] These data indicate minimal disruption of the peptide folding upon installation of the N20C mutation.

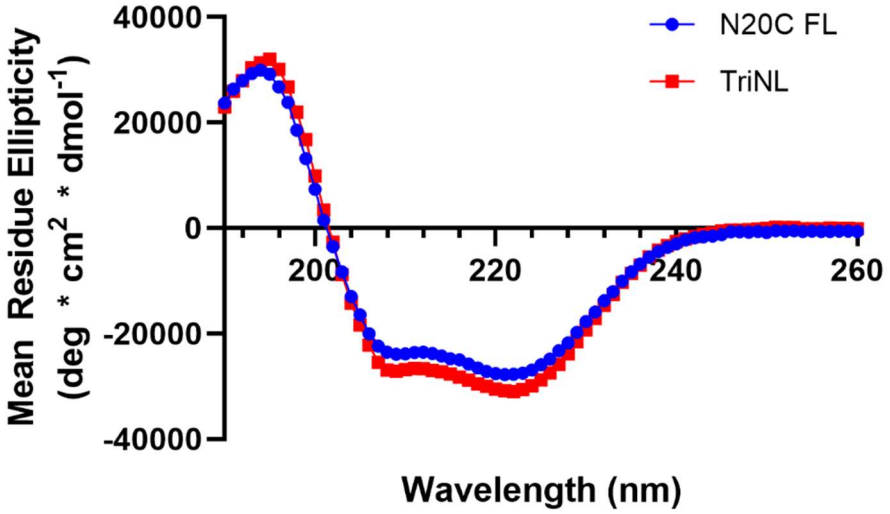

Figure 5.3. Circular dichroism spectra of mutated **N20C FL** (50 μM) compared to native **TriNL** (50 μM) in phosphate buffer (20 mM, pH 7.4).

With the knowledge that the cysteine mutation did not disrupt coiled-coil folding, we investigated the higher order assembly of the peptides. **TriNL** and **N20C FL** (1 mM) were each incubated in 3-(N-morpholino)propanesulfonic acid (MOPS) buffer (125 mM, pH 7.4) for 30 min at room temperature to induce higher order assembly. Upon visualization of the assemblies via scanning electron microscopy (SEM), similar nanorod morphology was observed for both peptides with lengths of 1-3 μm (Figure 5.4A-B). Transmission electron microscopy (TEM) revealed a banding pattern within both peptide assemblies (Figure 5.4C-F). Each band in the images corresponds to the length of a coiled-coil (~4.5 nm), and shows the organization of the coiled-coils in a head-to-tail fashion (Figure 5.4G). This pattern observed in both **TriNL** and **N20C FL** reveals similar peptide organizations within the assembly of the nanorods.

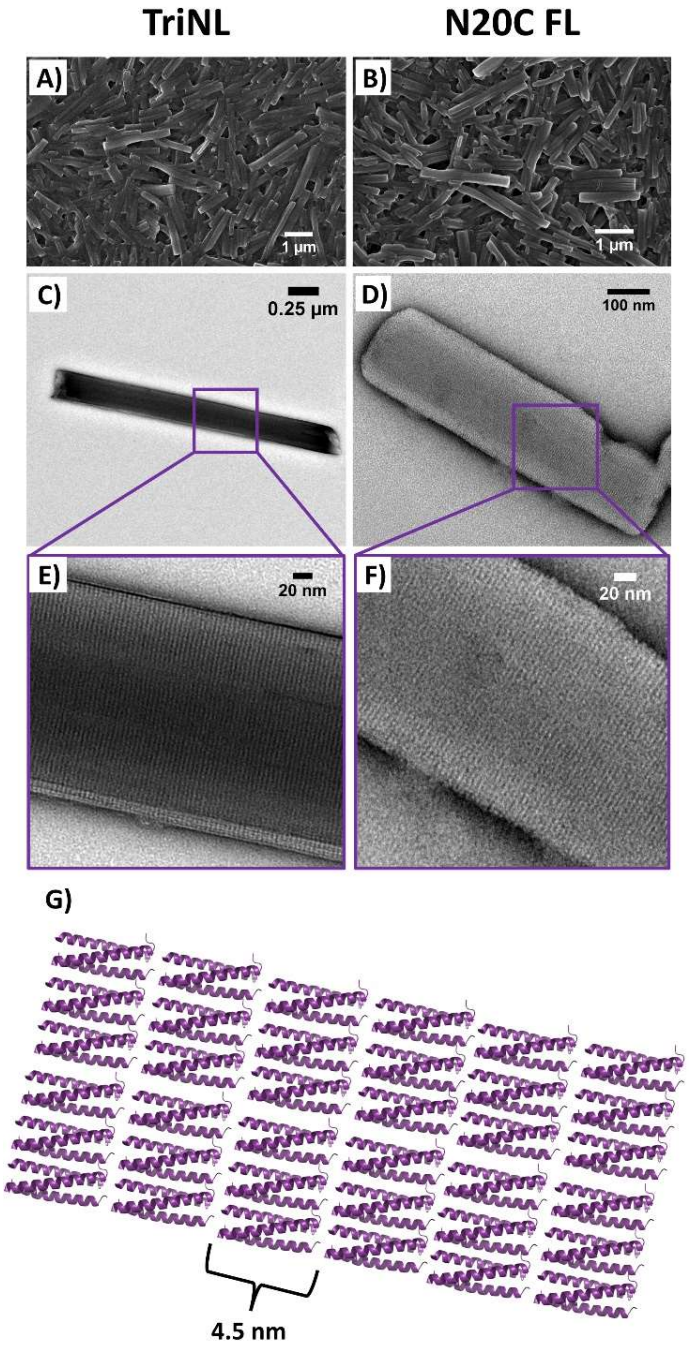

Figure 5.4. SEM visualization of (A) **TriNL** and (B) **N20C FL** nanorods in MOPS buffer (125 mM, pH 7.4). (C-F) TEM visualization of **TriNL** and **N20C FL** with an observed banding pattern (~4.5 nm bands) at higher magnifications. (G) Cartoon representation of the banding pattern observed in TEM.

5.2.4 Circular Dichroism of Peptide Fragments

To understand the templating effect of **N20C FL** on the peptide fragments, the folding of **N20C F1** and **N20C F2** was investigated via CD. Both the cysteine and thioester fragments alone (50 μM each) exhibited random coil behavior in phosphate buffer (20 mM, pH 7.4) with the only notable signal being a local minimum near 200 nm (**Figure 5.5** and **Figure 5.6**).[36] However, the presence of full-length template (12.5 μM) in these solutions led to an increase in α-helicity with stronger signals at 208 nm and 222 nm and a positive signal at 195 nm. The cysteine fragment (**N20C F1**) increased α-helicity from 9% to 29%, and the thioester fragment (**N20C F2**) from 13% to 21% (Figure 5.5 and Figure 5.6). These increases are similar to those of previously published systems.[37] The improved folding in the presence of **N20C FL** reveals a moderate templating effect from the full length peptide to the fragments. To determine if the two fragments had any templating effect on each other, a CD spectrum was taken with both **N20C F1** and **N20C F2** (25 μM each) in MOPS buffer (20 mM, pH 7.4). The spectrum was taken immediately after solution preparation to prevent the fragments from reacting. The α-helicity of this solution was 3% (**Figure 5.7**). This low helicity may indicate no templating effect of the fragments to each other.

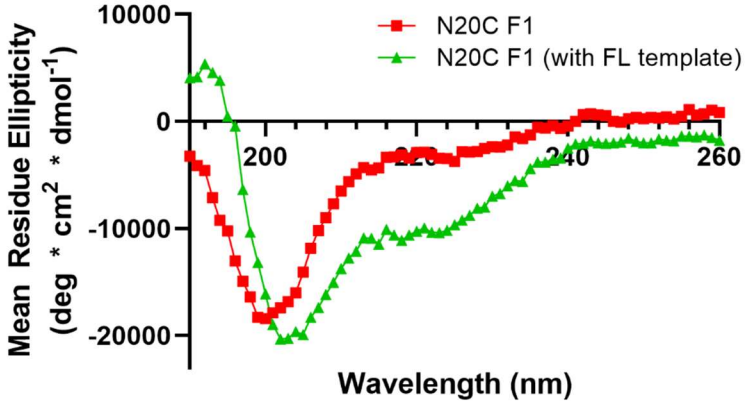

Figure 5.5. CD spectra of **N20C F1** (50 μM) without and with **N20C FL** template (12.5 μM) in phosphate buffer (20 mM, pH 7.4).

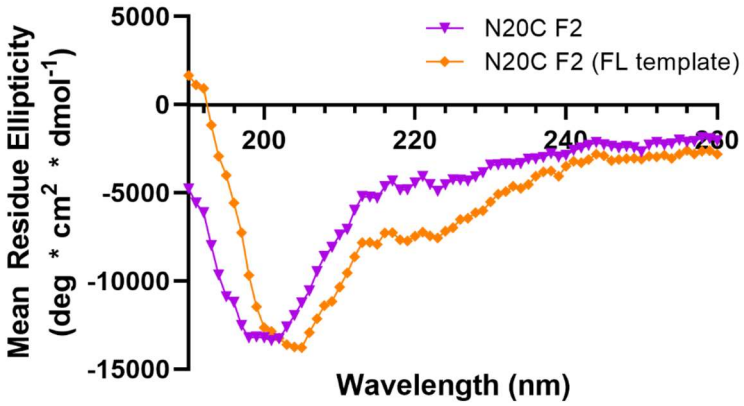

Figure 5.6. CD spectra of **N20C F2** (50 μM) without and with **N20C FL** template (12.5 μM) in phosphate buffer (20 mM, pH 7.4).

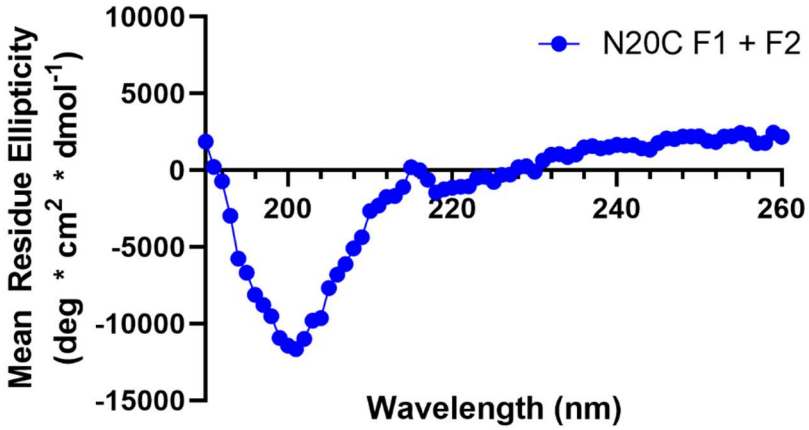

Figure 5.7. CD spectrum of **N20C F1** (25 μM) and **N20C F2** (25 μM) in phosphate buffer (20 mM, pH 7.4).

5.2.5 Native Chemical Ligation Reaction Rate

With a moderate templating effect from the full-length peptide observed by CD, the rate of the native chemical ligation reaction was probed. Dilute concentrations of **N20C FL** (≤ 200 μM) do not result in a detectable higher order assembly (**Figure 5.8**). In this way, the reaction rate could be investigated without the effects of higher order assembly. **N20C F1** (100 μM), **N20C F2** (100 μM), and varying amounts of **N20C FL** (0, 10, 25, 50 μM) were added to MOPS buffer (12.5 mM, pH 7.4) with (TCEP, 2 mM), and the reaction rate was monitored via RP-UPLC using a standard

curve (**Figure 5.9**). As the reaction progressed, the peaks from **N20C F1** and **N20C F2** diminished while the **N20C FL** peak increased (**Figure 5.10**A-D). Although the two peptide fragments reacted to form **N20C FL**, no enhanced product formation was observed when initial **N20C FL** was added (**Figure 5.10**E). Specifically, all conditions formed ~15 μM of **N20C FL** from the fragments at the same rate. The low yield from this reaction may be a result of remaining unreacted fragments as well as hydrolysis of the thioester fragment.[4,5] The lack of autocatalytic behavior may be due to the peptide's ability to self-assemble. Otto and coworkers have found that self-assembly plays a significant role in the autocatalysis of their large macrocycles containing thiol appendages.[15] The absence of auto-catalytic behavior in the **N20C FL** system is likely a result of **N20C FL** templating itself in addition to the fragments. While no precipitate forms in these dilute conditions, this self-templating effect formed transient assemblies that were observed by dynamic light scattering (Figure 5.10F). The signal at ~3 nm corresponds to coiled-coil monomer, and the signal at ~500 nm likely corresponds to an aggregate of **N20C FL** that remained in solution. The integration of the peak areas for the 3 nm and 500 nm signals correspond to <1% and >99%, respectively. The aggregates that form may prevent **N20C FL** from acting as an effective template and consequently inhibit auto-catalytic activity.

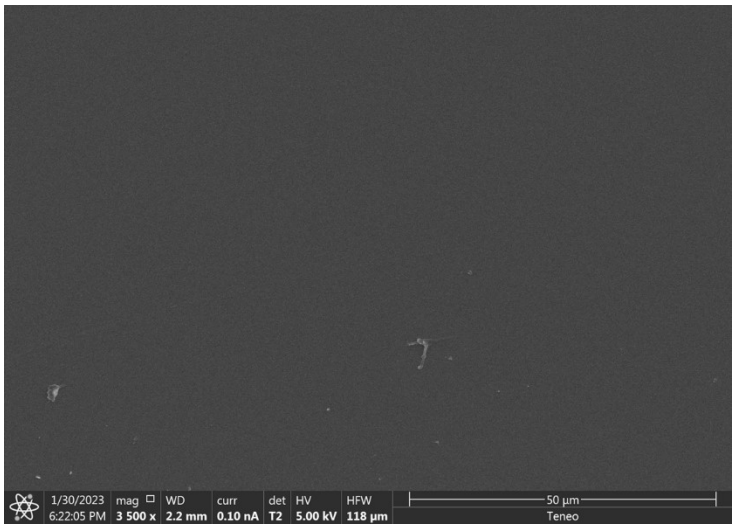

Figure 5.8. SEM visualization of **N20C FL** (200 μM) incubated in MOPS buffer (12.5 mM, pH 7.4) and TCEP (2 mM) after 8 hrs.

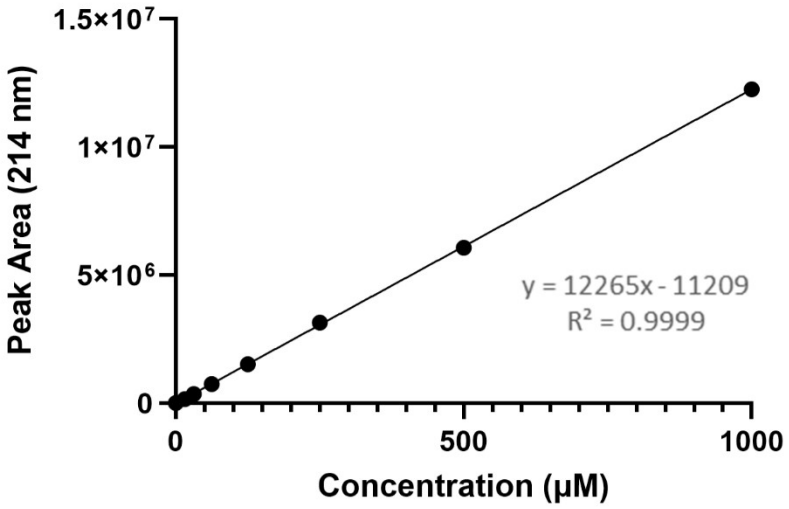

Figure 5.9. Standard curve of **N20C FL** on UPLC (214 nm absorbance).

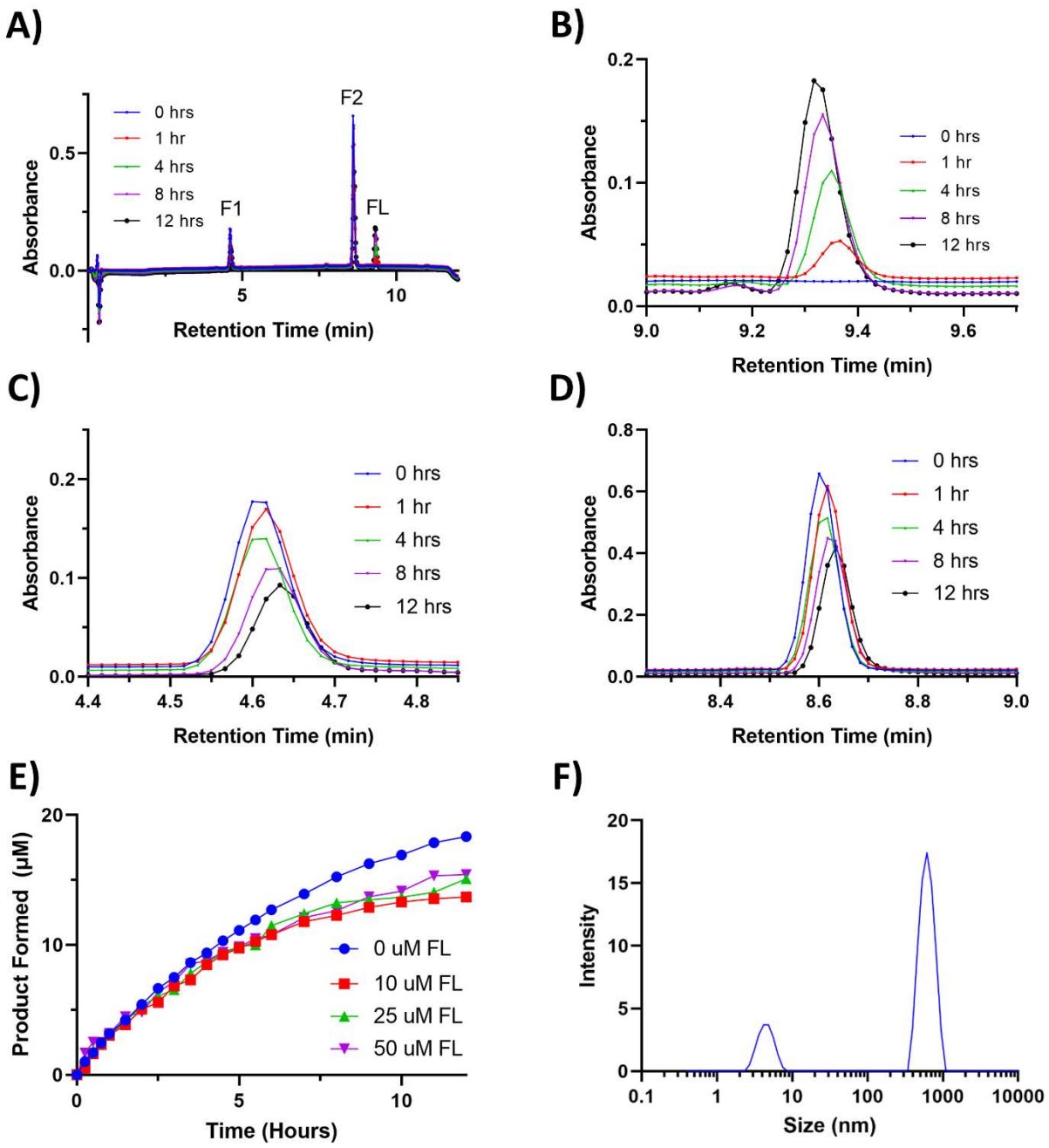

Figure 5.10. (A) UPLC trace (214 nm) of the native chemical ligation reaction from **N20C F1** (100 μM) and **N20C F2** (100 μM) at various time points without initial **N20C FL** added. (B) Zoomed in spectra of the **N20C FL** UPLC peak, (C) **N20C F1** UPLC peak, and (D) **N20C F2** UPLC peak. (E) **N20C FL** production from two fragments, **N20C F1** and **N20C F2**, at dilute conditions (100 μM each) with varying amounts of **N20C FL** template initially added to the solution. (F) DLS spectrum of **N20C FL** (50 μM) in MOPS (12.5 mM, pH 7.4) and TCEP (2 mM).

5.2.6 Native Chemical Ligation and Assembly

With a successful native chemical ligation reaction established, an investigation on the system's assembly following native chemical ligation was conducted. A similar reaction setup as above was carried out but now with higher peptide concentrations to induce higher order assembly. Specifically, **N20C F1** and **N20C F2** (1 mM each) were added to MOPS buffer (125 mM, pH 7.4) and TCEP (20 mM) with varying amounts of **N20C FL** (0, 50, 100, 200 μM) to perform native chemical ligation. In this design, all peptides were initially in solution. As the reaction progressed, the concentration of **N20C FL** increased and produced higher order assembly over time. The reaction rate was monitored by dissolving assembly aliquots in aqueous HCl (pH 2) followed by quantitation using RP-UPLC (**Figure 5.11**). In all conditions, ~300 μM of **N20C FL** was produced over the course of 8 hrs (**Figure 5.11**E). Similar to the dilute conditions described above, adding increasing amounts of initial **N20C FL** did not accelerate product formation. The resulting assembly after 8 hrs was subsequently washed and imaged via SEM (**Figure 5.12**). While a 1 mM **N20C FL** assembly led to small nanorods (**Figure 5.4**B), the slower formation of **N20C FL** from the native chemical ligation reaction produced strikingly large nanorods, ranging from 100-300 μm in length. Some of these materials appeared to become hexagonal and contain solid interiors as well. This dramatic size difference may be explained through the nucleation and growth phenomena.[38,39] A fast nucleation leads to the formation of smaller, more uniform materials whereas a slow nucleation creates assemblies of varying sizes.

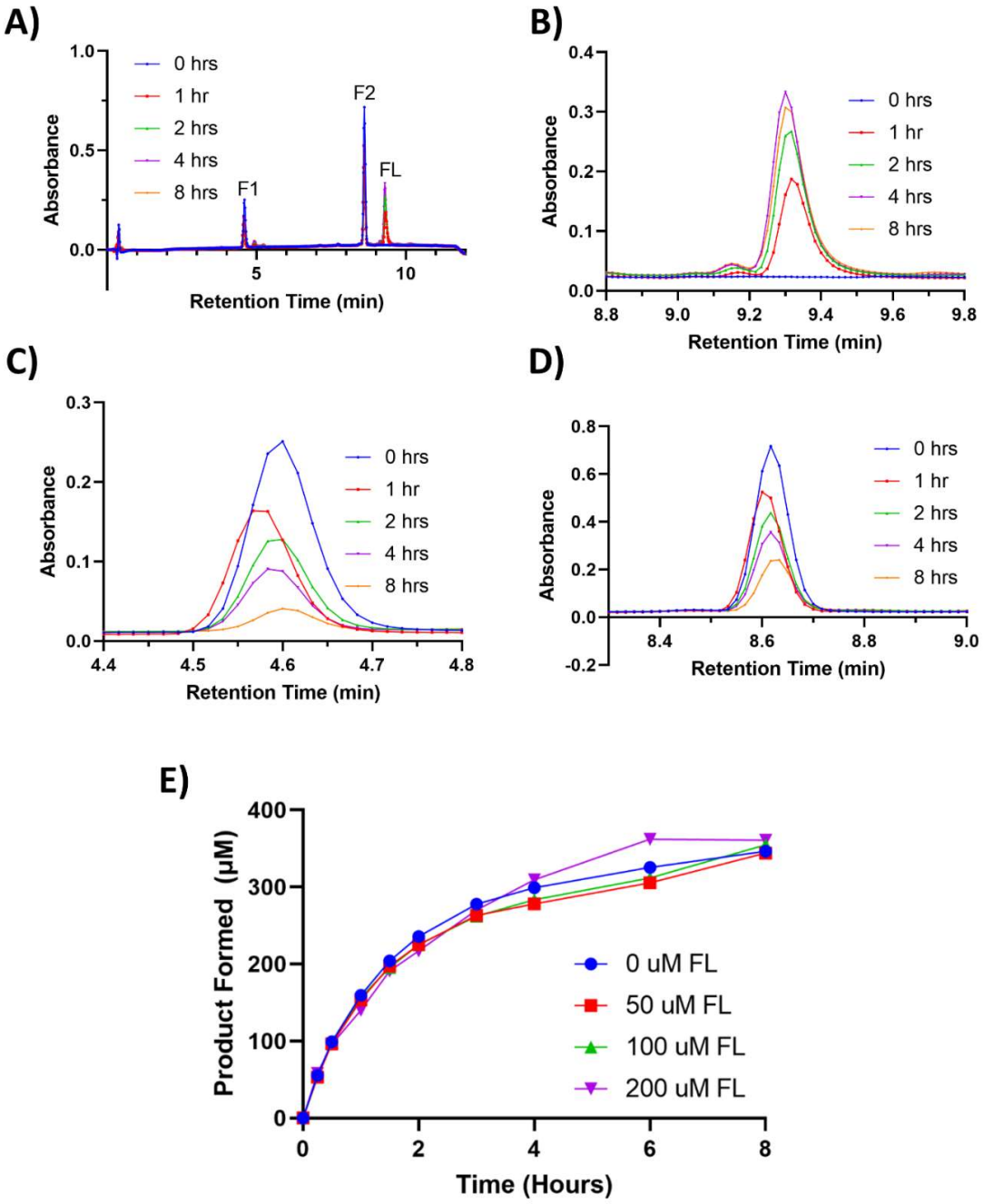

Figure 5.11. (A) UPLC trace (214 nm) of the native chemical ligation reaction from **N20C F1** (1 mM) and **N20C F2** (1 mM) at various time points without initial **N20C FL** added. (B) Zoomed in spectra of the **N20C FL** UPLC peak, (C) **N20C F1** UPLC peak, and (D) **N20C F2** UPLC peak. (D) **N20C FL** production from two fragments, **N20C F1** and **N20C F2** at high concentrations (1 mM each) with varying amounts of N20C FL template initially added to the solution.

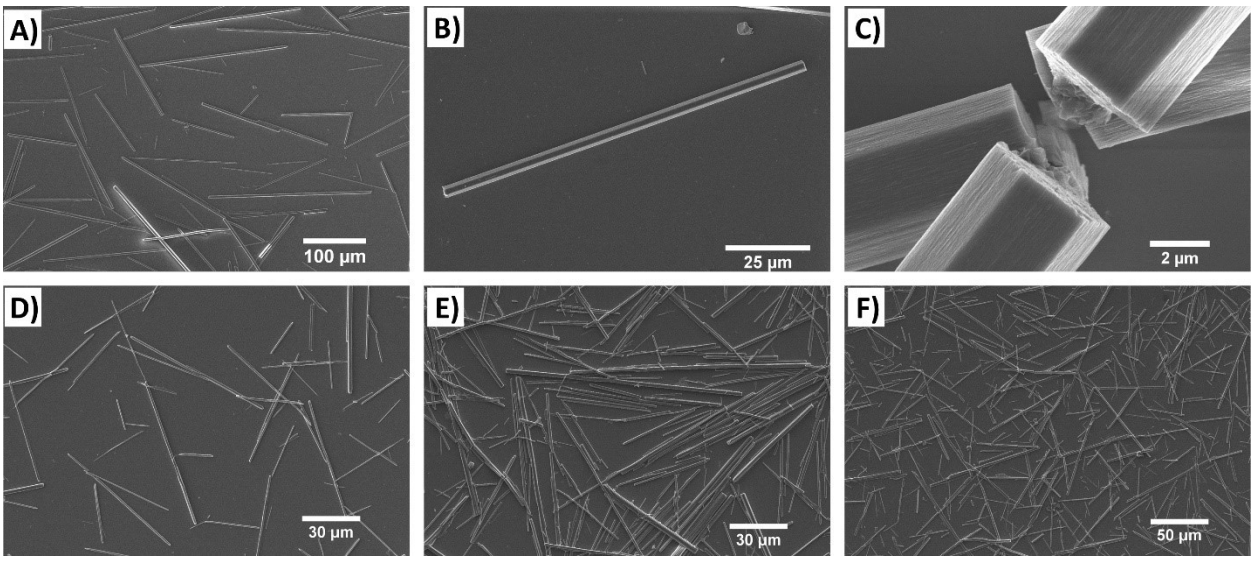

Figure 5.12. SEM visualization of peptide assembly following native chemical ligation (8 hrs) with (A-C) 0 µM initial **N20C FL** template, (D) 50 µM template, (E) 100 µM template, and (F) 200 µM template.

With the observed size increase in the material produced from native chemical ligation, we sought out a means to control the length of the resulting nanorod. As the large nanorods are likely a result of slow nucleation, we hypothesized that supplying the native chemical ligation system with preassembled nanorod seeds may control the final length of the material. As such, a similar experiment was designed using different amounts of **N20C FL** *preassembled* rather than *in solution*. **N20C FL** (1 mM) was first incubated in MOPS buffer (125 mM, pH 7.4) for 30 min and the supernatant of the assembly was analyzed via UPLC to quantify the extent of peptide assembly (~80% assembled, **Figure 5.13**). The desired amount of material was subsequently added to each native chemical ligation system. Specifically, preassembled **N20C FL** (0-200 µM) was added to MOPS buffer (125 mM, pH 7.4) with TCEP (20 mM) and both peptide fragments (1 mM each). Aliquots of the solution were acidified at designated time points with aqueous HCl (pH 2) and product formation was measured via RP-HPLC (**Figure 5.14**). Similar **N20C FL** production was observed (~300 µM) when compared to its solution counterparts (**Figure 5.14**E vs **Figure 5.11**E). However, SEM visualization revealed a dramatic difference in morphology. With low levels of nucleated seeds supplied to the system (0 µM and 50 µM), the nanorods remained large in length (>100 µm) (**Figure 5.15**A-B). As more preassembled seeds were added (100 µM and 200 µM), the nanorods appeared flatter with lengths as low as 5 µm (**Figure 5.15**C-D). These resulting

nanorods more closely resembled the original **N20C FL** assembly when rapid nucleation had occurred (Figure 5.4A). This is likely a result of the produced **N20C FL** from the ligation reaction growing the preassembled seeds rather than creating more nucleation events. This observation not only allowed for control over the length of the assembly but showed a promising way to control secondary growth of an assembly.

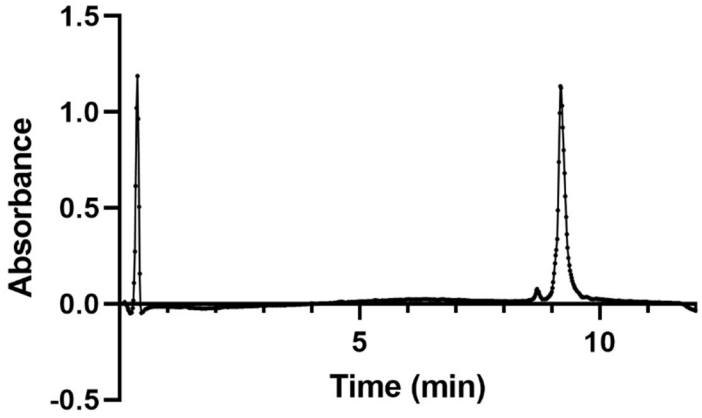

Figure 5.13. Supernatant of **N20C FL** (1 mM) assembly in MOPS buffer (125 mM, pH 7.4) after a 30 min incubation.

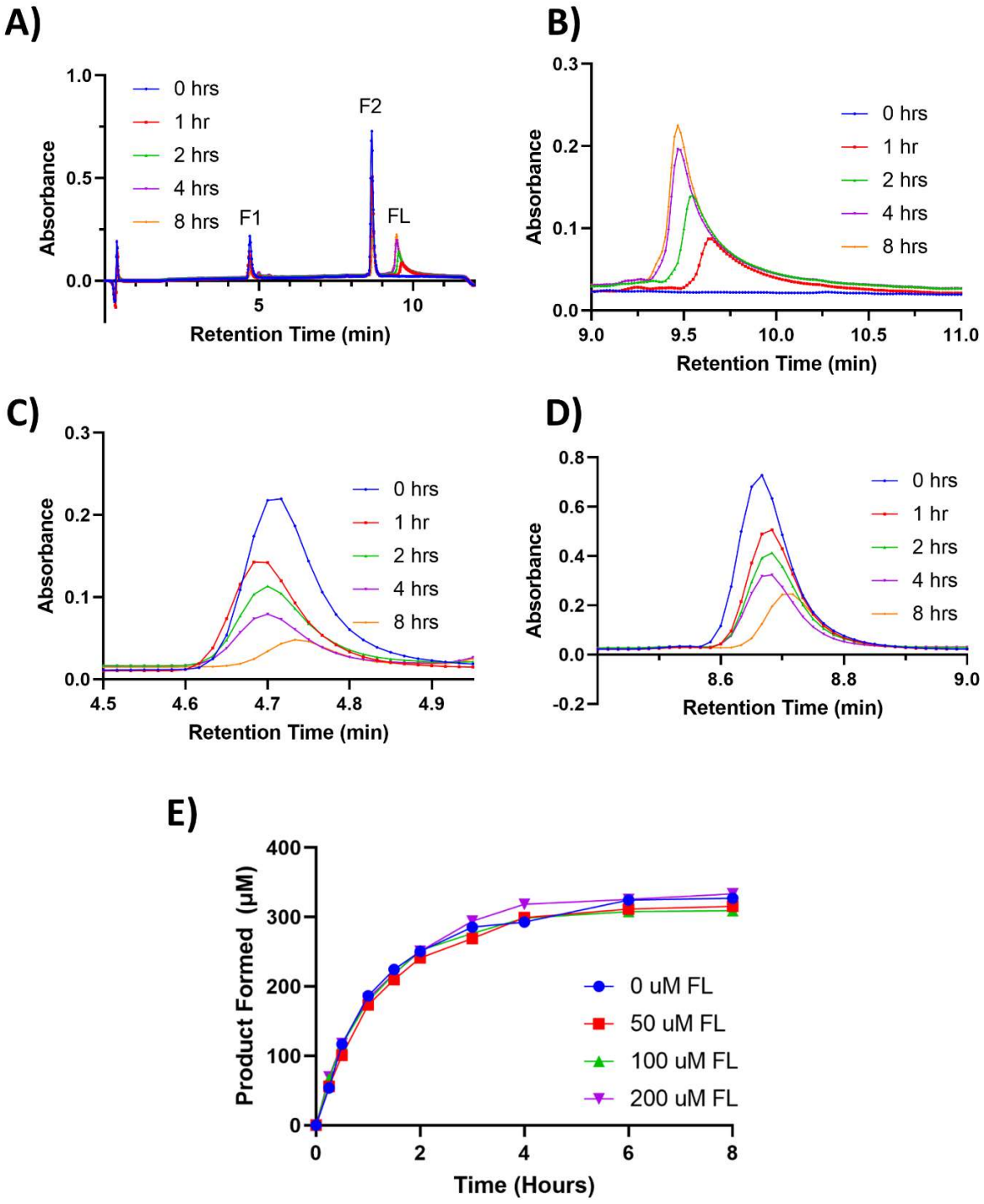

Figure 5.14. (A) UPLC trace (214 nm) of the native chemical ligation reaction from **N20C F1** (1 mM) and **N20C F2** (1 mM) at various time points without initial **N20C FL** template added. (B) Zoomed in spectra of the **N20C FL** UPLC peak, (C) **N20C F1** UPLC peak, and (D) **N20C F2** UPLC peak. (E) **N20C FL** production from two fragments, **N20C F1** and **N20C F2**, using preassembled **N20C FL** as a seed template (0-200 µM).

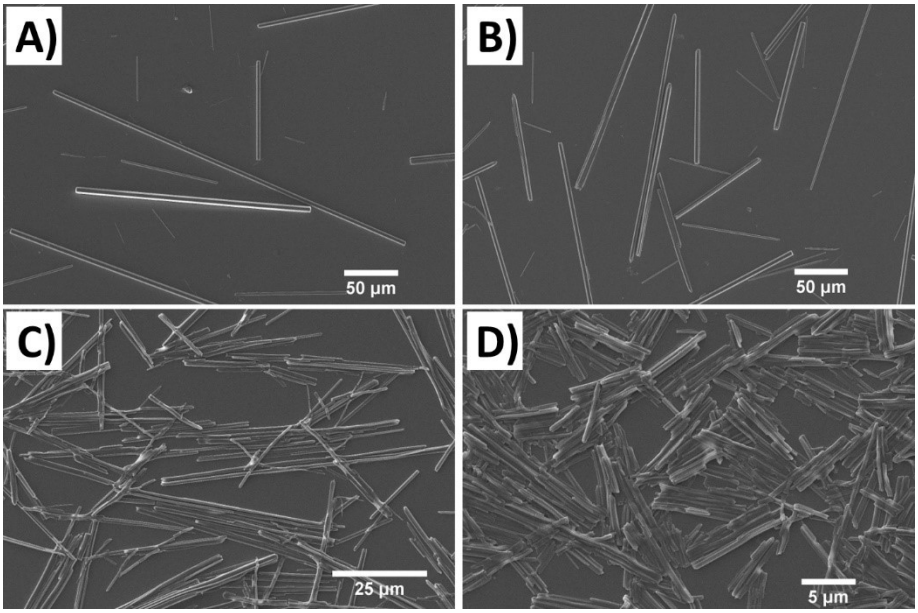

Figure 5.15. SEM visualization of peptide assembly after native chemical ligation (8 hrs) with (A) 0 µM initial **N20C FL** template, (B) 50 µM template, (C) 100 µM template, and (D) 200 µM template.

5.3 Alternative Studies for Catalytic Materials

Because **N20C FL** did not exhibit auto-catalytic self-replicating activity, other systems and methods were tested. The absence of this catalytic activity is likely stemmed from the self-templating of the full-length coiled-coil. We hypothesized that by destabilizing the coiled-coil, the self-templating ability may be inhibited. In addition to destabilization strategies, methods to improve the folding of the fragments were also investigated. **Table 5.1** contains all peptide mutations that were screened. All full-length peptides were synthesized using standard solid-phase peptide synthesis.

Table 5.1. TriNL mutants for native chemical ligation with mutated residues labeled in red.

Peptide	*abcdefg*	*abcdefg*	*abcdefg*	*abcdefg*	*abcdefg*
TriNL	Ac-MKQIEDK	IEEILSK	IYHIENE	IARIKKL	IGE-NH_2
H17C FL	Ac-MKQIEDK	IEEILSK	IY**C**IENE	IARIKKL	IGE-NH_2
N20C FL	Ac-MKQIEDK	IEEILSK	IYHIE**C**E	IARIKKL	IGE-NH_2
H17P FL	Ac-MKQIEDK	IEEILSK	IY**P**IE**C**E	IARIKKL	IGE-NH_2
N20C Truncated FL	Ac-	IEEILSK	IYHIE**C**E	IARIKKL	IGE-NH_2
I18N FL	Ac-MKQ**L**EDK	IEE**L**LSK	IYH**N**E**C**E	IAR**L**KKL	IGE-NH_2
I15N FL	Ac-MKQIEDK	IEEILSK	**N**YHIE**C**E	IARIKKL	IGE-NH_2
N20C Ghadiri FL	Ac-MKQ**L**EDK	**V**EE**L**LSK	**V**YH**L**E**C**E	**V**AR**L**KKL	**V**GE-NH_2
E1K2 FL	Ac-E-LYALEKE	LGALEKE	LACLKEK	LGALKEK	LYALKE-NH_2
E1K2-Ligand FL	**NTA**-G-E-LYALEKE	LGALEKE	LACLKEK	LGALKEK	LYALKE-G-**HH**
H17C F1			H_2N-**C**IENE	IARIKKL	IGE-NH_2
H17C F2	Ac-MKQIEDK	IEEILSK	IY-SR		
N20C Truncated F1			H_2N-**C**E	IARIKKL	IGE-NH_2
N20C Truncated F2	Ac-	IEEILSK	IYHIE-SR		
I18N F1			H_2N-**C**E	IAR**L**KKL	IGE-NH_2
I18N F2	Ac-MKQ**L**EDK	IEE**L**LSK	IYH**N**E-SR		
I15N F1			H_2N-**C**E	IARIKKL	IGE-NH_2
I15N F2	Ac-MKQIEDK	IEEILSK	**N**YHIE-SR		
N20C Ghadiri F1			H_2N-**C**E	**V**AR**L**KKL	**V**GE-NH_2
N20C Ghadiri F2	Ac-MKQ**L**EDK	**V**EE**L**LSK	**V**YH**L**E-SR		

5.3.1 H17C Mutation

One of the simplest modifications to the self-replicating peptide was to change the position of the cysteine residue. By installing an H17C mutation rather than N20C, the fragments would be more equal in length, and the cysteine residue would be at the *c* position of the coiled-coil rather than the *f* position. Once synthesized, **H17C FL** (50 μM) was added to phosphate buffer (20 mM, pH 7.4), and a CD spectrum was taken. The peptide still exhibited coiled-coil behavior with minima at 208 nm and 222 nm, although α-helicity somewhat decreased (57%, **Figure 5.16**A). This may be a result of the positional change of the cysteine residue on the coiled-coil from *f* to *c*. Namely, the cysteine at the *c* position is closer to the other α-helices within the coiled-coil and may disrupt the folding. The peptide was subsequently tested for self-assembly. **H17C FL** (1 mM) was added to MOPS buffer (100 mM, pH 7.4) and had significant difficulty forming higher-order assembly. After 6 days, a precipitate was collected and visualized via SEM (**Figure 5.16**B). Few nanorods were observed. The decrease in α-helicity may have contributed to this lack of assembly.

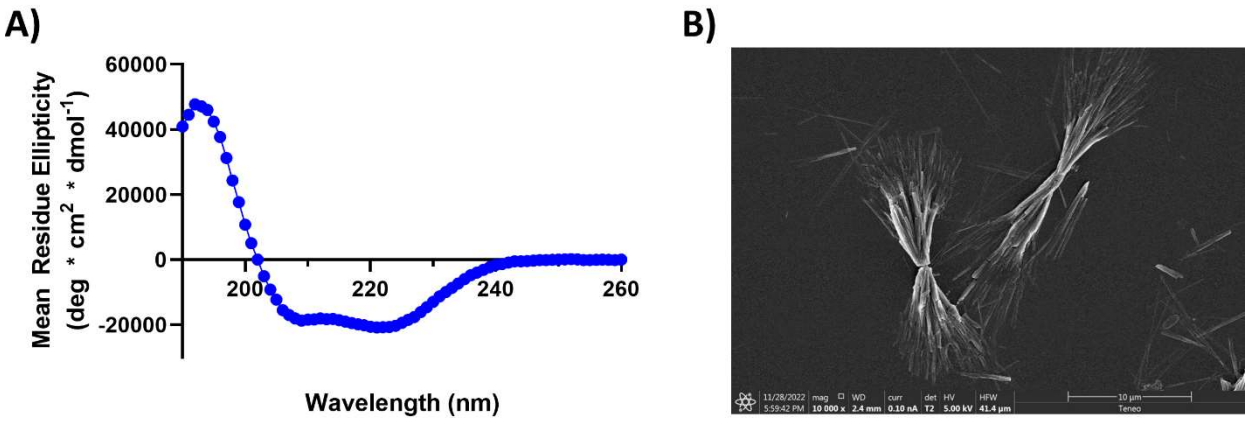

Figure 5.16. (A) CD spectrum of **H17C FL** (50 μM) in phosphate buffer (20 mM, pH 7.4). (B) SEM visualization of **H17C FL** (1 mM) assembled in MOPS (125 mM, pH 7.4) and TCEP (10 mM) after 6 days.

While **H17C FL** did not readily assembly as well as **N20C FL**, the ligation rate was still investigated to determine the importance of the cysteine position on the coiled-coil. As such, the cysteine and thioester fragments, **H17C F1** and **H17C F2**, respectively, were synthesized. **H17C F1** was synthesized using similar methods to **N20C F1**. Because the first residue of **H17C F2** was

not glutamate, an alternative synthetic route was required for the thioester fragment (**Scheme 5.3**). Specifically, the peptide was synthesized on hydrazine 2-chlorotrityl resin using standard solid-phase peptide synthesis, and the N-terminus was acetylated. The peptide was cleaved from resin using a TFA cocktail and purified to homogeneity via RP-HPLC. The C-terminal hydrazine was oxidized through *in situ* sodium nitrite activation followed by thiolysis with Mesna. The reaction was purified via RP-HPLC and characterized using MALDI-ToF.

With both peptide fragments in hand, the native chemical ligation reaction rate was investigation. **H17C F1** and **H17C F2** (250 μM each) were added to MOPS buffer (62.5 mM, pH 7.4), TCEP (10 mM) and 4-mercaptophenylacetic acid (MPAA, 5 mM) with and without **H17C FL** template (0 or 250 μM). While the thioester and cysteine fragments still reacted to form **H17C FL (**Figure 5.17A-D), no enhanced product formation was observed when initial **H17C FL** was added (**Figure 5.17**E). When the reaction was tested at higher concentrations (1 mM fragments), similar results occurred (**Figure 5.17**F). Furthermore, no assembly occurred after this ligation reaction. These data suggest factors other than cysteine positioning affect the peptide's autocatalytic properties.

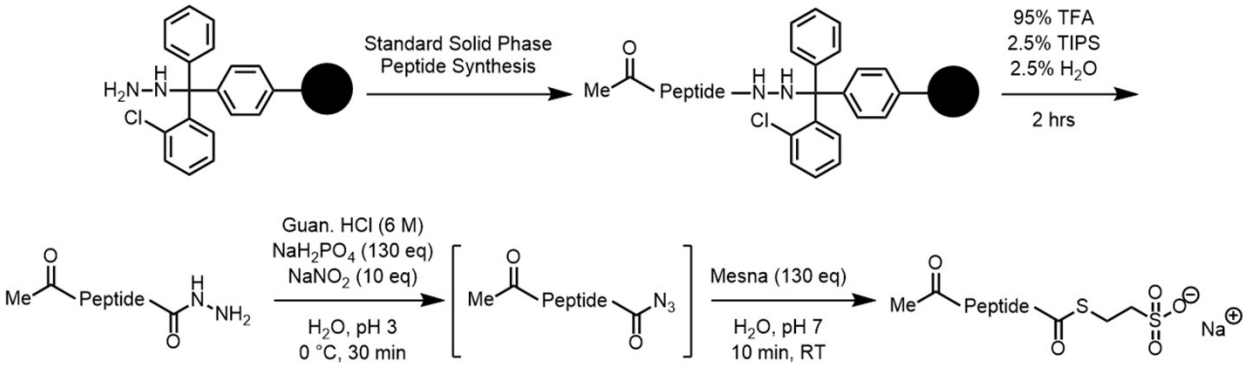

Scheme 5.3. Synthesis of the Mesna thioester fragment, **H17C F2**, through a C-terminal hydrazine strategy.

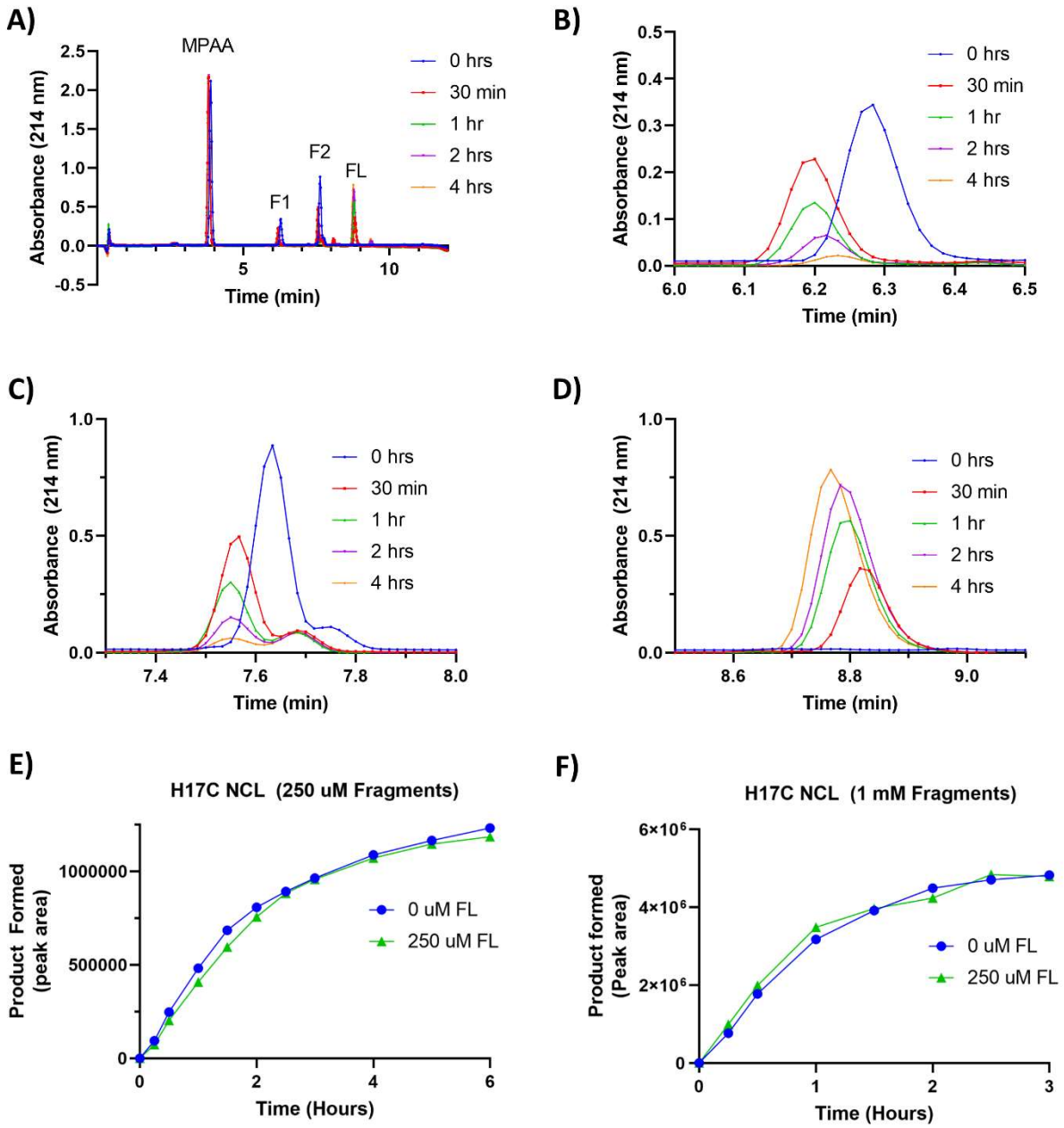

Figure 5.17. (A) UPLC trace (214 nm) of the native chemical ligation reaction from **H17C F1** (1 mM) and **H17C F2** (1 mM) at various time points without initial **H17C FL** template added. (B) Zoomed in spectra of the H**17C FL** UPLC peak, (C) **H17C F1** UPLC peak, and (D) **H17C F2** UPLC peak. (E) Native chemical ligation reaction rate at dilute conditions (250 mM fragments) and (F) concentrated conditions (1 mM fragments).

5.3.2 H17P Mutation

Using the **N20C FL** peptide as the backbone, a proline kink was installed at a nearby position (H17P). Installing a proline residue in a coiled-coil motif would cause a kink in the coiled-

coil folding and could potentially provide more access for the fragments to react when templated onto the full-length peptide.[12] The mutated peptide, **H17P FL** (50 μM), in citrate buffer (20 mM, pH 3.0) exhibited a 75% α-helicity and maintained its coiled-coil folding (**Figure 5.18**A). Unfortunately, this peptide did not readily assemble. After 24 hrs in 2-(N-morpholino)ethanesulfonic acid (MES) buffer (50 mM, pH 6.0), the peptide (1 mM) produced a small amount of broken nanorods (**Figure 5.18**B). While high α-helicity was maintained, the proline kink may have prevented the coiled-coils from aligning and subsequently assembling. The amount of assembly produced was not significant, and the peptide was not carried forward for native chemical ligation studies.

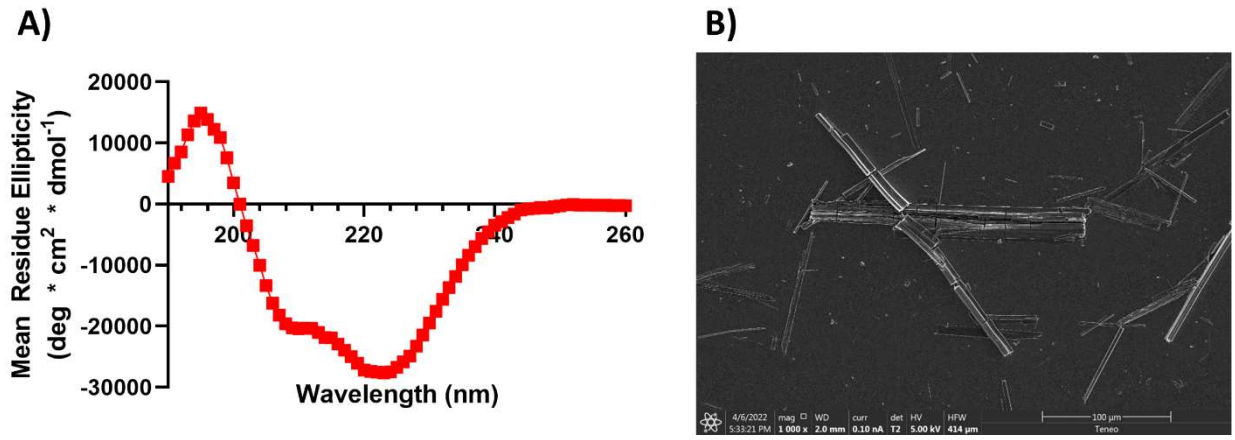

Figure 5.18. (A) CD spectrum of **H17P FL** (50 μM) in citrate buffer (20 mM, pH 3.0). (B) SEM visualization of **H17P FL** (500 μM) assembly in MES buffer (50 mM, pH 6.0) after 24 hrs.

5.3.3 N20C Truncated

The next destabilization strategy was to design a shortened coiled-coil peptide. Peptides require ~3.5 heptad repeats to properly fold into a coiled-coil.[40] With this in mind, **N20C Truncated FL** was designed, where the N-terminal heptad repeat was removed. Despite the truncated sequence, the peptide (50 μM) in citrate buffer (20 mM, pH 3.0) still retained coiled-coil folding (85% α-helicity, **Figure 5.19**A). When **N20C Truncated FL** was added to MES buffer (100 mM, pH 6.0) for 1 hr, fibril structures obtained (**Figure 5.19**B). The cysteine (**N20C Truncated F1**) and thioester (**N20C Truncated F2**) fragments were subsequently synthesized using standard solid-phase peptide synthesis and methods from **Scheme 5.1**, respectively. Insolubility of the thioester fragment prevented further studies with this truncated system.

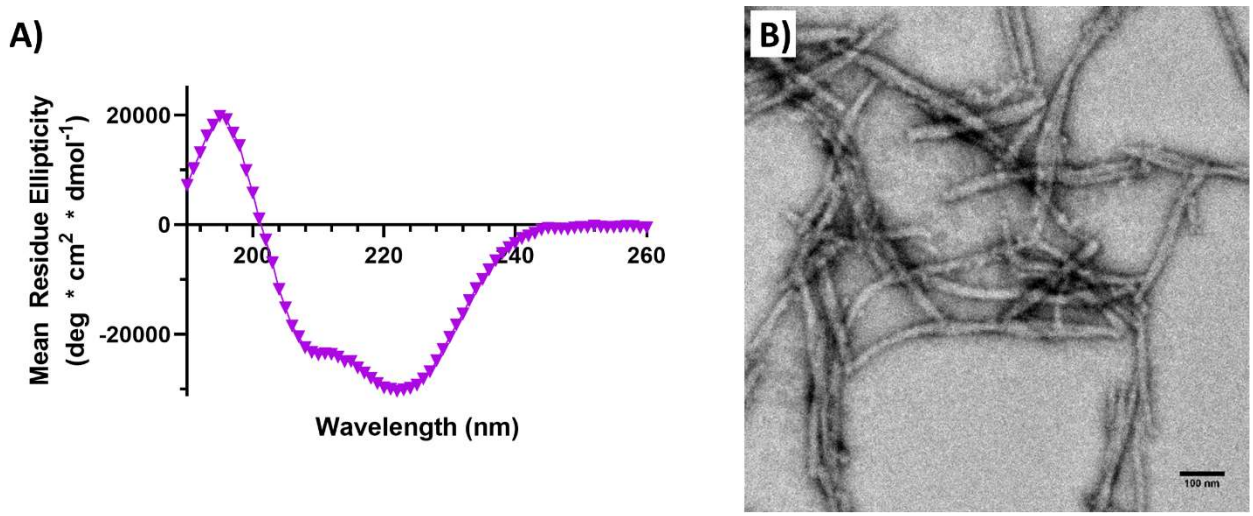

Figure 5.19. (A) CD spectrum of **N20C Truncated FL** (50 μM) in citrate buffer (20 mM, pH 3.0). (B) TEM visualization of **N20C Truncated FL** assembly (1 mM) in MES buffer (100 mM, pH 6.0) after 1 hr.

5.3.4 I18N Mutation

The **I18N FL** peptide contained more complex modifications. Rather than simply destabilizing a coiled-coil, this peptide focused on creating an equilibrium between a dimeric and trimeric coiled-coil. Perhaps this equilibrium would allow the full-length peptide in dimeric form to act as a template for the fragments and make a subsequent trimeric coiled-coil after the native chemical ligation reaction. In the **I18N FL** sequence, isoleucine and leucine residues were installed at the *a* and *d* residues to favor a dimeric coiled-coil.[25] Asparagine residues have been reported to favor a trimeric coiled-coils when installed at the *d* position.[40,41] Consequently, an I18N mutation was incorporated in the peptide to potentially create a dimeric and trimeric equilibrium. This peptide (50 μM) in citrate buffer (20 mM, pH 3.0) still exhibited coiled-coil behavior (86% α-helicity, **Figure 5.20**A). **I18N FL** (1 mM) assembled into fibrils after MOPS incubation (50 mM, pH 7.4) for 1 hr (**Figure 5.20**B). With this peptide assembling, the two fragments, **I18N F1** and **I18N F2**, were subsequently synthesized using standard solid-phase peptide synthesis and methods from **Scheme 5.1**, respectively. When the fragments (1 mM each) were incubated in MOPS buffer (125 mM, pH 7.4) and TCEP (20 mM), **I18N FL** was indeed produced (**Figure 5.21**A-B). However, no auto-catalytic activity was observed when the full-length peptide was initially added to the reaction (**Figure 5.21**C). Namely, the rate of the native chemical ligation was very similar across all initial **I18N FL** concentrations (0-50 μM). Like its **N20C FL** counterpart, the fibrils

produced after the ligation were much larger than the fast nucleation conditions of full-length peptide alone (**Figure 5.21**D vs **Figure 5.20**B). The absence of auto-catalytic activity may be due to the dimeric nature of the coiled-coil. It is possible that the peptide is primarily a dimer and the asparagine effect at the N18 position was not strong enough to create an equilibrium with a trimeric coiled-coil.

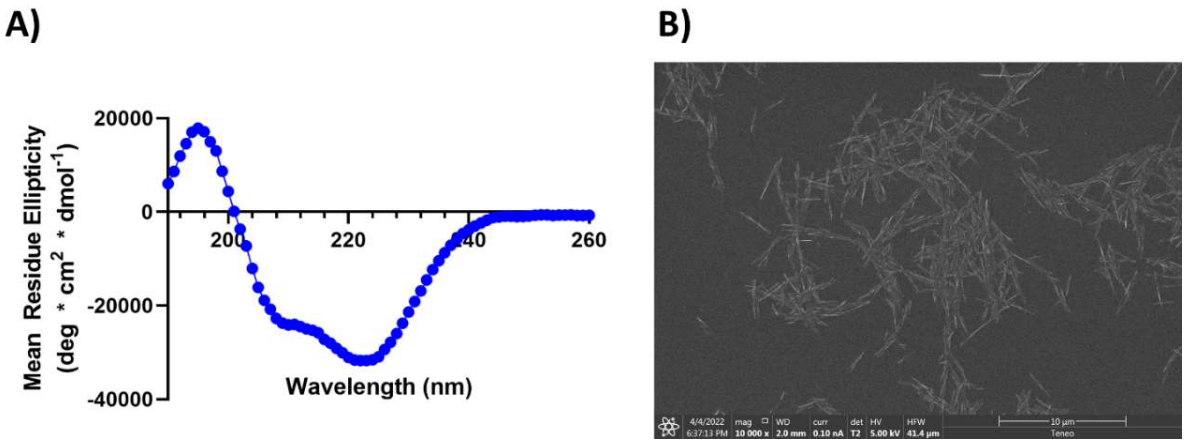

Figure 5.20. (A) CD spectrum of **I18N FL** (50 μM) in citrate buffer (20 mM, pH 3.0). (B) SEM visualization of **I18N FL** assembly (500 μM) in MOPS buffer (50 mM, pH 7.4) after 24 hrs.

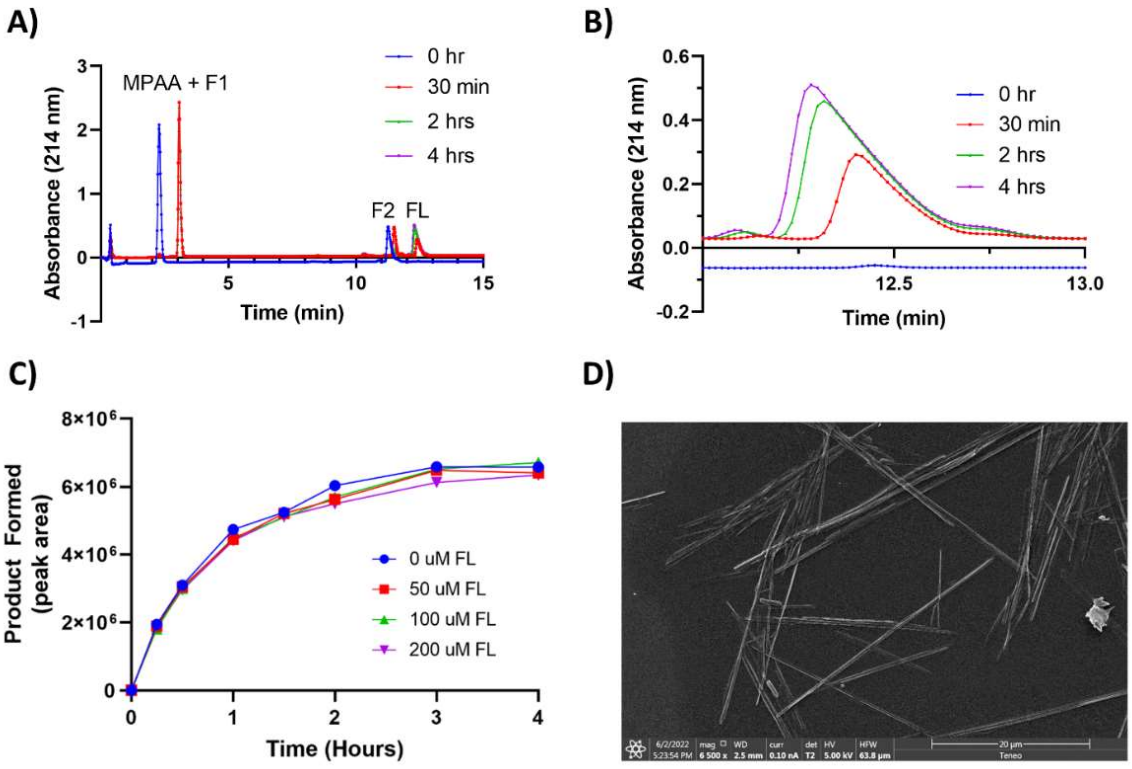

Figure 5.21. (A) UPLC trace (214 nm) of the native chemical ligation reaction from **I18N F1** (1 mM) and **I18N F2** (1 mM) at various time points without initial **I18N FL** template added. (B) Zoomed in spectra of the **I18N FL** peak. (C) Native chemical ligation reaction rate with 1 mM of each fragment and (D) its corresponding assembly upon reaction completion (0 μM template).

5.3.5 I15N Mutation

Similar to the **I18N FL** peptide, the **I15N FL** peptide was designed to create an equilibrium between oligomeric states of the coiled-coil. Specifically, the *a* and *d* positions were both isoleucine residues to favor a trimeric coiled-coil and an asparagine residue was installed at the *a* position of the coiled-coil (I15N) to favor a dimeric coiled-coil.[25,40,41] This peptide (50 μM) still exhibited coiled-coil folding in citrate buffer (20 mM, pH 3.0) but had a weaker α-helical signal (57% α-helicity, **Figure 5.22**A). The assemblies of this peptide (500 μM) also exhibited dramatic morphological differences based on buffer identity. In MES buffer (50 mM, pH 6.0), twisted capsules were formed, but in MOPS buffer (50 mM, pH 7.4), nanosheets were observed (**Figure 5.22**B-C). With these interesting results, **I15N F1** and **I15N F2** were synthesized using standard peptide synthesis and methods from **Scheme 5.1**, respectively. The native chemical ligation reaction rate was tested in MOPS buffer to mimic physiological pH (**Figure 5.23**). Unfortunately,

this peptide also did not exhibit auto-catalytic activity when **I15N FL** (0-200 μM) was initially added to the reaction (**Figure 5.23**C). Unexpectedly, the produced assembly from the ligation reaction was not a nanosheet morphology but rather a nanorod structure (**Figure 5.23**D). Just like the **I18N FL** peptide, it is possible that a true equilibrium between a dimeric and trimeric coiled-coil was not achieved.

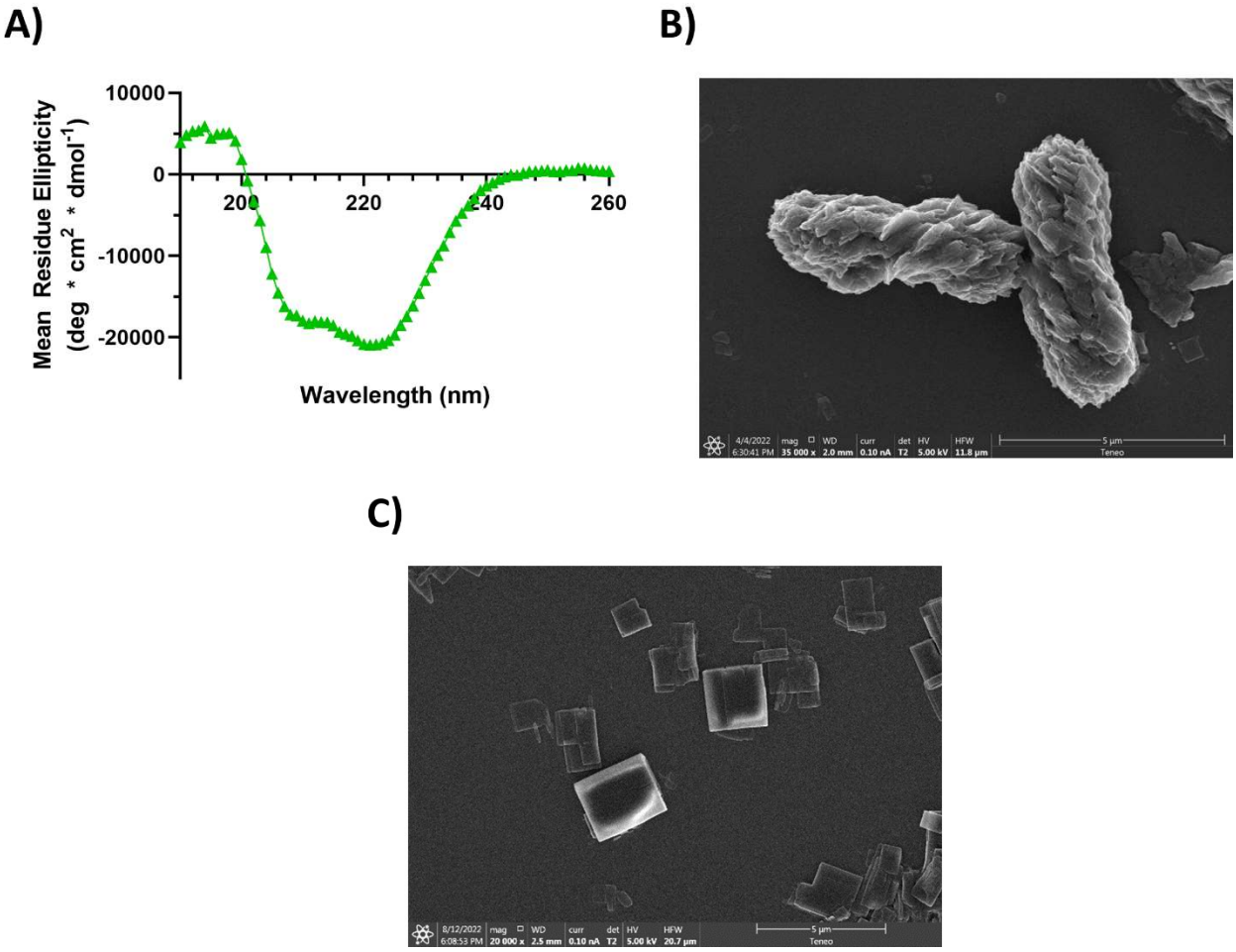

Figure 5.22. (A) CD spectrum of **I15N FL** (50 μM) in citrate buffer (20 mM, pH 3.0). (B) SEM visualization of **I15N FL** assembly (500 μM) in MES buffer (50 mM, pH 6.0) after 1 hr and (C) in MOPS buffer (50 mM, pH 7.4) after 24 hrs.

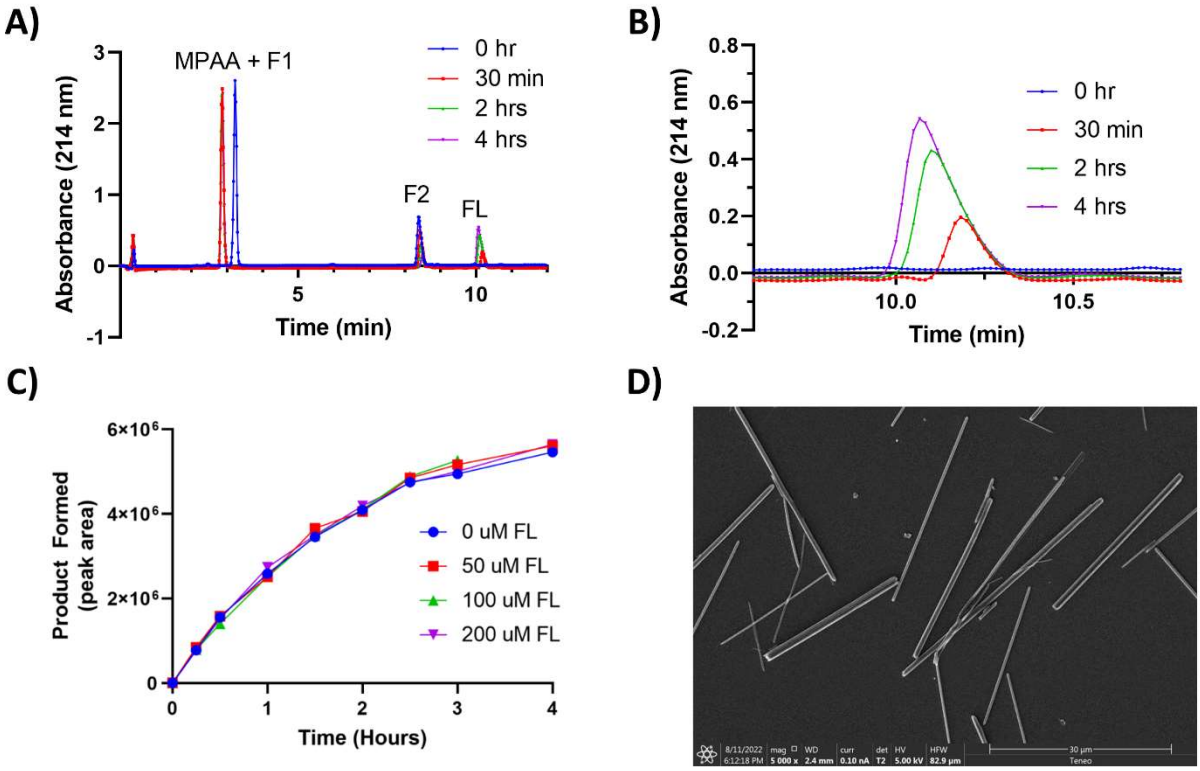

Figure 5.23. (A) UPLC trace (214 nm) of the native chemical ligation reaction from **I15N F1** (1 mM) and **I15N F2** (1 mM) at various time points without initial **I15N FL** template added. (B) Zoomed in spectra of the **I15N FL** peak. (C) **I15N FL** production from two fragments, **I15N F1** and **I15N F2** (1 mM each) with varying amounts of **115N FL** template initially added to the solution. (D) SEM visualization of assembly after ligation (0 μM template).

5.3.6 N20C Ghadiri

The next peptide was based on the sequences of Kim[25] and Ghadiri[4] with known equilibriums between dimeric and trimeric coiled-coils. Specifically, installing valine in the *a* positions and leucine in the *d* positions of the GCN4 leucine zipper would create this oligomeric equilibrium. Once synthesized, the peptide **N20C Ghadiri FL** (1 mM) was tested for higher order assemblies. The peptide was found to assemble into nanosheets in MES buffer (100 mM, pH 6.0) after 1 hr but did not assemble in MOPS buffer (100 mM, pH 7.4) (**Figure 5.24**). The cysteine (**N20C Ghadiri F1**) and thioester fragments (**N20C Ghadiri F2**) were synthesized using standard peptide synthesis and methods from **Scheme 5.1**, respectively. With standard native chemical ligation occurring at physiological pH, the reaction rate was first tested in MOPS buffer (125 mM, pH 7.4) with TCEP (20 mM) and 4-mercaptophenylacetic acid (MPAA, 10 mM) using 1 mM fragment concentrations. In these conditions, the peptide did not assemble and no auto-catalytic

activity was observed (**Figure 5.25**). While the lack of catalytic activity is not fully understood, it is possible that the slight differences in the Ghadiri sequence such as the N-terminal cap or amino acid differences could have affected the peptide's templating ability (Table 5.2).

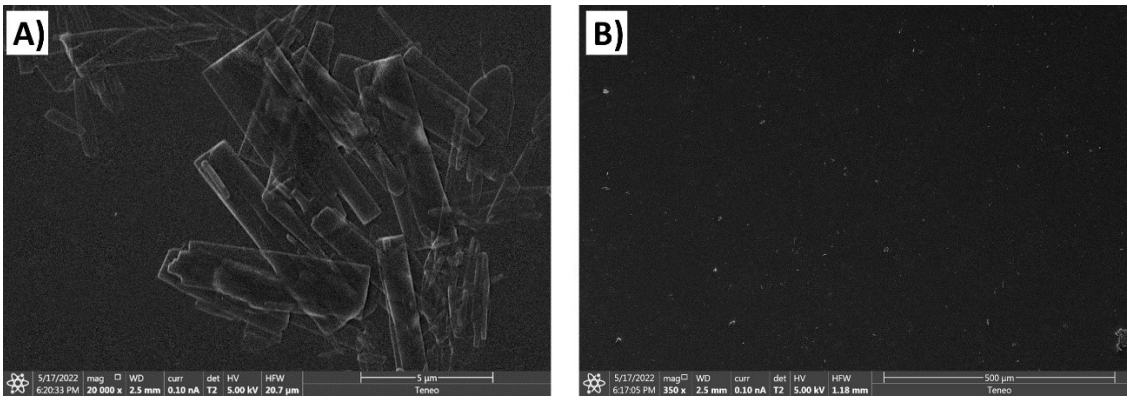

Figure 5.24. SEM visualization of **N20C Ghadiri FL** (1 mM) in (A) MES buffer (100 mM, pH 6.0) and (B) MOPS buffer (100 mM, pH 7.4) after 1 hr.

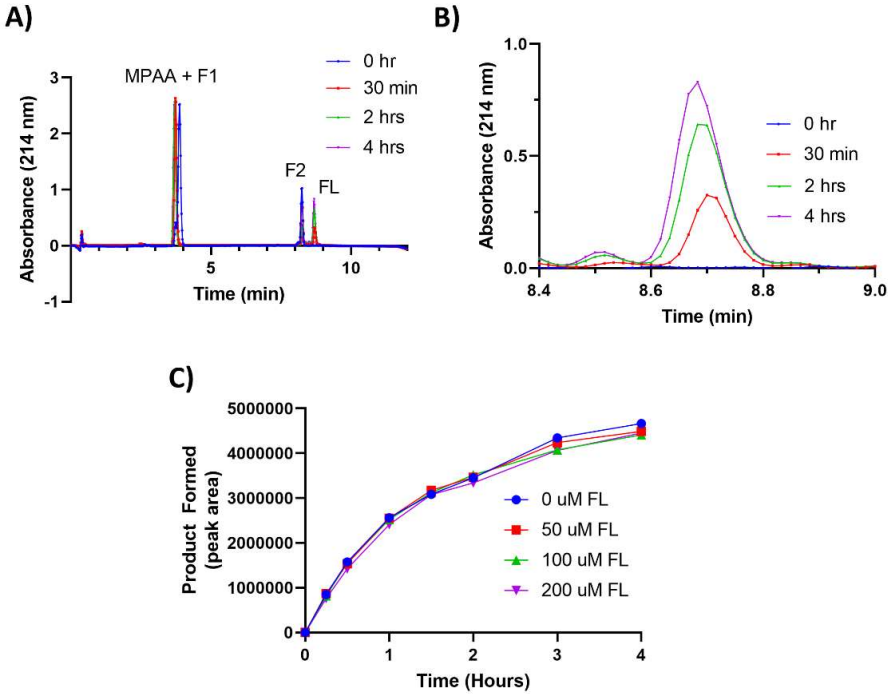

Figure 5.25. (A) UPLC trace (214 nm) of the native chemical ligation reaction from **N20C Ghadiri F1** (1 mM) and **N20C Ghadiri F2** (1 mM) at various time points without initial **N20C Ghadiri FL** template added. (B) Zoomed in spectra of the N20C Ghadiri **FL** UPLC peak. (C) **N20C Ghadiri FL** production from two fragments, **N20C Ghadiri F1** and **N20C Ghadiri F2** (1 mM each) with varying amounts of **N20C Ghadiri FL** template initially added to the solution.

Table 5.2. Sequence comparisons between **N20C Ghadiri FL** and the previously published Ghadiri peptide **T**.[4]

	abcdefg	*abcdefg*	*abcdefg*	*abcdefg*	*abcdefg*
N20C Ghadiri FL	Ac-MKQLEDK	VEELLSK	VYHLECE	VARLKKL	VGE-NH2
T	**Ar**-**R**-MKQLE**E**K	V**Y**ELLSK	V**A**C**L**E**Y**E	VARLKKL	VGE-NH2

Ar = 4-acetamidobenzoic acid

5.3.7 Trifluoroethanol

Solvent effects using trifluoroethanol (TFE) were also investigated to study the N20C FL templating effect on the fragments. TFE has been reported to disrupt coiled-coil folding through destabilization of the hydrophobic cavity while strengthening α-helicity of peptides.[35,42] This could not only potentially destabilize the coiled-coil template but also promote folding of the fragments. The **N20C FL** peptide (50 μM) in citrate buffer (20 mM, pH 3.0) decreased coiled-coil behavior with increasing amounts of TFE (0-50% TFE v/v) where $\theta_{222}/\theta_{208}$ approached 1 (**Figure 5.26**A). The fragments, on the other hand, increased α-helicity with a dramatic shift at 20% TFE (v/v) (**Figure 5.26**B-C). With this in mind, we sought out to test the native chemical ligation using a 20% TFE solution. First, the **N20C FL** peptide (500 μM) was confirmed to still assemble in 20% TFE (v/v) in MOPS buffer (50 mM, pH 7.4) with TCEP (20 mM) and MPAA (10 mM) (**Figure 5.26**D). After 1 hr, the assembly was collected and visualized via SEM. Somewhat longer nanorods were produced when compared to solutions without TFE (Figure 5.4B). After confirming TFE did not prevent assembly, the ligation rate of the cysteine and thioester fragments (1 mM each) was subsequently measured in MOPS (125 mM, pH 7.4) with TCEP (20 mM) and MPAA (10 mM) in 20% TFE (v/v). Similar to other systems, the two fragments did indeed ligate and form **N20C FL** (Figure 5.27A-B). Unfortunately, no enhanced product formation was observed when **N20C FL** was initially added to the reaction. This may be caused by **N20C FL** forming transient assemblies similar to solutions without TFE (**Figure 5.10**F).

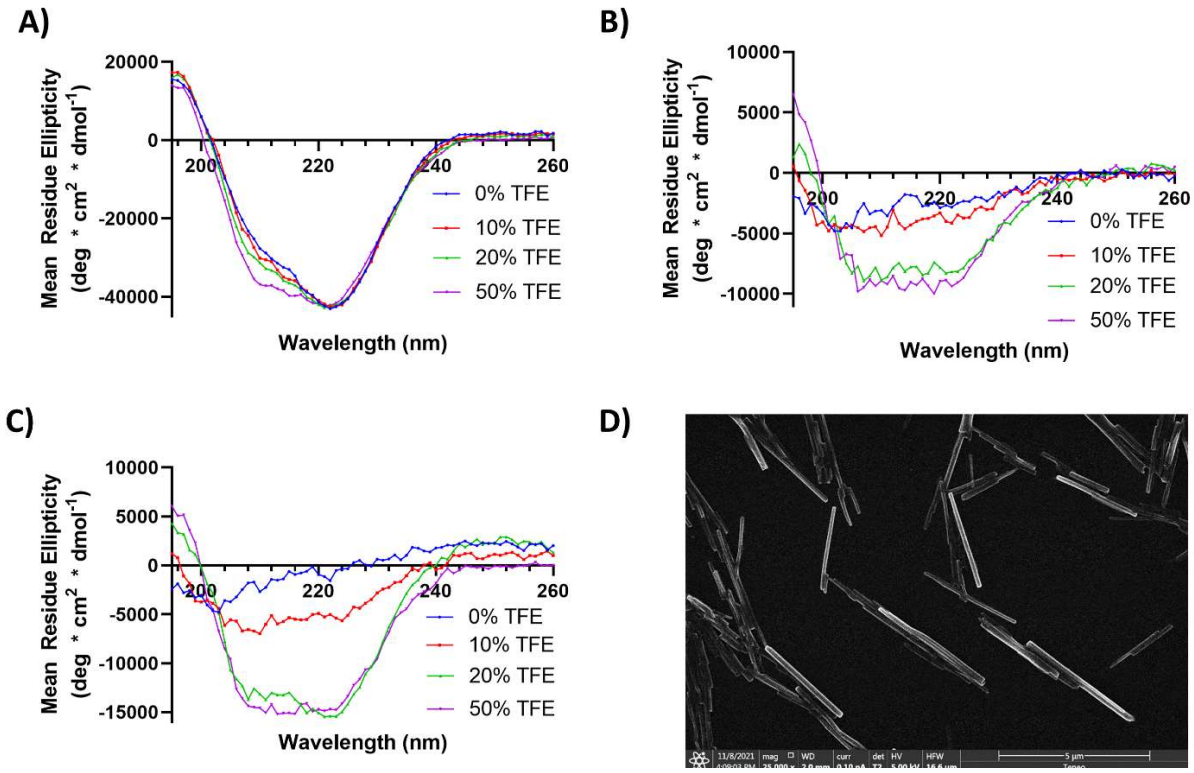

Figure 5.26. CD spectra of (A) **N20C FL** (50 µM), (B) **N20C F1** (50 µM), and (C) **N20C F2** (50 µM) at varying TFE concentrations (v/v) in citrate buffer (20 mM, pH 3.0). (D) SEM visualization of **N20C FL** (1mM) assembled in MOPS buffer (125 mM, pH 7.4), TECP (20 mM), MPAA (10 mM), and TFE (20%) after 1 hr.

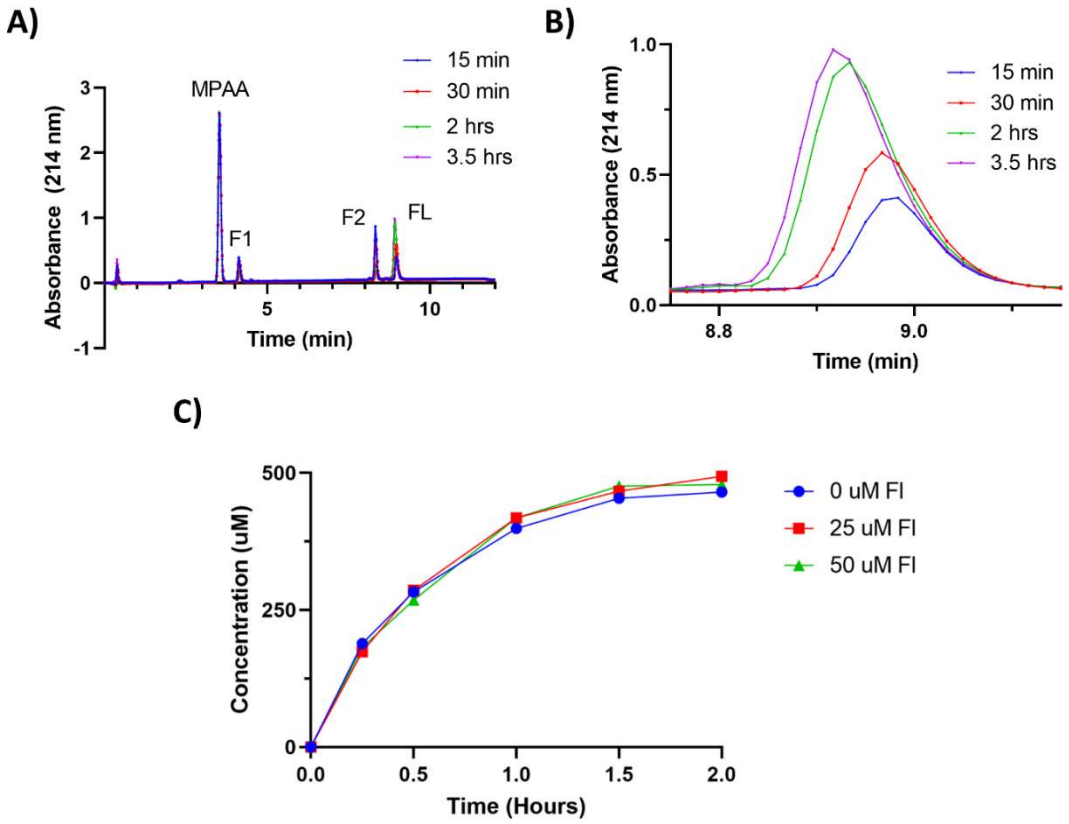

Figure 5.27. (A) UPLC trace (214 nm) of the native chemical ligation reaction from N20C F1 (1 mM) and **N20C F2** (1 mM) at various time points without initial N20C FL template added in 20% TFE (v/v). (B) Zoomed in spectra of the N20C **FL** UPLC peak. (C) **N20C FL** production from two fragments, **N20C F1** and **N20C F2** (1 mM each) with varying amounts of **N20C FL** template initially added to the solution.

5.3.8 E1K2

So far, peptide design has been centered around taking a self-assembling peptide and creating a catalytic native chemical ligation system. Here, the reverse was tested. Previously reported **E1K2** exhibited auto-catalytic activity where the introduction of initial full-length peptide affected the reaction rate of the ligation.[2] This peptide (1 mM), however, did not assemble over extended periods of time (> 1 week) in MOPS (100 mM, pH 7.4), MES (100 mM, pH 6.0), and N-cyclohexyl-2-aminoethanesulfonic acid (CHES, 100 mM, pH 9.0) buffer.

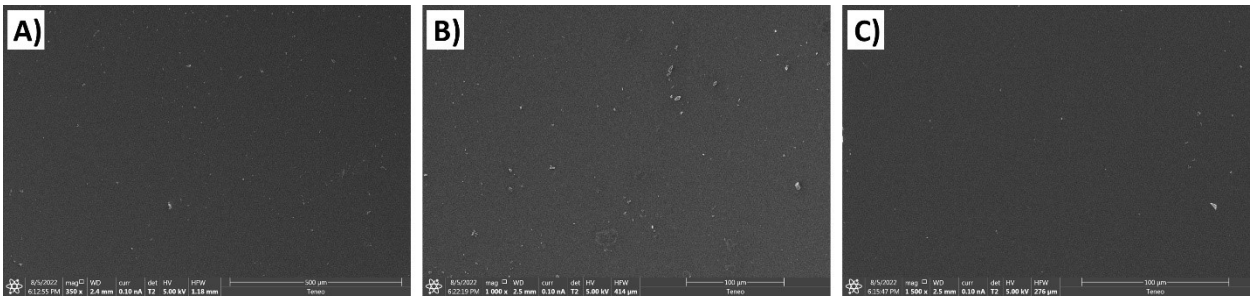

Figure 5.28. SEM visualization of **E1K2** (1 mM) incubated in (A) MOPS (100 mM, pH 7.4), (B) MES (100 mM, pH 6.0) and (C) CHES buffer (100 mM, pH 9.0)

5.3.9 E1K2-Ligand

While **E1K2** did not self-assemble, this peptide building block may potentially assemble with the addition of metal binding ligands nitrilotriacetic acid (NTA) and di-histidine at the N- and C-terminus, respectively (**E1K2-Ligand**). With this in mind, the peptide (1 mM) was added to MOPS buffer (100 mM, pH 7.4) with either $ZnCl_2$ or $CoCl_2$ (1 mM) for 1 hr. While a precipitate did occur upon addition of zinc or cobalt ions, only amorphous materials were obtained (**Figure 5.29**). This morphology could potentially be the result of the antiparallel orientation of the coiled-coil. With each face of the coiled-coil containing both NTA and di-histidine, it is possible for a single coiled-coil to create a complete metal-ligand complex rather than creating head-to-tail assembly like the parallel GCN4 sequences. Consequently, this potential interaction would disrupt any defined morphology from forming.

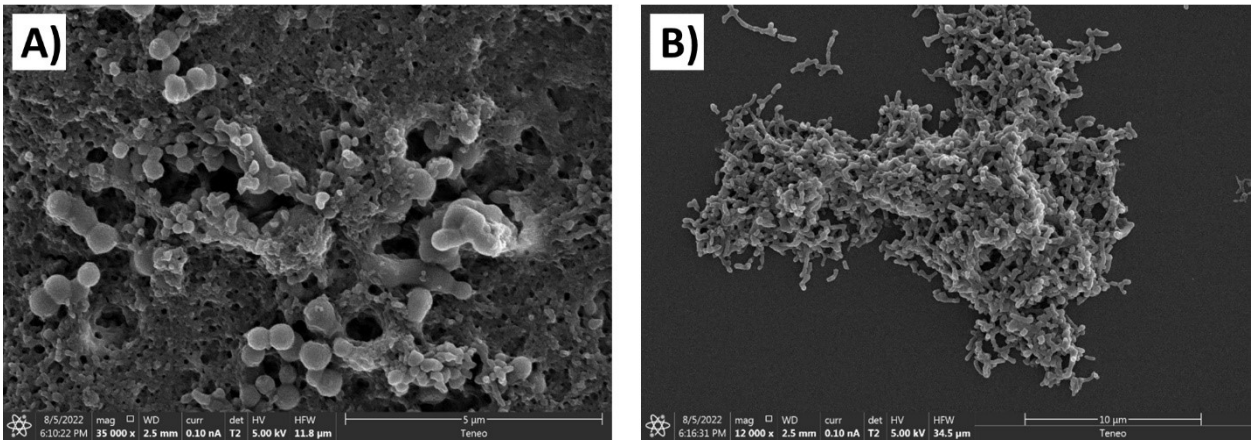

Figure 5.29. SEM visualization of **E1K2-Ligand** (1 mM) in MOPS buffer (100 mM, pH 7.4) after 1 hr with (A) $ZnCl_2$ (1 mM) and (B) $CoCl_2$ (1 mM).

5.4 Conclusion

To summarize, the peptide **TriNL** was strategically modified at central, solvent exposed position 20 from asparagine to cysteine (N20C) to create a self-replicating peptide system. Cysteine and thioester fragments **N20C F1** and **N20C F2**, respectively, showed increase in α-helicity in the presence of the full length **N20C FL** peptide and upon native chemical ligation, assembled into large nanorods. The size of the resulting nanorods were controlled through varying the number of nucleated seeds added to the ligation system. This discovery gave insight on potential multi-step peptide assemblies utilizing preformed nucleated seeds. While other cysteine modifications were tested, no peptide system exhibited auto-catalytic behavior for the native chemical ligation reaction.

5.5 Materials and Methods

5.5.1 Materials

All amino acids and reagents for peptide synthesis were purchased from ChemPep or Chem-Impex. All solvents were purchased from Fisher Scientific. Diisopropylethylamine (DIEA) was purchased from Alfa Aesar. Triisopropylsilane (TIPS), phenylsilane, tetrakis(triphenylphosphine)palladium(0), N,N'-Diisopropylcarbodiimide (DIC), and piperidine were purchased from Sigma-Aldrich. Rink Amide resin LL was purchased from CEM, and Fmoc-Glu-(Wang resin)-OAllyl was purchased from aapptec. Tris(2-carboxyethyl)phosphine (TCEP) was purchased from GoldBio. Hydroxybenzotriazole (HOBT) and sodium 2-mercaptoethanesulfonate (Mesna) were purchased from Oakwood Chemical. The chemical 3,6-dioxa-1,8-ocatanedithiol (DODT) was purchased from TCI.

5.5.2 Peptide Amide Synthesis and Purification

TriNL, all full-length peptides, and all cysteine fragments (F1) were synthesized using standard Fmoc-based chemistry on Rink Amide ProTide Resin (low loading, 300 mg, 0.06 mmol). The first amino acid (4 eq, 0.24 mmol) was coupled on resin with hexafluorophosphate azabenzotriazole tetramethyl uronium (HATU) and diisopropylethylamine (8 eq, 0.48 mmol) in dimethylformamide (DMF, 10 mL) for 2.5 hrs. The resin was washed with DMF (3 x 10 mL),

dichloromethane (DCM, 3 x 10 mL), methanol (MeOH, 3 x 10 mL), DCM (3 x 10 mL), and DMF (3 x 10 mL). The newly added amino acid was subsequently deprotected in 25% piperidine in DMF (v/v, 10 mL) for 30 min. After washing like above, the next amino acid was coupled. **TriNL** and all full-length peptides were acetylated using acetic anhydride (5%) and DIEA (8.5%) (v/v) in DMF (10 mL) for 25 min. The resins were dried, and the peptides were cleaved from resin using a 92.5% trifluoroacetic acid (TFA), 2.5% TIPS, 2.5% H_2O, and 2.5% DODT (v/v) cocktail (10 mL) for 2.5 hrs. The cocktail solution was concentrated under reduced pressure, and the peptide was precipitated using cold diethyl ether (30 mL). The solid was centrifuged at 2000 g, decanted, and dissolved in a 10 mg/mL solution with water. The peptides were purified to homogeneity via reverse-phase high performance liquid chromatography (RP-HPLC) using a Luna C18 semi-prep column with an eluent consisting of solvent A (CH_3CN/0.1% TFA) and solvent B (H_2O/0.1% TFA), a 60-min gradient consisting of 20% to 70% A (Full-length peptides) or 5% to 45% A (cysteine fragment peptides) and a flow rate of 12 mL/min. The peptides were characterized via matrix-assisted laser desorption ionization time-of-flight (MALDI-ToF) mass spectrometry.

5.5.3 Peptide Thioester Synthesis and Exchange

The thioester fragments (F2), with the exception of H17C F2, were all synthesized on Fmoc-Glu-(Wang resin)-OAllyl resin (300 mg, 0.12 mmol). After standard solid-phase peptide synthesis (see Section 5.5.2), the peptide underwent an allyl deprotected using $Pd(PPh_3)_4$ (0.5 eq, 69 mg, 0.06 mmol) and $PhSiH_3$ (40 eq, 4.8 mmol, 590 μL) in DCM (10 mL) for 30 minutes. After washing as described in Section 5.5.2, this process was repeated. Thioesterification was performed on resin with the addition of benzyl mercaptan (24 eq, 2.9 mmol, 335 μL), HOBt (30 eq, 486 mg, 3.6 mmol), DIC (30 eq, 3.6 mmol, 560 μL) and DIEA (36 eq, 4.3 mmol, 750 μL) in DCM/DMF (4:1, 10 mL) for 16 hrs. The resin was dried, and the peptide was cleaved using a TFA cocktail (95% TFA, 2.5% TIPS, 2.5% water) for 2.5 hrs. The cocktail solution was concentrated under reduced pressure, and the peptide was precipitated using cold diethyl ether (30 mL). The solid was centrifuged at 2000 g, decanted, and dissolved in a 10 mg/mL solution with water. The peptide was purified to homogeneity via RP-HPLC using a Luna C18 semi-prep column with an eluent consisting of solvent A (CH_3CN/0.1% TFA) and solvent B (H_2O/0.1% TFA), a 60-min gradient consisting of 20-70% A and a flow rate of 12 mL/min. The peptide was characterized via MALDI-ToF mass spectrometry. After lyophilization, the peptide (0.012 mmol) was dissolved in phosphate

buffer (200 mM, pH 6.5, 8 mL) with guanidine HCl (6 M), TCEP (50 mM), and Mesna (200 mM) and stirred for 12 hrs. The peptide was purified using the same conditions as the benzyl thioester and characterized via MALDI-ToF mass spectrometry.

5.5.4 H17C F2 Thioester Synthesis

H17C F2 was synthesized on hydrazine 2-chlorotrityl resin (300 mg, 0.15 mmol) using standard solid-phase peptide synthesis and acetylated after the last amino acid (see section 5.5.2). The resin was dried and the peptide was cleaved using a TFA cocktail (95% TFA, 2.5% TIPS, 2.5% water) for 2.5 hrs. The cocktail solution was concentrated under reduced pressure, and the peptide was precipitated using cold diethyl ether (30 mL). The solid was centrifuged at 2000 g, decanted, and dissolved in a 10 mg/mL solution with water. The peptide was purified to homogeneity via RP-HPLC using a Luna C18 semi-prep column with an eluent consisting of solvent A (CH_3CN/0.1% TFA) and solvent B (H_2O/0.1% TFA), a 60-min gradient consisting of 20-70% A and a flow rate of 12 mL/min. After lyophilization, the peptide (0.015 mmol) was dissolved in water (15 mL) with NaH_2PO_4 (200 mM, pH 3.0), guanidine hydrochloride (6 M) and $NaNO_2$ (10 eq, 15 mM) on ice for 30 min. The reaction was warmed to room temperature, Mesna (130 eq, 200 mM) was added, and the pH was raised to 7 using sodium NaOH (10 M, 0.5 mL). After 10 min, the reaction was purified using the same conditions as the benzyl thioester and characterized via MALDI-ToF mass spectrometry.

5.5.5 Circular Dichroism

TriNL, **N20C FL**, **N20C F1**, **N20C F2,** and **H17C FL** solutions (50 μM) were prepared in phosphate buffer (20 mM, pH 7.4) in 200 μL total volume. Solutions of either **N20C F1** or **N20C F2** (50 μM) with **N20C FL** (12.5 μM) were also prepared in phosphate buffer (20 mM, pH 7.4). A mixture of **N20C F1** and **N20C F2** (25 μM each) were also prepared in phosphate buffer (20 mM, pH 7.4) and a CD spectrum was immediately taken. All other peptides were prepared in citrate buffer (20 mM, pH 3.0). The CD spectra were taken using a JASCO J-810 CD spectropolarimeter at room temperature averaging three scans between 190 nm and 260 nm. The data pitch was 0.1 nm with a 1-nm bandwidth and a scan rate of 100 nm/min with a 1 s response time.

5.5.6 Peptide Assemblies

TriNL and **N20C FL** (5 mM, 10 μL) were added to MOPS buffer (250 mM, pH 7.4, 25 μL) and water (15 μL). Following a 30 min incubation at room temperature, the assemblies were centrifuged at 10,000 g for 3 min. The supernatant was removed and replaced with water (50 μL). This process was repeated two more times. The pelleted assemblies were resuspended and stored in 50 μL water.

5.5.7 Native Chemical Ligation – Dilute Conditions

All stock solutions were degassed for 10 minutes prior to ligation. The peptides **N20C F1** (100 μM) and **N20C FL** (0, 10, 25, 50 μM) were added to MOPS (12.5 mM, pH 7.4) and TCEP (2 mM) followed by **N20C F2** (100 μM) in 300 μL total volume. At given timepoints, 10 μL samples were directly injected to an ultra-performance liquid chromatography (UPLC) C18 column using an autosampler for analysis. The eluent conditions with a flow rate of 0.5 mL/minute were as follows. For 1 minute, the column was treated with an isocratic eluent of 15% acetonitrile/85% water with 0.1% TFA for 1 minute. For the next 5 minutes, the column was subject to an eluent gradient from 15% acetonitrile up to 35% acetonitrile. After that, the column was subjected to an eluent gradient from 35% acetonitrile up to 65% acetonitrile over 5 minutes. The area under the **N20C FL** peak at t = 0 was subtracted to obtain product formed from the native chemical ligation reaction.

5.5.8 Native Chemical Ligation – Concentrated Conditions

All stock solutions were degassed for 10 minutes prior to ligation. The peptides **N20C F1** (1 mM) and **N20C FL** (0, 50, 100, 200 mM) were added to MOPS (125 mM, pH 7.4) and TCEP (20 mM) followed by **N20C F2** (1 mM) in 300 μL total volume, and the reaction was gently spun for 8 hrs. At given timepoints, an aliquot (25 μL) was removed and diluted with water (70 μL) and HCl (10%, 5 μL) to dissolve any assembly. Each aliquot was analyzed using UPLC using the gradient conditions described in Section 5.5.7. The same procedure was completed with every peptide mutation. The area under the full-length peptide peak at t = 0 was subtracted to obtain product formed from the native chemical ligation reaction. After 8 hrs, the assemblies were centrifuged at 10,000 g for 3 min. The supernatant was removed and replaced with water (50 μL).

This process was repeated two more times. The pelleted crystals were resuspended and stored in 50 μL water.

5.5.9 Scanning Electron Microscopy

Aliquots of the assemblies described in Section 5.5.6 and Section 5.58 (3 μL) were placed on a glass coverslip attached to a metal stub with copper tape. The sample was allowed to air dry for 1 hr and coated with platinum for 60 seconds. Samples were imaged using an FEI Teneo Volumescope field emission scanning electron microscope using Everhart-Thornley detector (ETD) for magnifications < 10,000 or the high-resolution through the lens detector (TLD) for magnifications ≥ 10,000. Samples were imaged at an accelerating voltage of 5 kV and a working distance of 2-4 mm with a 30-μm aperture.

5.5.10 Transmission Electron Microscopy

Aliquots of the assemblies described in Section 5.5.6 and Section 5.58 (3 μL) were placed onto a glow discharged 400-mesh copper grid coated in formvar with a carbon film (Electron Microscopy Sciences) and allowed to absorb for 1 min. The droplet was wicked away and stained using 2% uranyl acetate (Electron Microscopy Sciences). The assembly was visualized using a FEI Tecnai T20 transmission electron microscope operated at 100 kV, with a spot size of 3, 200 μm condenser aperture, and 70 μm objective aperture. Images were captured using a Gatan US1000 2Kx2K CCD camera (Scientific Instruments and Application).

5.6 References

(1) Ruiz-Mirazo, K.; Briones, C.; De La Escosura, A. Prebiotic Systems Chemistry: New Perspectives for the Origins of Life. *Chem. Rev.* **2014**, *114* (1), 285–366. https://doi.org/10.1021/cr2004844.

(2) Issac, R.; Ham, Y. W.; Chmielewski, J. The Design of Self-Replicating Helical Peptides. *Curr. Opin. Struct. Biol.* **2001**, *11* (4), 458–463. https://doi.org/10.1016/S0959-440X(00)00233-5.

(3) von Kiedrowski, G. A Self-Replicating Hexadeoxynucleotide. *Angew. Chemie Int. Ed. English* **1986**, *25* (10), 932–935. https://doi.org/10.1002/anie.198609322.

(4) Lee, D. H.; Granja, J. R.; Martinez, J. A.; Severin, K.; Ghadiri, M. R. A Self-Replicating Peptide. *Nature*. 1996, pp 525–528. https://doi.org/10.1038/382525a0.

(5) Severin, K.; Lee, D. H.; Martinez, J. A.; Ghadiri, M. R. Peptide Self-Replication via Template-Directed Ligation. *Chemistry - A European Journal*. 1997, pp 1017–1024. https://doi.org/10.1002/chem.19970030706.

(6) Yao, S.; Ghosh, I.; Zutshi, R.; Chmielewski, J. A PH-Modulated, Self-Replicating Peptide. *J. Am. Chem. Soc.* **1997**, *119* (43), 10559–10560. https://doi.org/10.1021/ja9710619.

(7) Yao, S.; Ghosh, I.; Zutshi, R.; Chmielewski, J. Selective Amplification by Auto- and Cross-Catalysis in a Replicating Peptide System. *Nature* **1998**, *396* (6710), 447–450. https://doi.org/10.1038/24814.

(8) Yao, S.; Ghosh, I.; Zutshi, R.; Chmielewski, J. A Self-Replicating Peptide under Ionic Control. *Angew. Chemie - Int. Ed.* **1998**, *37* (4), 478–481. https://doi.org/10.1002/(SICI)1521-3773(19980302)37:4<478::AID-ANIE478>3.0.CO;2-V.

(9) Saghatelian, A.; Yokobayashi, Y.; Soltani, K.; Ghadiri, M. R. A Chiroselective Peptide Replicator. *Polym. Bull* **2001**, *1* (February), 797–801. https://doi.org/10.1038/35057238.

(10) Kennan, A. J.; Haridas, V.; Severin, K.; Lee, D. H.; Ghadiri, M. R. A de Novo Designed Peptide Ligase: A Mechanistic Investigation. *J. Am. Chem. Soc.* **2001**, *123* (9), 1797–1803. https://doi.org/10.1021/ja991266c.

(11) Issac, R.; Chmielewski, J. Approaching Exponential Growth with a Self-Replicating Peptide. *J. Am. Chem. Soc.* **2002**, *124* (24), 6808–6809. https://doi.org/10.1021/ja026024i.

(12) Li, X.; Chmielewski, J. Peptide Self-Replication Enhanced by a Proline Kink. *J. Am. Chem. Soc.* **2003**, *125* (39), 11820–11821. https://doi.org/10.1021/ja036569s.

(13) Ashkenasy, G.; Jagasia, R.; Yadav, M.; Ghadiri, M. R. Design of a Directed Molecular Network. *Proc. Natl. Acad. Sci. U. S. A.* **2004**, *101* (30), 10872–10877. https://doi.org/10.1073/pnas.0402674101.

(14) Ashkenasy, G.; Ghadiri, M. R. Boolean Logic Functions of a Synthetic Peptide Network. *J. Am. Chem. Soc.* **2004**, *126* (36), 11140–11141. https://doi.org/10.1021/ja046745c.

(15) Jacqui M. A. Carnall; Waudby, C. A.; Belenguer, A. M.; Marc C. A. Stuart; Peyralans, J. J.-P.; Sijbren Otto. Mechanosensitive Self-Replication Driven by Self-Organization. *Science* **2010**, *327* (5972), 1501–1502. https://doi.org/10.1126/science.1182767.

(16) Colomb-Delsuc, M.; Mattia, E.; Sadownik, J. W.; Otto, S. Exponential Self-Replication Enabled through a Fibre Elongation/Breakage Mechanism. *Nat. Commun.* **2015**, *6* (May). https://doi.org/10.1038/ncomms8427.

(17) Yang, S.; Schaeffer, G.; Mattia, E.; Markovitch, O.; Liu, K.; Hussain, A. S.; Ottelé, J.; Sood, A.; Otto, S. Chemical Fueling Enables Molecular Complexification of Self-Replicators. *Angew. Chemie - Int. Ed.* **2021**, *60* (20), 11344–11349. https://doi.org/10.1002/anie.202016196.

(18) Liu, B.; Pappas, C. G.; Ottelé, J.; Schaeffer, G.; Jurissek, C.; Pieters, P. F.; Altay, M.; Marić, I.; Stuart, M. C. A.; Otto, S. Spontaneous Emergence of Self-Replicating Molecules Containing Nucleobases and Amino Acids. *J. Am. Chem. Soc.* **2020**, *142* (9), 4184–4192. https://doi.org/10.1021/jacs.9b10796.

(19) Malakoutikhah, M.; Peyralans, J. J. P.; Colomb-Delsuc, M.; Fanlo-Virgós, H.; Stuart, M. C. A.; Otto, S. Uncovering the Selection Criteria for the Emergence of Multi-Building-Block Replicators from Dynamic Combinatorial Libraries. *J. Am. Chem. Soc.* **2013**, *135* (49), 18406–18417. https://doi.org/10.1021/ja4067805.

(20) Pappas, C. G.; Mandal, P. K.; Liu, B.; Kauffmann, B.; Miao, X.; Komáromy, D.; Hoffmann, W.; Manz, C.; Chang, R.; Liu, K.; Pagel, K.; Huc, I.; Otto, S. Emergence of Low-Symmetry Foldamers from Single Monomers. *Nat. Chem.* **2020**, *12* (12), 1180–1186. https://doi.org/10.1038/s41557-020-00565-2.

(21) Pappas, C. G.; Liu, B.; Marić, I.; Ottelé, J.; Kiani, A.; Van Der Klok, M. L.; Onck, P. R.; Otto, S. Two Sides of the Same Coin: Emergence of Foldamers and Self-Replicators from Dynamic Combinatorial Libraries. *J. Am. Chem. Soc.* **2021**, *143* (19), 7388–7393. https://doi.org/10.1021/jacs.1c00788.

(22) Rubinov, B.; Wagner, N.; Rapaport, H.; Ashkenasy, G. Self-Replicating Amphiphilic β-Sheet Peptides. *Angew. Chemie - Int. Ed.* **2009**, *48* (36), 6683–6686. https://doi.org/10.1002/anie.200902790.

(23) Rubinov, B.; Wagner, N.; Matmor, M.; Regev, O.; Ashkenasy, N.; Ashkenasy, G. Transient Fibril Structures Facilitating Nonenzymatic Self-Replication. *ACS Nano* **2012**, *6* (9), 7893–7901. https://doi.org/10.1021/nn302223v.

(24) Nanda, J.; Rubinov, B.; Ivnitski, D.; Mukherjee, R.; Shtelman, E.; Motro, Y.; Miller, Y.; Wagner, N.; Cohen-Luria, R.; Ashkenasy, G. Emergence of Native Peptide Sequences in Prebiotic Replication Networks. *Nat. Commun.* **2017**, *8* (1), 1–8. https://doi.org/10.1038/s41467-017-00463-1.

(25) Harbury, P. B.; Zhang, T.; Kim, P. S.; Alber, T. A Switch between Two-, Three-, and Four-Stranded Coiled Coils in GCN4 Leucine Zipper Mutants. *Science* **1993**, *262* (5138), 1401–1407. https://doi.org/10.1126/science.8248779.

(26) Harbury, P. B.; Kim, P. S.; Alber, T. Crystal Structure of an Isoleucine-Zipper Trimer. *Nature*. 1994, pp 80–83. https://doi.org/10.1038/371080a0.

(27) Nambiar, M.; Nepal, M.; Chmielewski, J. Self-Assembling Coiled-Coil Peptide Nanotubes with Biomolecular Cargo Encapsulation. *ACS Biomater. Sci. Eng.* **2019**, *5* (10), 5082–5087. https://doi.org/10.1021/acsbiomaterials.9b01304.

(28) Jorgensen, M. D.; Chmielewski, J. Co-Assembled Coiled-Coil Peptide Nanotubes with Enhanced Stability and Metal-Dependent Cargo Loading. *ACS Omega* **2022**, *7*, 20945–20951. https://doi.org/10.1021/acsomega.2c01669.

(29) Agouridas, V.; El Mahdi, O.; Diemer, V.; Cargoët, M.; Monbaliu, J. C. M.; Melnyk, O. Native Chemical Ligation and Extended Methods: Mechanisms, Catalysis, Scope, and Limitations. *Chem. Rev.* **2019**, *119* (12). https://doi.org/10.1021/acs.chemrev.8b00712.

(30) Ficht, S.; Payne, R. J.; Guy, R. T.; Wong, C. H. Solid-Phase Synthesis of Peptide and Glycopeptide Thioesters through Side-Chain-Anchoring Strategies. *Chem. - A Eur. J.* **2008**, *14* (12), 3620–3629. https://doi.org/10.1002/chem.200701978.

(31) Thomas, F.; Burgess, N. C.; Thomson, A. R.; Woolfson, D. N. Controlling the Assembly of Coiled-Coil Peptide Nanotubes. *Angew. Chemie - Int. Ed.* **2016**, *55* (3), 987–991. https://doi.org/10.1002/anie.201509304.

(32) Johnson, E. C. B.; Kent, S. B. H. Insights into the Mechanism and Catalysis of the Native Chemical Ligation Reaction. *J. Am. Chem. Soc.* **2006**, *128* (20), 6640–6646. https://doi.org/10.1021/ja058344i.

(33) Fang, G.-M.; Li, Y.-M.; Shen, F.; Huang, Y.-C.; Li, J.-B.; Lin, Y.; Cui, H.-K.; Liu, L. Protein Chemical Synthesis by Ligation of Peptide Hydrazides. *Angew. Chemie* **2011**, *123* (33), 7787–7791. https://doi.org/10.1002/ange.201100996.

(34) Zheng, J. S.; Tang, S.; Qi, Y. K.; Wang, Z. P.; Liu, L. Chemical Synthesis of Proteins Using Peptide Hydrazides as Thioester Surrogates. *Nat. Protoc.* **2013**, *8* (12), 2483–2495. https://doi.org/10.1038/nprot.2013.152.

(35) Lau, S. Y. M.; Taneja, A. K.; Hodges, R. S. Synthesis of a Model Protein of Defined Secondary and Quaternary Structure. Effect of Chain Length on the Stabilization and Formation of Two-Stranded α-Helical Coiled-Coils. *J. Biol. Chem.* **1984**, *259* (21), 13253–13261. https://doi.org/10.1016/s0021-9258(18)90686-1.

(36) Venyaminov, S. Y.; Baikalov, I. A.; Shen, Z. M.; Wu, C. S. C.; Yang, J. T. Circular Dichroic Analysis of Denatured Proteins: Inclusion of Denatured Proteins in the Reference Set. *Anal. Biochem.* **1993**, *214* (1), 17–24. https://doi.org/10.1006/abio.1993.1450.

(37) Yao, S.; Ghosh, I.; Zutshi, R.; Chmielewski, J. A PH-Modulated , Self-Replicating Peptide. *J. Am. Chem. Soc.* **1997**, *119*, 10559–10560. https://doi.org/10.1021/ja9710619.

(38) Vekilov, P. G. Nucleation. *Cryst. Growth Des.* **2010**, *10* (12), 5007–5019. https://doi.org/10.1021/cg1011633.

(39) Thanh, N. T. K.; Maclean, N.; Mahiddine, S. Mechanisms of Nucleation and Growth of Nanoparticles in Solution. *Chem. Rev.* **2014**, *114* (15), 7610–7630. https://doi.org/10.1021/cr400544s.

(40) Woolfson, D. N. Coiled-Coil Design: Updated and Upgraded. *Subcell. Biochem.* **2017**, *82*, 35–61. https://doi.org/10.1007/978-3-319-49674-0_2.

(41) Akey, D. L.; Malashkevich, V. N.; Kim, P. S. Buried Polar Residues in Coiled-Coil Interfaces. *Biochemistry* **2001**, *40* (21), 6352–6360. https://doi.org/10.1021/bi002829w.

(42) Zhou, N. E.; Kay, C. M.; Hodges, R. S. Synthetic Model Proteins. Positional Effects of Interchain Hydrophobic Interactions on Stability of Two-Stranded α-Helical Coiled-Coils. *J. Biol. Chem.* **1992**, *267* (4), 2664–2670. https://doi.org/10.1016/s0021-9258(18)45932-7.

APPENDIX: FIGURES

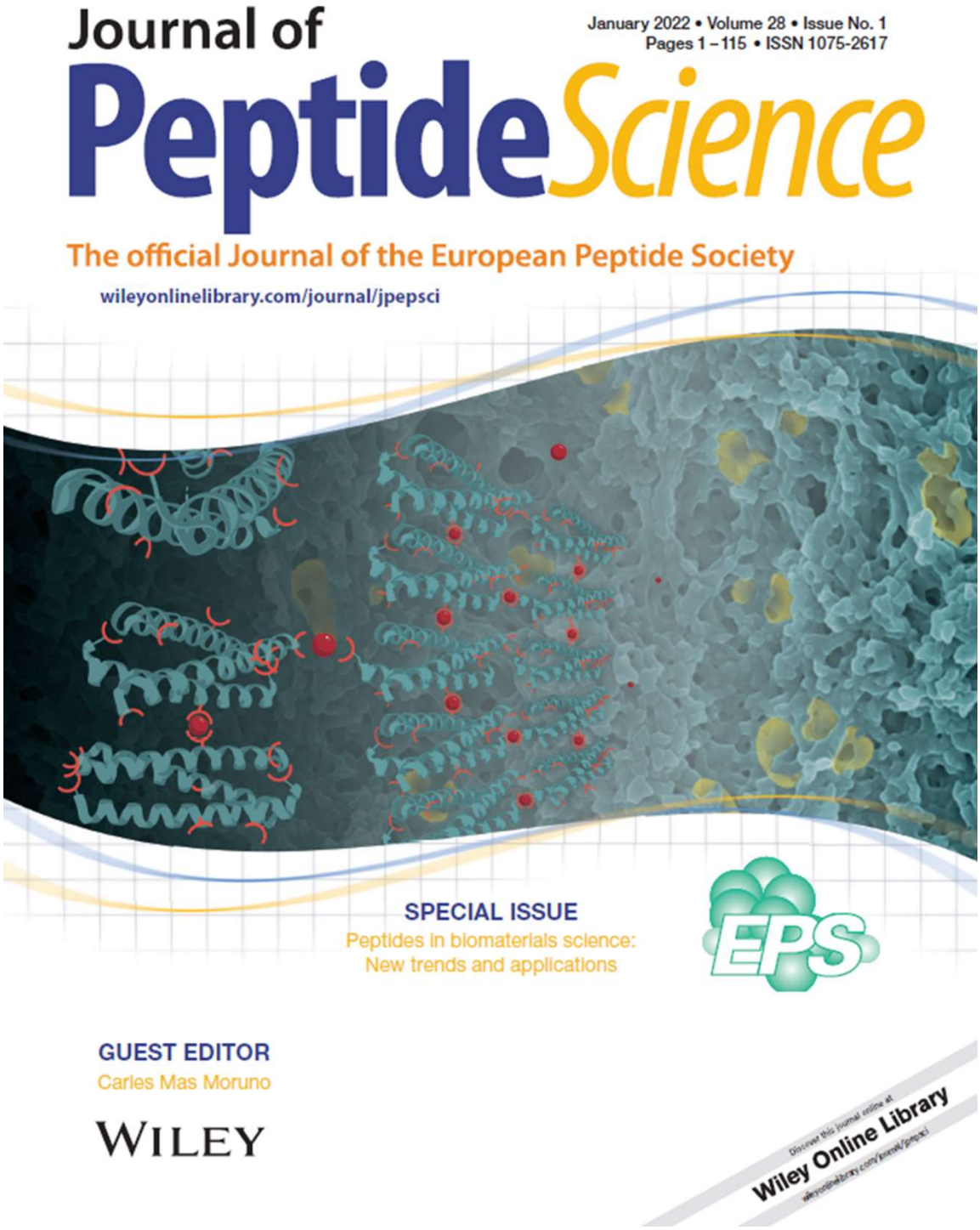

Figure A1. TriCross cover art for the Journal of Peptide Science's Special Issue - *Peptides in Biomaterials Science: New Trends and Applications*.

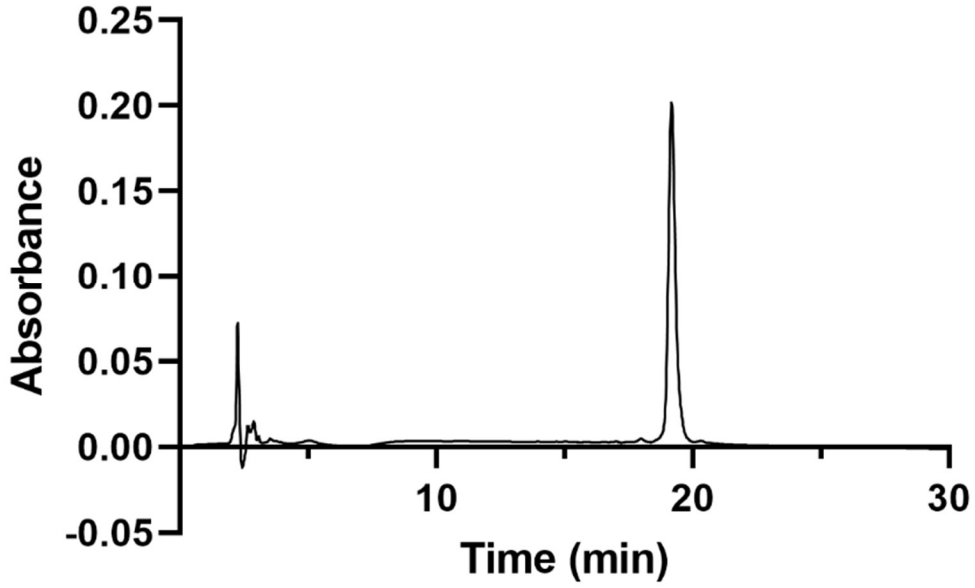

Figure A2. Purity trace of **TriCross** (214 nm) with a solvent gradient of 20-70% acetonitrile/water (0.1% TFA) for 30 min.

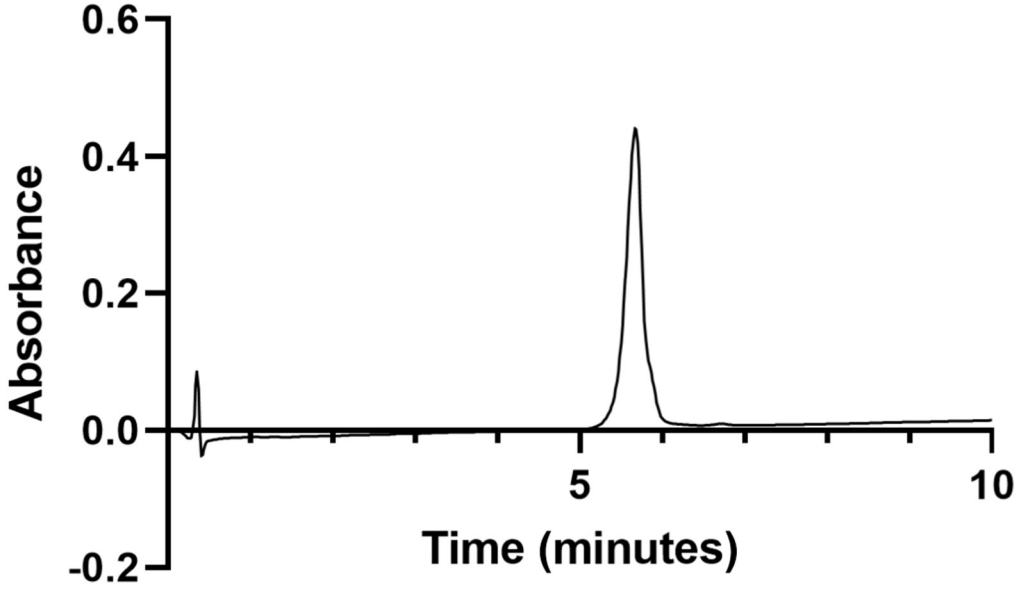

Figure A3. Purity trace of **HBN** (214 nm) with a solvent gradient of 5-25% acetonitrile/water (0.1% TFA) for 10 min.

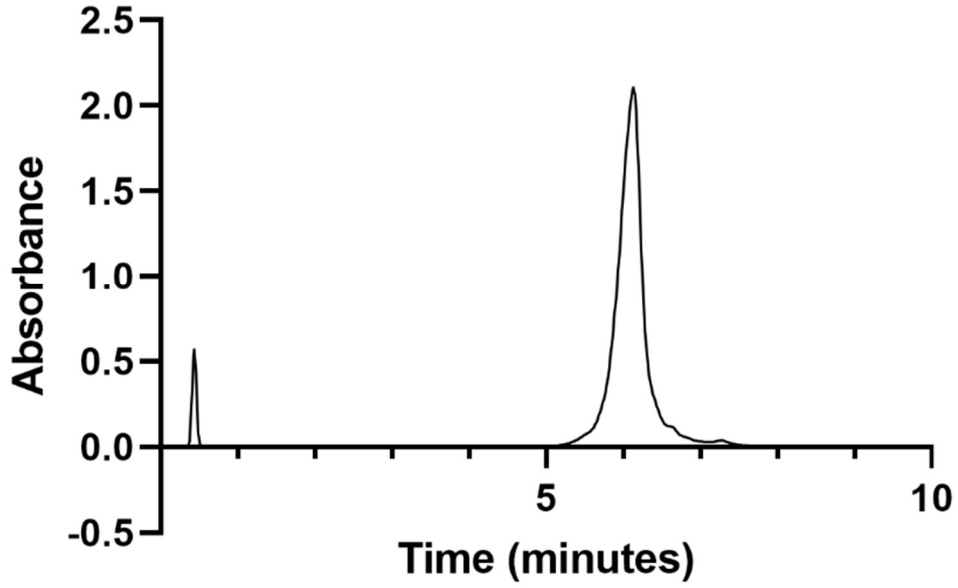

Figure A4. Purity trace of **HBRDGS** (214 nm) with a solvent gradient of 5-25% acetonitrile/water (0.1% TFA) for 10 min.

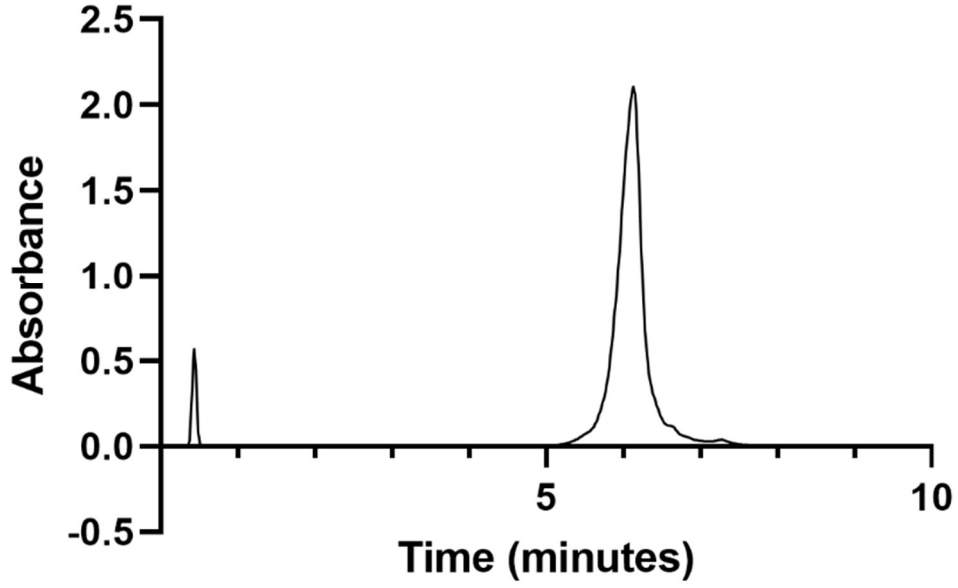

Figure A5. Purity trace of **RGDS-His$_7$** (214 nm) with a solvent gradient of 5-25% acetonitrile/water (0.1% TFA) for 10 min.

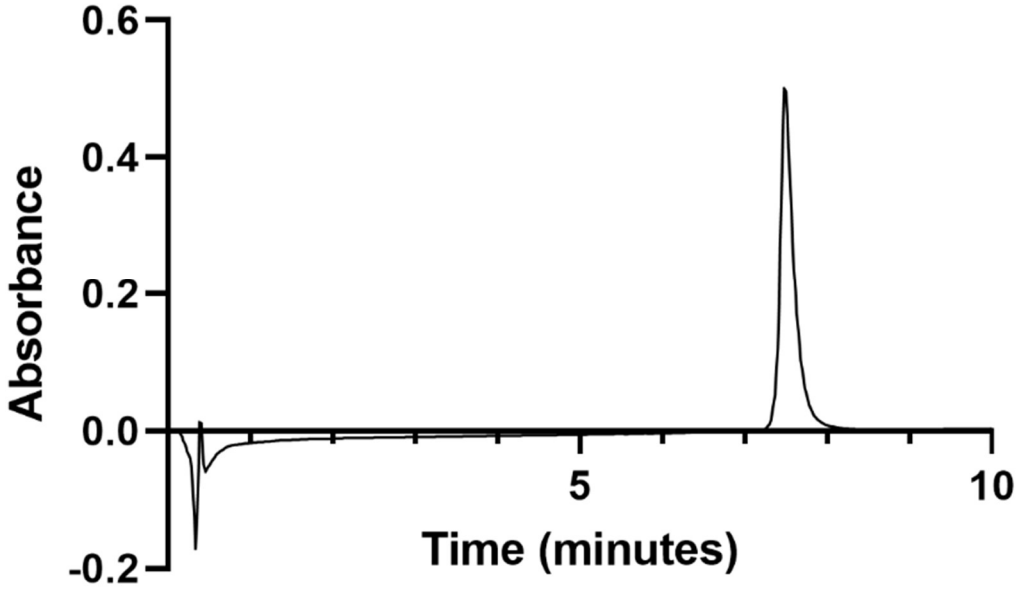

Figure A6. Purity trace of **IKVAV-His$_6$** (214 nm) with a solvent gradient of 5-25% acetonitrile/water (0.1% TFA) for 10 min.

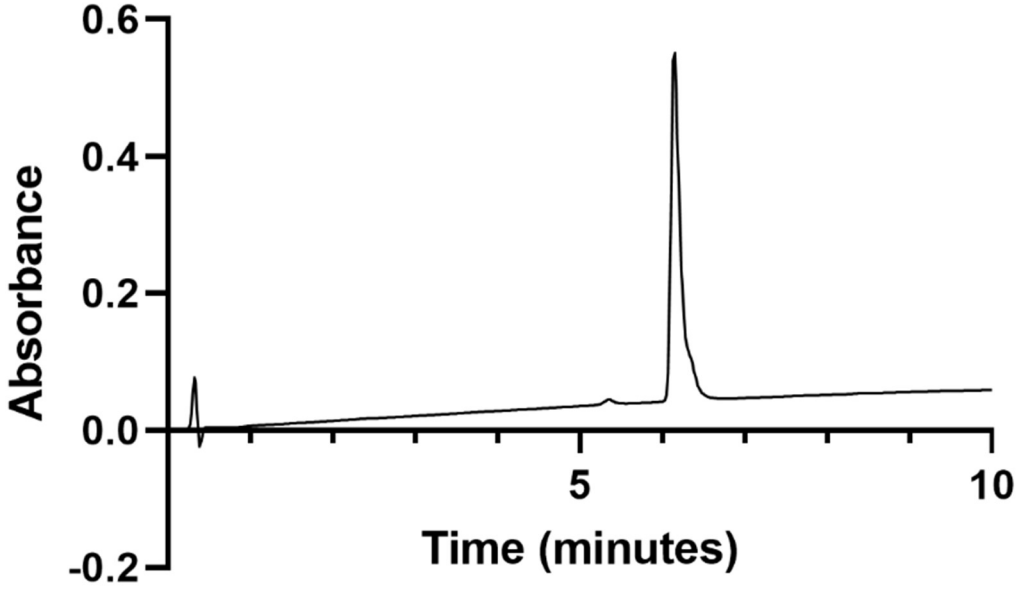

Figure A7. Purity trace of **TriNL** (214 nm) with a solvent gradient of 20-70% acetonitrile/water (0.1% TFA) for 10 min.

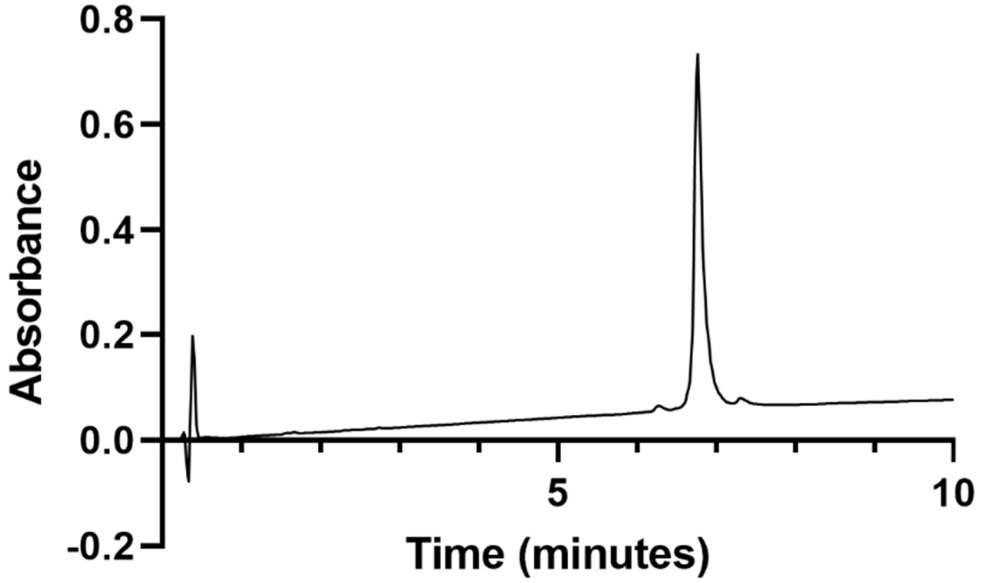

Figure A8. Purity trace of **TriNL-FL** (214 nm) with a solvent gradient of 20-70% acetonitrile/water (0.1% TFA) for 10 min.

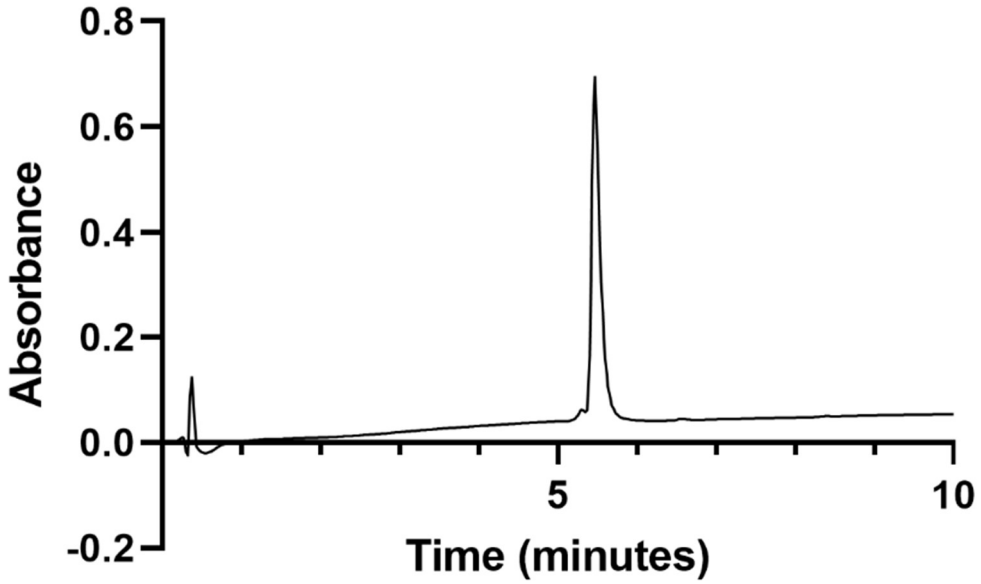

Figure A9. Purity trace of **p2L** (214 nm) with a solvent gradient of 20-70% acetonitrile/water (0.1% TFA) for 10 min.

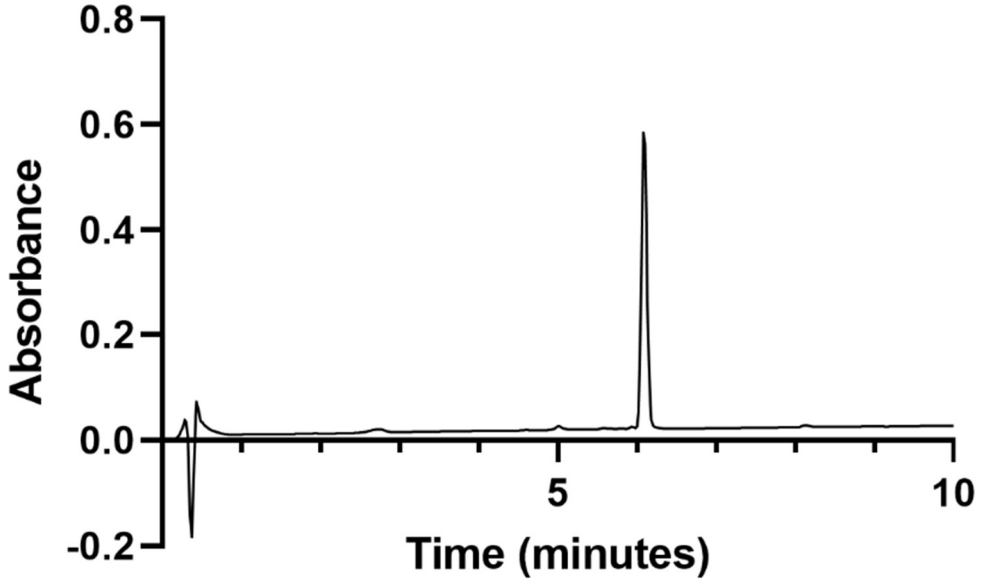

Figure A10. Purity trace of **Rh-Biotin** (214 nm) with a solvent gradient of 15-40% acetonitrile/water (0.1% TFA) for 10 min.

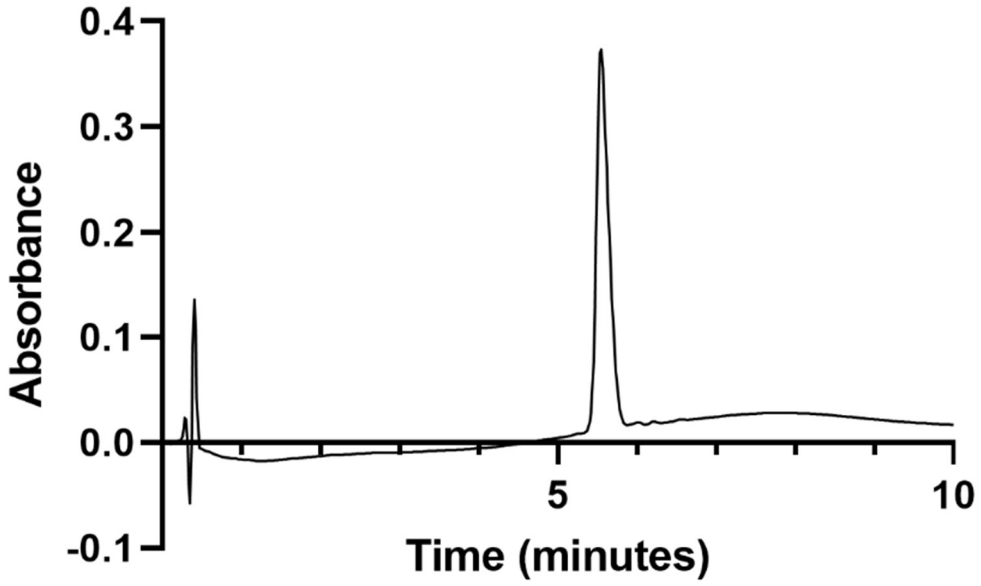

Figure A11. Purity trace of **Cou-His6** (214 nm) with a solvent gradient of 10-25% acetonitrile/water (0.1% TFA) for 10 min.

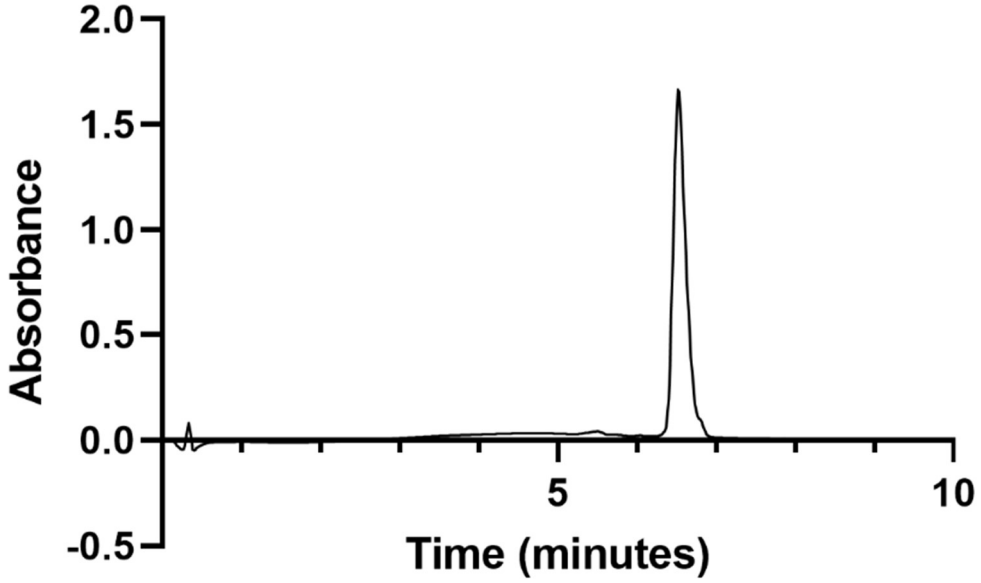

Figure A12. Purity trace of **N20C FL** (214 nm) with a solvent gradient of 20-70% acetonitrile/water (0.1% TFA) for 10 min.

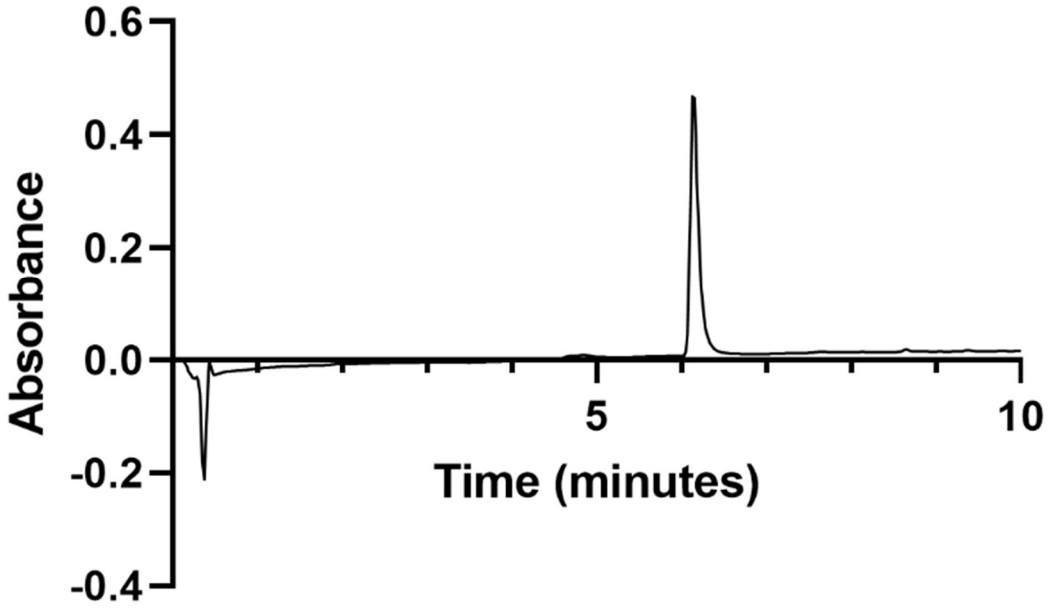

Figure A13. Purity trace of **N20C F1** (214 nm) with a solvent gradient of 5-45% acetonitrile/water (0.1% TFA) for 10 min.

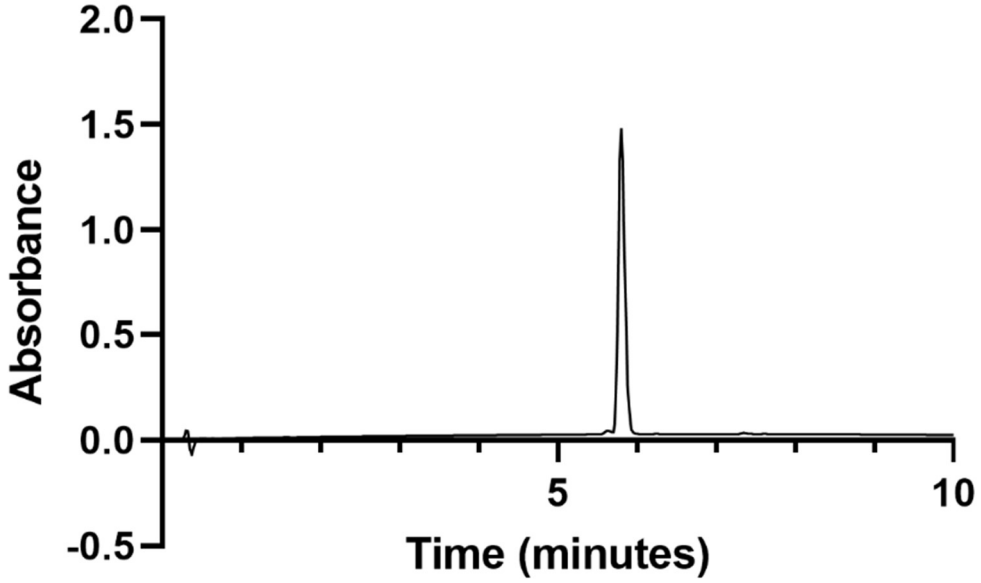

Figure A14. Purity trace of **N20C F2** (214 nm) with a solvent gradient of 20-70% acetonitrile/water (0.1% TFA) for 10 min.

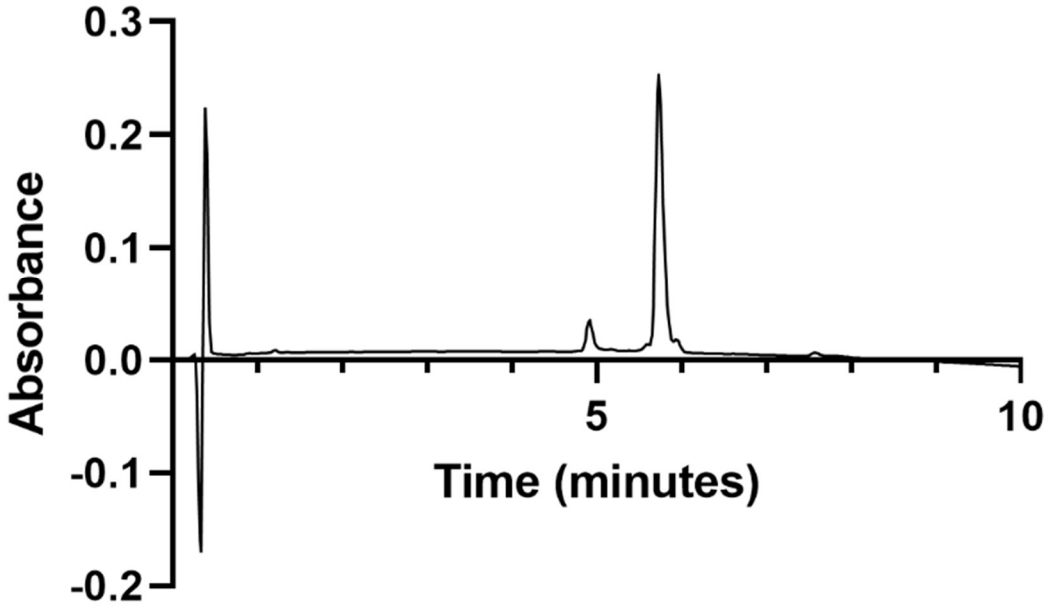

Figure A15. Purity trace of **H17C FL** (214 nm) with a solvent gradient of 30-70% acetonitrile/water (0.1% TFA) for 10 min.

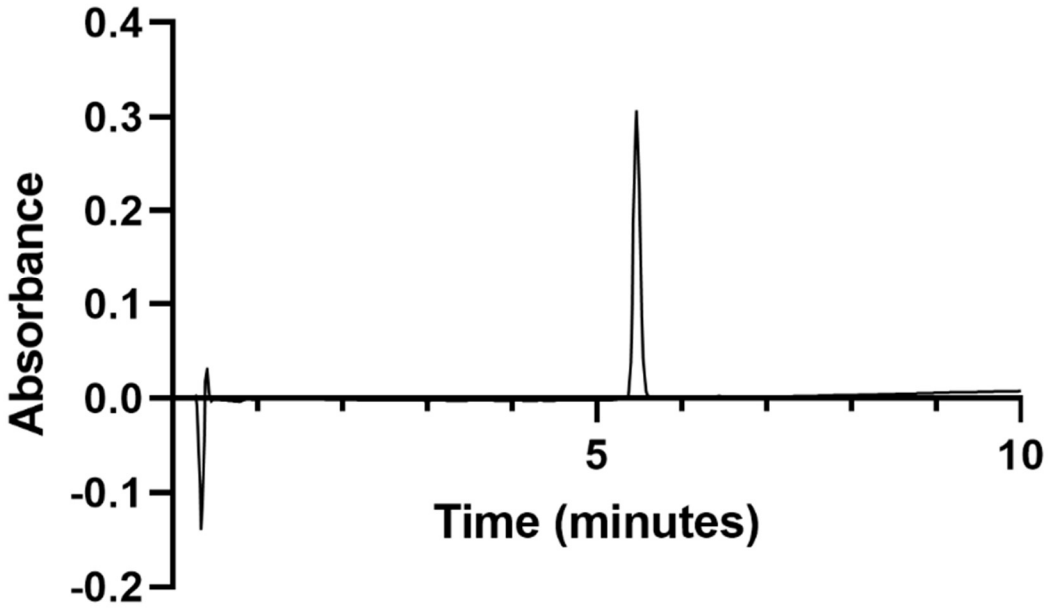

Figure A16. Purity trace of **H17C F1** (214 nm) with a solvent gradient of 15-50% acetonitrile/water (0.1% TFA) for 10 min.

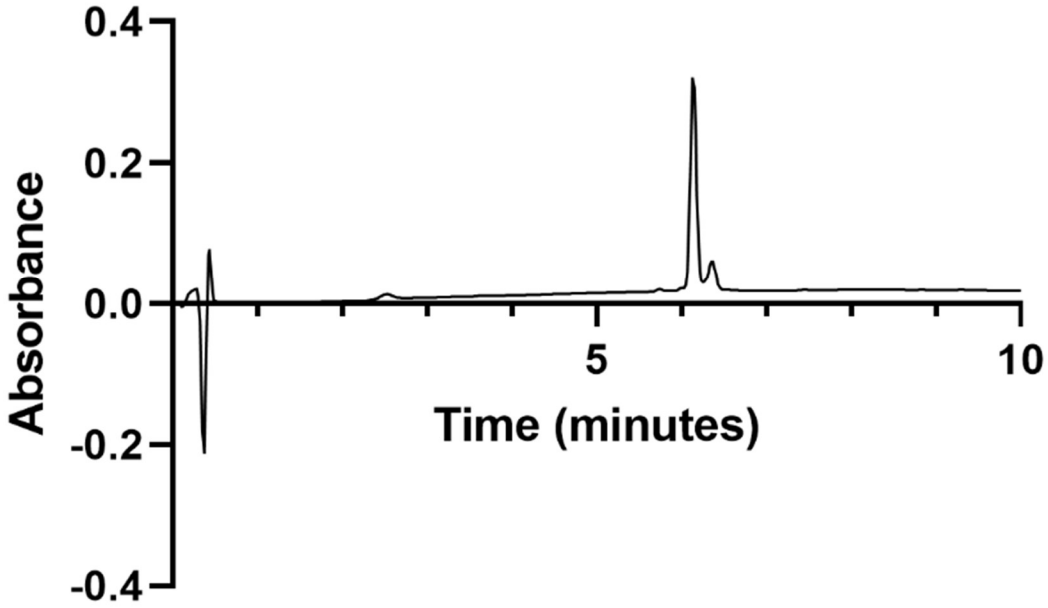

Figure A17. Purity trace of **H17C F2** (214 nm) with a solvent gradient of 15-60% acetonitrile/water (0.1% TFA) for 10 min.

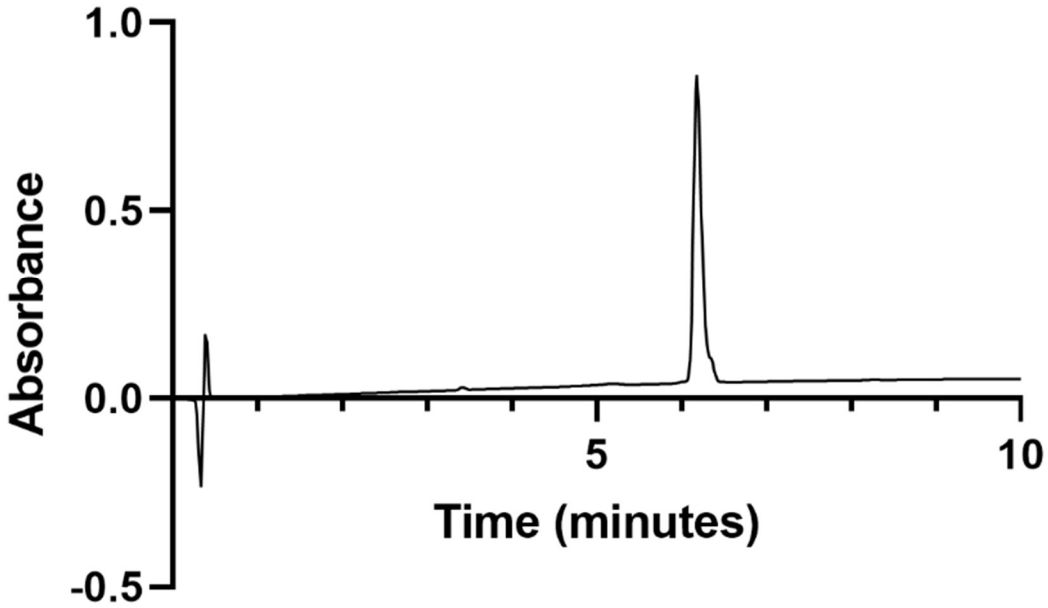

Figure A18. Purity trace of **N20C Truncated FL** (214 nm) with a solvent gradient of 20-70% acetonitrile/water (0.1% TFA) for 10 min.

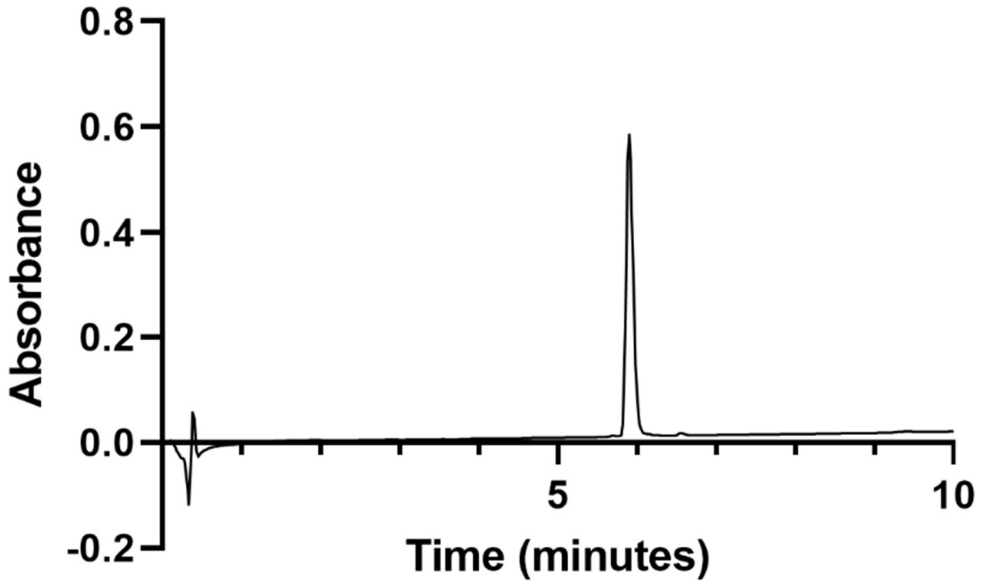

Figure A19. Purity trace of **N20C Truncated F1** (214 nm) with a solvent gradient of 5-45% acetonitrile/water (0.1% TFA) for 10 min.

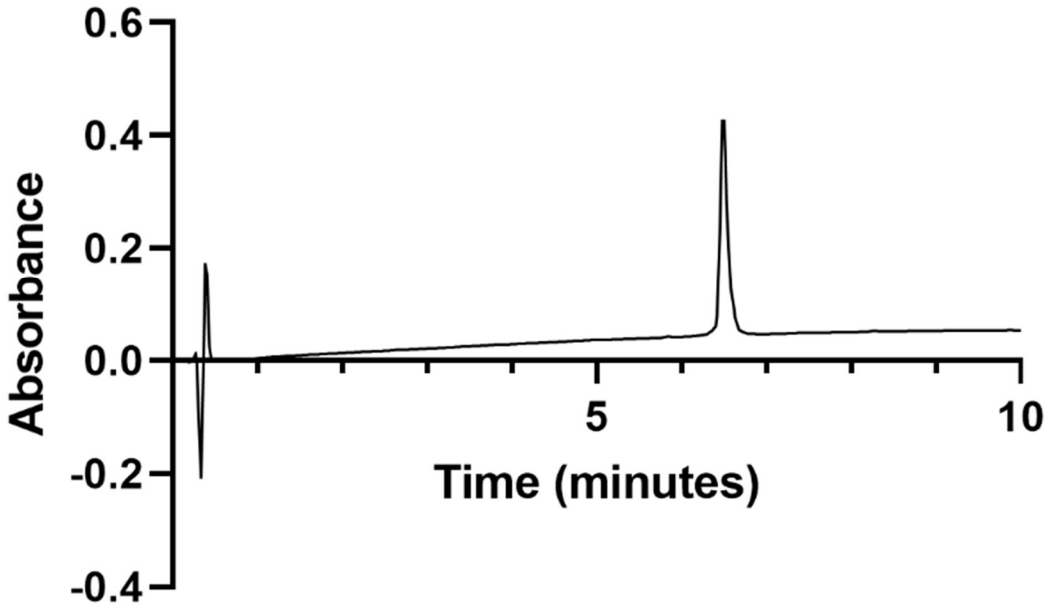

Figure A20. Purity trace of **H17P FL** (214 nm) with a solvent gradient of 20-70% acetonitrile/water (0.1% TFA) for 10 min.

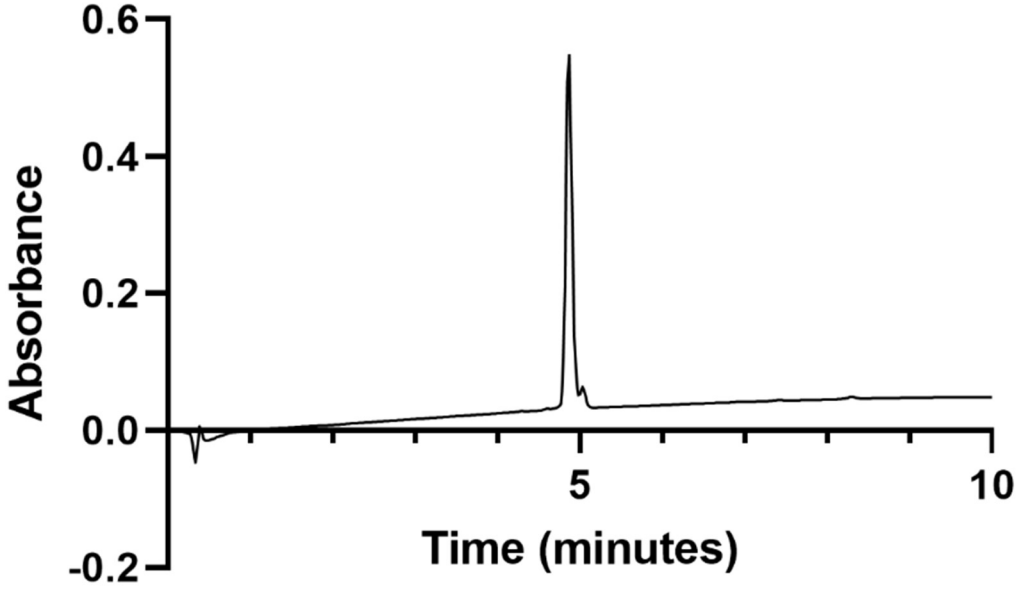

Figure A21. Purity trace of **I15N FL** (214 nm) with a solvent gradient of 20-70% acetonitrile/water (0.1% TFA) for 10 min.

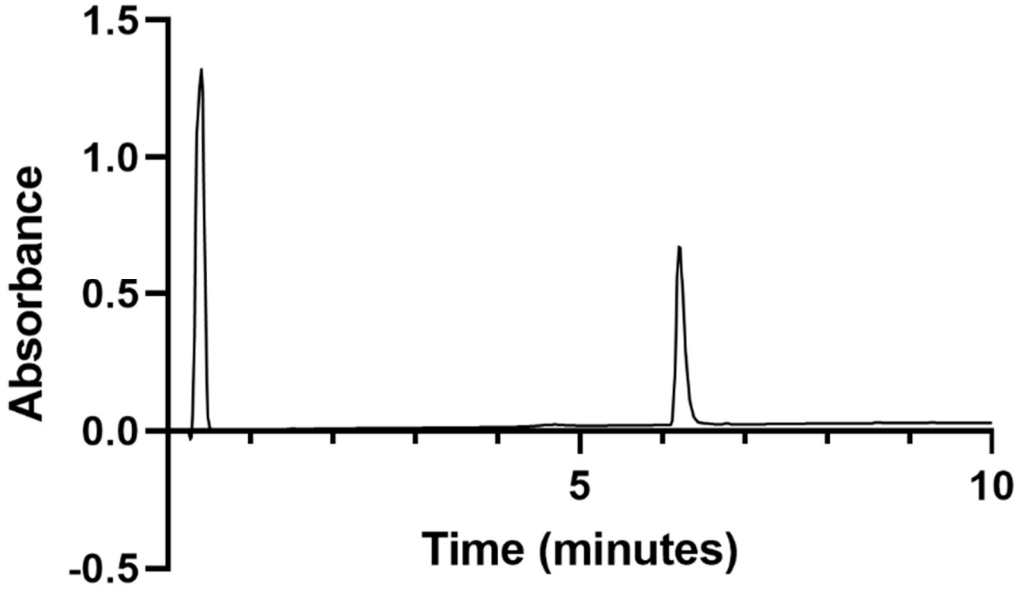

Figure A22. Purity trace of **I15N F1** (214 nm) with a solvent gradient of 5-45% acetonitrile/water (0.1% TFA) for 10 min.

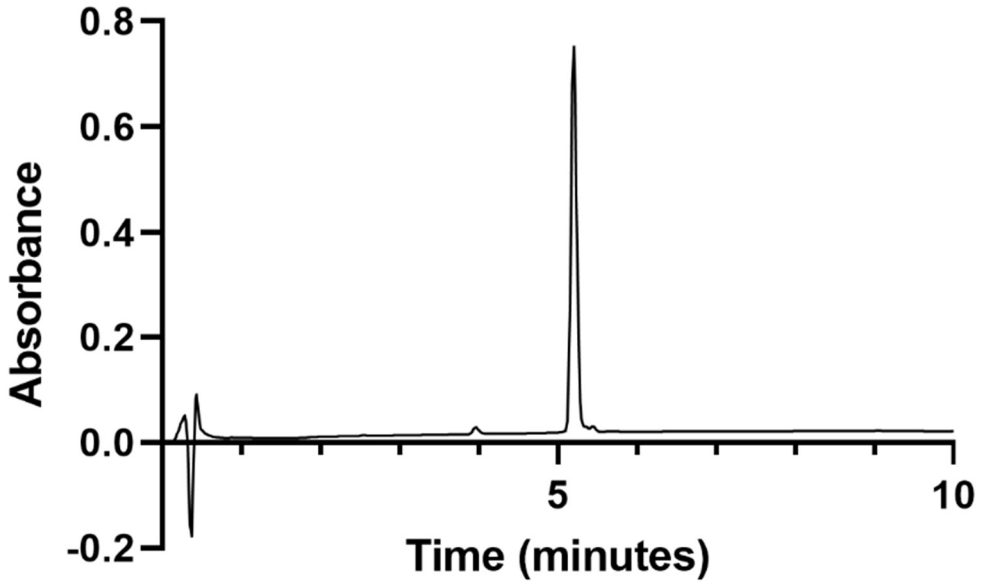

Figure A23. Purity trace of **I15N F2** (214 nm) with a solvent gradient of 20-70% acetonitrile/water (0.1% TFA) for 10 min.

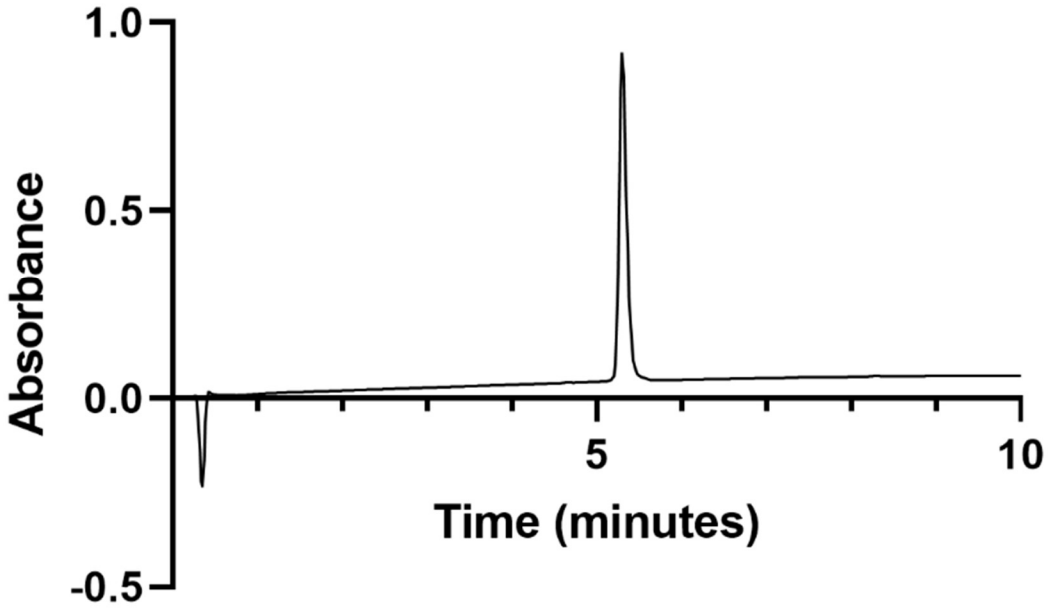

Figure A24. Purity trace of **I18N FL** (214 nm) with a solvent gradient of 20-70% acetonitrile/water (0.1% TFA) for 10 min.

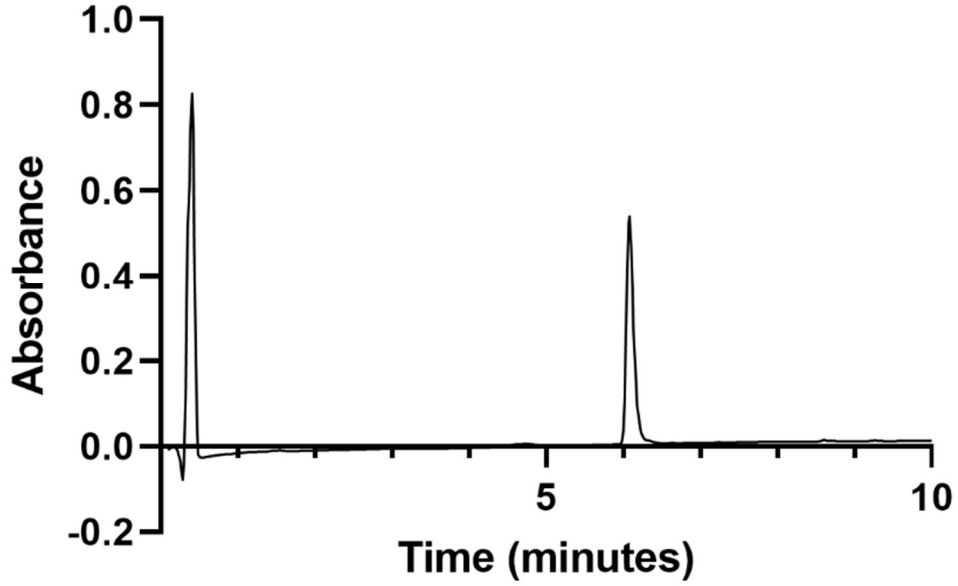

Figure A25. Purity trace of **I18N F1** (214 nm) with a solvent gradient of 5-45% acetonitrile/water (0.1% TFA) for 10 min.

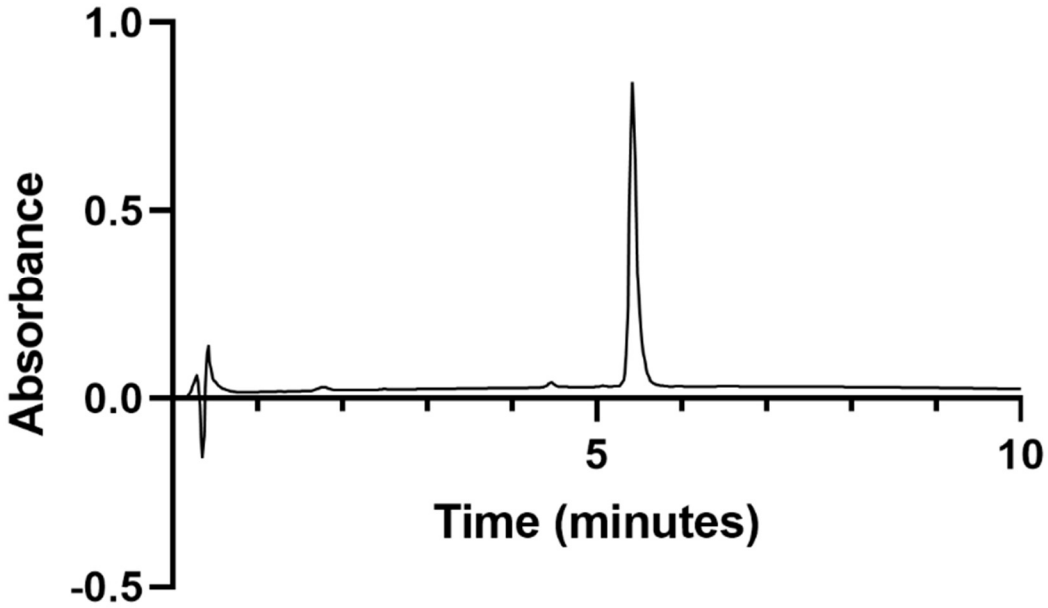

Figure A26. Purity trace of **I18N F2** (214 nm) with a solvent gradient of 20-70% acetonitrile/water (0.1% TFA) for 10 min.

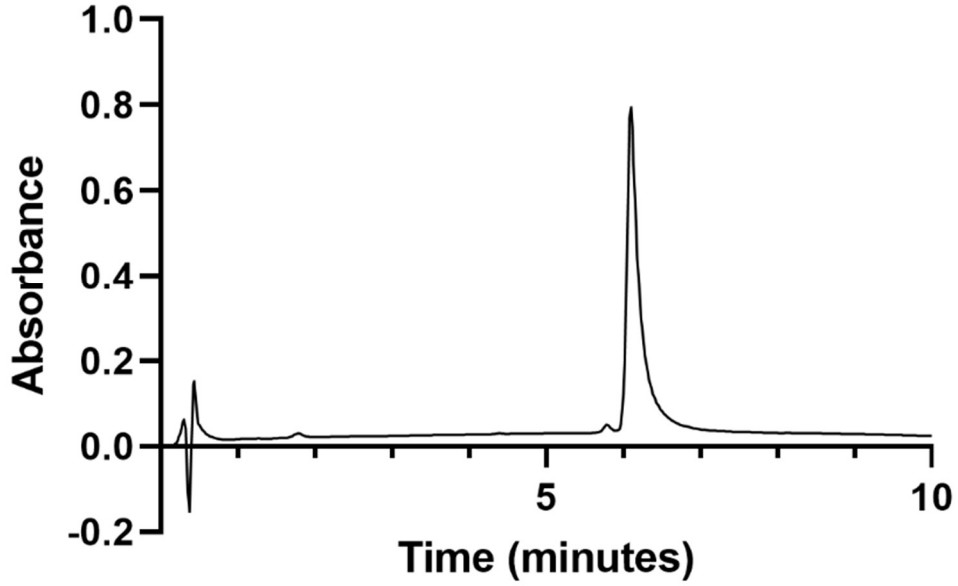

Figure A27. Purity trace of **N20C Ghadiri FL** (214 nm) with a solvent gradient of 20-70% acetonitrile/water (0.1% TFA) for 10 min.

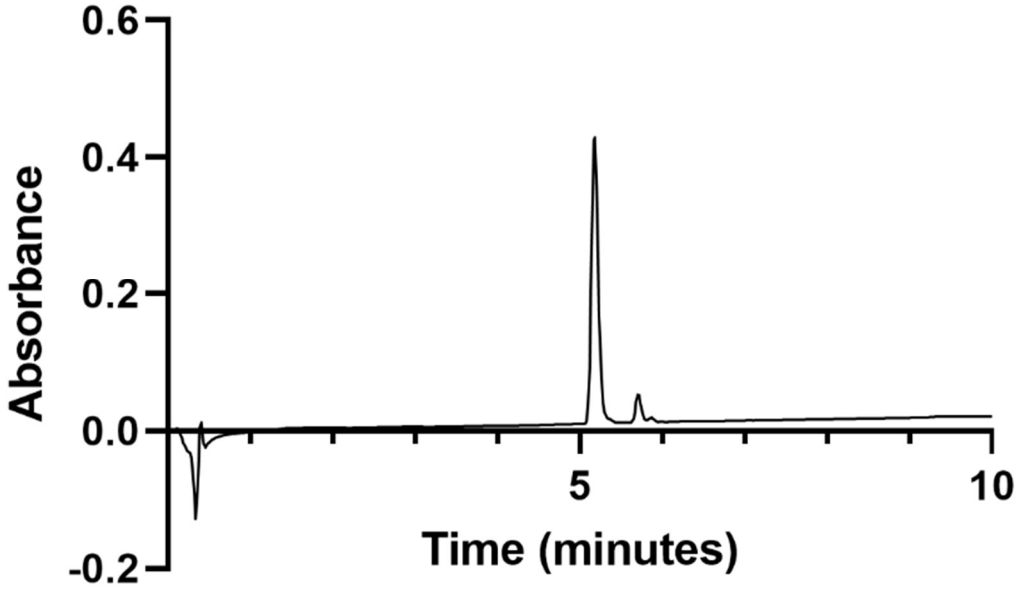

Figure A28. Purity trace of **N20C Ghadiri F1** (214 nm) with a solvent gradient of 5-45% acetonitrile/water (0.1% TFA) for 10 min.

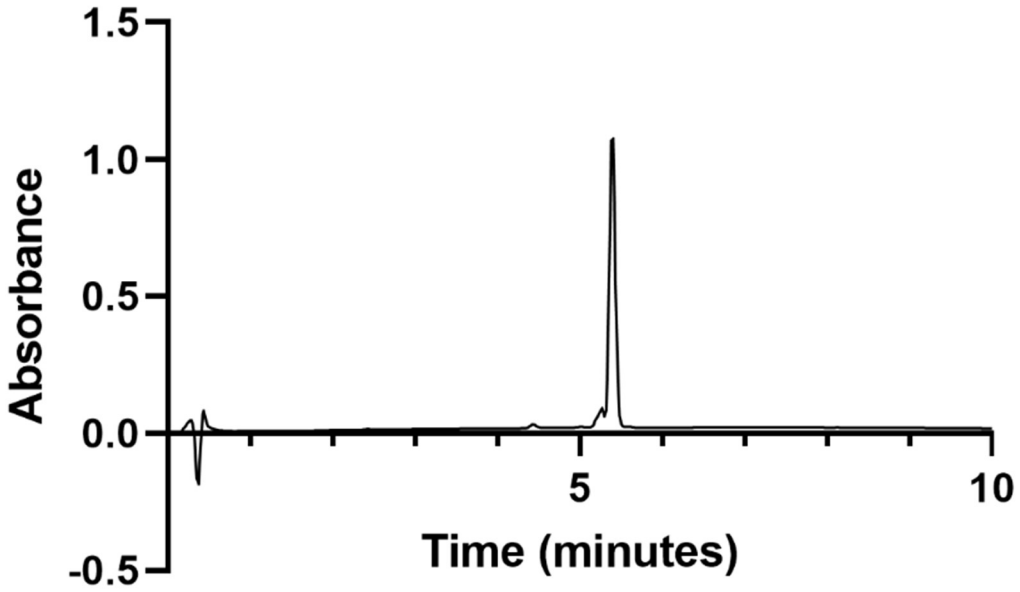

Figure A29. Purity trace of **N20C Ghadiri F2** (214 nm) with a solvent gradient of 20-70% acetonitrile/water (0.1% TFA) for 10 min.

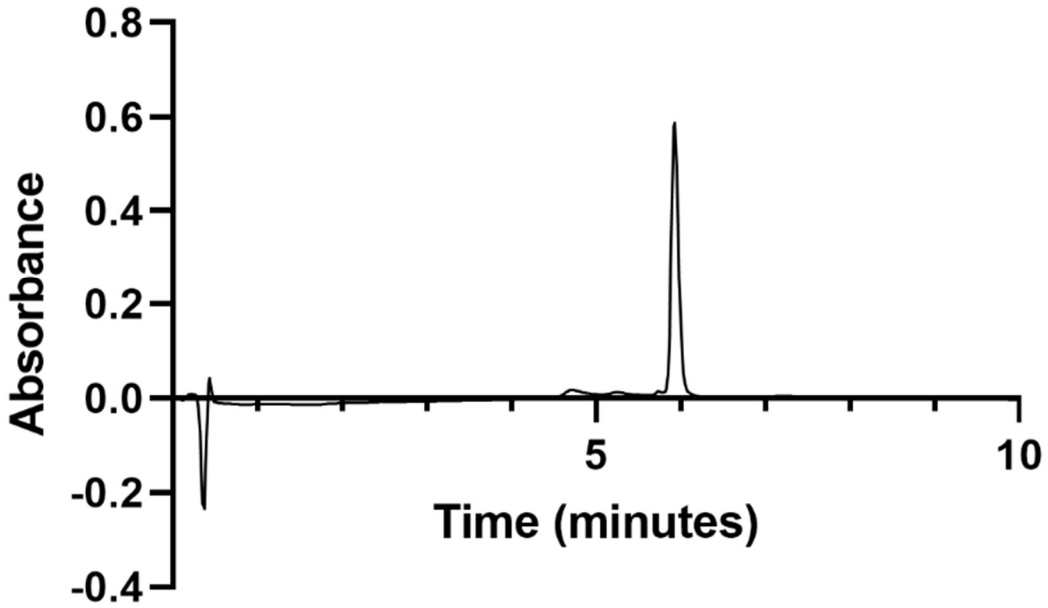

Figure A30. Purity trace of **E1K2** (214 nm) with a solvent gradient of 20-70% acetonitrile/water (0.1% TFA) for 10 min.

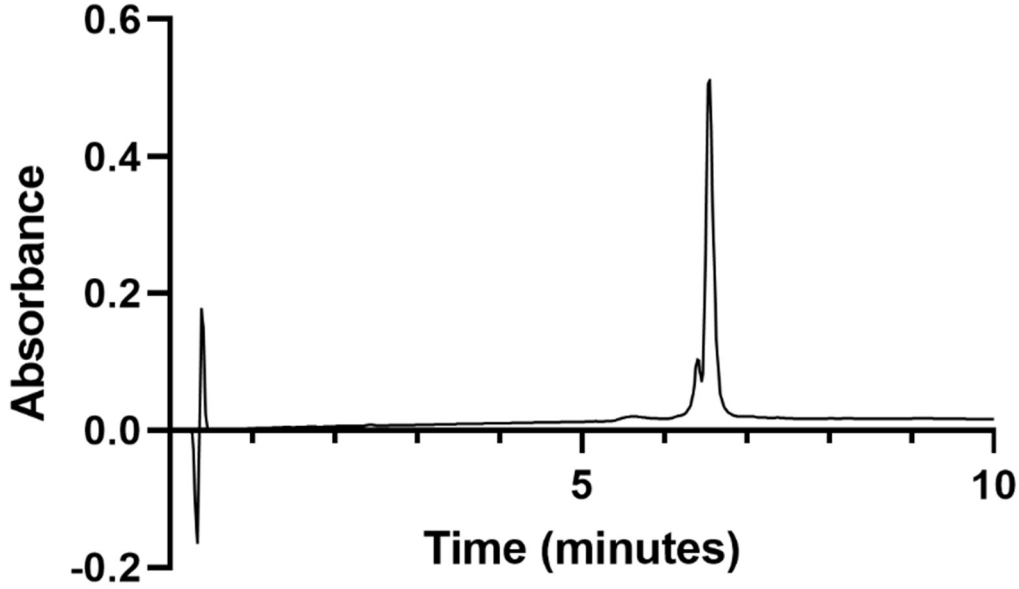

Figure A31. Purity trace of **E1K2-Ligand** (214 nm) with a solvent gradient of 20-60% acetonitrile/water (0.1% TFA) for 10 min.

Table A1. Mass spectrometry data for peptides.

Peptide	Expected Mass	Observed ($[M + H]^+$ or $[M + Na]^+$)
TriCross	4592	4591
HBN	3151	3146
HBRGDS	3478	3472
RGDS-His_7	1450	1476
IKVAV-His_6	1433	1452
TriNL	3764	3764
TriNL-FL	4080	4079
TriNL Monotether	4086	4083
$TriNL_2$	7834	7828
p2L	4355	4354
Rh-Biotin	831	831
Cou-His_6	1082	1084
N20C FL	3753	3752
N20C F1	1371	1371
N20C F2	2523	2525
H17C FL	3730	3730
H17C F1	1726	1728
H17C F2	2144	2163
N20C Truncated FL	2881	2881
N20C Truncated F1	1371	1372
N20C Truncated F2	1651	1656
H17P FL	3713	3713
I15N FL	3754	3754
I15N F1	1371	1371
I15N F2	2524	2525
I18N FL	3754	3755
I18N F1	1371	1371
I18N F2	2524	2527
N20C Ghadiri FL	3697	3697
N20C Ghadiri F1	1343	1344
N20C Ghadiri F2	2598	2594
E1K2	4017	4018
E1K2-Ligand	4608	4605

PUBLICATIONS

ChemComm

ROYAL SOCIETY OF CHEMISTRY

FEATURE ARTICLE

View Article Online
View Journal | View Issue

Cite this: *Chem. Commun.*, 2022, 58, 11625

Received 8th August 2022,
Accepted 22nd September 2022

DOI: 10.1039/d2cc04434j

rsc.li/chemcomm

Recent advances in coiled-coil peptide materials and their biomedical applications

Michael D. Jorgensen* and Jean Chmielewski *

Extensive research has gone into deciphering the sequence requirements for peptides to fold into coiled-coils of varying oligomeric states. More recently, additional signals have been introduced within coiled-coils to promote higher order assembly into biomaterials with a rich distribution of morphologies. Herein we describe these strategies for association of coiled-coil building blocks and biomedical applications. With many of the systems described herein having proven use in protein storage, cargo binding and delivery, three dimensional cell culturing and vaccine development, the future potential of coiled-coil materials to have significant biomedical impact is highly promising.

1. Introduction

Engineered biomaterials have been studied extensively for numerous applications, such as drug delivery and tissue regeneration.[1–3] Peptide-based materials specifically have drawn attention for their programmability and biocompatibility.[4–7] The use of natural and unnatural amino acid building blocks allows for facile modification of the peptide sequence and generation of various secondary and supersecondary folds. The coiled-coil motif, for instance, has drawn substantial interest due to its clear sequence-to-structure relationship and ease of tunability.[8,9]

Purdue University, Department of Chemistry, 560 Oval Drive, West Lafayette, Indiana, USA. E-mail: mjorgen@purdue.edu, chml@purdue.edu; Fax: 765 494 0239; Tel: 765 427 7096

The coiled-coil structure is widely observed in nature, and plays an essential role in many biological processes, including DNA recognition and gene regulation. The coiled-coil motif is composed of two or more alpha-helices that wrap around each other to form a left-handed supercoil (Fig. 1). Each alpha-helix contains heptad repeats (*abcdefg*), with the usually hydrophobic *a* and *d* residues influencing the oligomeric state of the coiled-coil from dimers to heptamers.[10–12] The *e* and *g* residues are commonly ionic, with complementary charges between individual helices within the coiled-coil, while the remaining positions (*b*, *c*, and *f*) are solvent exposed and are typically filled with hydrophilic residues.

With these well-established structural parameters, general guidelines to design *de novo* coiled-coils have been developed.[8,9] Meanwhile, others have drawn inspiration from naturally occurring coiled-coils, such as those found in the transcription factors GCN4 and Jun–Fos.[10,13,14] A few recent reviews on the use of

Michael D. Jorgensen

Michael D. Jorgensen received a BS in chemical engineering from the University of Illinois, Urbana Champagne in 2017, while working with Professor Jefferson Chan. He then began pursuing a PhD at Purdue University, and joined the research group of Professor Jean Chmielewski. His research focuses on the metal-mediated assembly of coiled-coil peptides into biomaterials and probing their applications.

Jean Chmielewski

Jean Chmielewski received her PhD from Columbia University with Ronald Breslow, followed by an NIH postdoctoral fellowship first with E. T. Kaiser at Rockefeller University, and with Peter Schultz at the University of California, Berkeley. She joined the faculty of Purdue University in 1990, and is the A. W. Kramer Distinguished Professor of Chemistry. Her chemical biology research develops unique chemical approaches to solve significant issues in human health, including multidrug resistance and regenerative medicine.

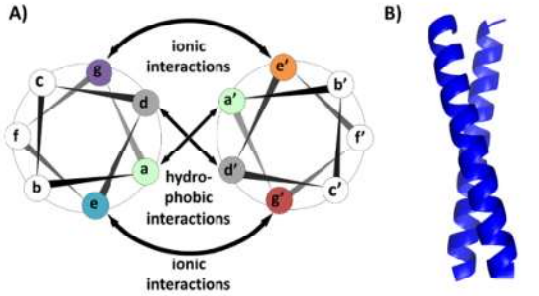

Fig. 1 (A) Helical wheel diagram of a coiled-coil dimer. (B) 3D model of a dimeric coiled-coil.

these coiled-coil building blocks for higher order assembly have emerged in the past five years. These have been focused on the use of orthogonal coiled-coil sequences within a single chain to create coiled-coil protein origami,[15] the development of multi-component peptide assemblies with coiled-coils as one example of many other peptide secondary structures,[16] the use of coiled-coils to mediate the assemble of protein structures,[17] a comparison of collagen mimetic and coiled-coil peptides for metal-promoted assembly,[18] and applications of coiled-coil materials in drug delivery.[19] This review focuses on a broader investigation of the range of strategies that have been employed to create higher order assemblies from coiled-coil building blocks, the reversible nature of coiled-coil assemblies, and a selection of their biomedical applications that emphasizes the future potential of this field. Throughout this review a number of coiled-coils are discussed, and these sequences can be found in Table 1.

2. Higher order assembly of coiled-coil building blocks

2.1 Design strategies for assembly

Starting with various oligomeric versions of the coiled-coil motif, a number of strategies have been developed to facilitate higher order assembly of the starting building blocks. These assembly approaches include integrating additional interactions within the coiled-coil sequences, including ionic and metal–ligand interactions, and engineering covalent linkages and hetero oligomeric coiled coils. Significant effort has been expended to understand and control the morphologies of these coiled-coil-derived materials as described below.

Ionic interactions. A highly successful method to facilitate higher order assembly of coiled-coil peptides is through ionic interactions. For example, the Woolfson lab has used *de novo* designed dimeric to heptameric coiled-coils as building blocks (Fig. 2A).[20] The peptides included charged residues at the termini to allow assembly in a head-to-tail fashion (Fig. 2A). Specifically, a lysine or glutamate residue was installed at the C-terminus to complement either a glutamate or free amino group at the N-terminus, respectively. This approach to linear assembly led to immediate fiber formation in phosphate buffered saline (PBS, pH 7.4) (100 μM peptide) with trimeric to heptameric coiled-coil modules. To improve the organization, these assemblies were subsequently thermally annealed to produce different morphologies depending on the oligomeric state of the building block. For instance, the tetrameric peptide (**CC-Tet2-F**) transitioned to thicker fibers (from 60–65 nm to 130–135 nm in width), whereas the pentameric coiled-coil transitioned from fibers to broad, sheet-like structures. This difference in the two morphologies upon annealing may stem from the lack of a complete denaturation for both peptides, suggesting incomplete transitions when annealed. Interestingly, the annealing process of the hexameric coiled-coil, **CC-Hex-T**, produced highly ordered fibers (~70 nm) that allowed for the elucidation of the packing through X-ray crystallography, revealing a square packed arrangement.[20] Additionally, the hydrophobic channel present within the hydrophobic cavity of each pentameric, hexameric, and heptameric coiled-coil (50 μM) was used to sequester the hydrophobic dye 1,6-diphenylhexatriene. The trimeric and tetrameric coiled-coils, however, did not trap the hydrophobic dye presumably because the hydrophobic cores did not contain a cavity.

While Woolfson and coworkers designed *de novo* coiled-coils as described above, others have used naturally occurring peptide sequences to create ionic-based assemblies. Conticello and coworkers reported a heptameric coiled-coil based on the GCN4 transcription factor (**7HSAP1**).[21] These researchers also used a head-to-tail strategy, but, they employed the free C- and N-termini for assembly, with two arginine residues installed at the *f* position to limit lateral association. The peptide (2 mM) formed fibers (479 ± 93 Da $Å^{-1}$, Fig. 2B) in MES buffer (10 mM, pH 6.0) and could trap the dye PRODAN within the hydrophobic cavity of the heptameric coiled-coil. Because of the arginine residues, these fibers were much thinner (3 nm) when compared to those of Woolfson (85 nm). The Montclare lab has studied coiled-coil assemblies derived from the cartilage oligomeric matrix protein (**Q**).[22] This pentameric coiled-coil was designed to include a positively charged histidine-tag at the N-terminus, lysine and arginine residues at the C-terminus, and glutamate and aspartate residues in the middle of the peptide to allow for staggered assembly of the coiled-coil building blocks. This design led to fibril formation at 10 μM **Q** (20–560 nm in diameter) in phosphate buffer (50 mM, pH 4) with a brick-layer-like organization of the coiled-coils (Fig. 2C). The peptide also assembled in the presence of the hydrophobic dye curcumin (5 : 1 molar ratio of curcumin to peptide). Assembling in the presence of this dye was found to promote packing of the coiled-coils and increase the fibril diameter significantly (16.0 ± 5.6 μm). While some evidence indicated curcumin binding to the hydrophobic coiled-coil interior, the change in morphology also suggests potential binding between protofibrils. This is in contrast to Woolfson's and Conticello's works where the hydrophobic dyes had no effect on morphology.

Assemblies based on non-covalent interactions can also be reversible using pH. For instance, Conticello and coworkers installed histidine residues at the interior *d* position of the GCN4 trimeric coiled-coil (**TZ1H**). So that only deprotonated histidine would lead to coiled-coil formation (pH > 5.8).[23]

Table 1 Peptide sequences of this review with structures of unnatural modifications

Peptide name	Oligomeric state	Peptide sequence
CC-Tet2-F	Tetramer	H_2N-NILQE(VKNILKE)(VKNILWE)(VKNILQE)VK-OH
CC-Hex-T	Hexamer	H_2N-(LKAIAQE)(LKAIAKE)(LKAIAWE)(LKAIAQE)-OH
7HSAP1	Heptamer	H_2N-(KLAQAVE)(KLARAVE)(KLAYANE)(KLARAVE)(KLAQAVE)-OH
Q subunit	Pentamer	-VKE(ITFLKNT)(APQMLRE)(LQETNAA)(LQDVREL)(LRQQSKL)-OH
TZ1H	Trimer	Ac-E(IAQHEKE)(IQAIEKK)(IAQHEYK)(IQAIEEK)(IAQHKEK)IQAIK-OH
AFD19	Hexamer	Ac-(LKELAKV)(LHELAKL)(VSEALHA)-OH
TriByp1	Trimer	Ac-(MKQIEDK)(IEEILBK)(IYHIENE)(IARIKKL)IGE-NH_2
TriByp2	Trimer	Ac-(MKQIEDK)(IEEILBK)(IYHIEBE)(IARIKKL)IGE-NH_2
TriByp3	Trimer	Ac-(MKQIEBK)(IEEILBK)(IYHIEBE)(IARIKKL)IGE-NH_2
AQ-Pal14	Dimer	Ac-K(IEALEGK)(IEALEPalK)(IEACEGK)(IEALEGK)G-NH_2
H21	Dimer	Ac-K(IEALEGK)$_2$(IEALEHK)(IEALEGK)G-NH_2
p2L (x = S), **TriCross** (x = B)	Trimer	NTA-G(MKQIEDK)(IEEILxK)(IYKIENE)(IARIKKL)IGEGHH-NH_2
1 (Horne)	Dimer	Ac-E(IAALKTpyE)(NAALKEE)(IAALKKE)(IAALTpyKG)-NH_2
2 (Horne)	Trimer	Ac-E(ITpyAIKKE)(IEAIKKE)(IAEIKKE)(IATpyIKK)-NH_2
3 (Horne)	Tetramer	Ac-E(LAAIKEE)(LAAIKTpyE)(LAAIKQE)(LAAIKQ)-NH_2
TZ1C2	Trimer	Ac-E(IAQIEEE)(CQAIEER)(IAQIEYR)(IQAIEEK)(CAQIKEK)IQAIK-NH_2
CC-Hex-T + co	Hexamer	H_2N-(CKAIAKE)(LKAIAYE)(LKAIAKE)(LKAIAKQ)-BBzl
Peptide 1 (Pochan)	Tetramer	Mal-(DEKIKNM)(ADQIKHM)(AWMIDRM)(AEKIDRE)A-NH_2
Peptide 2 (Pochan)	Tetramer	H_2N-C(DEEIRRM)(AEEIRQM)(AERIQQM)(AEQIQQE)A-NH_2
4A	Dimer	Ac-WE(NAKLENI)(VARLEND)(NANLEKD)(IANLEKD)(IANLERD)VAR-Az
4B	Dimer	az-NT(VKELKNY)(IQELEER)(NAELKNL)(KEHLKFA)(KAELEFE)LAA-NH_2
EPE subunit	Pentamer	-APQM(LRELQET)(NAALQDV)(RELLRQQ)(VKEITFL)(KVTVMES)DAS-
PC10P subunit	Pentamer	-(APQMLRE)(LQETNAA)(LQDVREL)(LRQQVKE)(ITFLKNT)(VMESDAS)-
AC10A subunit	Tetramer	-(SGDLENE)(VAQLERE)(VRSLEDE)(AAELEQK)(VSRLKNE)(IEDLKAE)-
C_2-$S^H{}_{48}$-C_2-D^A subunit	Dimer	-LEIR(AAFLRQR)(NTALRTE)(VAELEQE)(VQRLENE)(VSQYETR)(YGPLGGG)KG-OH
C_2-$S^H{}_{48}$-C_2D^B subunit	Dimer	-LEIE(AAFLERE)(NTALETR)(VAELRQR)(VQRLRNR)(VSQYRTR)(YGPLGGG)KG-OH
EZ (x = E), **KZ** (x = K)	Dimer	H_2N-(AQALxKx)(LQALxKx)(LQALxWx)(LQALxKx)LSGSGC-OH
EV	Dimer	H_2N-(EVSALEK)(EVSALEK)(ENSALEW)(EVSALEK)C-OH
EI	Dimer	H_2N-C(KVSALKE)(KVSALKE)(KNSALKW)(KVSALKE)-OH
KV	Dimer	H_2N-(EIAALEK)(EIAALEK)(ENAALEW)(EIAALEK)C-OH
KI	Dimer	H_2N-C(KIAALKE)(KIAALKE)(KNAALKW)(KIAALKE)-OH
A_{4H3}	Dimer	Ac-CGG(EIAALEH)(EIAALEH)(ENAALEH)(EIAALEQ)GG-NH_2
B_{4H3}	Dimer	Ac-GG(KIAALKH)(KIAALKH)(KNAALKH)(KIAALKQ)GGC-NH_2
EE subunit	Dimer	-(IAALEKE)$_3$-
KK subunit	Dimer	-(LAAIKEK)$_3$-
1coi-dC18-PEG2K subunit	Trimer	-E(VEALEKK)(VAALESK)(VQALEKK)(VEALEHG)-
CC-Tri3	Trimer	Ac-G(EIAAIKK)(EIAAIKQ)(EIAAIKQ)GYG-NH_2
CC-DiA (x = E, y = W), **CC-DiB** (x = K, y = Y)	Dimer	Ac-G(XIAALXK)(XNAALXQ)(XIAALXQ)GyW-NH_2
JR2EC (x = E), **JR2KC** (x = K)	Dimer	H_2N-N(AADLxKA)(IxALxKH)(LxAKGPC)(DAAQLxK)(QLxQAFx)AFxRAG-NH_2
TriNL	Trimer	Ac-(MKQIEDK)(IEEILSK)(IYKIENE)(IARIKKL)IGE-NH_2
E3	Dimer	H_2N-GY(EIAALEK)$_3$GC-OH
K3	Dimer	H_2N-GY(KIAALKE)$_3$GC-OH
hSAF x = A/Q, y = A/Q, z = I/N	Dimer	H_2N-K(IxxLKyK)(ZxxLKyE)(IxxLExE)(yxxLEx)-OH
bRGD-CUBE	Tetramer	H_2N-(AVGP)$_{42}$-D_{88}-CGGNGEPRGDTYRAY-GN[(ADELYRM)(LDALREH)(LQSLRRK)]$_2$LRSG-OH
SAPN template	Trimer and Pentamer	Ac-DEM(LRELQET)(NAALQDV)(RELLRQQ)(VKQITFL)KCLLM-GG-RLLCR(LEELERR)(LEELERR)(LEELERR)-NH_2
CpA	Dimer	Ac-(CKQLEDK)(IEELLSK) AA (CKQLEDK)(IEELLSK) NH_2
γPFD	Dimer	H_2N-MVNEVIDINEAVRAYIAQIEGLRAEIGRLDATIATLRQSLATLKSLKTLGEGKTVLVPVGSIAQVEMK-VEKMDKVVVSVGQNISAELEYEEALKYIEDEIKKLLTFRLVLEQAIAELYAKIEDIAEAQQTSEEE-KAEEENEEKAE-OH

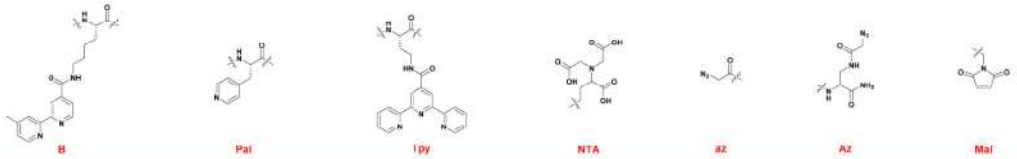

Upon incubation in phosphate buffer (10 mM, pH 8.2), **TZ1H** (1 mg mL^{-1}) assembled into bundles of fibers (40–100 nm) over a period of 3 h (Fig. 3A). Charged histidine residues, on the other hand, disrupted the coiled-coil structure by destabilizing the hydrophobic pocket, and the absence of this supercoil prevented the higher order assembly *via* ionic interactions from occurring. The fiber assembly and disassembly, therefore, was controlled through the addition of base or acid, respectively.

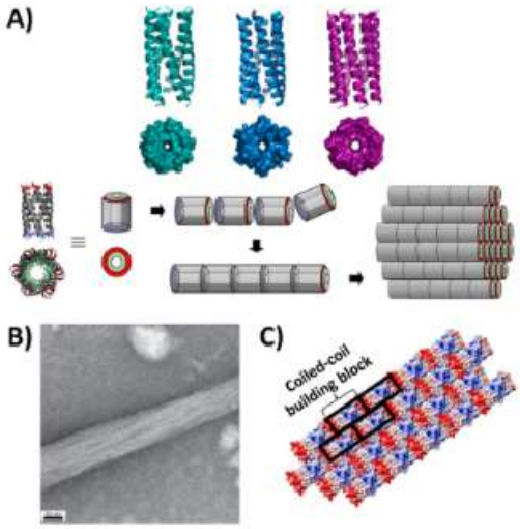

Fig. 2 (A) X-Ray crystal structures of pentameric to heptameric coiled-coils and the proposed mechanism of fiber assembly. (B) TEM micrograph of **7HSAP1** assembled in MES buffer (10 mM, pH 6.0). (C) Schematic representation of peptide **Q** organization upon fiber formation in phosphate buffer (50 mM, pH 4). Reprinted with permission from ref. 15–17. Copyright 2013, 2014, 2015, American Chemical Society.

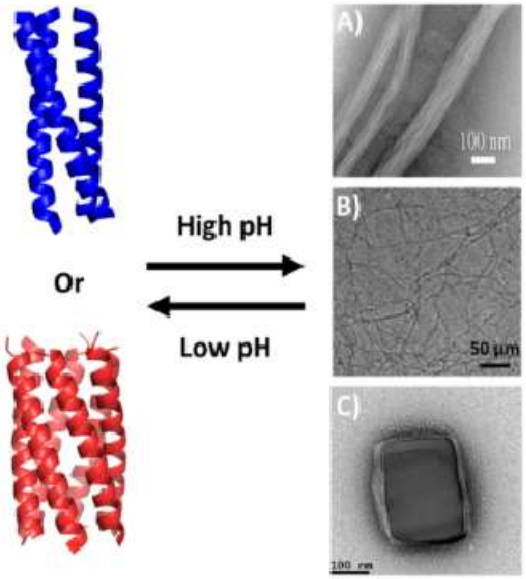

Fig. 3 Transmission electron microscopy (TEM) images of reversible assemblies *via* pH. (A) **TZ1H** fibers, (B) **AFD19** fibers, and (C) **TriByp3** assembly. Reprinted with permission from ref. 18–20. Copyright 2006, 2011, 2018, American Chemical Society and Royal Society of Chemistry.

Alternatively, Dexter and coworkers designed a highly charged *de novo* peptide with histidine, lysine, and glutamate residues at solvent exposed positions of the coiled-coil backbone (**AFD19**).[24] The peptide (1.75 mM), under conditions where the net charge was close to zero (pH 5.9), first formed fibrils due to misalignment of the helices producing overhangs, followed by hydrogel formation on a time scale of seconds to hours depending on the peptide concentration (Fig. 3B). Highly charged versions of **AFD19** led to no assembly and a low viscosity solution. The researchers also demonstrated rapid hydrogel dissolution by adjusting the pH. The Chmielewski lab has also developed a coiled-coil assembly that is responsive to pH.[25] They introduced bipyridine moieties at the solvent exposed *f* position of a trimeric coiled-coil derived from GCN4. One to three bipyridines were installed on the coiled-coil peptide by substituting solvent exposed residues with lysine (D6K, S13K, and N20K) and subsequent bipyridine modification (**TriByp1**, **TriByp2**, and **TriByp3**). Incubation of the peptides (250 µM) in MOPS buffer (10 mM, pH 7.0) promoted radial association of the building blocks *via* aromatic interactions across the coiled-coils, leading to nano- to micron-scaled rectangular assemblies (Fig. 3C). An increase in the number of bipyridine units led to a decrease in the aspect ratio of the assemblies (16 : 1 to 0.9 : 1). When subjected to acidic conditions (pH 3.0), the protonated bipyridine groups caused disruption of the coiled-coil interfaces, rapidly leading to dissolution of the assembly. The material could then reassemble upon addition of base, and this overall process went through numerous cycles without a change in the morphology of the assembly. Despite using different strategies, each lab created a pH-switchable material capable of assembly and disassembly on command.

Changes in pH may also lead to changes in morphology of the assembly. For instance, Montclare and coworkers investigated the hydrogelation properties of peptide **Q** (*vide supra*) as a function of pH.[26] At neutral and basic conditions (pH 7.4 and 10) a fiber-based hydrogel formed with **Q** (2 mM) in 96 and 24 h, respectively.

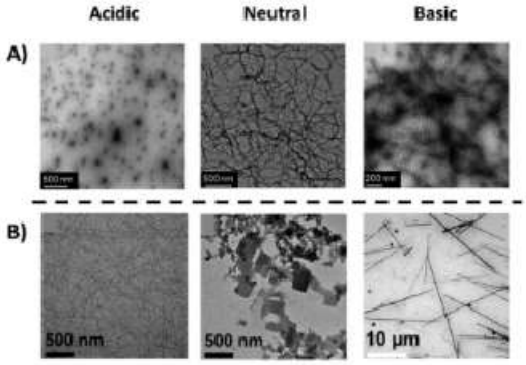

Fig. 4 pH Controlled assemblies. (A) TEM of Montclare's assembled **Q** peptide in acidic, neutral, and basic conditions to produce either nanoparticles or fibers. (B) TEM of Pochan's assembled peptide in acidic, neutral, and basic conditions to produce nanotubes, platelets, and needles, respectively. Reprinted with permission from ref. 21 and 22. Copyright 2018, 2021, American Chemical Society and Royal Society of Chemistry.

Acidic conditions (pH 6.0), on the other hand, led to polydispersed nanoparticles with no gelation after a two-week period (Fig. 4A). This shift in morphology from fibers to nanospheres was due to an increase in electron repulsion of the highly charged coiled-coil. Pochan and coworkers have also found changes in morphology of the assembly of a designed coiled-coil peptide depending on the pH.[27,28] Acidic conditions (10 mM sodium acetate buffer, pH 4.5) led to nanotubes (21.3 ± 2.8 nm in length) with 1 mM peptide, while neutral (10 mM phosphate buffer, pH 7) and basic (10 mM borate buffer, pH 10) conditions led to stacked platelets (50–500 nm in length) and needles (100–250 nm in length), respectively (Fig. 4B).[27] These notable differences arise from packing the coiled-coils so as to minimize electrostatic repulsion. In an acidic environment, the coiled-coils are tilted in the assembly to minimize electron repulsion of the positively charged free N-terminus. Under neutral conditions, the two-dimensional plates form through lysine-aspartate salt bridges whereas basic conditions weaken these salt bridges and lead to a primarily unidirectional assembly.

Overall, the examples provided above demonstrate that ionic-based assemblies are a simple yet powerful strategy to create a diverse range of structures. Loading of additional small molecule cargoes within the structures demonstrates potential for drug loading, and the developed feature of reversibility embedded within some of these materials may be harnessed for drug delivery as well.

Metal–ligand interactions. The introduction of metal-binding ligands onto the coiled-coil scaffold has been shown to be a powerful technique to facilitate higher order assemblies. Early studies from Ogawa and coworkers installed a pyridine ligand at a centrally located, solvent exposed *f* position of a dimeric coiled-coil containing an IAALEQK heptad repeat (**AQ-Pal14**).[29,30] Complexation of the dimeric **AQ-Pal14** with platinum at 60 °C for a week was found to induce assembly into both nanometer-scaled globular structures and a smaller population of nanofibrils. In a subsequent study by Ogawa, the pyridyl alanine ligands were substituted with histidine (**H21**), and this dimeric coiled coil was treated with cobalt(III) protoporphyrin IX at 60 °C overnight.[31] Evaporating this solution for scanning electron microscopy (SEM) analysis showed that the mixture formed much larger fibrils than the previous study, presumably due to bis-axial ligation between the imidazole ligands of the dimeric coiled coil and a cobalt complex.[31]

Chmielewski and coworkers have successfully used metal–ligand interactions for assembly using a trimeric coiled coil building block based on the GCN4 sequence.[32–34] This design is different from the above work of the Ogawa in that the ligands for metal ions are at the termini of the peptide to promote head-to-tail assembly, rather than at a central heptad of the coiled-coil, and a trimeric module was used.[32] The peptide (**p2L**) contained nitrilotriacetic acid (NTA) and di-histidine ligands at the N- and C-termini, respectively. Addition of Zn(II), Cu(II) and Co(II) (0.4 eq.) to **p2L** (1 mM) rapidly (30 min) provided well-ordered hexagonal crystals at room temperature, whereas 0.1 eq. of zinc produced hexagonal disks. The crystal structure of the zinc-promoted crystals was solved

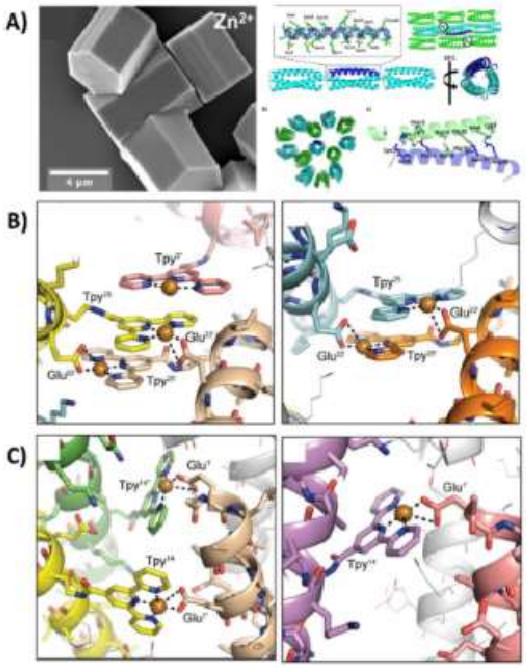

Fig. 5 (A) Scanning electron micrograph (SEM) of crystals of **p2L** (1 mM) with zinc ions (1 mM) and its corresponding crystal structure. (B) Views of crystal structure of peptide **2** and (C) peptide **3**. Reprinted with permission from ref. 27 and 30. Copyright 2016, 2017, American Chemical Society and Royal Society of Chemistry.

and a hexagonal open-packed assembly was observed with the ligands directed towards the P3 face of the crystals (Fig. 5A). Alternatively, nanospheres were observed with metal-mediated assembly using Ni(II), a morphology that was observed to some extent at much shorter time periods (5 min) with Zn(II), but which then evolved into crystals.[32] These researchers took advantage of the unsatisfied ligands within and on the P3 face of the growing and preformed crystals, respectively, to introduce His-tagged fluorophores with the crystals in a metal-dependent fashion.

Horne and coworkers have also studied metal-mediated coiled-coil assembly, but in their work, they used *de novo* designed sequences and terpyridine ligands. They investigated three different oligomerization states of the coiled-coil (dimer, trimer and tetramer), each with a different positioning of the ligand(s). For instance, the dimeric coiled coil (peptide **1**) contained terpyridines in the *f* position of the first heptad, and the *e* position of the last, whereas the trimeric peptide (**2**) had these ligands at the *a* and *c* positions of the first and last heptads. A tetrameric variant (peptide **3**) contained a single ligand at an internal *f* position. Although a number of divalent transition metals were investigated, only Cu(II) (3–10 mM) was found to promote crystallization of the peptides (~2–4 mM, pH 6–6.5) using the hanging drop vapor diffusion method (time not indicated).[35,36] Crystal structures revealed that the Cu^{2+} ions bind to these ligands in addition to

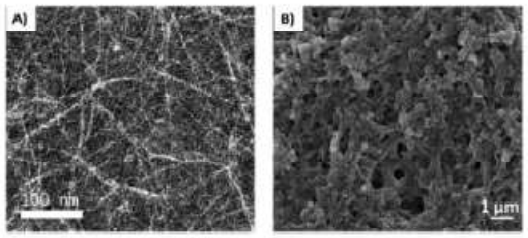

Fig. 6 (A) TEM image of **TZ1C2** fibrils (500 μM) in TAPS buffer (10 mM, pH 8.5) and NaCl (100 mM) before Cd(II) addition. (B) SEM image of **TriCross** assembly with $ZnCl_2$ (1 mM each) in Dulbecco's Modified Eagle Medium (DMEM) with 10% fetal bovine serum (FBS) after 1 h. Reprinted with permission from ref. 28 and 35. Copyright 2013, 2021, American Chemical Society and John Wiley and Sons.

nearby glutamate residues (Fig. 5b) yielding a complex packing arrangement for the peptides **1** and **2**, and a 2D net embedded in the lattice for **3** (Fig. 5C). In an interesting comparison, **TriByp1/2/3** described above (250 μM, pH 7), which contained bipyridine ligands in central heptad repeats based on the trimeric coiled-coil of GCN4, did not require metal ions for assembly. The bipyridine ligands alone mediated aromatic interactions leading to a hexagonal, close-packed assembly of trimeric coiled coils after 48 h.[28]

Ogawa and coworkers introduced a single CXXC metal binding motif within oligomeric coiled-coils, with the Cys residues in the interior *a* and *d* positions of the coil.[37,38] Their goal was to form metal complexes inside an individual coiled-coil, however, and not promote higher order assembly of the building block. As described above, Conticello and coworkers, introduced His and Cys ligands also within the hydrophobic core of the coiled coil.[39,40] In their case, however, three His residues (**TZ1H**) or two Cys residues (**TZ1C2**) were introduced per helix. This allowed individual helices to form staggered coiled coils in a metal-dependent fashion. Higher order assembly into long aspect ratio fibers and fibrils were observed in the presence of Ag(I) (1 eq.) with **TZ1H** (70 μM) or Cd(II) (2 eq.) with **TZ1C2** (500 μM) (Fig. 6A).

A strategy to use metal–ligand interactions to make highly crosslinked structures with coiled-coils for tissue engineering has also been investigated by Chmielewski and Jorgensen. In this case the central bipyridine moiety of **TriByp1** was combined with the NTA and His_2 ligands of **p2L** to create the peptide **TriCross**.[33] The use of ligands for metals at both the middle and ends of the coiled-coil indeed created a more complex metal-promoted assembly, with Zn(II), Ni(II), Cu(II), Co(II) (1 eq., 1 mM TriCross) producing a crosslinked three-dimensional (3D) mesh within minutes (Fig. 6B). The matrix formed from **TriCross** contained micron sized cavities that were suitable for cell encapsulation (*vide infra*). An advantage of metal-mediated assembly is that the association can be abolished with metal-chelating agents. For example, the formation of both the **p2L** (hexagonal crystals, Fig. 5A) and **TriCross** (3D matrix, Fig. 6B) assemblies was found to be reversible through the addition of low levels of ethylenediaminetetraacetic acid (EDTA).[32,33]

Overall, integrating metal–ligand interactions within coiled-coil peptides is an important advancement in the field, especially as it pertains to the crystalline arrays and 3D matrices generated above. The use of metal ion-promoted assembly is a powerful means to rapidly generate crystals on demand and incorporate cargo in a metal-dependent manner. Additionally, the judicious placement of multiple ligands on the coiled-coil building block allowed for metal-promoted formation of a 3D scaffold that encapsulated cells simultaneously. A notable feature of this strategy for assembly is the inherent reversibility that is available for the dissolution upon treatment with chelators – a feature with interesting potential in tissue engineering.

Covalent linkages and heterocoiled-coils. An alternate way to generate biomaterials from coiled-coil peptides is to link the building blocks together *via* covalent bonds. This has been accomplished in one set of examples by using different click chemistries. For instance, Woolfson and coworkers used native chemical ligation between hexameric coiled-coils. **CC-Hex-T**, described above, was optimized to minimize lateral association and maximize linear assembly (**CC-Hex-T + co**).[41] Native chemical ligation was used to link the building blocks using either two cysteine amino acids or two thioester moieties at each termini of a single coiled-coil. Rather than the previously described ionic driven assembly, the fibers that were generated (30–40 nm after 30 min and 100 nm after 1 week) were due to the covalent bond formed through the ligation chemistry to link the coiled-coils.

Similarly, Pochan and coworkers have used bond formation between coiled-coils using thiol and maleimide moieties. They used two tetrameric coiled-coils, one bearing terminal maleimides (**Peptide 1**) and the other flanked with cysteine residues (**Peptide 2**).[42,43] This design produced nanorods (>30 microns) with an alternating **Peptide 1** and **Peptide 2** pattern. Additionally, the Kirshenbaum lab has used the Huisgen cycloaddition for covalently linking coiled coils. In this case, the resulting triazole linkage was used to connect a dimeric coiled coil, based on the **SYNZIP** peptide, in a central position with 1–2 different dimeric coiled coil sequences (**4A** and **4B**).[44] Depending on the location of **4A** and **4B**, a barbell or quadrilateral assembly was observed. These strategies described above provide a facile route to design of coiled-coil materials based on chemical reactions.

Yet another covalent technique to induce higher order assembly is to install flexible peptide and polymeric linkers between helices of the coiled-coils. Jerala and coworkers, for example, elegantly designed a tetrahedron assembly using a mixture of homomeric and heteromeric coiled-coils with flexible peptide linkers (**TET12**).[45,46] The tetrahedron material was composed of a single polypeptide chain containing twelve coiled-coil domains each flanked with a flexible tetrapeptide spacer (SGPG) to prevent extended helix formation with a neighboring coiled-coil (Fig. 7A). To confirm the topological fold of the peptide, the N- and C-termini of the polypeptide were grafted with split yellow fluorescent protein fragments that provided a strong fluorescent signal.

Tirrell and coworkers have used a triblock design to create an assembly from the protein **EPE**, with E representing an

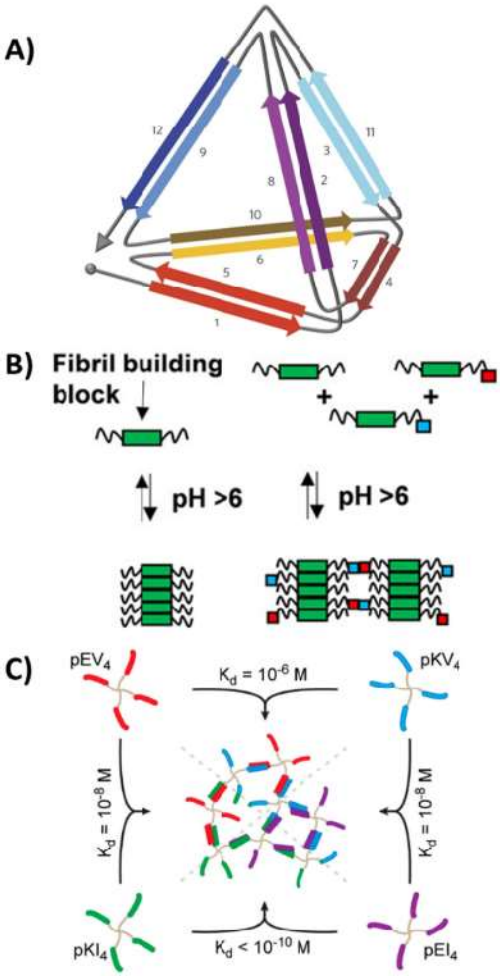

Fig. 7 (A) Schematic representation of the polypeptide path forming a tetrahedron. (B) Cartoon diagram of fibril forming triblock with and without heterocoiled-coil installation. (C) Relationship between coiled-coils and their corresponding binding affinities. Reprinted with permission from ref. 40, 45 and 47. Copyright 2013, 2016, American Chemical Society and Springer Nature.

elastin-like sequence flanked with cysteines and **P** representing the coiled-coil sequence from cartilage oligomeric matrix protein.[47,48] The **EPE** protein was conjugated to a 4-arm PEG linker to initiate the crosslinked network. To control the strength and rigidity of the hydrogel, the strength of the coiled-coil was altered, either through sequence modification or the addition of denaturants. In a somewhat analogous study from Tirrell and coworkers, triblock peptides were investigated in which two coiled-coil forming peptides were connected with a peptide linker. In this example, a central random coil peptide was connected to a pentameric coiled-coil peptide from the cartilage oligomeric matrix **P** and a tetrameric coiled-coil peptide **A** (**PC10A**). This design generated a crosslinked network that was notably stronger (100-fold increase) when compared to the homodimeric counterparts (**AC10A** and **PC10P**).[49] Similarly, De Vries and coworkers used a self-assembling triblock linked to heterocoiled-coil peptides ($\mathbf{C_2}$-$\mathbf{S^H_{48}}$-$\mathbf{C_2}$-$\mathbf{D^A}$ and $\mathbf{C_2}$-$\mathbf{S^H_{48}}$-$\mathbf{C_2}$-$\mathbf{D^B}$).[50] Without the heterocoiled-coil building blocks, simple fibrils were observed at pH $\geq$ 6 from $\mathbf{C_2}$-$\mathbf{S^H_{48}}$-$\mathbf{C_2}$ alone. The installation of the coiled-coils, however, led to a heavily crosslinked morphology of the fibrils (Fig. 7B). The degree of crosslinking was controllable by varying the density of coiled-coil labeled blocks.

Polymeric linkers have also been used to create more extensive structures with coiled-coils. Early work by Ghosh and coworkers used complementary alpha-helices that were conjugated to PAMAM dendrimers through cysteine-maleimide chemistry (**D-EZ$_4$** and **D-KZ$_4$**).[51] Upon mixing the two peptide conjugates in phosphate buffer, the alpha-helices formed coiled-coils and created fibers (>10 μm in length) after 8 h. More recently, Aili and Blank connected alpha helices to four-armed PEG linkers in a design to control the crosslinking properties.[52–54] Aili used dimeric coiled-coils with either isoleucine or valine at the *a* position (**pEV$_4$**, **pEI$_4$**, **PKV$_4$**, and **PKI$_4$**) to control the strength of the network by taking advantage of the coiled-coil binding affinities (Fig. 7C).[52] The peptides were linked to the PEG polymer *via* Cys/maleimide chemistry, and hydrogels were formed with the peptide conjugates (250 μM) in phosphate buffer (pH 7) within hours. Hydrogels that were composed of only isoleucine coiled-coils (**PEI4**/**PKI4**) resulted in a stronger gel when compared hydrogels with both valine and isoleucine alpha-helices (**PEI4**/**PKV4**) (G' of 1000 Pa *vs.* 200 Pa). Blank, on the other hand, controlled the strength of the crosslinked network through both covalent coiled-coil formation with a star-PEG polymer and metal–ligand interactions. Specifically, histidine ligands were installed at the solvent exposed *f* position of dimeric coiled-coil forming peptides ($\mathbf{A_{4H3}}$ and $\mathbf{B_{4H3}}$) to create a second layer of crosslinking.[53,54] The hydrogel formed without added metal ions (0.5 mM peptide conjugate, pH 8.1) exhibited a large linear viscoelastic range, whereas addition of zinc ions (1 eq.) increased the degree of crosslinking and transitioned from viscoelastic to elastic-like gels. Similar to metal-mediated assemblies, the addition of metal chelators like EDTA (4 eq.) returned the hydrogel to its original state. While Aili explored the binding affinities of covalently linked coiled coils to control the strength of the hydrogel, Blank used a covalent strategy in conjunction with a metal-mediated strategy to tune hydrogel properties.

The covalent strategies outlined above are a powerful means to swiftly link together coiled-coil peptides *via* various "click" reactions or with peptidic/polymeric linkers. These approaches lead to assemblies with morphologies that are often distinct from those obtained with the coiled-coil building block alone. The peptide origami approaches are an especially compelling example of the power of using heterocoiled-coils to tune stability and precisely control the resulting assemblies. The chemical approach allows for multiple modifications away from natural amino acids, whereas the ability to express the proteins, as in the case with the origami sequences, may provide a cost-effective way to generate the desired proteins.

2.2 Applications

Cargo storage and delivery. Perhaps the most studied application to biomaterials is cargo storage and delivery. While lyophilized powders remain the gold standard for protein storage, the lyophilization process can be harsh for the proteins and lead to degradation.[55,56] Meanwhile drug delivery remains a challenge and continues to be optimized to improve solubility of hydrophobic drugs, increase bioavailability, and minimize off target effects.[57–59]

Incorporating proteins within coiled-coil assemblies is one possible strategy to stabilize proteins. To this end, Chmielewski and co-workers used their **p2L** coiled-coil crystals described above to include proteins within the crystal. During the metal-mediated assembly, His-tagged protein guests were incorporated in an ordered fashion *via* metal–ligand interactions inside the crystal host in an hourglass pattern.[32] By incorporating His-tagged EGFP and derivatives inside the crystalline matrix, significant stabilization of the folded protein was achieved, even at 100 °C. These data demonstrate the potential of this assembly for room temperature storage of thermally sensitive proteins (Fig. 8A).[34] In an alternate strategy, Clark and coworkers stabilized citrate synthase (CS) by incorporating the enzyme covalently in coiled-coil filaments.[60] These filaments were composed of the coiled-coil peptide building blocks **EE** and **KK** derived from the γPFD protein. While CS aggregates in solution at 43 °C, embedding CS in the filaments through covalent linkages stabilized the enzyme. These two coiled-coil peptide materials, while using different mechanisms of assembly, provide great promise for protein stabilization and may provide a scaffold for enzymes.

Cargo delivery using nanoparticles derived from coiled-coil assemblies has seen notable recent advances. The Xu lab has developed a micelle composed of a coiled-coil peptide with a poly(ethylene glycol) side-conjugate and a terminal hydrophobic tail modification (**1coi-dC18-PEG2K**, Fig. 8B). In collaboration with the Ferrara and Bankiewicz labs, they investigated the numerous properties of the micelle nanoparticles for anticancer agent delivery.[61–68] For example, doxorubicin-loaded micelles were used to treat prostate and breast cancers in mice.[63] Later generations of these nanoparticles included trimeric and tetrameric coiled-coil species to control the location and cluster size of the drug on the micelle,[67] and cysteine modifications for redox reactive micelles.[68] Similarly, Kobatake and coworkers also reported drug delivery nanoparticles using a coiled-coil motif conjugated to an elastin-like peptide (ELP).[69] In this design, a heterocoiled-coil was used with helix A conjugated to single-chain vascular endothelial growth factor (VEGF) while helix B was conjugated to the ELP. Nanoparticle formation in the presence of paclitaxel created an anticancer delivery vehicle, whereby the external VEGF decoration directed the particles to the VEGF-receptor of cancer cells with paclitaxel ultimately causing cell death.

Different types of nanospheres have also been investigated for cargo delivery. Woolfson and coworkers have designed self-assembling cage-like particles (**SAGEs**) through a combination of heterocoiled-coil design and disulfide linkages (Fig. 8C).[70–72]

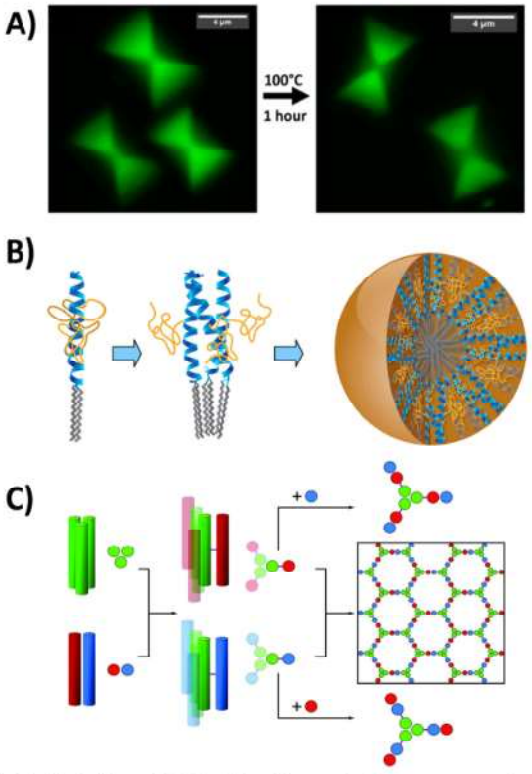

Fig. 8 (A) Stability of EGFP within **p2L** crystals. Fluorescence confocal images of Chmielewski's **p2L** crystals with enhanced green fluorescent protein guests before and after incubation at 100 °C for 1 h. (B) Schematic drawing of Xu's micelle, where the shell is composed of the 3-helix bundles and the core is composed of aliphatic chains. (C) Design of Woolfson's peptide cages through disulfide linkages and heterocoiled-coils. Reprinted with permission from ref. 29, 56 and 65. Copyright 2012, 2013, 2016, American Chemical Society and American Association for the Advancement of Science.

A homotrimeric coiled-coil (**CC-Tri3**) was linked to either alpha-helix **A** or **B** with a disulfide bridge, and subsequent mixing of the two sets led to **AB** heterocoiled-coil formation. Whereas the nanoparticles developed by Xu and Kobatake had hydrophobic cores, this **SAGE** has a hollow interior. **SAGEs** were modified at their termini with proteins (green fluorescent protein or luciferase) to decorate the interior or exterior of the cages without compromising the integrity of the material.[71] The cages were also modified to optimize cell uptake by introducing charged residues at the surface.[72] Stevens and coworkers, on the other hand, created nanoparticles using a layer-by-layer assembly on a colloidal surface.[73] The layers were generated with heterocoiled-coil components (**JR2EC** and **JR2KC**) linked to a polymer *via* cysteine-maleimide chemistry. Using this strategy, up to four layers could be assembled, with each layer containing trapped dextran. In this way, controlled release of cargo was accomplished through enzymatic degradation of each layer.

Coiled-coil assemblies using different morphologies have also been investigated as potential cargo delivery vehicles. Chmielewski and coworkers, for instance, generated nanotubes based on a trimeric GCN4 leucine zipper (**TriNL**) that selectively encapsulated fluorescently labelled anionic dextran.[74] A second generation of these nanotubes was created to stabilize the tubes and thereby expand the scope of this material as a delivery vehicle.[75] By introducing metal-binding ligands into this nanotube using heterotrimers composed of the coiled-coil peptides **p2L** (*vide supra*) and **TriNL**, the tube stability was increased in a metal-dependent manner. These tubes were still able to include dextrans within their interior, with inclusion of His-tagged fluorophores at either the ends of the tubes, or throughout, with the addition of metal ions.[70] Montclare and coworkers have created coiled-coil nanofibers (C_{CC}^{S}) based on the cartilage oligomeric matrix protein that encapsulate BMS493, a small molecule used for osteoarthritis treatment.[76] BMS493 readily degrades and isomerizes, making delivery of this drug difficult. Trapping the drug in the coiled-coil nanofibers was found to stabilize this therapeutic.

Hydrogels have also been investigated for cargo binding and delivery. For instance, Montclare and coworkers designed a hydrogel from the coiled-coil peptide **Q** for controlled drug release.[77] This hydrogel was successful as a vehicle for sustained release of curcumin. Alternatively, Zhong and coworkers designed a pH-responsive nanogel by conjugating helices of a heterocoiled-coil to hyaluronic acid (**HA-K3** and **HA-E3**).[78] The hyaluronic acid targeted breast cancer cells with overexpressed CD44 receptors, and when saporin, a ribosome inactivating protein, was included as cargo, the nanogel was reported to exhibit potent anticancer activity.

These efforts demonstrate an impressive array of materials with the capacity to bind both small molecules and proteins. Of particular interest is the inclusion of proteins within 3D crystals and filaments. The enhanced thermal stability of the protein guests points to interesting applications in room temperature storage of biopharmaceuticals and enzymes. The ability to bind and release cargo within coiled-coil materials and interact with cells, as demonstrated by the **SAGEs** cages, brings the use of coiled-coil materials as drug delivery vehicles closer to reality.

Three-dimensional cell culturing. Creating biocompatible three-dimensional scaffolds has been a major goal in support of tissue engineering. The extracellular matrix is very structurally complex, and 2D cell culturing is severely limited in mimicking *in vivo* settings.[79–81] While natural 3D scaffolds like Matrigel are commonly used, batch to batch variation and an ill-defined composition limit the tunability.[82]

Creating highly crosslinked 3D structures from sequence defined coiled-coil peptides has been used to circumvent these issues. Woolfson and coworkers, for instance, have designed coiled-coil sequences that form hydrogels through sticky ends using hydrogen bonding or hydrophobic interactions (**hSAFs**).[83,84] This, in turn, allowed them to control the strength of the hydrogel through heating. Rat adrenal pheochromocytoma cells and neural stem cells were seeded onto the gels, and gel penetration and subsequent differentiation was observed.

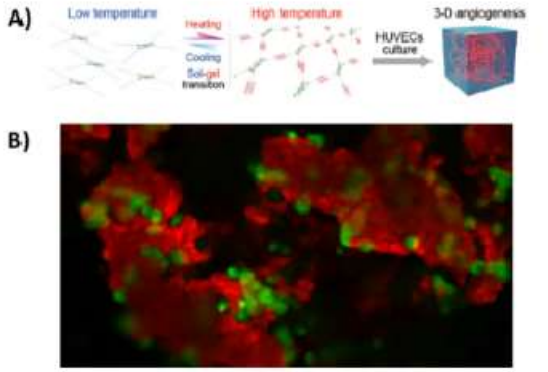

Fig. 9 (A) Schematic illustration of temperature-responsive hydrogel and the formation of blood vessels. (B) Confocal microscopy image of live HeLa cells (green) encapsulated within the **TriCross** assembled labeled with Rh-His_6 (red) in DMEM with 10% FBS. Reprinted with permission from ref. 28 and 80. Copyright 2020, 2021, American Chemical Society and John Wiley and Sons.

In an alternate strategy, Kobatake and coworkers developed a conjugate (**CUBE**) between a tetrameric, antiparallel coiled-coil and elastin-like polypeptide to prepare a hydrogel. By heating (37 °C) **CUBE**, the ELP segments aggregated leading to a crosslinked hydrogel.[85] Upon introducing the cell adhesion sequence RGD and heparin-binding angiogenic growth factors into these hydrogels, HUVEC cells that were encapsulated in the 3D network were found to undergo angiogenesis, a process that is usually only observed within 3D matrices (Fig. 9A). Alternatively, the George lab used a triblock strategy whereby two GCN4 coiled-coil peptides were linked with a random coil peptide containing the RGDS sequence. Strategically placed cysteine residues allowed for hydrogel formation through disulfide bond formation.[86] Added human marrow stem cells adhered to the hydrogel and subsequent neovascularization was observed. Dexter and coworkers modified the **AFD19** sequence described above with an S16K substitution so that a hydrogel could form at physiological pH.[87] This gel exhibited low cell toxicity, and was suitable for the growth of mouse fibroblast cells with a spread morphology.

While hydrogels remain the most prevalent type of three-dimensional networks based on coiled-coil sequences, Chmielewski and Jorgensen have developed a coiled-coil-based assembly (**TriCross**) that achieved the same crosslinked morphology while not exhibiting gelation.[33] Their assembly design, as described above, was based on a trimeric GCN4 leucine zipper, and used metal–ligand interactions at both the center and termini of the peptide. The conditions for assembly enabled HeLa cells to be added during the process to fully encapsulate the cells into the 3D matrix (Fig. 9B). The cells showed excellent viability within the scaffold after 6 days, and cells released from the matrix with a mild EDTA treatment demonstrated high viability. The reversibility of this matrix under mild conditions has promise for the isolation of grown tissue.

Overall, the examples of coiled-coil crosslinked assemblies provided above demonstrate significant potential as mimics of

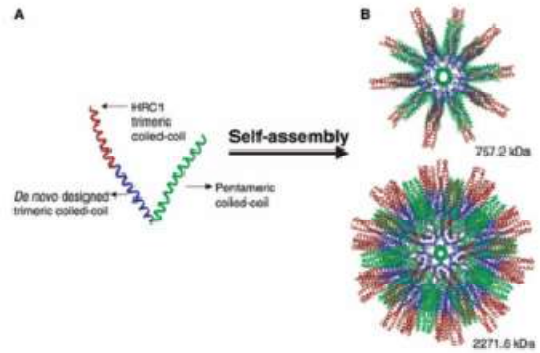

Fig. 10 (A) 3D monomeric building block of **P6HRC1** composed of a modified pentameric coiled-coil domain from COMP (green) and trimeric *de novo* designed coiled-coil domain (blue) which is extended by the coiled-coil sequence of SARS HRC1 (red). (B) Computer models of the complete peptide nanoparticle **P6HRC1** with varying degrees of icosahedral symmetry. The calculated diameters of these particles are about 23 and 28 nm and the molecular weight 757 and 2271 kDa, respectively. Reprinted with permission from ref. 87. Copyright 2009, John Wiley and Sons.

the extracellular matrix for tissue engineering. The coiled-coil 3D matrices have great potential for implantable materials and for 3D patterning of cell/tissue/material constructs. The ability to reverse the assembly process to release tissue in a chelation-controlled manner, as demonstrated by **TriCross**, could be particularly useful in regenerative medicine applications.

Vaccine development and immunology. Vaccines derived from coiled-coil assemblies have recently been developed for multivalent display of epitopes. These potential vaccine candidates show great promise when compared to soluble antigens for their ability to present a high level of antigens and elicit a stronger immune response.[88] For instance, Burkhard developed a nanoparticle with dodecahedral symmetry that was composed of a trimeric coiled-coil sequence linked to a pentameric coiled-coil sequence *via* a disulfide (**SAPNs**, Fig. 10).[89,90] The solvent exposed terminus of the peptides within the nanoparticle was functionalized with the coiled-coil of the HIV surface protein gp41 to create an adjuvant-free immunogen.[89,91] A follow up study functionalized the particles with a spike protein epitope for SARS-CoV-1. Animal studies with these nanoparticles revealed potent neutralization activity.[92]

Since then, Burkhard's nanoparticle design has been used for a number of vaccine candidates. Lanar and coworkers, for instance, have installed B and T cell epitopes for malaria within the nanoparticle.[93,94] Mouse studies showed protection against the malaria parasite *P. berghei* for up to six months with just the B cell epitope, whereas the combined epitopes doubled the length of protection, and also provided protection against transgenic *P. berghei*. Bissati and coworkers have also used these nanoparticles for *toxoplasma gondii* infection,[95–97] whereas Khan and coworkers used this platform to generate vaccine candidates against avian influenza,[98,99] seasonal influenza,[100] and an infectious bronchitis virus.[101] Indeed, this simple coiled-coil platform allows for facile tunability and shows great promise for future vaccine development.

Other coiled-coil assemblies have also been used for multivalent display of epitopes for use in potential vaccines. The Robinson lab, for example, designed a virus-like nanoparticle using a coiled-coil peptide with a lipid tail, rather than the two coiled-coils used by Burkhard.[102] The outer shell of the nanoparticle was decorated with an HIV-1 sequence to illicit an immune response. Collier and coworkers used a CD4+ T-cell epitope-containing coiled-coil that assembles into nanofibers and elicits an immune response in mice.[103] This material was subsequently optimized by controlling the length of the nanofibers.[104] Corradin and coworkers used the coiled-coil domains of malaria epitopes and connected them with non-immunogenic linkers.[105] A cellular assay revealed inhibition of parasite growth in the presence of this assembly. Finally, using Woolfson's **SAGEs** described above, Davidson and coworkers decorated the cages with tetanus toxoid, ovalbumin, or hemagglutinin antigens.[106] Both *in vitro* and *in vivo* studies revealed immune responses following exposure to these nanocages.

Coiled-coil nanoparticles are an excellent vehicle for the 3D display of multivalent ligands. This feature is ideal for applications in vaccine development. Additionally, striking animal data is emerging to support the future application of these strategies in humans.

3. Conclusions

The coiled-coil motif has been an area of great interest for *de novo* peptide design. More recently this building block has been successfully employed to generate a wide range of materials with morphologies that include fibrils, fibers, cages, crystals, tetrahera, nanotubes, hydrogels and 3D matrices. Because of the programmability of coiled-coils, assemblies can be formed through a number of methods, including complementary ionic and metal–ligand interactions, and through covalent chemistry. While significant progress has been made in the development of coiled-coil biomaterials, the rules for the various types of assembly are still being elucidated, an area where machine learning approaches may be useful in the future. Whereas we have focused in this review on biomedical applications, a growing number of coiled-coil assemblies are also being used as conductive materials, including photoelectronically active fibrils and conductive nanofilaments using metalloproteins within a coiled-coil assembly.[107–111]

With many of the systems described herein having proven use in protein storage, cargo delivery, cell culture and vaccine development, the future potential of coiled-coil materials to have significant biomedical impact is highly promising. Future applications of coiled-coil materials could include the combination of multi-layered nanoscale coiled-coil assemblies with cargo loading and cell interactions for the delivery of biological cargoes, such as therapeutic proteins and oligonucleotides. Importantly, such biopharmaceuticals could also be stabilized for room temperature storage and transport through inclusion within coiled-coil crystals and tubes. Additionally, the 3D patterning of cells and the peptide

biomaterials, in a reversible manner when needed, would be a powerful means to create complex tissues for drug testing and as implantable materials for *in vivo* use.

Conflicts of interest

The authors declare no conflicts of interest.

Acknowledgements

This work was supported by the National Science Foundation through Grant CHE-2108722.

References

1 X. Liu, C. Wang and Z. Liu, *Adv. Healthcare Mater.*, 2018, **7**, 1800913.
2 A. W. Xie and W. L. Murphy, *Curr. Opin. Biomed. Eng.*, 2019, **10**, 1–10.
3 A. K. Gaharwar, I. Singh and A. Khademhosseini, *Nat. Rev. Mater.*, 2020, **5**, 686–705.
4 K. H. A. Lau, *Biomater. Sci.*, 2014, **2**, 627–633.
5 J. Durão and L. Gales, *Curr. Org. Chem.*, 2015, **19**, 1874–1881.
6 M. P. Hendricks, K. Sato, L. C. Palmer and S. I. Stupp, *Acc. Chem. Res.*, 2017, **50**, 2440–2448.
7 K. Lin, D. Zhang, M. H. Macedo, W. Cui, B. Sarmento and G. Shen, *Adv. Funct. Mater.*, 2019, **29**, 1804943.
8 M. K. Yadav, J. E. Redman, L. J. Leman, J. M. Alvarez-Gutiérrez, Y. Zhang, C. D. Stout and M. R. Ghadiri, *Biochemistry*, 2005, **44**, 9723–9732.
9 W. M. Dawson, F. J. O. Martin, G. G. Rhys, K. L. Shelley, R. L. Brady and D. N. Woolfson, *Chem. Sci.*, 2021, **12**, 6923–6928.
10 P. B. Harbury, T. Zhang, P. S. Kim and T. Alber, *Science*, 1993, **262**, 1401–1407.
11 N. R. Zaccai, B. Chi, A. R. Thomson, A. L. Boyle, G. J. Bartlett, M. Bruning, N. Linden, R. B. Sessions, P. J. Booth, R. L. Brady and D. N. Woolfson, *Nat. Chem. Biol.*, 2011, **7**, 935–941.
12 J. Liu, Q. Zheng, Y. Deng, C. S. Cheng, N. R. Kallenbach and M. Lu, *Proc. Natl. Acad. Sci. U. S. A.*, 2006, **103**, 15457–15462.
13 J. M. Mason, M. A. Schmitz, K. M. Müller and K. M. Arndt, *Proc. Natl. Acad. Sci. U. S. A.*, 2006, **103**, 8989–8994.
14 M. ElGamacy and B. Hernandez Alvarez, *Curr. Opin. Struct. Biol.*, 2021, **68**, 224–234.
15 F. Lapenta, J. Aupič, Ž. Strmšek and R. Jerala, *Chem. Soc. Rev.*, 2018, **47**, 3530–3542.
16 D. M. Raymond and B. L. Nilsson, *Chem. Soc. Rev.*, 2018, **47**, 3659–3720.
17 W. M. Park, *Int. J. Mol. Sci.*, 2020, **21**, 3584.
18 R. W. Curtis and J. Chmielewski, *Pept. Sci.*, 2021, **113**, e224190.
19 J. Utterström, S. Naeimipour, R. Selegård and D. Aili, *Adv. Drug Delivery Rev.*, 2021, **170**, 26–43.
20 N. C. Burgess, T. H. Sharp, F. Thomas, C. W. Wood, A. R. Thomson, N. R. Zaccai, R. L. Brady, L. C. Serpell and D. N. Woolfson, *J. Am. Chem. Soc.*, 2015, **137**, 10554–10562.
21 C. Xu, R. Liu, A. K. Mehta, R. C. Guerrero-Ferreira, E. R. Wright, S. Dunin-Horkawicz, K. Morris, L. C. Serpell, X. Zuo, J. S. Wall and V. P. Conticello, *J. Am. Chem. Soc.*, 2013, **135**, 15565–15578.
22 J. Hume, J. Sun, R. Jacquet, P. D. Renfrew, J. A. Martin, R. Bonneau, M. L. Gilchrist and J. K. Montclare, *Biomacromolecules*, 2014, **15**, 3503–3510.
23 Y. Zimenkov, S. N. Dublin, R. Ni, R. S. Tu, V. Breedveld, R. P. Apkarian and V. P. Conticello, *J. Am. Chem. Soc.*, 2006, **128**, 6770–6771.
24 N. L. Fletcher, C. V. Lockett and A. F. Dexter, *Soft Matter*, 2011, **7**, 10210–10218.
25 M. Nambiar, L. S. Wang, V. Rotello and J. Chmielewski, *J. Am. Chem. Soc.*, 2018, **140**, 13028–13033.
26 M. Meleties, P. Katyal, B. Lin, D. Britton and J. K. Montclare, *Soft Matter*, 2021, **17**, 6470–6476.
27 Y. Tian, F. B. Polzer, H. V. Zhang, K. L. Kiick, G. Saven and D. J. Pochan, *Biomacromolecules*, 2018, **19**, 4286–4298.
28 Y. Tian, H. V. Zhang, K. L. Kiick, J. G. Saven and D. J. Pochan, *Chem. Mater.*, 2018, **30**, 8510–8520.
29 M. V. Tsurkan and M. Y. Ogawa, *Chem. Commun.*, 2004, 2092–2093.
30 M. V. Tsurkan and M. Y. Ogawa, *Biomacromolecules*, 2007, **8**, 3908–3913.
31 I. M. M. Carvalho and M. Y. Ogawa, *J. Braz. Chem. Soc.*, 2010, **21**, 1390–1394.
32 M. Nepal, M. J. Sheedlo, C. Das and J. Chmielewski, *J. Am. Chem. Soc.*, 2016, **138**, 11051–11057.
33 M. D. Jorgensen and J. Chmielewski, *J. Pept. Sci.*, 2021, e3302.
34 R. W. Curtis, K. L. Scrudders, J. R. W. Ulcickas, G. J. Simpson, S. T. Low-nam and J. Chmielewski, *ACS Biomater. Sci. Eng.*, 2022, **8**, 1860–1866.
35 N. A. Tavenor, M. J. Murnin and W. S. Horne, *J. Am. Chem. Soc.*, 2017, **139**, 2212–2215.
36 K. A. Scheib, N. A. Tavenor, M. J. Lawless, S. Saxena and W. S. Horne, *Chem. Commun.*, 2019, **55**, 7752–7755.
37 V. A. Morozov and M. Y. Ogawa, *Inorg. Chem.*, 2013, **52**, 9166–9168.
38 D. V. Zaytsev, V. A. Morozov, J. Fan, X. Zhu, M. Mukherjee, S. Ni, M. A. Kennedy and M. Y. Ogawa, *J. Inorg. Biochem.*, 2013, **119**, 1–9.
39 S. N. Dublin and V. P. Conticello, *J. Am. Chem. Soc.*, 2008, **130**, 49–51.
40 P. Anzini, C. Xu, S. Hughes, E. Magnotti, T. Jiang, L. Hemmingsen, B. Demeler and V. P. Conticello, *J. Am. Chem. Soc.*, 2013, **135**, 10278–10281.
41 F. Thomas, N. C. Burgess, A. R. Thomson and D. N. Woolfson, *Angew. Chem., Int. Ed.*, 2016, **55**, 987–991.
42 D. Wu, N. Sinha, J. Lee, B. P. Sutherland, N. I. Halaszynski, Y. Tian, J. Caplan, H. V. Zhang, J. G. Saven, C. J. Kloxin and D. J. Pochan, *Nature*, 2019, **574**, 658–662.
43 K. Kim, C. J. Kloxin, G. Saven and D. J. Pochan, *ACS Appl. Mater. Interfaces*, 2021, **13**, 26339–26351.
44 L. Jiang, X. Zuo, J. Li, N. J. Traaseth and K. Kirshenbaum, *Angew. Chem., Int. Ed.*, 2022, e202201895.
45 H. Gradišar, S. Božič, T. Doles, D. Vengust, I. Hafner-Bratkovič, A. Mertelj, B. Webb, A. Šali, S. Klavžar and R. Jerala, *Nat. Chem. Biol.*, 2013, **9**, 362–366.
46 J. Aupič, Ž. Strmšek, F. Lapenta, D. Pahovnik, T. Pisanski, I. Drobnak, A. Ljubetič and R. Jerala, *Nat. Commun.*, 2021, **12**, 1–12.
47 L. J. Dooling, M. E. Buck, W. Bin Zhang and D. A. Tirrell, *Adv. Mater.*, 2016, **28**, 4651–4657.
48 L. J. Dooling and D. A. Tirrell, *ACS Cent. Sci.*, 2016, **2**, 812–819.
49 W. Shen, K. Zhang, J. A. Kornfield and D. A. Tirrell, *Nat. Mater.*, 2006, **5**, 153–158.
50 N. E. Domeradzka, M. W. T. Werten, F. A. De Wolf and R. De Vries, *Biomacromolecules*, 2016, **17**, 3893–3901.
51 M. Zhou, D. Bentley and I. Ghosh, *J. Am. Chem. Soc.*, 2004, **126**, 734–735.
52 S. Dånmark, C. Aronsson and D. Aili, *Biomacromolecules*, 2016, **17**, 2260–2267.
53 I. Tunn, A. S. De Léon, K. G. Blank and M. J. Harrington, *Nanoscale*, 2018, **10**, 22725–22729.
54 I. Tunn, M. J. Harrington and K. G. Blank, *Biomimetics*, 2019, **4**, 1–17.
55 K. M. Polizzi, A. S. Bommarius, J. M. Broering and J. F. Chaparro-Riggers, *Curr. Opin. Chem. Biol.*, 2007, **11**, 220–225.
56 A. Butreddy, K. Y. Janga, S. Ajjarapu, S. Sarabu and N. Dudhipala, *Int. J. Biol. Macromol.*, 2021, **167**, 309–325.
57 R. Juliano, *Biochem. Soc.*, 2007, **35**, 29–31.
58 B. J. Boyd, C. A. S. Bergström, Z. Vinarov, M. Kuentz, J. Brouwers, P. Augustijns, M. Brandl, A. Bernkop-Schnürch, N. Shrestha, V. Préat, A. Müllertz, A. Bauer-Brandl and V. Jannin, *Eur. J. Pharm. Sci.*, 2019, **137**, 104967.
59 M. Z. Ahmad, M. Rizwanullah, J. Ahmad, M. Y. Alasmary, M. H. Akhter, B. A. Abdel-Wahab, M. H. Warsi and A. Haque, *Int. J. Polym. Mater. Polym. Biomater.*, 2022, **71**, 602–623.
60 D. J. Glover, S. Lim, D. Xu, N. B. Sloan, Y. Zhang and D. S. Clark, *ACS Synth. Biol.*, 2018, **7**, 2447–2456.
61 H. Dong, N. Dube, J. Y. Shu, J. W. Seo, L. M. Mahakian, K. W. Ferrara and T. Xu, *ACS Nano*, 2012, **6**, 5320–5329.
62 J. Y. Shu, R. Lund and T. Xu, *Biomacromolecules*, 2012, **13**, 1945–1955.

63 N. Dube, J. Y. Shu, H. Dong, J. W. Seo, E. Ingham, A. Kheirolomoom, P. Y. Chen, J. Forsayeth, K. Bankiewicz, K. W. Ferrara and T. Xu, *Biomacromolecules*, 2013, **14**, 3697–3705.
64 N. Dube, J. W. Seo, H. Dong, J. Y. Shu, R. Lund, L. M. Mahakian, K. W. Ferrara and T. Xu, *Biomacromolecules*, 2014, **15**, 2963–2970.
65 J. W. Seo, J. C. Ang, L. M. Mahakian, S. Tam, B. Fite, E. S. Ingham, J. Beyer, J. Forsayeth, K. S. Bankiewicz, T. Xu and K. W. Ferrara, *J. Controlled Release*, 2015, **220**, 51–60.
66 J. Ang, D. Ma, R. Lund, S. Keten and T. Xu, *Biomacromolecules*, 2016, **17**, 3262–3267.
67 J. Ang, D. Ma, B. T. Jung, S. Keten and T. Xu, *Biomacromolecules*, 2017, **18**, 3572–3580.
68 Y. Xue, B. T. Jung and T. Xu, *Pept. Sci.*, 2020, **112**, e24117.
69 Y. Assal, Y. Mizuguchi, M. Mie and E. Kobatake, *Bioconjugate Chem.*, 2015, **26**, 1672–1677.
70 J. M. Fletcher, R. L. Harniman, F. R. H. Barnes, A. L. Boyle, A. Collins, J. Mantell, T. H. Sharp, M. Antognozzi, P. J. Booth, N. Linden, M. J. Miles, R. B. Sessions, P. Verkade and D. N. Woolfson, *Science*, 2013, **340**, 595–599.
71 J. F. Ross, A. Bridges, J. M. Fletcher, D. Shoemark, D. Alibhai, H. E. V. Bray, J. L. Beesley, W. M. Dawson, L. R. Hodgson, J. Mantell, P. Verkade, C. M. Edge, R. B. Sessions, D. Tew and D. N. Woolfson, *ACS Nano*, 2017, **11**, 7901–7914.
72 J. L. Beesley, H. E. Baum, L. R. Hodgson, P. Verkade, G. S. Banting and D. N. Woolfson, *Nano Lett.*, 2018, **18**, 5933–5937.
73 A. J. Gormley, R. Chandrawati, A. J. Christofferson, C. Loynachan, C. Jumeaux, A. Artzy-Schnirman, D. Aili, I. Yarovsky and M. M. Stevens, *Chem. Mater.*, 2015, **27**, 5820–5824.
74 M. Nambiar, M. Nepal and J. Chmielewski, *ACS Biomater. Sci. Eng.*, 2019, **5**, 5082–5087.
75 M. D. Jorgensen and J. Chmielewski, *ACS Omega*, 2022, **7**, 20945–20951.
76 L. Yin, A. S. Agustinus, C. Yuvienco, T. Minashima, N. L. Schnabel, T. Kirsch and J. K. Montclare, *Biomacromolecules*, 2018, **19**, 1614–1624.
77 L. K. Hill, M. Meleties, P. Katyal, X. Xie, E. Delgado-Fukushima, T. Jihad, C. F. Liu, S. O'Neill, R. S. Tu, P. D. Renfrew, R. Bonneau, Y. Z. Wadghiri and J. K. Montclare, *Biomacromolecules*, 2019, **20**, 3340–3351.
78 L. Ding, Y. Jiang, J. Zhang, H. A. Klok and Z. Zhong, *Biomacromolecules*, 2018, **19**, 555–562.
79 C. Frantz, K. M. Stewart and V. M. Weaver, *J. Cell Sci.*, 2010, **123**, 4195–4200.
80 S. A. Langhans, *Front. Pharmacol.*, 2018, **9**, 1–14.
81 T. Nii, K. Makino and Y. Tabata, *Cancers*, 2020, **12**, 2754.
82 E. A. Aisenbrey and W. L. Murphy, *Nat. Rev. Mater.*, 2020, **5**, 539–551.
83 E. F. Banwell, E. S. Abelardo, D. J. Adams, M. A. Birchall, A. Corrigan, A. M. Donald, M. Kirkland, L. C. Serpell, M. F. Butler and D. N. Woolfson, *Nat. Mater.*, 2009, **8**, 596–600.
84 N. Mehrban, B. Zhu, F. Tamagnini, F. I. Young, A. Wasmuth, K. L. Hudson, A. R. Thomson, M. A. Birchall, A. D. Randall, B. Song and D. N. Woolfson, *ACS Biomater. Sci. Eng.*, 2015, **1**, 431–439.
85 Y. Mizuguchi, Y. Mashimo, M. Mie and E. Kobatake, *Biomacromolecules*, 2020, **21**, 1126–1135.
86 C. C. Huang, S. Ravindran, Z. Yin and A. George, *Biomaterials*, 2014, **35**, 5316–5326.
87 A. F. Dexter, N. L. Fletcher, R. G. Creasey, F. Filardo, M. W. Boehm and K. S. Jack, *RSC Adv.*, 2017, **7**, 27260–27271.
88 C. M. Snapper, *Front. Immunol.*, 2018, **9**, 598.
89 S. Raman, G. Machaidze, A. Lustig, U. Aebi and P. Burkhard, *Nanomed.: Nanotechnol., Biol. Med.*, 2006, **2**, 95–102.
90 T. A. P. F. Doll, R. Dey and P. Burkhard, *J. Nanobiotechnol.*, 2015, **13**, 1–12.
91 N. Wahome, T. Pfeiffer, I. Ambiel, Y. Yang, O. T. Keppler, V. Bosch and P. Burkhard, *Chem. Biol. Drug Des.*, 2012, **80**, 349–357.
92 T. A. P. F. Pimentel, Z. Yan, S. A. Jeffers, K. V. Holmes, R. S. Hodges and P. Burkhard, *Chem. Biol. Drug Des.*, 2009, **73**, 53–61.
93 S. A. Kaba, C. Brando, Q. Guo, C. Mittelholzer, S. Raman, D. Tropel, U. Aebi, P. Burkhard and D. E. Lanar, *J. Immunol.*, 2009, **183**, 7268–7277.
94 S. A. Kaba, M. E. McCoy, T. A. P. F. Doll, C. Brando, Q. Guo, D. Dasgupta, Y. Yang, C. Mittelholzer, R. Spaccapelo, A. Crisanti, P. Burkhard and D. E. Lanar, *PLoS One*, 2012, **7**, e48304.
95 K. El Bissati, Y. Zhou, D. Dasgupta, D. Cobb, J. P. Dubey, P. Burkhard, D. E. Lanar and R. McLeod, *Vaccine*, 2014, **32**, 3243–3248.
96 K. El Bissati, Y. Zhou, S. M. Paulillo, S. K. Raman, C. P. Karch, C. W. Roberts, D. E. Lanar, S. Reed, C. Fox, D. Carter, J. Alexander, A. Sette, J. Sidney, H. Lorenzi, I. J. Begeman, P. Burkhard and R. McLeod, *npj Vaccines*, 2017, **2**, 1–11.
97 K. El Bissati, Y. Zhou, S. M. Paulillo, S. K. Raman, C. P. Karch, S. Reed, A. Estes, A. Estes, J. Lykins, P. Burkhard and R. McLeod, *Sci. Rep.*, 2020, **10**, 1–13.
98 S. Babapoor, T. Neef, C. Mittelholzer, T. Girshick, A. Garmendia, H. Shang, M. I. Khan and P. Burkhard, *Influenza Res. Treat.*, 2011, **2011**, 1–12.
99 J. Li, Z. Helal, B. Ladman, C. Karch, J. Gelb Jr, P. Burkhard and M. I. Khan, *J. Virol. Antivir. Res.*, 2018, **7**, 1–5.
100 C. P. Karch, J. Li, C. Kulangara, S. M. Paulillo, S. K. Raman, S. Emadi, A. Tan, Z. H. Helal, Q. Fan, M. I. Khan and P. Burkhard, *Nanomed.: Nanotechnol., Biol. Med.*, 2017, **13**, 241–251.
101 J. Li, Z. H. Helal, C. P. Karch, N. Mishra, T. Girshick, A. Garmendia, P. Burkhard and M. I. Khan, *PLoS One*, 2018, **13**, 1–17.
102 F. Boato, R. M. Thomas, A. Ghasparian, A. Freund-Renard, K. Moehle and J. A. Robinson, *Angew. Chem., Int. Ed.*, 2007, **46**, 9015–9018.
103 Y. Wu, P. K. Norberg, E. A. Reap, K. L. Congdon, C. N. Fries, S. H. Kelly, J. H. Sampson, V. P. Conticello and J. H. Collier, *ACS Biomater. Sci. Eng.*, 2017, **3**, 3128–3132.
104 C. N. Fries, Y. Wu, S. H. Kelly, M. Wolf, N. L. Votaw, S. Zauscher and J. H. Collier, *Adv. Mater.*, 2020, **32**, 2003310.
105 S. Olugbile, V. Villard, S. Bertholet, A. Jafarshad, C. Kulangara, C. Roussilhon, G. Frank, G. W. Agak, I. Felger, I. Nebie, K. Konate, A. V. Kajava, P. Schuck, P. Druilhe, F. Spertini and G. Corradin, *Vaccine*, 2011, **29**, 7090–7099.
106 C. Morris, S. J. Glennie, H. S. Lam, H. E. Baum, D. Kandage, N. A. Williams, D. J. Morgan, D. N. Woolfson and A. D. Davidson, *Adv. Funct. Mater.*, 2019, **29**, 1807357.
107 D. E. Wagner, C. L. Phillips, W. M. Ali, G. E. Nybakken, E. D. Crawford, A. D. Schwab, W. F. Smith and R. Fairman, *Proc. Natl. Acad. Sci. U. S. A.*, 2005, **102**, 12656–12661.
108 B. Kokona, A. M. Kim, R. C. Roden, J. P. Daniels, B. J. Pepe-mooney, B. C. Kovaric, J. C. De Paula, K. A. Johnson and R. Fairman, *Biomacromolecules*, 2009, **10**, 1454–1459.
109 B. J. Pepe-Mooney, B. Kokona and R. Fairman, *Biomacromolecules*, 2011, **12**, 4196–4203.
110 J. C. Taggart, E. Z. Welch, M. F. Mulqueen, V. B. Dioguardi, A. G. Cauer, B. Kokona and R. Fairman, *Biomacromolecules*, 2014, **15**, 4544–4550.
111 Y. X. Chen, N. L. Ing, F. Wang, D. Xu, N. B. Sloan, N. T. Lam, D. L. Winter, E. H. Egelman, A. I. Hochbaum, D. S. Clark and D. J. Glover, *ACS Nano*, 2020, **14**, 6559–6569.

Received: 29 September 2020 | Revised: 16 December 2020 | Accepted: 13 January 2021
DOI: 10.1002/psc.3302

SPECIAL ISSUE ARTICLE

Journal of PeptideScience WILEY

Reversible crosslinked assembly of a trimeric coiled-coil peptide into a three-dimensional matrix for cell encapsulation and release

Michael D. Jorgensen | Jean Chmielewski

Department of Chemistry, Purdue University, West Lafayette, Indiana, USA

Correspondence
Jean Chmielewski, Department of Chemistry, Purdue University, West Lafayette, IN 47906, USA.
Email: chml@purdue.edu

Funding information
National Science Foundation. Grant/Award Number: 1609406-CHE

Mimicking the extracellular matrix (ECM) continues to be a goal in the field of regenerative medicine. Herein, we report a modified trimeric GCN4 coiled-coil sequence containing three ligands for metal ions specifically positioned for crosslinked assembly (**TriCross**). In the presence of metal ions, **TriCross** assembles into a three-dimensional (3D) matrix with significant cavities to accommodate cells. The matrix was found to be stable in media with serum, and mild removal of the metal leads to disassembly. By assembling **TriCross** with a suspension of cells in media, the matrix encapsulates cells during the assembly process leading to high cell viability. Further disassembly under mild conditions allows for the release of cells from the scaffold. As such, this peptide-based material displays many of the characteristics necessary for successful 3D cell culture.

KEYWORDS
cell encapsulation, coiled-coil, extracellular matrix, metal-mediated assembly

1 | INTRODUCTION

The extracellular matrix (ECM) is composed primarily of proteoglycans and fibrous proteins that provide complex microenvironments for cell and tissue growth.[1] As such, mimicking the ECM has been a goal for tissue engineering in recent decades. Although two-dimensional cell culturing has been the standard method for experimentation, these methods are significantly limited in their ability to mimic *in vivo* settings. By creating three-dimensional (3D) cell culture, however, scaffolds can act as mimetics that are closer to *in vivo* environments.

To this end, natural materials have been extensively explored for tissue engineering. Materials like Matrigel and collagen gels have been used to culture various cell types,[2–4] as well as act as scaffolds for tumor modeling.[5,6] Although these materials mimic many components in the ECM, batch to batch differences remains a common problem due to their variable and ill-defined composition.[1,7]

Alternatively, self-assembling peptides have emerged as promising biomaterials for cell culture and tissue growth.[8–11] A range of peptide motifs have been investigated, including coiled-coils,[12–15] collagen mimetic peptides,[16–22] and amphiphilic peptides.[23–38] Coiled-coils have previously been reported that undergo reversible assembly via temperature, pH, and introduction of PBS.[13–15] Herein, we describe the higher order assembly of a designed trimeric coiled-coil (**TriCross**) based on the leucine zipper region of the transcription factor GCN4 using metal-mediated crosslinking. Through this approach, a 3D matrix was obtained that provided a scaffold for cell encapsulation and growth, with the ability of releasing the cells under mild conditions.

Abbreviations: 3D, three-dimensional; CD, circular dichroism; DCM, dichloromethane; DIEA, diisopropylethylamine; DMEM, Dulbecco's Modified Eagle Medium; DMF, dimethylformamide; ECM, extracellular matrix; EDTA, ethylenediaminetetraacetic acid; FBS, fetal bovine serum; HATU, hexafluorophosphate azabenzotriazole tetramethyl uranium; HFIP, 1,1,1,3,3,3-hexafluoroisopropanol; MeOH, methanol; MOPS, 3-(N-morpholino)propanesulfonic acid; Mtt, 4-methyltrityl; NTA, nitrilotriacetic acid; PI, propidium iodide; Rh-His_6, rhodamine-labeled His_6; RP-HPLC, reverse phase high performance liquid chromatography; RPM, revolutions per minute; SEM, scanning electron microscopy; TEM, transmission electron microscopy; TFA, trifluoroacetic acid; TIPS, triisopropylsilane.

were added to the HeLa cells (100 μl total volume) and the mixture was allowed to assemble at 37°C and 5% CO_2 for 2 min to allow for encapsulation of the cells within the matrix. Each well was then diluted with 400 μl of DMEM with 10% FBS and incubated for 1, 3, or 6 days at 37°C and 5% CO_2. Cells were then stained with calcein AM (2.5 μM) and PI (2.5 μM, when applicable) for 15 min with subsequent washing using DMEM with 10% FBS. The samples were imaged using a Nikon A1R multiphoton inverted confocal microscope under a 20x oil objective. Rh-His_6 and PI were excited using a 561-nm laser while calcein AM was excited using a 488-nm laser.

2.8 | Cell release

After encapsulation of HeLa cells within the matrix using the protocol above, the contents of the wells were transferred to Eppendorf tubes and a solution of ethylenediaminetetraacetic acid (EDTA, 100 mM, 50 μl) was added to the mixture to breakdown the matrix. The mixture was incubated at 37°C for 15 min. The cells were centrifuged at 1200 revolutions per minute (RPM) for 7 min and washed with DMEM with 10% FBS followed staining with 0.4% trypan blue at room temperature for 1 min. The cells were then counted using a Neubauer Hemacytometer with DMEM and 10% FBS alone used as a negative control and a treatment with taxol (10 μM) for 3 days in DMEM with 10% FBS as the positive control.

3 | RESULTS AND DISCUSSION

3.1 | Peptide design and synthesis

The peptide design was based on the well-studied GCN4 leucine-zipper motif with modifications for a crosslinked assembly mechanism. The coiled-coil domain of this transcription factor has been studied for self-assembly, as well as for encapsulating small molecules for drug delivery.[41–43] We envisioned installing ligands for metal ions at both the N- and C-termini and the center portion of a trimeric variant of the GCN4 coiled-coil sequence. With this in mind, di-histidine and NTA ligands were installed at the C- and N-termini, respectively (Figures 1 and S1), to facilitate metal ion-promoted linear growth. A bipyridine moiety was also installed within the peptide at a central location on the *f*-face of the coiled-coil to promote radial growth through metal–ligand interactions. The bipyridine ligand installation was completed by replacing Ser14 with an Mtt protected Lys14. In

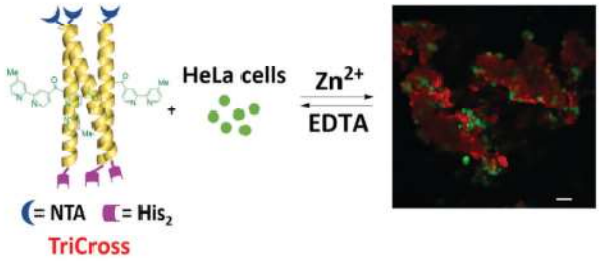

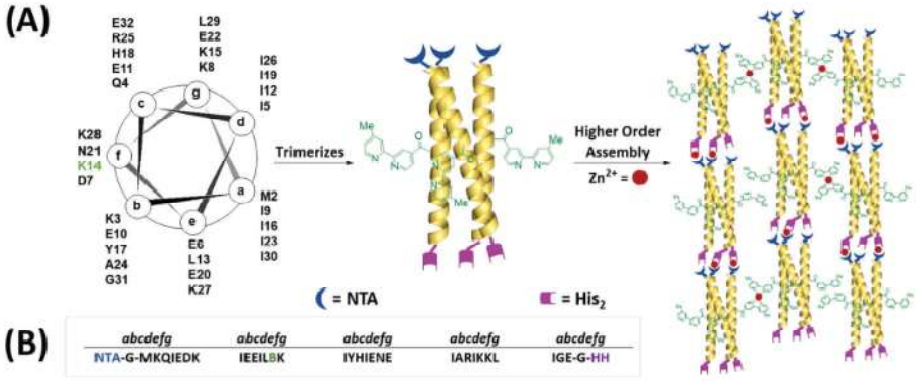

FIGURE 1 TriCross peptide design. (A) Helical wheel representation of **TriCross** with K14 (green) as the site of the bipyridine modification with residues at the *a* and *d* positions dictating a trimeric oligomeric state. Upon addition of metal ions, **TriCross** assembles into a higher order crosslinked structure. (B) GCN4 sequence with modifications for linear (NTA and His_2) and radial (B—bipyridine) growth

2 | MATERIALS AND METHODS

2.1 | Materials

All amino acids and reagents for peptide synthesis were purchased from Chem-Impex Inc and ChemPep. All solvents were purchased from Fisher Scientific. Triisopropylsilane (TIPS), and propidium iodide (PI) were purchased from Sigma-Aldrich. Diisopropylethylamine (DIEA), and all metal salts were purchased from Alfa Aesar. Trifluoroacetic acid (TFA) was purchased from Acros Organics. NovaPEG Rink Amide resin LL was purchased from Novabiochem. The mixed isomer 5/6-carboxy-tetramethyl-rhodamine succinimidyl ester was purchased from ThermoFisher Scientific. Dulbecco's Modified Eagle Medium (DMEM) was purchased from Corning Inc. and fetal bovine serum (FBS) was purchased from R&D Systems. Calcein AM was purchased from BioLegend.

2.2 | General peptide synthesis and purification

TriCross was synthesized using standard Fmoc peptide chemistry on resin. Specifically, Fmoc-His (4 eq) was coupled to NovaPEG Rink Amide resin LL with hexafluorophosphate azabenzotriazole tetramethyl uranium (HATU, 4 eq) and DIEA (8 eq) in dimethylformamide (DMF) for 2.5 h. The resin was washed with DMF (3x), dichloromethane (DCM, 3x), methanol (MeOH, 3x), DCM (3x), and DMF (3x). The newly added histidine was deprotected in 25% piperidine in DMF (V/V) for 30 min. The resin was washed as above, and the next amino acid was coupled. This process was repeated for the remainder of the peptide. After deprotection of the final glycine with piperidine/DMF, tert-butyl protected nitrilotriacetic acid[39] (NTA, 6 eq) was coupled with HATU (6 eq) and DIEA (8 eq) at room temperature for 6 h and washed. Selective on-resin deprotection of the 4-methyltrityl (Mtt) group on lysine was conducted with 30% 1,1,1,3,3,3-hexafluoroisopropanol (HFIP) in DCM (2x) and the resin was washed as above. Treatment with 4′-methyl-2,2′-bipyridine-4-carboxylic acid[40] (6 eq), HATU (6 eq), and DIEA (8 eq) for 6 h followed by the same washing steps afforded the final peptide.

The resin was dried under reduced pressure and cleaved using a 95% TFA, 2.5% TIPS, 2.5% H_2O cocktail for 2.5 h. The resin was washed once with the cleavage cocktail and twice with DCM. The washes were combined and the solvent was removed under reduced pressure. The peptide was precipitated using cold diethyl ether. The precipitate was centrifuged at 2000 g for 10 min, and the supernatant was decanted. The solid was dried under reduced pressure and dissolved in water to create a 10-mg/ml solution. The peptide was purified to homogeneity on a Waters reverse phase high performance liquid chromatography (RP-HPLC) instrument using a Luna C18 semi-prep column with an eluent consisting of solvent A (CH_3CN/0.1% TFA) and solvent B (H_2O/0.1% TFA), a 60-min gradient consisting of 20% to 80% A, and a flow rate of 10 ml/min. The peptide was characterized using matrix-assisted laser desorption ionization time-of-flight mass spectrometry (mass calculated: 4595 g/mol, mass observed: 4593 g/mol).

2.3 | Circular Dichroism

A solution of peptide (50 μM) was prepared in citrate buffer (20 mM, pH 3.0). The circular dichroism (CD) spectrum was taken using a JASCO J-810 CD spectropolarimeter (Jasco Inc.) at room temperature, averaging three scans between 190 and 260 nm. The data pitch was 0.1 nm with a 1-nm bandwidth and the scan rate was 100 nm/min with a 1-s response time.

2.4 | TriCross assembly

TriCross was assembled using a 1-mM peptide and metal concentration ($ZnCl_2$, $NiCl_2$, $CuCl_2$, and $CoCl_2$) in either 3-(N-morpholino)propanesulfonic acid (MOPS, 20 mM, pH = 7.4) or DMEM with 10% FBS. The mixture was incubated at 37°C for 1 hr. The assembly was centrifuged at 10 g for 3 minutes and the supernatant removed and replaced with water. This process was repeated twice.

2.5 | Scanning Electron microscopy

Samples were prepared by placing an aliquot (3 μl) on a glass side attached to a metal stub with copper tape. The sample was allowed to air dry and coated with platinum for 60 seconds. The sample was imaged using an FEI NOVA NANO SEM field emission scanning electron microscope (SEM) using an Everhart-Thornley or high-resolution through the lens detector. Samples were imaged at an accelerating voltage of 5 kV and a working distance of 3–5 mm with a 30-μm aperture.

2.6 | Transmission Electron microscopy

Samples were prepared by placing an aliquot (3 μl) onto a 400-mesh copper grid coated in formvar with a carbon film (Electron Microscopy Sciences) that was glow discharged and allowed to absorb for 1 min. The droplet was wicked away and stained using 2% uranyl acetate (Electron Microscopy Sciences). The assembly was visualized using a Tecnai T20 transmission electron microscope (TEM, FEI Company) operated at 100 KV, with a spot size of 3, 200-μm condenser aperture, and 70-μm objective aperture. Images were captured using a Gatan US1000 2Kx2K CCD camera (Scientific Instruments and Application).

2.7 | Cell encapsulation

HeLa cells were cultured in DMEM supplemented with 10% FBS and 1% penicillin/streptomycin at 37°C and 5% CO_2. A suspension of HeLa cells (50,000 per well) in DMEM with 10% FBS was prepared in an 8-well Lab-Tek chambered slide. **TriCross** (1 mM), $ZnCl_2$ (1 mM), and rhodamine-labeled His_6 (Rh-His_6)[41] (20 μM, when applicable)

this way, the three ligands on each peptide strand of the trimer would be organized within the coiled-coil trimer to promote crosslinked assembly in the presence of metal ions. This unique peptide was dubbed **TriCross** to represent the Trimeric oligomeric state and its Crosslinked assembly strategy (Figure 1).

Standard solid-phase peptide synthesis was conducted for the preparation of **TriCross** using ChemMatrix resin containing a Rink amide linker. The NTA and bipyridine ligands were synthesized using protocols described previously, and the NTA moiety was installed at the N-terminus.[39,40] Selective removal of the Mtt protecting group using HFIP, followed by treatment with 4′-methyl-2,2′-bipyridine-4-carboxylic acid installed the bipyridine moiety within the peptide. The peptide was cleaved from resin using a TFA cocktail, purified to homogeneity via RP-HPLC (95% purity, Figure S2), and characterized by matrix-assisted laser desorption ionization time-of-flight mass spectrometry.

3.2 | Assembly of TriCross

The triple functionalization of the trimeric variant of the GCN4 coiled-coil could potentially lead to a disruption of the helical conformation of the peptide. The structure of **TriCross** was investigated using CD spectroscopy (Figure 2). The spectrum revealed an alpha helical conformation with ~60% helicity, indicated by the local minima at 208 nm and 222 nm and a local maximum at 194 nm. Though the bipyridine, NTA, and di-histidine moieties did decrease the helicity somewhat when compared to the native trimeric peptide (90% helicity),[44] **TriCross** retained an alpha helical conformation. Furthermore, the coiled-coil nature of **TriCross** was confirmed through comparison of the magnitude of the ellipticities at 208 and 222 nm. A value of $\theta_{222}/\theta_{208} \geq 1$ has been shown for coiled-coil peptides, and the value for TriCross (1.4) confirms the coiled-coil nature of this sequence.[45]

With the vision of using **TriCross** as a scaffold for 3D cell culturing, the metal-mediated peptide assembly was attempted in DMEM with 10% FBS using a 1-mM concentration of **TriCross** and $ZnCl_2$. An immediate (~1 min) precipitate was observed upon addition of the metal, and the morphology of the peptide assembly was studied using SEM following a 1 h incubation at 37°C. These assembly conditions (1:1 peptide:metal ratio) led to a 3D matrix structure (Figure 3). Additional peptide to metal ratios of 1:0.4 and 1:0.1 were analyzed, and as the concentration of the metal ion was decreased there was a corresponding decrease in the amount of assembly observed (Figure S3). A 1:2 ratio led to a similar morphology as that obtained for the 1:1 ratio (Figure S3). Therefore, to limit potential excess of metal ions, a 1:1 ratio of **TriCross** to Zn^{2+} was pursued for cell studies. Different metal ions were tested, including Ni^{2+}, Cu^{2+}, and Co^{2+}, and these led to similar morphologies as the Zn^{2+} experiments (Figure S4). Although the coordination geometry is different around these divalent metal ions, their corresponding 3D assemblies are similar. Also, the binding of His to a Ni (II) – NTA complex is about an order of magnitude tighter than for the corresponding Zn^{2+} complex.

Previous hierarchical assembly of coiled-coils revealed a banding pattern representative of the length of a coiled-coil.[46] With this in mind, we investigated the **TriCross** assemblies formed in MOPS buffer (20 mM, pH 7.4) by TEM. Evidence of pronounced banding was observed with assemblies in MOPS buffer (Figure 4—see Figure S5 for SEM data). The separation of the bands in this pattern (4.5 ± 0.7 nm, n = 15) correlates to the length of the **TriCross** coiled-coil (4.8 nm), indicating organized structural features within the assembly.

With a robust **TriCross** assembly, cells might be encapsulated and grown over an extended period of time. Therefore, it is essential that the assembly was stable to prolonged treatment with media. To this end, **TriCross** was incubated with DMEM with 10% FBS at 37°C for seven days. SEM micrographs showed minimal changes in the morphology of the matrix (Figure S6), indicating that this material could be used for 3D cell culturing. Interestingly, the **TriCross** matrix could be disassembled under mild conditions with EDTA (Figure 5), thereby providing a potential means to release cells from the 3D matrix on demand.

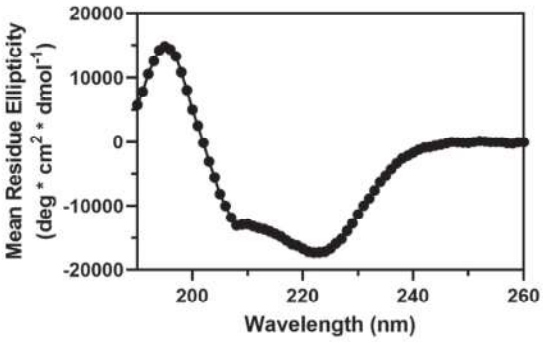

FIGURE 2 Circular dichroism (CD) spectrum of the coiled-coil peptide, **TriCross** (50 μM), measured in citrate buffer (pH 3.0, 20 mM)

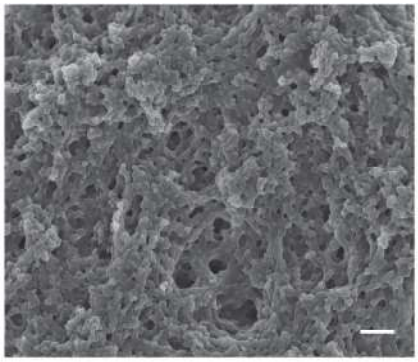

FIGURE 3 Scanning electron microscopy (SEM) image of **TriCross** assembly with $ZnCl_2$ (1 mM each) in Dulbecco's Modified Eagle Medium (DMEM) with 10% fetal bovine serum (FBS) after 1 hr (scale bar: 1 μm)

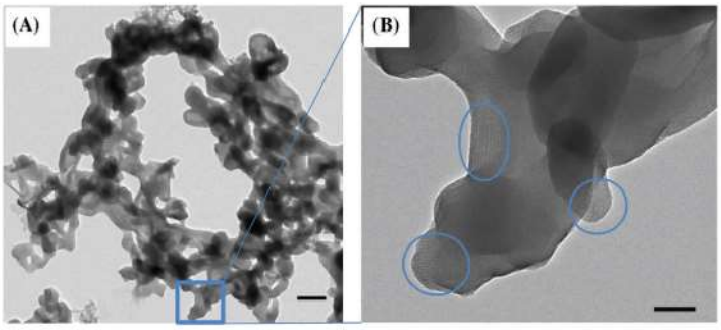

FIGURE 4 Transmission electron microscopy (TEM) images of **TriCross** assembly with $ZnCl_2$ (1 mM each) in 20-mM MOPS buffer (pH 7.4) after 1 h. (A) A wider view (scale bar: 250 nm) and (B) a closer view with some areas of banding indicated with blue circles (scale bar: 50 nm)

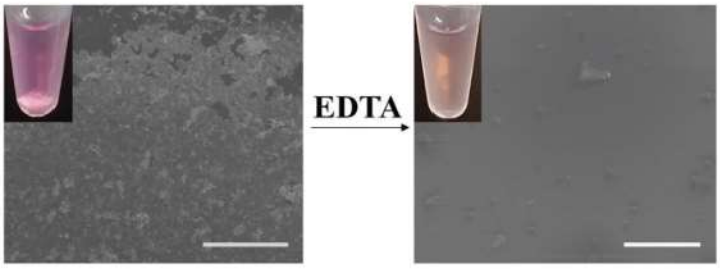

FIGURE 5 Scanning electron microscopy (SEM) images of **TriCross** assembly and disassembly in Dulbecco's Modified Eagle Medium (DMEM) (pink) with 10% fetal bovine serum (FBS) through addition of EDTA (100 mM) (scale bar: 100 μm)

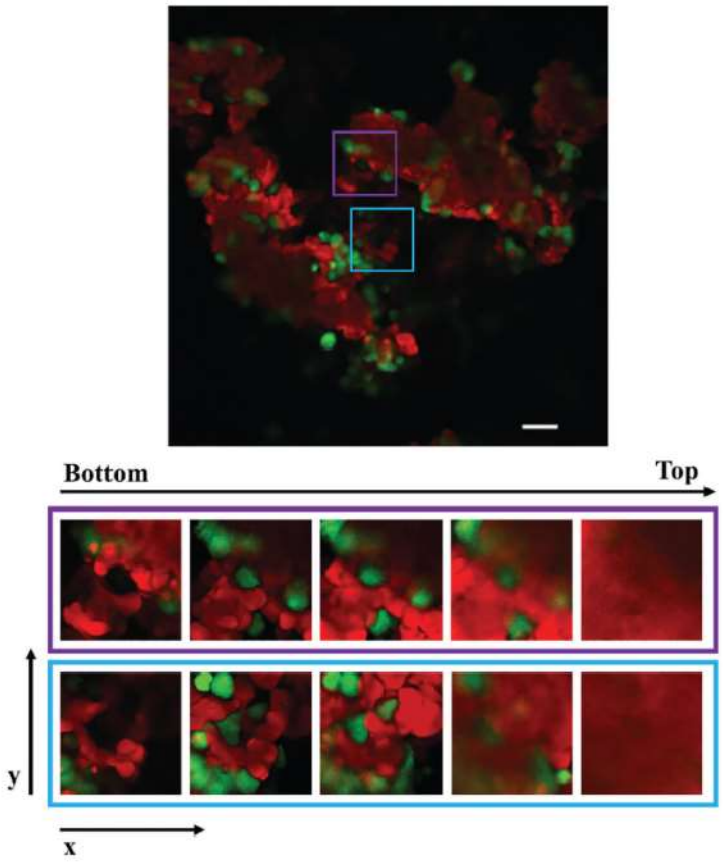

FIGURE 6 Confocal microscopy image of live HeLa cells (green) encapsulated within the **TriCross** assembly labeled with Rh-His_6 (red) in DMEM with 10% FBS (scale bar: 50 μm)

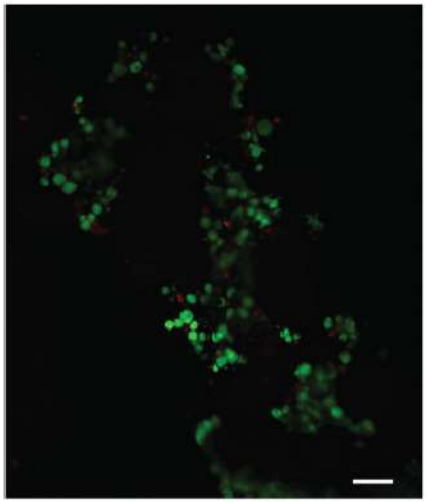

FIGURE 7 Confocal microscopy image of HeLa cells encapsulated within the **TriCross** assembly in Dulbecco's Modified Eagle Medium (DMEM) with 10% fetal bovine serum (FBS) (live—green and dead—red) after a 3-day encapsulation period (scale bar: 50 μm)

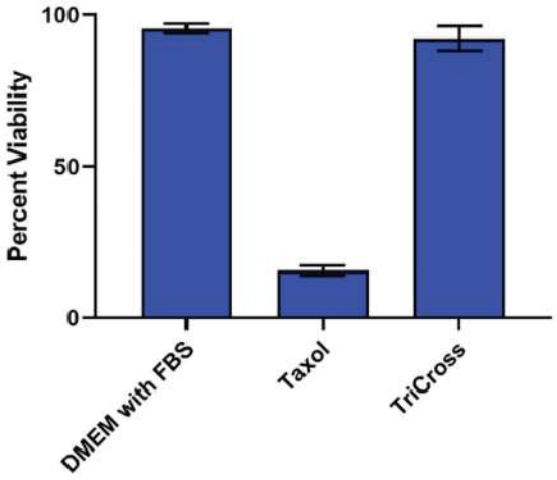

FIGURE 8 Viability of HeLa cells upon disassembly of the **TriCross** matrix with EDTA as compared to untreated cells (Dulbecco's Modified Eagle Medium, DMEM, and 10% fetal bovine serum, FBS) and cells treated with taxol (10 μM)

3.3 | HeLa cell encapsulation

With the ability to assemble and disassemble **TriCross** under mild conditions suitable for cells, we sought to encapsulate cells within the 3D matrix. HeLa cells were first suspended in DMEM with 10% FBS, followed by addition of **TriCross** and $ZnCl_2$ (1 mM each) to the cells in media to create the 3D scaffold around the cells. In order to visualize the matrix, we added Rh-His_6 (20 μM) during the assembly, thereby incorporating the fluorophore through His_6-metal ion interactions and staining the matrix red, an addition that did not change the morphology of the assembly (see Figure S7 for SEM data). Live cells were stained post-assembly with calcein AM (2.5 μM) (Figure 6). Through visualization of varying planes of focus with confocal microscopy, it was confirmed that the HeLa cells were indeed encapsulated within the 3D matrix (Figure 6).

Following the initial encapsulation, cell viability in this 3D cell culture environment was studied over extended time periods. HeLa cells were suspended in DMEM with 10% FBS and encapsulated upon addition of **TriCross** and $ZnCl_2$ (1 mM each) as described above. Although encapsulated, live and dead cells were stained after a 3 day period using calcein AM and PI, respectively (2.5 μM each), and visualized by confocal microscopy. Increased levels of cells were observed encapsulated within the 3D matrix as a function of time, and these displayed significant viability (Figure 7), as was also observed after a 6 day period (Figure S8).

3.4 | Release of encapsulated cells

Finally, the viability of the encapsulated cells was quantified following disassembly of the 3D scaffold with EDTA. After a 3 day encapsulation period, the matrix was collected and subjected EDTA (100 mM, 50 μl) for 15 min at 37°C. The added EDTA chelates Zn^{2+}, effectively reversing metal–ligand interactions between coiled-coils and disassembles the matrix. Upon breakdown of the material, the cells were collected, washed with DMEM and stained with 0.4% trypan blue for 1 min. Live/dead cell populations were counted and viability was compared to untreated cells and cells subjected to taxol (10 μM) (Figure 8). Excellent cell viability was observed with cells encapsulated within the **TriCross** material for 3 days (~92%). These data demonstrate that the assembly and disassembly of **TriCross** occurs under conditions that are mild to cells, and the scaffold is suitable for 3D cell culture.

4 | CONCLUSIONS

To summarize, the trimeric variant of the GCN4 coiled-coil was modified to facilitate a cross-linked, higher-order assembly through installation of metal binding ligands at the termini and center of the peptide. This approach led to assembly of a robust 3D matrix in media with serum, that remained stable for extended periods of time. These data are interesting in comparison to the peptide **TriByp1** with only the bipyridine ligand, which formed banded ribbons in a metal-independent fashion.[46] Utilizing the reversibility of the assembly through addition and removal of metal, HeLa cells were encapsulated and subsequently released from the **TriCross** 3D scaffold with minimal cytotoxicity. Overall, the design of the **TriCross** peptide led to a biomaterial with the potential to serve as a ECM mimic with controllable functions in vitro.

ACKNOWLEDGEMENT

This work was funded by the National Science Foundation, 1609406-CHE.

CONFLICT OF INTEREST

The authors declare no potential conflict of interest.

ORCID

Michael D. Jorgensen https://orcid.org/0000-0001-9273-7955
Jean Chmielewski https://orcid.org/0000-0003-4958-7175

REFERENCES

1. Frantz C, Stewart KM, Weaver VM. The extracellular matrix at a glance. *J Cell Sci*. 2010;123(24):4195-4200. https://doi.org/10.1242/jcs.023820
2. Lee S, Lee HJ, Hwang HS, Ko K, Wook D, Ko K. Optimization of Matrigel-based culture for expansion of neural stem cells. *Animal Cells Syst*. 2015;19(3):175-180. https://doi.org/10.1080/19768354.2015.1035750
3. Laflamme MA, Chen KY, Naumova AV, et al. Cardiomyocytes derived from human embryonic stem cells in pro-survival factors enhance function of infarcted rat hearts. *Nat Biotechnol*. 2007;25(9):1015-1024. https://doi.org/10.1038/nbt1327
4. Ghanaati S, Schlee M, Webber MJ, et al. Evaluation of the tissue reaction to a new Bilayered collagen matrix in vivo and its translation to the clinic. *Biomed Mater*. 2011;6(1):015010. https://doi.org/10.1088/1748-6041/6/1/015010
5. Liu Z, Vunjak-novakovic G. Modeling tumor microenvironments using custom-designed biomaterial scaffolds. *Curr Opin Chem Eng*. 2016;11:94-105. https://doi.org/10.1016/j.coche.2016.01.012
6. Lv D, Hu Z, Lu LIN, Lu H, Xu X. Three-dimensional cell culture: a powerful tool in tumor research and drug discovery (review). *Oncol Lett*. 2017;14:6999-7010. https://doi.org/10.3892/ol.2017.7134
7. Aisenbrey EA, Murphy WL. Synthetic alternatives to Matrigel. *Nat Rev Mater*. 2020;5(7):539-551. https://doi.org/10.1038/s41578-020-0199-8
8. Wu Y, Collier JH. α-helical coiled-coil peptide materials for biomedical applications. *WIREs Nanomed Nanobiotechnol*. 2017;9(April):1-17. https://doi.org/10.1002/wnan.1424
9. Acar H, Srivastava S, Ji E, et al. Self-assembling peptide-based building blocks in medical applications. *Adv Drug Deliv Rev*. 2017;110–111:65-79. https://doi.org/10.1016/j.addr.2016.08.006
10. Yang Z, Xu H, Zhao X. Designer self-assembling peptide hydrogels to engineer 3D cell microenvironments for cell constructs formation and precise oncology remodeling in ovarian cancer. *Adv Sci*. 2020;7(9):1903718. https://doi.org/10.1002/advs.201903718
11. Strauss K, Chmielewski J. Advances in the design and higher-order assembly of collagen mimetic peptides for regenerative medicine. *Curr Opin Biotechnol*. 2017;46:34-41. https://doi.org/10.1016/j.copbio.2016.10.013
12. Banwell EF, Abelardo ES, Adams DJ, et al. Rational design and application of responsive α-helical peptide hydrogels. *Nat Mater*. 2009;8(7):596-600. https://doi.org/10.1038/nmat2479
13. Yao M, Yang J, Du M, et al. Polypeptide-engineered physical hydrogels designed from the coiled-coil region of cartilage Oligomeric matrix protein for three-dimensional cell culture. *J Mater Chem B*. 2014;2(20):3123-3132. https://doi.org/10.1039/c4tb00107a
14. Dexter AF, Fletcher NL, Creasey RG, Filardo F, Boehm MW, Jack KS. Fabrication and characterization of hydrogels formed from designer coiled-coil fibril-forming peptides. *RSC Adv*. 2017;7(44):27260-27271. https://doi.org/10.1039/c7ra02811c
15. Mizuguchi Y, Mashimo Y, Mie M, Kobatake E. Temperature-responsive multifunctional protein hydrogels with elastin-like polypeptides for 3-D angiogenesis. *Biomacromolecules*. 2020;21(3):1126-1135. https://doi.org/10.1021/acs.biomac.9b01496
16. Sun X, He M, Wang L, Luo L, Wang J, Xiao J. Luminescent biofunctional collagen mimetic nanofibers. *ACS Omega*. 2019;4(15):16270-16279. https://doi.org/10.1021/acsomega.9b00740
17. Hernandez-gordillo V, Chmielewski J. Mimicking the extracellular matrix with functionalized. *Metal-Assembled Collagen Peptide Scaffolds Biomaterials*. 2014;35(26):7363-7373. https://doi.org/10.1016/j.biomaterials.2014.05.019
18. Jin H, Jang J, Chung J, et al. Biomimetic self-templated hierarchical structures of collagen-like peptide Amphiphiles. *Nano Lett*. 2015;15(10):7138-7145. https://doi.org/10.1021/acs.nanolett.5b03313
19. Strauss K, Chmielewski J. Metal-promoted assembly of two collagen mimetic peptides into a biofunctional "spiraled horn" scaffold. *Materials*. 2016;9(10):838-848. https://doi.org/10.3390/ma9100838
20. Rubert Perez CM, Panitch A, Chmielewski J. A collagen peptide-based physical hydrogel for cell encapsulation. *Macromol Biosci*. 2011;11(10):1426-1431. https://doi.org/10.1002/mabi.201100230
21. Pires MM, Przybyla DE, Chmielewski J. A metal–collagen peptide framework for three-dimensional cell culture. *Angew Chem*. 2009;121(42):7953-7957. https://doi.org/10.1002/ange.200902375
22. Luo J, Tong YW. Self-assembly of collagen-mimetic peptide Amphiphiles into biofunctional Nanofiber. *ACS Nano*. 2011;5(10):7739-7747. https://doi.org/10.1021/nn202822f
23. Onak G, Gokumen O, Yarali ZB, Karaman O. Enhanced osteogenesis of human Mesenchymal stem cells by self-assembled peptide hydrogel functionalized with glutamic acid Templated peptides. *J Tissue Eng Regen Med*. 2020;14:1236-1249. https://doi.org/10.1002/term.3095
24. Yamada Y, Patel NL, Kalen JD, Schneider JP. Design of a Peptide-Based Electronegative Hydrogel for the direct encapsulation, 3D culturing, in vivo syringe-based delivery, and long-term tissue engraftment of cells. *ACS Appl Mater Interfaces*. 2019;11(38):34688-34697. https://doi.org/10.1021/acsami.9b12152
25. Koutsopoulos S, Zhang S. Long-term three-dimensional neural tissue cultures in functionalized self-assembling peptide hydrogels. *Matrigel and Collagen I Acta Biomater*. 2013;9(2):5162-5169. https://doi.org/10.1016/j.actbio.2012.09.010
26. Hogrebe NJ, Gooch KJ. Direct influence of culture dimensionality on human Mesenchymal stem cell differentiation at various matrix Stiffnesses using a fibrous self-assembling peptide hydrogel. *J Biomed Mater Res Part a*. 2016;104A(9):2356-2368. https://doi.org/10.1002/jbm.a.35755
27. Kisiday J, Jin M, Kurz B, et al. Self-assembling peptide hydrogel fosters chondrocyte extracellular matrix production and cell division: implications for cartilage tissue repair. *PNAS*. 2002;99(15):9996-10001.
28. Wee Y, Moore AN, Jia S, Zhou J, Colombo JS, D'Souza RN. A single-step self-assembly approach for the fabrication of aligned and multilayered three-dimensional tissue constructs using multidomain peptide hydrogel. *SLAS Technol*. 2019;24(1):55-65. https://doi.org/10.1177/2472630318777759
29. Black KA, Lin BF, Wonder EA, et al. Biocompatibility and characterization of a peptide Amphiphile hydrogel for applications in peripheral nerve regeneration. *Tissue Eng Part a*. 2015;21(7-8):1333-1342. https://doi.org/10.1089/ten.tea.2014.0297
30. Ji W, Zaida A, Edelbrock AN, Sato K, Stupp SI. Bioactive nano fibers induce neural Transdifferentiation of human bone marrow Mesenchymal stem cells. *ACS Appl Mater Interfaces*. 2018;10(48):41046-41055. https://doi.org/10.1021/acsami.8b13653
31. Greene JJ, Mcclendon MT, Stupp SI, Richter CP. Electrophysiological assessment of a peptide amphiphile nanofiber nerve graft for facial nerve repair. *J Tissue Eng Regen Med*. 2018;12(6):1389-1401. https://doi.org/10.1002/term.2669

32. Stevenson MD, Piristine H, Hogrebe NJ, et al. A self-assembling peptide matrix used to control stiffness and binding site density supports the formation of microvascular networks in three dimensions. *Acta Biomater*. 2013;9(8):7651-7661. https://doi.org/10.1016/j.actbio.2013.04.002
33. Semino CE, Kasahara J, Hayashi Y. Entrapment of migrating hippocampal neural cells in three-dimensional peptide Nanofiber scaffold. *Tissue Eng*. 2004;10(3):643-655.
34. Gungormus M, Branco M, Fong H, Schneider JP, Tamerler C, Sarikaya M. Self assembled bi-functional peptide hydrogels with biomineralization-directing peptides. *Biomaterials*. 2010;31(28):7266-7274. https://doi.org/10.1016/j.biomaterials.2010.06.010
35. Haines-butterick L, Rajagopal K, Branco M, et al. Controlling hydrogelation kinetics by peptide design for three-dimensional encapsulation and injectable delivery of cells. *PNAS*. 2007;104(19):7791-7796.
36. Holmes TC, de Lacalle S, Su X, Liu G, Rich A, Zhang S. Extensive neurite outgrowth and active synapse formation on self-assembling peptide scaffolds. *PNAS*. 2000;97(12):6728-6733.
37. Gelain F, Bottai D, Vescovi A, Zhang S. Designer self-assembling peptide Nanofiber scaffolds for adult mouse neural stem cell 3-dimensional cultures. *PLoS One*. 2006;1(1):e119. https://doi.org/10.1371/journal.pone.0000119
38. Beniash E, Hartgerink JD, Storrie H, Stendahl JC, Stupp SI. Self-assembling peptide amphiphile nanofiber matrices for cell entrapment. *Acta Biomater*. 2005;1(4):387-397. https://doi.org/10.1016/j.actbio.2005.04.002
39. Huang Z, Park JI, Watson DS, Hwang P, Szoka FC. Facile synthesis of multivalent Nitrilotriacetic acid (NTA) and NTA conjugates for analytical and drug delivery applications. *Bioconjug Chem*. 2006;17(6):1592-1600. https://doi.org/10.1021/bc060222b
40. Banerjee T, Rawalekar S, Das A, Ghosh HN. Interfacial electron transfer dynamics of two newly synthesized catecholate bound RuII polypyridyl-based sensitizers on TiO_2 nanoparticle surface—a femtosecond pump probe spectroscopic study. *Eur J Inorg Chem*. 2011;2011(27):4187-4197. https://doi.org/10.1002/ejic.201100411
41. Nepal M, Sheedlo MJ, Das C, Chmielewski J. Accessing three-dimensional crystals with incorporated guests through metal-directed coiled-coil peptide assembly. *J am Chem Soc*. 2016;138(34):11051-11057. https://doi.org/10.1021/jacs.6b06708
42. Nambiar M, Chmielewski J. Self-assembling coiled-coil peptide nanotubes with biomolecular cargo encapsulation. *ACS Biomater Sci Eng*. 2019;5(10):5082-5087. https://doi.org/10.1021/acsbiomaterials.9b01304
43. More HT, Zhang KS, Srivastava N, Frezzo JA, Montclare JK. Influence of fluorination on protein-engineered coiled-coil fibers. *Biomacromolecules*. 2015;16(4):1210-1217. https://doi.org/10.1021/bm5019062
44. O'Shea EK, Rutkowski R, Kim PS. Evidence that the leucine zipper is a coiled coil. *Science*. 1989;243(4890):538-542.
45. Lau SYM, Taneja AK, Hodges S. Synthesis of a model protein of defined secondary and quaternary structure. *J Biol Chem*. 1984;21:13253-13261.
46. Nambiar M, Wang LS, Rotello V, Chmielewski J. Reversible hierarchical assembly of Trimeric coiled-coil peptides into banded Nano- and Microstructures. *J am Chem Soc*. 2018;140(40):13028-13033. https://doi.org/10.1021/jacs.8b08163

SUPPORTING INFORMATION

Additional supporting information may be found online in the Supporting Information section at the end of this article.

How to cite this article: Jorgensen MD, Chmielewski J. Reversible crosslinked assembly of a trimeric coiled-coil peptide into a three-dimensional matrix for cell encapsulation and release. *J Pep Sci*. 2021;e3302. https://doi.org/10.1002/psc.3302

ACS OMEGA

http://pubs.acs.org/journal/acsodf

Article

Co-assembled Coiled-Coil Peptide Nanotubes with Enhanced Stability and Metal-Dependent Cargo Loading

Michael D. Jorgensen and Jean Chmielewski*

Cite This: *ACS Omega* 2022, 7, 20945−20951

Read Online

ACCESS | Metrics & More | Article Recommendations | Supporting Information

ABSTRACT: Peptide nanotube biomaterials are attractive for their range of applications. Herein, we disclose the co-assembly of coiled-coil peptides, one with ligands for metal ions that demonstrate hierarchical assembly into nanotubes, with spatial control of the metal-binding ligands. Enhanced stability of the nanotubes to phosphate-buffered saline was successfully accomplished in a metal-dependent fashion, depending on the levels and placement of the ligand-containing coiled-coil peptide. This spatial control also allowed for site-specific labeling of the nanotubes with His-tagged fluorophores through the length of the tubes or at the termini, in a metal-dependent manner.

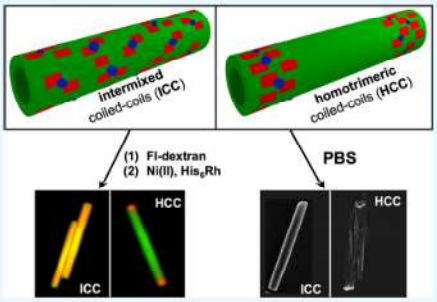

INTRODUCTION

Nanotube biomaterials have drawn significant attention for their applications ranging from piezoelectric devices to cargo delivery.[1] While less common than simpler nanofibrils, these three-dimensional materials contain an inner cavity and outer shell to allow for multifunctionality. Peptide-based nanotubes specifically are an attractive choice owing to their tunability and biocompatibility.[2−4] As such, peptide nanotubes have been derived from a diverse collection of structures including dipeptides,[5−9] cyclic peptides,[10−25] peptoids,[26−29] triple helices,[30,31] β-sheets,[32−35] and coiled-coils.[36−42]

The assembly and morphology of peptide nanotubes provide the opportunity for a range of interesting biological applications. For example, early studies with cyclic peptide nanotubes focused on interactions with the cell membrane to mimic membrane-bound proteins and form ion channels.[10,11,19−21,23] Since then, nanotubes have been developed with antibacterial properties, including dipeptide nanotubes clearing biofilms[7] and cyclic peptide nanotubes lysing bacterial membranes.[12,25] β-sheet nanotubes have been used for directed delivery of an anticancer agent to metastatic melanoma,[34] whereas coiled-coil nanotubes, composed of the peptide **TriNL** (Figure 1A), for instance, have been loaded with a biopolymer cargo.[42]

Coiled-coil nanotubes of **TriNL** have the potential for molecular storage and drug delivery, but instability in phosphate-buffered saline (PBS) limited biological applications. Herein, we demonstrate the co-assembly of **TriNL** with a variant containing metal-binding ligands that produces nanotubes with enhanced PBS stability in a metal-dependent manner while also promoting His-tagged cargo binding.

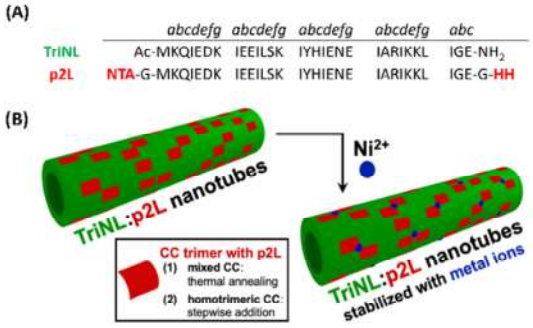

Figure 1. Peptide nanotube co-assemblies. (A) Peptide sequences of the coiled-coil (CC) peptides **TriNL** and **p2L**. (B) Schematic of co-assembly strategies for incorporating **p2L** into **TriNL** nanotubes for potential stabilization with metal ions: forming mixed peptide CC through thermal annealing and using stepwise addition to bring in CC trimers of **p2L**.

Received: March 19, 2022
Accepted: May 30, 2022
Published: June 10, 2022

https://doi.org/10.1021/acsomega.2c01669
ACS Omega 2022, 7, 20945−20951

EXPERIMENTAL SECTION

Circular Dichroism. A **TriNL-Fl** solution (50 μM) was prepared in citrate buffer (10 mM, pH 3.0). The circular dichroism (CD) spectrum was taken at 4 and at 90 °C by averaging three scans between 190 and 260 nm.

Fluorimetry. A 15 μL aliquot of a 550 μM **TriNL-Fl** solution with varying **p2L** concentrations was annealed (90 °C for 30 min, 4 °C for >18 h). The samples were diluted with 985 μL of PBS and fluorescence measurements were conducted with an excitation wavelength of 490 ± 2.5 nm and an emission bandwidth of 0.5 nm.

Annealed Assemblies. Peptide solutions were prepared in 15 μL aliquots and annealed (90 °C for 30 min, 4 °C for >18 h). These aliquots were added to 35 μL of 2-(*N*-morpholino)-ethanesulfonic acid buffer (MES, pH 6.0) to create a final buffer concentration of 50 mM and a total peptide concentration of 500 μM. Following a 30 min incubation at room temperature, the assemblies were centrifuged at 10,000*g* for 3 min where the supernatant was removed and replaced with water. This process was repeated two more times.

Stepwise Assemblies. Assemblies were conducted with a total peptide concentration of 500 μM in a final MES buffer concentration of 50 mM (pH 6.0). Specifically, **TriNL** and **p2L** were separately added to the MES buffer in the same buffer ratio as the peptide ratio. After a 2 min incubation at room temperature, **p2L** was added to **TriNL** and allowed to assemble for an additional 30 min. The samples were centrifuged at 10,000*g* for 3 min. The supernatant was removed, replaced with water, and the process was repeated twice.

Scanning Electron Microscopy. Aliquots of the assemblies described above (3 μL) were placed on a glass coverslip attached to a metal stub via a copper tape. The samples were either air-dried or lyophilized and platinum-coated. Samples were imaged using an FEI Teneo Volumescope field emission scanning electron microscope.

Degradation Studies. Peptides were assembled using the protocol above. Following washing, the samples were incubated in 1 mM $NiCl_2$ for 1 h at room temperature. The material was centrifuged at 10,000*g* for 3 min, the supernatant was removed, and the samples were resuspended in 50 μL of 1× PBS for 24 h at room temperature.

Cargo Binding. Peptides were assembled using the protocol above in the presence of 1 mg/mL fluorescein-labeled anionic dextran (MW 40,000). Following washing, the samples were incubated in 1 mM $NiCl_2$ for 1 h at room temperature. The material was centrifuged at 10,000*g* for 3 min, and the supernatant was removed followed by resuspension in 50 mM MES buffer (pH 6.0) and 20 μM Rh-His_6. After a 48 h incubation, the samples were washed as above and imaged on a Nikon A1R multiphoton inverted confocal microscope under a 100× oil objective using 488 and 561 nm excitation lasers.

RESULTS AND DISCUSSION

Co-assembled Peptide Nanotube Design. The design of the stabilized nanotubes is based on the leucine-zipper motif of the transcription factor GCN4. A dimeric coiled-coil in its native form and the GCN4 sequence have been modified to form trimeric coiled-coils.[43] This trimeric sequence was the basis of the **TriNL** peptide (Figure 1A) that assembles into nanotubes while encapsulating the biopolymer cargo.[42] However, upon exposure to PBS, these coiled-coil peptide tubes were found to rapidly deteriorate. To promote stability, therefore, we hypothesized that the introduction of a coiled-coil peptide with metal-binding ligands as a part of the nanotubes might strengthen the interactions between coiled-coils in a metal-dependent fashion and potentially decrease the rate of tube degradation (Figure 1B). To this end, we looked at the coiled-coil peptide **p2L** with di-histidine and nitrilotriacetic acid (NTA) ligands at the C- and N-termini, respectively (Figures 1A and S1).[44] The **p2L** peptide alone has been shown to form hexagonal crystals with zinc ions,[44] but here we wished to investigate what levels of **p2L** could be added to **TriNL** while retaining the tube morphology and whether stabilized nanotubes would result (Figure 1B).

In the design of nanotubes comprised of two peptides, heterotrimeric coiled-coil mixtures composed of both **TriNL** and **p2L** or individual homotrimers of **TriNL** and **p2L** could be used as building blocks (Figure 1B). Herein, both coiled-coil assemblies were explored, either through prior thermal annealing or sequential addition of the two peptides, to allow for spatial control of **p2L** within the nanotubes. These co-assemblies, in turn, may allow us to tune nanotube stability and bring in His-tagged cargo in a metal-dependent fashion.

Peptide Synthesis. Peptides were synthesized using standard Fmoc-based solid-phase peptide synthesis on the ChemMatrix Rink Amide resin with hexafluorophosphate azabenzotriazole tetramethyl uronium (HATU) as a coupling reagent. The protected NTA amino acid was synthesized as previously described.[45] The peptides were cleaved from the resin using a trifluoroacetic acid (TFA) cocktail, purified to homogeneity via reverse-phase high-performance liquid chromatography (HPLC), and characterized via matrix-assisted laser desorption ionization time-of-flight (MALDI-ToF) mass spectrometry (Figures S2 and S3).

Intermixed Coiled-Coil Formation: Thermal Annealing. Previous studies have shown that thermal annealing of two different dimeric coiled-coils can give rise to mixed coiled-coils at statistical levels with their homodimeric counterparts.[46] Motivated by this work, and that of others studying mixed coiled-coils,[47−66] we first pursued a strategy to co-assemble **p2L** and **TriNL** within nanotubes by intermixing the peptides at the supersecondary structure level using thermal annealing. In this way, we could create a mixture of coiled-coils with some containing both **TriNL** and **p2L**.

Circular dichroism (CD) was initially used to study coiled-coil folding by monitoring the two negative absorption bands at 222 and 208 nm. CD spectra were taken at 4 and 90 °C using a 2:1 ratio of **TriNL** and **p2L** (500 μM total peptide concentration, Figure S4). Elevated temperature (90 °C) led to a decrease in helical content from 90 to 58%, and subsequent cooling to 4 °C promoted refolding to 97% α-helicity. It is worth noting that in the low-temperature spectra the magnitude of the absorption at 222 nm is higher than that at 208 nm ($\theta_{222}/\theta_{208} \sim 1.5$), which has been shown to be indicative of the presence of a coiled-coil.[67] At 90 °C, however, this ratio decreased to ~1.1, demonstrating lower levels of the coiled-coil fold.

With CD supporting the refolding of the coiled-coils through thermal annealing, the formation of heterotrimeric coiled-coils was verified using the fluorometric assay of Xiao and co-workers.[68] This assay relies on fluorescence self-quenching of fluorophores at the termini of peptides' trimeric assemblies. With this in mind, fluorescein was installed at the

https://doi.org/10.1021/acsomega.2c01669
ACS Omega 2022, 7, 20945−20951

N-terminus of **TriNL** (**TriNL-Fl**, Figures S5 and S6). If unlabeled **p2L** is introduced into the labeled coiled-coil through thermal annealing, an increase in fluorescence due to less fluorescein self-quenching should result. The coiled-coil refolding process was monitored by measuring the fluorescence of **TriNL-Fl** (8.5 μM) with varying amounts of **p2L** before and after thermal annealing (Figures 2 and S7). All solutions

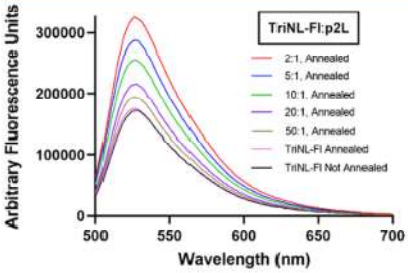

Figure 2. Fluorescence spectra of **TriNL-Fl** (8.5 μM) before and after annealing in the presence of increasing levels of **p2L**.

exhibited similar initial fluorescence readings prior to annealing. Following annealing, however, an increase in fluorescence was observed relative to the amount of **p2L** in solution, with up to a 1.9-fold increase at a ratio of 2:1 **TriNL-Fl:p2L** (Figure 2). Additionally, the fluorescence of **TriNL-Fl** did not increase when annealed in the absence of **p2L**, further demonstrating that any observed increase in fluorescence was due to intermixed coiled-coil formation rather than the annealing process.

Nanotube Formation: Thermally Annealed Samples. With intermixed coiled-coils available through thermal annealing, nanotube formation was investigated. All assembly experiments were conducted with a total peptide concentration of 500 μM in MES buffer (50 mM, pH 6.0) at room temperature for 30 min, with a range of **TriNL:p2L** ratios (1:1−50:1). Upon assembly, the precipitate was collected via centrifugation and washed. Peptide levels within the assemblies were determined by first dissolving the material with aqueous HCl, followed by quantitation using reverse-phase UPLC (Figure S8 and Table S1). The experimentally determined ratios of **TriNL** and **p2L** in the assemblies were quite similar to starting ratios of the two peptides in solution, indicating that both of the peptides entered the materials at levels close to the added amounts.

Scanning electron microscopy (SEM) was used to determine if the **TriNL** nanotube morphology (Figure 3A) was maintained with the added **p2L**. Indeed, upon increasing the amount of **p2L** up to a ratio of 10:1 **TriNL:p2L** (Figure 3B−D), we observed definitive nanotubes, with lengths in the 10−15 μm range and inner diameters in the range of 400−800 nm (n = 10). From these experiments and the UPLC data, we can confirm that up 9% incorporation of **p2L** (10:1) still allows the nanotubes to form. Interestingly, assemblies that form with 17−33% of **p2L** (5:1 and 2:1) have a hexagonal rod morphology (Figure 3E,F), with an inner channel in the case of the 5:1 ratio. A 1:1 ratio of peptides provided similar rods as the 2:1 mixtures (Figure S9), although lower levels of assembly were observed. Although no metals are used in these experiments, this observed morphology is reminiscent of the assemblies formed with **p2L** and metal ions, albeit the current

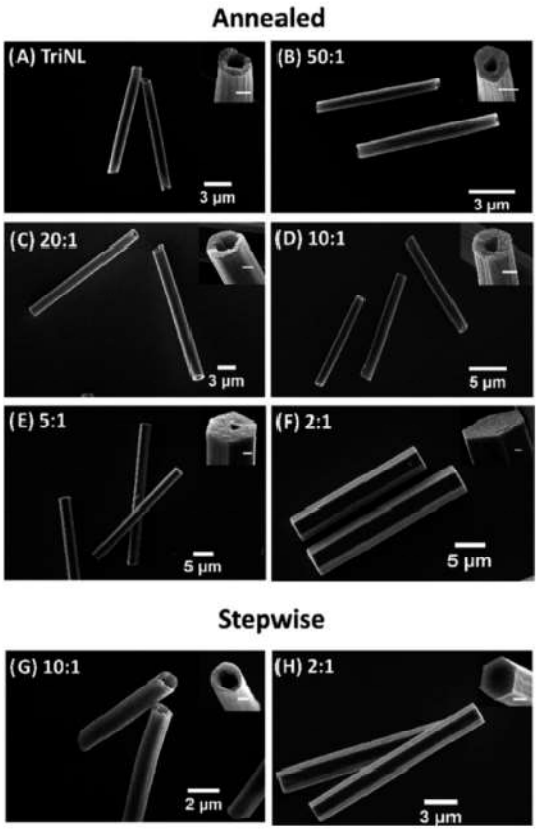

Figure 3. SEM visualization of assemblies of (A) **TriNL** and at different ratios of **TriNL:p2L**. (B−F) Annealed samples and (G, H) stepwise addition of the peptide. Insets show the interior morphology of the assemblies (inset scale bar: 500 nm).

assemblies have an increased aspect ratio (~3.5-times increase in the length/diameter).[44] It is important to note that **p2L** does not assemble on its own, without metal ions, under these conditions.

Nanotube Stability Studies: Thermally Annealed Samples. Nanotubes formed only with **TriNL** exhibit limited stability in the presence of PBS buffer with degradation of the tubes at the termini and dissolution into shard-like tube fragments (Figure 4A).[42] The introduction of the ligand-containing **p2L** peptide, through thermal annealing, allows for the potential of using metal−ligand interactions to increase the stability of the tubes. With this in mind, the degradation of the nanotube co-assemblies in PBS was investigated at different **TriNL:p2L** ratios with added **Ni**(II), a metal ion that has been used extensively for **H**is-tags with NTA. Preformed nanotubes were first incubated in $NiCl_2$ (1 mM, 1 h) and subsequently resuspended in PBS (10 mM phosphate, 137 mM NaCl, pH 7.4) for 24 h. The resulting materials were imaged using SEM. With low levels of **p2L** (2−5%), there was distinct erosion at the ends into the center of the nanotubes upon exposure to PBS (Figure 4B,C). Increasing the **p2L** content to 9%, however, resulted in intact nanotubes (Figure 4D). In the absence of Ni(II), the co-assembled nanotubes were found to degrade more substantially than with **TriNL** alone, with only

https://doi.org/10.1021/acsomega.2c01669
ACS Omega 2022, 7, 20945−20951

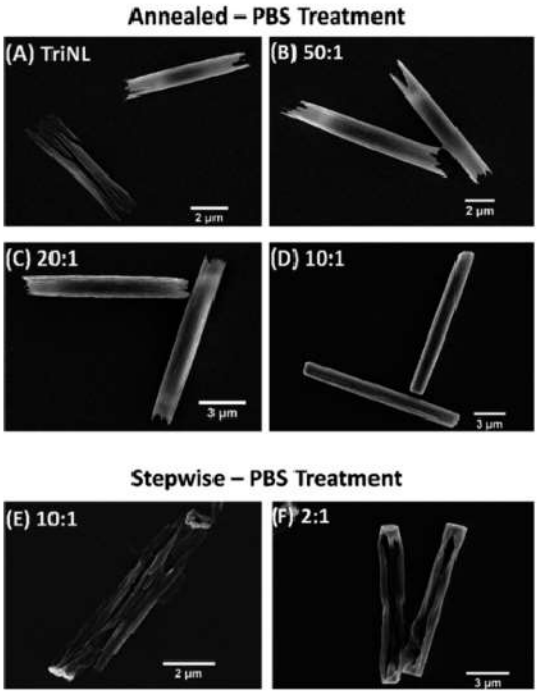

Figure 4. Stability of nanotubes formed with **TriNL** or **TriNL:p2L** ratios after a 24 h incubation with PBS. (A) **TriNL** alone; (B–D) pre-annealed **TriNL:p2L** at a (B) 50:1 ratio, (C) 20:1 ratio, and (D) 10:1 ratio; and (E, F) stepwise addition of **TriNL:p2L** at a (E) 10:1 ratio and (F) 2:1 ratio.

small pieces of nanotubes remaining (Figure S10). The addition of **p2L** may be destabilizing the tubes due to the charge ligands at each terminus. Overall, these data support the idea that the observed nanotube stabilization is derived from metal–ligand interactions from **p2L** within the nanotubes.

Nanotube Cargo Loading: Thermally Annealed Samples. The presence of ligands for metal ions within the mixed coiled-coil nanotubes presents the opportunity of using these interactions to facilitate the binding of the cargo functionalized with metal-binding ligands. Previously, the **TriNL** nanotubes were shown to encapsulate fluorescently labeled anionic dextrans within their interior.[42] Similarly, the co-assembled nanotubes resulting from thermally annealed peptide mixtures also encapsulated anionic, fluorescein-labeled dextrans (Figure 5A). However, after treating both of these tubes with $NiCl_2$ (1 mM, 1 h), followed by treatment with His-tagged rhodamine (Rh-His_6, 20 μM, 48 h), only the nanotubes co-assembled with **p2L** were found to have rhodamine fluorescence throughout the tubes (Figure 5B vs S11). Also, without the addition of Ni(II), no Rh-His_6 association with the mixed coiled-coil tubes was observed (Figure S12). These data demonstrate the importance of metal-loaded ligands within the nanotubes for His-tagged fluorophore binding and suggest that **p2L** is distributed throughout the assembly.

Nanotube Formation and Stability: Stepwise Addition. Motivated by the results of nanotube cargo loading and stability after including **p2L** into the **TriNL** tubes using thermal annealing, we sought an additional way to control the

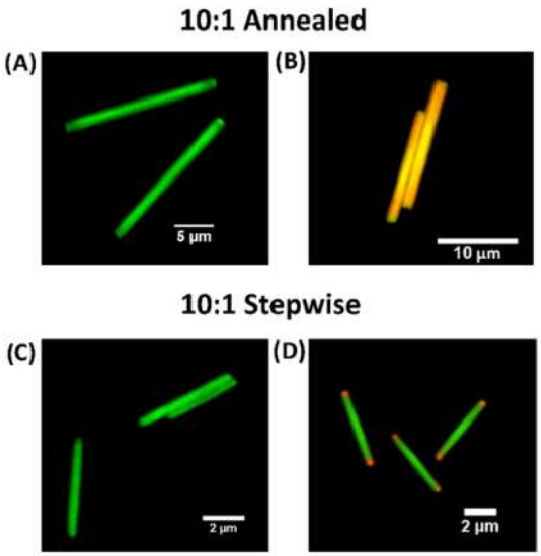

Figure 5. Confocal microscopy of co-assembled **TriNL:p2L** nanotubes. (A,B) Annealed nanotubes with encapsulated fluorescein-labeled dextran (1 mg/mL, 40 kD) (A) alone and (B) with pretreated $NiCl_2$ (1 mM) followed by Rh-His_6 (20 μM). (C,D) Nanotubes from stepwise addition with encapsulated fluorescein-labeled dextran (1 mg/mL, 40 kD) (C) alone and (D) with pretreated $NiCl_2$ (1 mM) followed by Rh-His_6 (20 μM). (B) and (D) Overlay of both the red and green channels.

location of the ligand-containing **p2L** peptide within the nanotubes. To this end, we investigated the addition of individual coiled-coils of **TriNL** and **p2L** in a stepwise fashion at 10:1 and 2:1 ratios. Attempts to simultaneously add the two peptides led to results that were difficult to replicate. Therefore, we chose to add the **p2L** coiled-coils to **TriNL** trimers after a 2 min incubation of the latter peptide in MES buffer (50 mM, pH 6.0). The combined peptides (500 μM total) were then incubated at room temperature for 30 min, and the precipitates were collected and washed. SEM analysis of the assemblies demonstrated morphologies that were similar to those obtained with the thermally annealed, co-assembled nanotubes. The 10:1 **TriNL:p2L** ratio provided nanotubes (Figure 3G), whereas the 2:1 ratio led to hexagonal rods with an aspect ratio of ~9 (length/diameter) (Figure 3H). UPLC analysis was used to determine the levels of **p2L** in the tubes/rods after acid treatment to dissolve the assemblies. As opposed to the thermally annealed samples, the assemblies formed from stepwise addition contained substantially lower levels of the ligand-containing **p2L** (10:0.3 and 2:0.5 **TriNL:p2L** ratios, respectively) (Table S2).

Although the nanotubes obtained from the two different assembly techniques at a 10:1 ratio of peptides looked similar at the micron scale, the two sets of tubes behaved quite differently when treated first with $NiCl_2$ and then with PBS. The nanotube morphology was retained in the thermally annealed co-assemblies in PBS after metal ion treatment (Figure 4D), whereas the sequential assemblies showed notable disintegration of the tube interior with PBS, with the ends of the tubes remained somewhat intact (Figure 4E). This latter PBS degradation pattern was also observed after Ni(II)

https://doi.org/10.1021/acsomega.2c01669
ACS Omega 2022, 7, 20945−20951

treatment of the nanorods derived from the sequential assembly of the 2:1 ratio of peptides (Figure 4F). Regions of the interior of the hexagonal rods were eaten away leaving hollow shells with defined ends. These data may indicate that the ends of these nanotubes/rods are rich in **p2L** coiled-coils and addition of metal ions could stabilize these regions. To determine if these terminal ends contain more **p2L** than the entire structure, the 10:1 and 2:1 stepwise assemblies and their corresponding PBS-degraded materials (Figure 4E,F) were dissolved with aqueous HCl, and their peptide contents were quantified via UPLC (Table S2). We observed an increase in the **p2L** levels after PBS treatment of 2.7- and 6.8-fold, respectively, compared to the intact nanotubes/rods. These data indicate that the percentage of **p2L** is higher at the ends than in the center of the material. It is likely that substantial nanotube/rod formation occurs with **TriNL** in the 2 min prior to **p2L** addition, thereby leading to an abundance of **p2L** near the ends of the assemblies.

Nanotube Cargo Loading: Sequential Coiled-Coil Addition. As an additional means to verify the location of the metal-binding **p2L**, we also investigated where His-tagged rhodamine binds to the co-assembled nanotubes formed from sequential addition. Preformed nanotubes (10:1) with encapsulated dextran (Figure 5C) were subjected to Ni(II) incubation followed by Rh-His_6. Even after extended periods of time (48 h), rhodamine fluorescence was only observed at the termini of the nanotubes (Figure 5D). In contrast to the annealed assemblies where the **p2L** peptide is likely distributed throughout the tubes, all of the above observations provide support for the **p2L** coiled-coils being substantially localized near the end of the nanotubes when added sequentially (Figure 6).

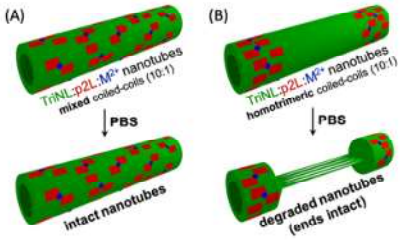

Figure 6. Schematic of PBS stability results for the two strategies of **p2L** incorporation into **TriNL** nanotubes. (A) Annealed samples led to **p2L** distribution throughout the tubes via intermixed coiled-coils resulting in metal ion stabilization throughout the length of the nanotubes. (B) Stepwise addition of individual coiled-coils led to the concentration of **p2L** near the ends of the nanotubes, followed by treatment with metal ions, resulting in PBS degradation of the center of the tubes.

CONCLUSIONS

Peptide-based nanotubes hold great promise for molecular storage and drug delivery. Coiled-coil nanotubes derived from the peptide **TriNL** have been shown to encapsulate biopolymers, but instability to PBS has limited their bioapplications.[42] Herein, we have demonstrated a means of incorporating the coiled-coil forming peptide **p2L**, which contains ligands for metal ions at both termini, into nanotube assemblies with **TriNL**. It was possible to tune the position of **p2L** in the assemblies, either distributed throughout the tubes or localized near the ends, depending on whether intermixed or individual coiled-coils of **p2L** and **TriNL** were used. Indeed, this spatial control of the position of **p2L** has led to both stabilized nanotubes or tubes with stabilized ends, upon addition of metal ions (Figure 6). Metal-charged ligands derived from **p2L** were also harnessed to bring His-tagged fluorophores to the full length or the termini of the nanotubes, providing an additional readout for the placement of the **p2L** peptide in the assemblies. The encapsulated cargo within the nanotubes should have differing release profiles depending on the stability of the tubes. It is likely that metal ion-based stabilization will slow down the kinetics of the release of the cargo from the nanotubes, since the tubes are more intact. Future experiments will focus on the range of cargoes that may be placed on and within the structure of these coiled-coil nanotubes.

ASSOCIATED CONTENT

Supporting Information

The Supporting Information is available free of charge at https://pubs.acs.org/doi/10.1021/acsomega.2c01669.

Contains materials, synthesis and HPLC analysis, CD and fluorescence data, and microscopy images (PDF)

AUTHOR INFORMATION

Corresponding Author

Jean Chmielewski − *Department of Chemistry, Purdue University, West Lafayette, Indiana 47907, United States;* orcid.org/0000-0003-4958-7175; Email: chml@purdue.edu

Author

Michael D. Jorgensen − *Department of Chemistry, Purdue University, West Lafayette, Indiana 47907, United States*

Complete contact information is available at: https://pubs.acs.org/10.1021/acsomega.2c01669

Notes

The authors declare no competing financial interest.

ACKNOWLEDGMENTS

This work was supported by the National Science Foundation through grant CHE-2108722.

REFERENCES

(1) Shimizu, T.; Ding, W.; Kameta, N. Soft-Matter Nanotubes: A Platform for Diverse Functions and Applications. *Chem. Rev.* **2020**, *120*, 2347−2407.

(2) Hamley, I. W. Peptide Nanotubes. *Angew. Chem., Int. Ed.* **2014**, *53*, 6866−6881.

(3) Rodríguez-Vázquez, N.; Amorín, M.; Granja, J. R. Recent Advances in Controlling the Internal and External Properties of Self-Assembling Cyclic Peptide Nanotubes and Dimers. *Org. Biomol. Chem.* **2017**, *15*, 4490−4505.

(4) Song, Q.; Cheng, Z.; Kariuki, M.; Hall, S. C. L.; Hill, S. K.; Rho, J. Y.; Perrier, S. Molecular Self-Assembly and Supramolecular Chemistry of Cyclic Peptides. *Chem. Rev.* **2021**, *121*, 13936−13995.

(5) Yemini, M.; Reches, M.; Gazit, E.; Rishpon, J. Peptide Nanotube-Modified Electrodes for Enzyme - Biosensor Applications. *Anal. Chem.* **2005**, *77*, 5155−5159.

(6) Emtiazi, G.; Zohrabi, T.; Lee, L. Y.; Habibi, N.; Zarrabi, A. Covalent Diphenylalanine Peptide Nanotube Conjugated to Folic Acid/Magnetic Nanoparticles for Anti-Cancer Drug Delivery. *J. Drug Delivery Sci. Technol.* **2017**, *41*, 90−98.

(7) Porter, S. L.; Coulter, S. M.; Pentlavalli, S.; Thompson, T. P.; Laverty, G. Self-Assembling Diphenylalanine Peptide Nanotubes Selectively Eradicate Bacterial Biofilm Infection. *Acta Biomater.* **2018**, *77*, 96−105.
(8) Saha, P. C.; Bera, T.; Chatterjee, T.; Samanta, J.; Sengupta, A.; Bhattacharyya, M.; Guha, S. Supramolecular Dipeptide-Based Near-Infrared Fluorescent Nanotubes for Cellular Mitochondria Targeted Imaging and Early Apoptosis. *Bioconjugate Chem.* **2021**, *32*, 833−841.
(9) Yaman, Y. T.; Bolat, G.; Abaci, S.; Saygin, T. B. Peptide Nanotube Functionalized Molecularly Imprinted Polydopamine Based Single-Use Sensor for Impedimetric Detection of Malathion. *Anal. Bioanal. Chem.* **2021**, No. 0123456789.
(10) Ghadiri, M. R.; Granja, J. R.; Buehler, L. K. Artificial Transmembrane Ion Channels from Self-Assembling Peptide Nanotubes. *Nature* **1994**, *369*, 301−304.
(11) Granja, J. R.; Ghadiri, M. R. Channel-Mediated Transport of Glucose across Lipid Bilayers. *J. Am. Chem. Soc.* **1994**, *116*, 10785−10786.
(12) González-Freire, E.; Novelli, F.; Pérez-Estévez, A.; Seoane, R.; Amorín, M.; Granja, J. R. Double Orthogonal Click Reactions for the Development of Antimicrobial Peptide Nanotubes. *Chem. - Eur. J.* **2021**, *27*, 3029−3038.
(13) Novelli, F.; Vilela, M.; Pazó, A.; Amorín, M.; Granja, J. R. Molecular Plumbing to Bend Self-Assembling Peptide Nanotubes. *Angew. Chem., Int. Ed.* **2021**, *60*, 18838−18844.
(14) Lee, Y. H.; Chang, S. F.; Liaw, J. Anti-Apoptotic Gene Delivery with Cyclo-(D-Trp-Tyr) Peptide Nanotube via Eye Drop Following Corneal Epithelial Debridement. *Pharmaceutics* **2015**, *7*, 122−136.
(15) Ellacott, S. H.; Sanchez-Cano, C.; Mansfield, E. D. H.; Rho, J. Y.; Song, J. I.; Peltier, R.; Perrier, S. Comparative Study of the Cellular Uptake and Intracellular Behavior of a Library of Cyclic Peptide-Polymer Nanotubes with Different Self-Assembling Properties. *Biomacromolecules* **2021**, *22*, 710−722.
(16) Silk, M. R.; Price, J. R.; Mohanty, B.; Leiros, H. K. S.; Lund, B. A.; Thompson, P. E.; Chalmers, D. K. Side-Chain Interactions in d/l Peptide Nanotubes: Studies by Crystallography, NMR Spectroscopy and Molecular Dynamics. *Chem. - Eur. J.* **2021**, *27*, 14489−14500.
(17) Roy, S.; Zheng, L.; Silberbush, O.; Engel, M.; Atsmon-Raz, Y.; Miller, Y.; Migliore, A.; Beratan, D. N.; Ashkenasy, N. Mechanism of Side Chain-Controlled Proton Conductivity in Bioinspired Peptidic Nanostructures. *J. Phys. Chem. B* **2021**, *125*, 12741−12752.
(18) Hartgerink, J. D.; Granja, J. R.; Milligan, R. A.; Ghadiri, M. R. Self-Assembling Peptide Nanotubes. *J. Am. Chem. Soc.* **1996**, *118*, 43−50.
(19) Motesharei, K.; Ghadiri, M. R. Diffusion-Limited Size-Selective Ion Sensing Based on SAM-Supported Peptide Nanotubes. *J. Am. Chem. Soc.* **1997**, *119*, 11306−11312.
(20) Kim, H. S.; Hartgerink, J. D.; Ghadiri, M. R. Oriented Self-Assembly of Cyclic Peptide Nanotubes in Lipid Membranes. *J. Am. Chem. Soc.* **1998**, *120*, 4417−4424.
(21) Karle, I. L.; Perozzo, M. A.; Mishra, V. K.; Balaram, P. Crystal Structure of the Channel-Forming Polypeptide Antiamoebin in a Membrane-Mimetic Environment. *Proc. Natl. Acad. Sci. U.S.A.* **1998**, *95*, 5501−5504.
(22) Ranganathan, D.; Lakshmi, C.; Karle, I. L. Hydrogen-Bonded Self-Assembled Peptide Nanotubes from Cystine-Based Macrocyclic Bisureas. *J. Am. Chem. Soc.* **1999**, *121*, 6103−6106.
(23) Karle, I. L.; Ranganathan, D.; Kumar, M. G.; Nagaraj, R. Design, Synthesis, Conformational and Membrane Ion Transport Studies of Proline-Adamantane Hybrid Cyclic Depsipeptides. *Biopolymers* **2008**, *89*, 471−478.
(24) Rodríguez-Vázquez, N.; García-Fandiño, R.; Aldegunde, M. J.; Brea, J.; Loza, M. I.; Amorín, M.; Granja, J. R. Cis-Platinum Complex Encapsulated in Self-Assembling Cyclic Peptide Dimers. *Org. Lett.* **2017**, *19*, 2560−2563.
(25) Claro, B.; González-Freire, E.; Calvelo, M.; Bessa, L. J.; Goormaghtigh, E.; Amorín, M.; Granja, J. R.; García-Fandiño, R.; Bastos, M. Membrane Targeting Antimicrobial Cyclic Peptide Nanotubes − an Experimental and Computational Study. *Colloids Surf., B* **2020**, *196*, No. 111349.
(26) Vollrath, S. B. L.; Hu, C.; Bräse, S.; Kirshenbaum, K. Peptoid Nanotubes: An Oligomer Macrocycle That Reversibly Sequesters Water via Single-Crystal-to-Single-Crystal Transformations. *Chem. Commun.* **2013**, *49*, 2317−2319.
(27) Sun, J.; Jiang, X.; Lund, R.; Downing, K. H.; Balsara, N. P.; Zuckermann, R. N. Self-Assembly of Crystalline Nanotubes from Monodisperse Amphiphilic Diblock Copolypeptoid Tiles. *Proc. Natl. Acad. Sci. U.S.A.* **2016**, *113*, 3954−3959.
(28) Jin, H.; Ding, Y. H.; Wang, M.; Song, Y.; Liao, Z.; Newcomb, C. J.; Wu, X.; Tang, X. Q.; Li, Z.; Lin, Y.; Yan, F.; Jian, T.; Mu, P.; Chen, C. L. Designable and Dynamic Single-Walled Stiff Nanotubes Assembled from Sequence-Defined Peptoids. *Nat. Commun.* **2018**, *9*, No. 270.
(29) Luo, Y.; Song, Y.; Wang, M.; Jian, T.; Ding, S.; Mu, P.; Liao, Z.; Shi, Q.; Cai, X.; Jin, H.; Du, D.; Dong, W. J.; Chen, C. L.; Lin, Y. Bioinspired Peptoid Nanotubes for Targeted Tumor Cell Imaging and Chemo-Photodynamic Therapy. *Small* **2019**, *15*, No. 1902485.
(30) Merg, A. D.; Touponse, G.; van Genderen, E.; Blum, T. B.; Zuo, X.; Bazrafshan, A.; Siaw, H. M. H.; McCanna, A.; Dyer, R. B.; Salaita, K.; Abrahams, J. P.; Conticello, V. P. Shape-Shifting Peptide Nanomaterials: Surface Asymmetry Enables PH-Dependent Formation and Interconversion of Collagen Tubes and Sheets. *J. Am. Chem. Soc.* **2020**, *142*, 19956−19968.
(31) Jin, Y.; Cai, L.; Yang, Q.; Luo, Z.; Liang, L.; Liang, Y.; Wu, B.; Ding, L.; Zhang, D.; Xu, X.; Zhang, L.; Zhou, F. Anti-Leukemia Activities of Selenium Nanoparticles Embedded in Nanotube Consisted of Triple-Helix β -D-Glucan. *Carbohydr. Polym.* **2020**, *240*, No. 116329.
(32) Han, C.; Sun, X.; Liu, L.; Jiang, H.; Shen, Y.; Xu, X.; Li, J.; Zhang, G.; Huang, J.; Lin, Z.; Xiong, N.; Wang, T. Exosomes and Their Therapeutic Potentials of Stem Cells. *Stem Cells Int.* **2016**, *2016*, 1−11.
(33) Hamley, I. W.; Burholt, S.; Hutchinson, J.; Castelletto, V.; Da Silva, E. R.; Alves, W.; Gutfreund, P.; Porcar, L.; Dattani, R.; Hermida-Merino, D.; Newby, G.; Reza, M.; Ruokolainen, J.; Stasiak, J. Shear Alignment of Bola-Amphiphilic Arginine-Coated Peptide Nanotubes. *Biomacromolecules* **2017**, *18*, 141−149.
(34) Lei, L.; Xu, Z.; Hu, X.; Lai, Y.; Xu, J.; Hou, B.; Wang, Y.; Yu, H.; Tian, Y.; Zhang, W. Bioinspired Multivalent Peptide Nanotubes for Sialic Acid Targeting and Imaging-Guided Treatment of Metastatic Melanoma. *Small* **2019**, *15*, No. 1900157.
(35) Reja, A.; Afrose, S. P.; Das, D. Aldolase Cascade Facilitated by Self-Assembled Nanotubes from Short Peptide Amphiphiles. *Angew. Chem., Int. Ed.* **2020**, *59*, 4329−4334.
(36) Xu, C.; Liu, R.; Mehta, A. K.; Guerrero-Ferreira, R. C.; Wright, E. R.; Dunin-Horkawicz, S.; Morris, K.; Serpell, L. C.; Zuo, X.; Wall, J. S.; Conticello, V. P. Rational Design of Helical Nanotubes from Self-Assembly of Coiled-Coil Lock Washers. *J. Am. Chem. Soc.* **2013**, *135*, 15565−15578.
(37) Wang, F.; Gnewou, O.; Modlin, C.; Beltran, L. C.; Xu, C.; Su, Z.; Juneja, P.; Grigoryan, G.; Egelman, E. H.; Conticello, V. P. Structural Analysis of Cross α-Helical Nanotubes Provides Insight into the Designability of Filamentous Peptide Nanomaterials. *Nat. Commun.* **2021**, *12*, No. 407.
(38) Thomson, A. R.; Wood, C. W.; Burton, A. J.; Bartlett, G. J.; Sessions, R. B.; Brady, R. L.; Woolfson, D. N. Computational Design of Water-Soluble α-Helical Barrels. *Science* **2014**, *346*, 485−489.
(39) Burgess, N. C.; Sharp, T. H.; Thomas, F.; Wood, C. W.; Thomson, A. R.; Zaccai, N. R.; Brady, R. L.; Serpell, L. C.; Woolfson, D. N. Modular Design of Self-Assembling Peptide-Based Nanotubes. *J. Am. Chem. Soc.* **2015**, *137*, 10554−10562.
(40) Thomas, F.; Burgess, N. C.; Thomson, A. R.; Woolfson, D. N. Controlling the Assembly of Coiled-Coil Peptide Nanotubes. *Angew. Chem., Int. Ed.* **2016**, *55*, 987−991.
(41) Thanasupawat, T.; Bergen, H.; Hombach-Klonisch, S.; Krcek, J.; Ghavami, S.; Del Bigio, M. R.; Krawitz, S.; Stelmack, G.; Halayko, A.; McDougall, M.; Meier, M.; Stetefeld, J.; Klonisch, T. Platinum

(IV) Coiled Coil Nanotubes Selectively Kill Human Glioblastoma Cells. *Nanomed.: Nanotechnol., Biol. Med.* **2015**, *11*, 913−925.
(42) Nambiar, M.; Nepal, M.; Chmielewski, J. Self-Assembling Coiled-Coil Peptide Nanotubes with Biomolecular Cargo Encapsulation. *ACS Biomater. Sci. Eng.* **2019**, *5*, 5082−5087.
(43) Harbury, P. B.; Zhang, T.; Kim, P. S.; Alber, T. A Switch between Two-, Three-, and Four-Stranded Coiled Coils. *Science* **1993**, *262*, 1401−1407.
(44) Nepal, M.; Sheedlo, M. J.; Das, C.; Chmielewski, J. Accessing Three-Dimensional Crystals with Incorporated Guests through Metal-Directed Coiled-Coil Peptide Assembly. *J. Am. Chem. Soc.* **2016**, *138*, 11051−11057.
(45) Huang, Z.; Park, J. I.; Watson, D. S.; Hwang, P.; Szoka, F. C. Facile Synthesis of Multivalent Nitrilotriacetic Acid (NTA) and NTA Conjugates for Analytical and Drug Delivery Applications. *Bioconjugate Chem.* **2006**, *17*, 1592−1600.
(46) Holtzer, M. E.; Breiner, T.; Holtzer, A. Hetero-α-Helical, Two-Chain, Coiled Coils: Aβ Hybrid Tropomysin. *Biopolymers* **1984**, *23*, 1811−1833.
(47) Gauba, V.; Hartgerink, J. D. Self-Assembled Heterotrimeric Collagen Triple Helices Directed through Electrostatic Interactions. *J. Am. Chem. Soc.* **2007**, *129*, 2683−2690.
(48) Acevedo-Jake, A. M.; Clements, K. A.; Hartgerink, J. D. Synthetic, Register-Specific, AAB Heterotrimers to Investigate Single Point Glycine Mutations in Osteogenesis Imperfecta. *Biomacromolecules* **2016**, *17*, 914−921.
(49) O'Shea, E. K.; Lumb, K. J.; Kim, P. S. Peptide "Velcro": Design of a Heterodimeric Coiled Coil. *Curr. Biol.* **1993**, *3*, 658−667.
(50) Zhang, K.; Diehl, M. R.; Tirrell, D. A. Artificial Polypeptide Scaffold for Protein Immobilization. *J. Am. Chem. Soc.* **2005**, *127*, 10136−10137.
(51) Mason, J. M.; Schmitz, M. A.; Müller, K. M.; Arndt, K. M. Semirational Design of Jun-Fos Coiled Coils with Increased Affinity: Universal Implications for Leucine Zipper Prediction and Design. *Proc. Natl. Acad. Sci. U.S.A.* **2006**, *103*, 8989−8994.
(52) Thompson, K. E.; Bashor, C. J.; Lim, W. A.; Keating, A. E. Synzip Protein Interaction Toolbox: In Vitro and in Vivo Specifications of Heterospecific Coiled-Coil Interaction Domains. *ACS Synth. Biol.* **2012**, *1*, 118−129.
(53) Domeradzka, N. E.; Werten, M. W. T.; De Wolf, F. A.; De Vries, R. Cross-Linking and Bundling of Self-Assembled Protein-Based Polymer Fibrils via Heterodimeric Coiled Coils. *Biomacromolecules* **2016**, *17*, 3893−3901.
(54) Oude Blenke, E. E.; Van Den Dikkenberg, J.; Van Kolck, B.; Kros, A.; Mastrobattista, E. Coiled Coil Interactions for the Targeting of Liposomes for Nucleic Acid Delivery. *Nanoscale* **2016**, *8*, 8955−8965.
(55) Zheng, T.; Bulacu, M.; Daudey, G.; Versluis, F.; Voskuhl, J.; Martelli, G.; Raap, J.; Sevink, G. J. A.; Kros, A.; Boyle, A. L. A Non-Zipper-like Tetrameric Coiled Coil Promotes Membrane Fusion. *RSC Adv.* **2016**, *6*, 7990−7998.
(56) Chiang, C. H.; Fu, Y. H.; Horng, J. C. Formation of AAB-Type Collagen Heterotrimers from Designed Cationic and Aromatic Collagen-Mimetic Peptides: Evaluation of the C-Terminal Cation-π Interactions. *Biomacromolecules* **2017**, *18*, 985−993.
(57) Groth, M. C.; Rink, W. M.; Meyer, N. F.; Thomas, F. Kinetic Studies on Strand Displacement in: De Novo Designed Parallel Heterodimeric Coiled Coils. *Chem. Sci.* **2018**, *9*, 4308−4316.
(58) Tunn, I.; Harrington, M. J.; Blank, K. G. Bioinspired Histidine-Zn2+ Coordination for Tuning the Mechanical Properties of Self-Healing Coiled Coil Cross-Linked Hydrogels. *Biomimetics* **2019**, *4*, No. 25.
(59) Li, I. C.; Hulgan, S. A. H.; Walker, D. R.; Farndale, R. W.; Hartgerink, J. D.; Jalan, A. A. Covalent Capture of a Heterotrimeric Collagen Helix. *Org. Lett.* **2019**, *21*, 5480−5484.
(60) Walker, D. R.; Hulgan, S. A. H.; Peterson, C. M.; Li, I. C.; Gonzalez, K. J.; Hartgerink, J. D. Predicting the Stability of Homotrimeric and Heterotrimeric Collagen Helices. *Nat. Chem.* **2021**, *13*, 260−269.
(61) Bromley, E. H. C.; Sessions, R. B.; Thomson, A. R.; Woolfson, D. N. Designed α-Helical Tectons for Constructing Multicomponent Synthetic Biological Systems. *J. Am. Chem. Soc.* **2009**, *131*, 928−930.
(62) Fletcher, J. M.; Harniman, R. L.; Barnes, F. R. H.; Boyle, A. L.; Collins, A.; Mantell, J.; Sharp, T. H.; Antognozzi, M.; Booth, P. J.; Linden, N.; Miles, M. J.; Sessions, R. B.; Verkade, P.; Woolfson, D. N. Self-Assembling Cages from Coiled-Coil Peptide Modules. *Science* **2013**, *340*, 595−599.
(63) Thomas, F.; Boyle, A. L.; Burton, A. J.; Woolfson, D. N. A Set of de Novo Designed Parallel Heterodimeric Coiled Coils with Quantified Dissociation Constants in the Micromolar to Sub-Nanomolar Regime. *J. Am. Chem. Soc.* **2013**, *135*, 5161−5166.
(64) Nautiyal, S.; Woolfson, D. N.; King, D. S.; Alber, T. A Designed Heterotrimeric Coiled Coil. *Biochemistry* **1995**, *34*, 11645−11651.
(65) Chains, P.; Chao, H.; Houston, M. E.; Grothe, S.; Kay, C. M.; Connor-mccourt, M. O.; Irvin, R. T.; Hodges, R. S. Kinetic Study on the Formation of a de Novo Designed Heterodimeric Coiled-Coil: Use of Surface Plasmon Resonance To Monitor the Association and Dissociation Of. *Biochemistry* **1996**, *35*, 12175−12185.
(66) Litowski, J. R.; Hodges, R. S. Designing Heterodimeric Two-Stranded α-Helical Coiled-Coils. Effects of Hydrophobicity and α-Helical Propensity on Protein Folding, Stability, and Specificity. *J. Biol. Chem.* **2002**, *277*, 37272−37279.
(67) Lau, S. Y. M.; Taneja, A. K.; Hodges, R. S. Synthesis of a Model Protein of Defined Secondary and Quaternary Structure. Effect of Chain Length on the Stabilization and Formation of Two-Stranded α-Helical Coiled-Coils. *J. Biol. Chem.* **1984**, *259*, 13253−13261.
(68) Sun, X.; Fan, J.; Li, X.; Zhang, S.; Liu, X.; Xiao, J. Colorimetric and Fluorometric Monitoring of the Helix Composition of Collagen-like Peptides at the NM Level. *Chem. Commun.* **2016**, *52*, 3107−3110.

https://doi.org/10.1021/acsomega.2c01669
ACS Omega 2022, 7, 20945−20951